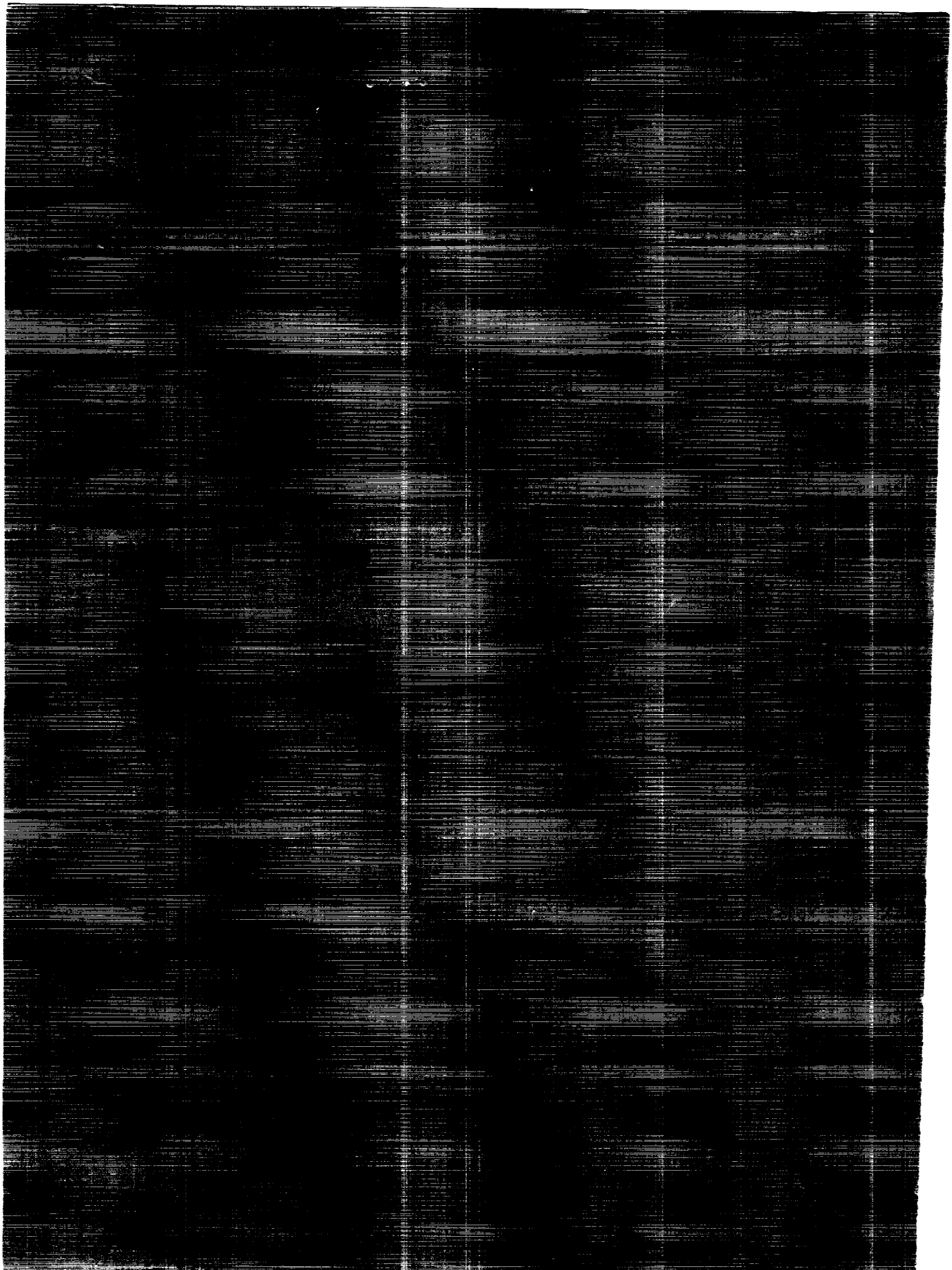

NASA Contractor Report 4175

Electro-Impulse De-Icing Testing Analysis and Design

G. W. Zumwalt, R. L. Schrag,
W. D. Bernhart, and R. A. Friedberg
Wichita State University
Wichita, Kansas

Prepared for
Lewis Research Center
under Grant NAG3-284

National Aeronautics
and Space Administration

**Scientific and Technical
Information Division**

1988

TABLE OF CONTENTS

TABLE OF CONTENTS

TABLE OF CONTENTS

TABLE OF CONTENTS

TABLE OF CONTENTS

CHAPTER 1. THE EIDI DEVELOPMENT PROJECT

I. Introduction

Ice accumulation on aircraft wings in flight has been a danger since the earliest days of flight. The total accumulation needs not be large to be fatal. Although ice normally is accrued on frontward facing surfaces only, giving a few centimeters thickness on the front 2 percent of the wing chord, this is enough to cause flow separation and destroy lift, particularly if the aircraft slows or maneuvers. Also, drag may increase enough to exhaust fuel reserves or destabilize the flight. Helicopter rotors are even more vulnerable to the detrimental effects of ice, and engine inlet diffusers require icing protection to a greater degree than lifting surfaces. This need brought the NASA Lewis Research Center into aircraft icing research almost from its start.

Although several methods of de-icing or anti-icing are available, all have some undesirable aspects in regard to energy requirements or effectiveness. A method suggested (Ref. 1-1) as early as 1937 offers an alternative which has not been adequately developed. The electro-magnetic impulse phenomenon has been used for metals forming, and holds the promise of ice removing with very low energy, minimal maintenance (no moving parts), great reliability, and weight and cost competitive with existing methods.

This report summarizes work done under a NASA-Lewis grant to develop the Electro-Impulse De-Icing (EIDI) system. Wichita State University has been the grant recipient, charged with researching the phenomena to provide the underlying technology, and also with coordinating the efforts of a team of participating industries. The program has consisted of basic analyses, laboratory tests, icing tunnel tests and flight tests. After five years,

the EIDI system has been tested and refined and shown to be a low-energy, highly reliable de-icing method. This report is a final technical report and a documenting of design methods developed.

II. The Basic Principles

The physical form of the Electro-Impulse De-Icing (EIDI) method is shown in Figure 1-1. Flat-wound coils made of copper ribbon wire are placed just inside the leading edge of a wing's skin with a small gap separating skin and coil. Either one or two coils are placed at a given spanwise station, depending on the size and shape of the leading edge. Two methods of supporting coils are shown; support by the front spar or from a beam attached to ribs is generally used, but mounting to the skin itself is sometimes used.

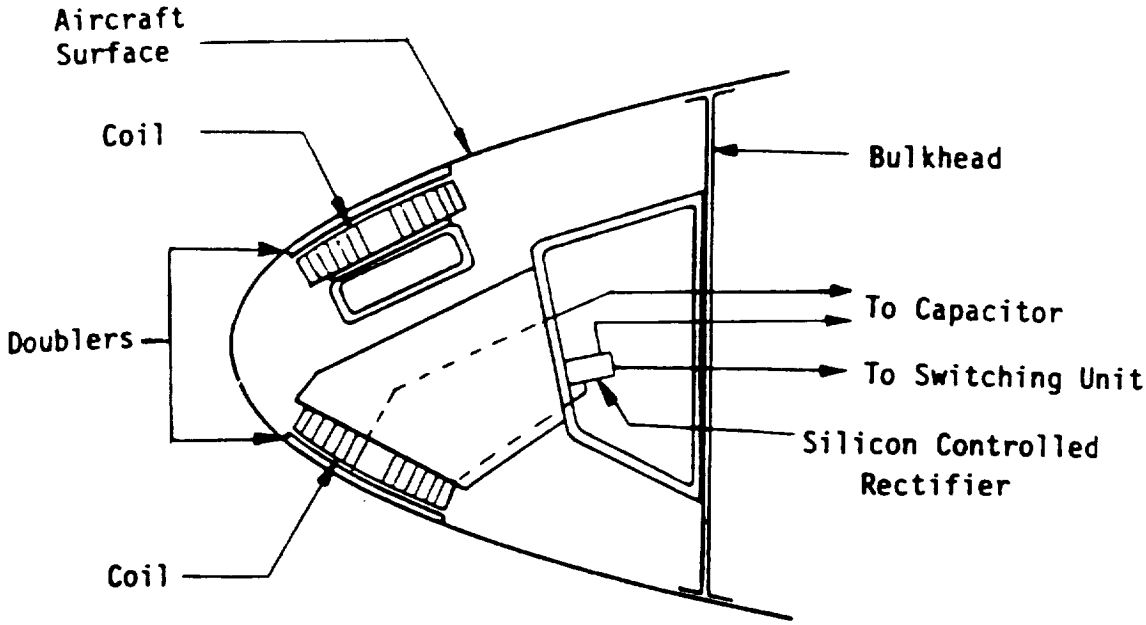

Fig. 1-1 Impulse Coils in a Leading Edge

The coils are connected by low resistance, low inductance cables to a high voltage capacitor bank, and energy is discharged through the coil by a remote signal to a silicon-controlled-rectifier ("thyristor"). Discharge of the capacitor through the coils creates a rapidly forming and collapsing electro-magnetic field which induces eddy currents in the metal skin. The fields resulting from current flow in the coil and skin create a repulsive force of several hundred pounds magnitude, but a duration only a fraction of a millisecond. A small amplitude, high acceleration movement of the skin acts to shatter, debond and expel the ice. Two or three such "hits" are performed sequentially, separated by the time required to recharge the capacitors, then ice is permitted to accumulate until it again approaches an undesirable thickness.

Figure 1-1 also shows "doublers," unalloyed aluminum discs, slightly larger than the coils, bonded to the skin opposite the coil. These are used when the skin thickness is less than the minimum required to provide adequate conductance for the eddy currents. Composite, non-metallic, leading edges require a similar special treatment. A fundamental study of the phenomena and parameters for electro-impulse was undertaken to provide a basis for such geometric and electrical design choices. Prof. R. L. Schrag of Wichita State University has led this study which is presented in Chapter 2. Ref. 1-2 reported initial results of this work, and Ref. 1-11 summarizes the final form of the computer modeling and its validations.

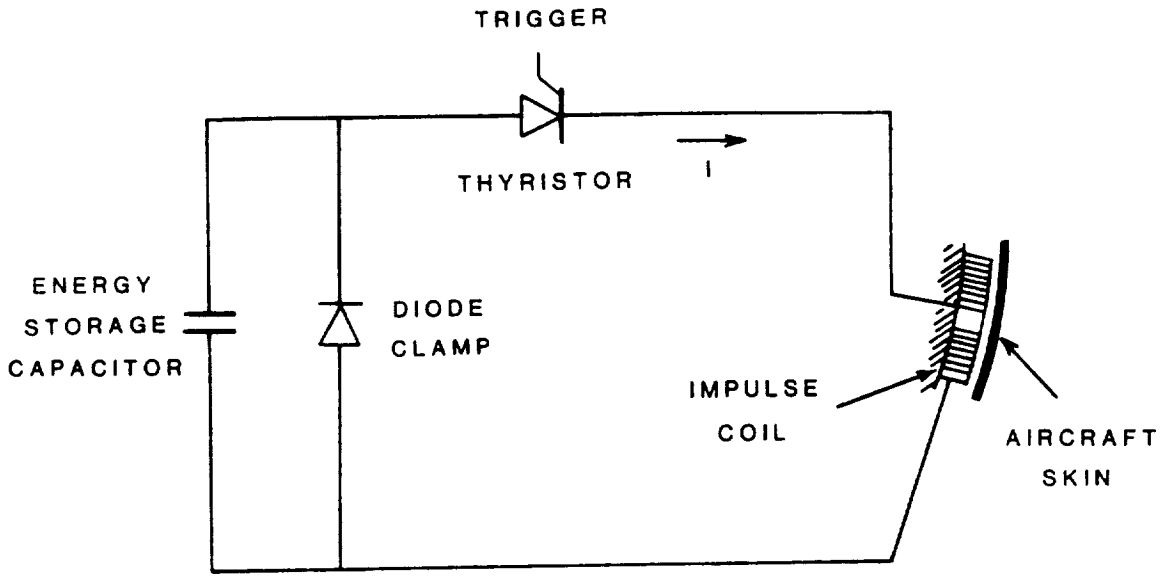

Fig. 1-2 Basic Circuit

In Figure 1-2, the basic circuit is illustrated. An electro-impulse is initiated by supplying a trigger pulse to the thyristor, allowing the capacitor to discharge through the coil. A typical current waveform is shown in Figure 1-3. Since a thyristor has diode properties, the current follows the first positive loop of the RLC response, after which the thyristor re-opens the circuit. This leaves the capacitor reverse-charged. Such reverse charging reduces capacitor life substantially. For that reason a clamping diode is placed across the capacitor. A typical current and resulting skin displacement are shown in Figure 1-3.

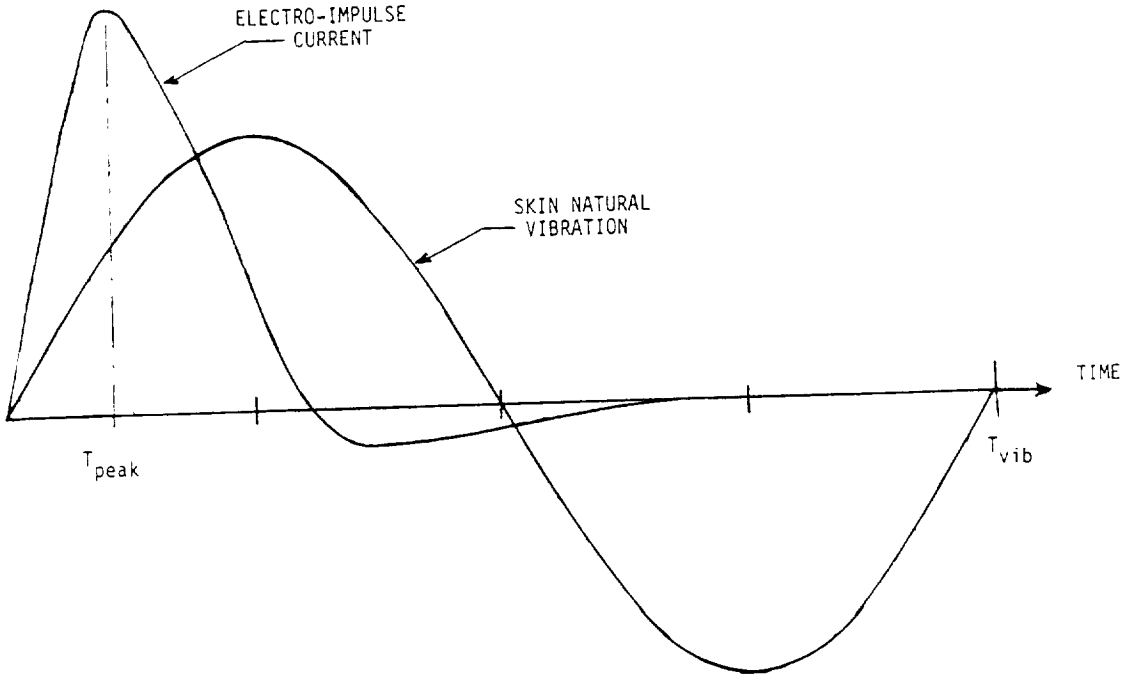

Fig. 1-3 Typical Coil Current and Skin Displacement

Figure 1-4 is a flat geometry illustration of the coil's magnetic field and induced eddy currents in the electrically conducting skin. The magnetic field due to the eddy currents is not shown, but it has a significant influence (by self induction) on the magnitude, time history, and radial distribution of the eddy currents. In addition, the electromagnetic "skin effect" phenomenon affects the eddy current distribution across the aluminum skin thickness. Current densities are greatest on the coil side. A reverse coupling effect is also present. Time-changing eddy currents induce a voltage in the impulse coil, modifying its current. From a circuit aspect, the consequence is a modification of the effective inductance and resistance of the coil. The effective inductance decreases, and the effective resistance increases, due to the proximity of the metal sheet.

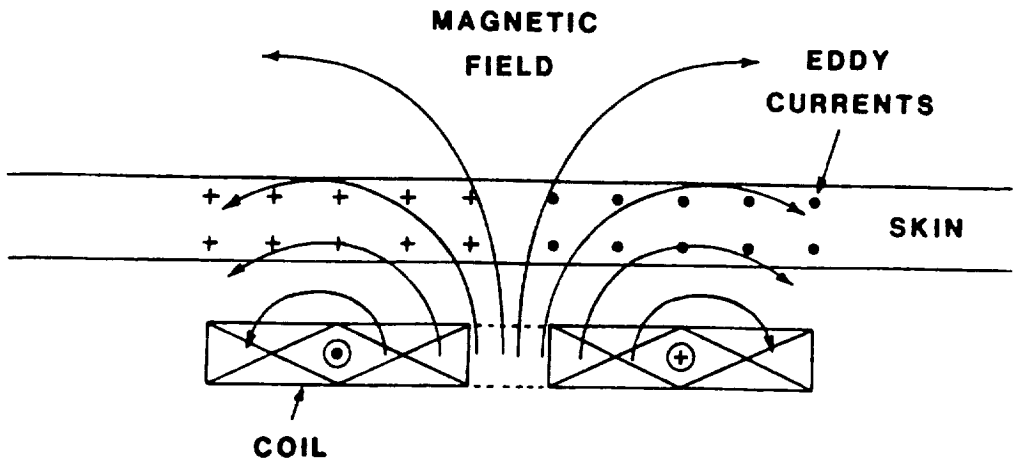

Fig. 1-4 Coil Magnetic Field Pattern and Resulting Eddy Currents

When the aircraft skin moves in response to the electro-impulse force the coil-to-skin gap changes and that modifies the magnitude of the proximity influence. In addition, the skin's movement relative to the coil's magnetic field further modifies (by motional induction) the electromotive forces that drive the eddy currents. These influences due to skin motion are, however relatively small because of the time delay involved in the motion, and appear to be negligible when the skin is ice loaded. The assertion is, in effect, that the coil current and the strength of the force impulse may be calculated without the need to also analyze the complex structural response. This is discussed in detail in Chapter 2.

Figure 1-5 shows a wing with coils placed spanwise, separated by about 0.4 meters. These are all supplied by a single power unit. A more effective modified version is shown in Fig. 1-6. Energy requirements are small,

being comparable to those typical of landing lights for the same size aircraft. De-icing has been accomplished in the icing wind tunnel and in flight for typical general aviation and transport wings under a wide range of velocities, angles of attack, icing rates and temperatures.

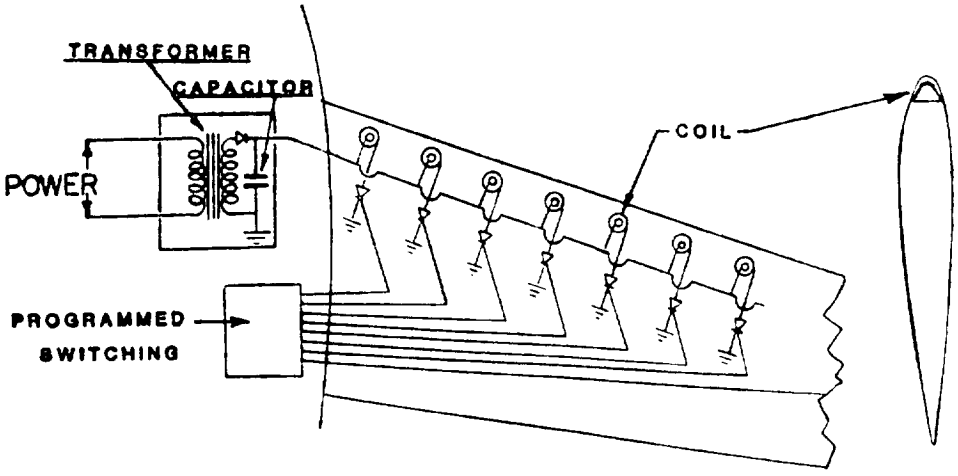

Fig. 1-5 Electro-Impulse Coils Installed in a Wing

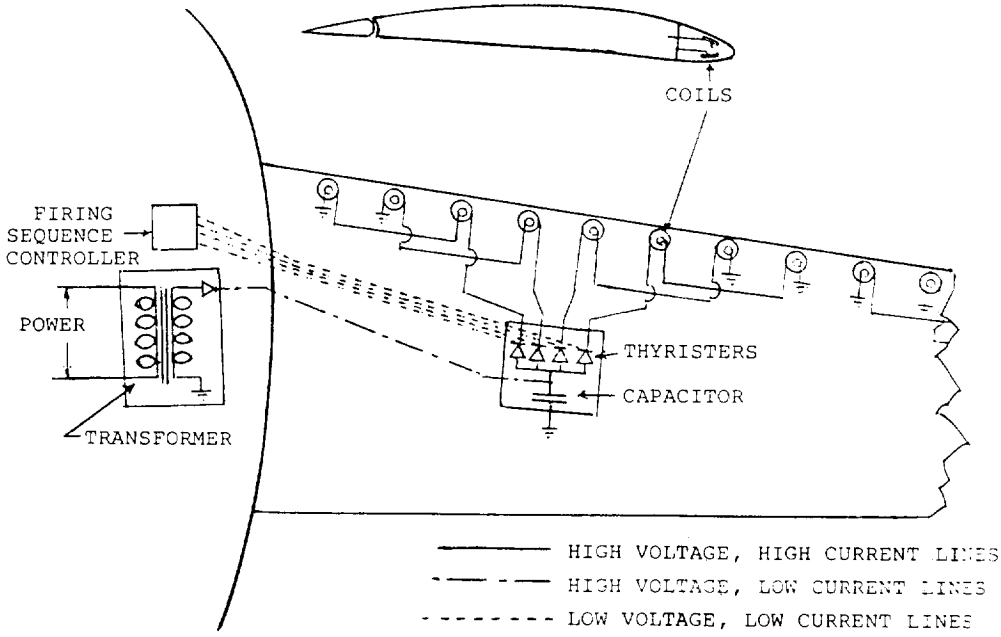

Fig. 1-6 EIDI with Series-Connected Coils
("Odds and Evens")

Just as effective de-icing by electro-impulse requires a matching of electric circuit dynamics and skin electrical properties, so also does it demand properly related structural dynamic matching. The propagation of skin movement in chordwise and spanwise directions from the EIDI coil is necessary. It is also a complex, three-dimensional, transient structural dynamic analysis problem; Ref. 1-3. Coil location and pulse duration must have the proper relations to the structural vibrational mode to be excited. Failure to do so severely impairs the effectiveness of de-icing.

The imposed force cannot be modeled as a simple impulse, since its duration is comparable to the period of the first vibrational mode. Similarly, the force cannot be treated as a concentrated "point" load, since the diameter of the coil is of the same order as the wave lengths of low-order vibrational modes. Thus, structure-dynamic analysis must include the details of the spatial and temporal results of the electro-dynamic analysis.

Under the leadership of Professor Walter D. Bernhart, analytical and experimental studies have been carried out on the structural dynamics of leading edge structures under EIDI-type impulsive loading. These are reported in Chapter 3.

The participation of industry in the project provided constant reminder of the practical aspects of safety, weight, cost and manufacturability. While research and testing were carried on, parallel efforts were made to develop fabricating and design method for the hardware. In particular, coil making and mounting were developed under the leadership of Robert Friedberg. The current state of materials and processes for these, together with testing methods, are given in Chapter 4.

Eleven sets of icing tunnel tests have been essential to the system development. The unique capabilities of the NASA-Lewis Icing Research Tunnel (IRT) provide testing conditions for confident evaluation of the system in flight. Chapter 5 summarizes the IRT tests and results. Reference 1-4 reports in more detail the engine nacelle and large wing testing. Reference 1-9 give additional engine nacelle work.

Chapter 6 gives a brief account of the two flight test programs. These were earlier reported in References 1-5 and 1-6. Finally, Chapter 7 describes systems tests for fatigue of skin or EIDI components and electro-magnetic interference with other aircraft systems." Design methodology was summarized in Reference 1-10.

III. Prior History

The use of electro-magnetic impulse force to remove ice was first suggested by Rudolf Goldschmidt, a German national residing in London before World War II. He was granted a patent (Ref. 1-1) and a series of patent extensions in 1937 through 1939. His patents, now expired, anticipated most of the applications now being used or considered. However, there is no evidence that Goldschmidt ever attempted to build the devices he imagined.

During the 1950's and 1960's, electro-impulse methods were used for metals forming in various industrial processes, but no record can be found of the use for de-icing until researchers in the USSR either discovered Goldschmidt's patents or rediscovered this application independently. In 1965, I.A. Levin in the Soviet Ministry of Power and Electrification, seeking methods for cleaning frozen and sticky materials from surfaces (coal bunkers, transformer boxes, towers, etc.) published work on electro-impulse possibilities. He immediately received inquiries from other ministries

(aviation, fisheries, dairy, housing) regarding de-icing of vehicles, buildings, ships, and for cleaning of dry milk from hoppers (Ref. 1-7 and 1-8). Responding to their requests involved him in bureaucratic territorial struggles and he was fired. Eventually, however, he was set up in his own laboratory under the State Committee for Meteorology and Environmental Monitoring, and apparently made some installations in aircraft; the Il-18 has been cited as having been the first, but confirmation by Western observers is difficult to obtain.

In any case, in the early 1970's, Russian representatives were granted EIDI patents in several Western nations, including the USA, and USSR salesmen began calling on American and European aircraft companies offering to sell their design and construction services for an EIDI system. Their lack of candor discouraged most customers, but interest was stirred and during the 1970's, work was done on this method in France (Air-Equipment division of DBA), Great Britain (Lucas Aerospace and B.A.C.), and the United States (Lockheed and McDonnell-Douglas). For various reasons, the development stopped short of full implementation. The system still lacked a well developed underlying technology and known design parameters.

IV. The NASA/WSU/Industry Project

A. Initial Feasibility Demonstration

In mid-1982, NASA Lewis Research Center funded a six-month grant to Wichita State University to work with two small plane makers, Beech and Cessna, and an aircraft electrical system manufacturer, the Engine Systems Division of Simmonds-Precision, to do a feasibility study resulting in an icing tunnel demonstration in Oct.-Nov. 1982. Two wing sections were tested, mid-wing portions from a Beech Bonanza and a Cessna 206. These

were similar in size and flight speeds, but had very different leading edge structures, one very stiff and small, the other flexible and large in extension from the front spar. Good cleaning was accomplished with fairly low energy expenditure for air speeds from 96 to 230 knots, air temperatures from 29° to -15°F (-2° to -26°C), angles of attack from 2 to 8 degrees and liquid moisture contents from 0.6 to 2.4 g/m^3.

B. The Industry Consortium

The results were encouraging enough to lead NASA to expand the aim to full development of the method for the whole range of civil aircraft. A consortium of participating industries was formed for this purpose. Each company agreed to contribute some services or equipment to the project, and in return became eligible to submit its own products for de-icing design and tests by the EIDI method. WSU was charged with doing the needed research into the electrodynamic and structural dynamic phenomena involved, and developing manufacturing methods for coils and their mountings. In addition, WSU coordinated the effort and conducted further tests in the NASA/Lewis Icing Research Tunnel (IRT). The industries represented a wide scope of aircraft sizes, air speeds, skin thicknesses and of attitudes regarding the introduction of a new device.

Realizing the ultimate requirement for certification, FAA personnel were invited into the group meeting so that their concerns could be considered as early as possible.

Consortium members for the 1982-83 period were:

Small Aircraft: Beech Aircraft Co., Wichita, KS
Cessna-Pawnee Div., Wichita, KS
Business Jet Aircraft: Gates Learjet Corporation, Wichita, KS
Cessna-Wallace Div., Wichita, KS
Composite, High Performance: LearFan Ltd., Reno, NV
Transport Aircraft: Boeing Commercial, Seattle, WA
McDonnell-Douglas, Co., Long Beach, CA
Electrical Equipment: Simmonds-Precision, Norwich, NY

In late 1983, Rohr Industries of Chula Vista, CA, joined the group with an interest in de-icing engine inlets. In 1984, a second aircraft electrical equipment developer was added, Electro-Delta of White Oak, Texas, and the first helicopter maker, Sikorsky Aircraft Co., Stratford, CT, also joined. In 1985, Bell Helicopter of Ft. Worth, TX, and the Boeing/Vertol Co. of Philadelphia, PA, joined the membership consortium.

In June 1985, a symposium was held at NASA-Lewis to present the work to nearly 100 representatives of U.S. Aerospace Industries. A NASA Contractor Report (Reference 1-12) was distributed at that time. This present report is a revision and extension of that work.

C. Objectives

The program objectives were, from the start, quite comprehensive:

1. Develop computer models for the structural dynamics of leading edge portions of wings and engine inlets to provide design guidance for coil location, coil size, impulse intervals and coil spanwise spacing. An alternative approach was also desired, namely the development of a standard measurement method for existing structures to extract the structural dynamics characteristics needed for the design. (See Chapter 3)

2. Develop a computer model for the electro-dynamics and provide detailed design data for the electro-impulse equipment, including coil design, power, voltage, insultion, pulse duration, and switching equipment. (See Chapter 2)

3. Test wing sections and engine inlets in the IRT to guide and prove EIDI designs. (See Chapter 4)

4. Consider practical aspects of retro-fitting the EIDI system to existing aircraft. (Test VII in Chapter 5 were retro-fit models)

5. Devise methods for optimal design of a wing structure for using the system.

6. Estimate and attempt to minimize the cost of the EIDI system in terms of weight, maintenance and capital outlay.

7. Details to be considered are:
   (a) Limits of application (size, stiffness, etc.)
   (b) Standardization of components
   (c) Fatigue of skin, mountings, switching gear, bondings (Chapter 7, Section I.)
   (d) Electro-magnetic interference problems and solutions (Chapter 7, Section II.)
   (e) Use with composite materials (See Chapter 5, Section IV and Chapter 7, Section I-B.)
   (f) Integration with present avionics and electrical systems

8. Conduct flight demonstrations using aircraft from NASA and participating industries. (See Chapter 5)

9. Carry out at least the first stages of FAA certification.

V. References

1-1. British Patent Specification No. 505,433 issued to Rudolf Goldschmidt; May 5, 1939.

1-2. Schrag, R.L. and Zumwalt, G.W., "Electro-Impulse De-Icing: Concept and Electrodynamic Studies," AIAA 22nd Aerospace Sciences Meeting, Reno, NV, Jan. 9-12, 1984, Paper No. 84-0021.

1-3. Bernhart, W.D., and Zumwalt, G.W. "Electro-Impulse De-Icing: Structural Dynamic Studies, Icing Tunnel Tests and Applications," AIAA 22nd Aerospace Sciences Meeting, Reno, NV, Jan. 9-12, 1984, AIAA Paper No. 84-0022.

1-4. Zumwalt, G.W., "Icing Tunnel Tests of Electro-Impulse De-Icing of an Engine Inlet and High-Speed Wings," AIAA 23rd Aerospace Sciences Meeting, Reno, Nevada, January 14-17, 1985. AIAA Paper No. 85-0466.

1-5. Zumwalt, G.W., and A.A. Mueller, "Flights and Wind Tunnel Tests of an Electro-Impulse De-Icing System", AIAA/NASA General Aviation Technology Conference, Hampton, VA, July 10-12, 1984. AIAA Paper No. 84-2234.

1-6. Mueller, A.A., Ellis D.R., and Bassett, D.C., "Flight Evaluation of an Electro-Impulse De-Icing System on a Light General Aviation Airplane." AIAA/AHS Aircraft Designs, Systems and Operations Meeting, San Diego, CA., October 1984. AIAA Paper No. 84-2495.

1-7. "From the Sky to the Earth," Pravda, (unsigned), Dec. 10, 1978.

1-8. "Development of De-Icing System," Pravda, (unsigned), Feb. 11, 1980.

1-9. Zumwalt, G.W., "Electromagnetic Impulse De-Icing Applied to a Nacelle Nose Lip" AIAA/SAE/ASME/ASEE 21st Joint Propulsion Conference," Monterey, CA, July 8-10, 1985. AIAA Paper No. 85-1118.

1-10. Zumwalt, G.W. and Friedberg, R.A., "Designing an Electro-Impulse De-Icing System," AIAA 24th Aerospace Sciences Meeting, Reno, NV, Jan. 6-9, 1986. AIAA Paper NO. 86-0545.

1-11. Bernhart, W.D. and Schrag, R.L.,"Electro-Impulse De-Icing: Electrodynamic Solution by Discrete Elements, "AIAA 26th Aerospace Sciences Meeting, Reno, NV, Jan. 11-14, 1988.

1-12. Zumwalt, G.W., Schrag, R.L., Bernhart, W.D., and Friedberg, R.A., "Analysis and Tests for Design of an Electro-Impulse De-Icing System," NASA CR-174919, May 1987.

CHAPTER 2

ELECTRODYNAMIC STUDIES AND TESTS

I. Introduction

The electrodynamics portion of this EIDI study involved an evaluation of the discharge circuit characteristics, a study of the magnetic field behavior near the impulse coil, ballistic pendulum tests, and modeling activities. This chapter describes these investigations and concludes with detailed design examples.

II. Approximate Characteristics of the Discharge Circuit

The current which flows through the coil following the firing of the SCR (and prior to clamp diode conduction) resembles that of an under-damped R-L-C circuit. The effective resistance and inductance of the coil is considerably influenced by the proximity of the metal aircraft skin, and this influence is frequency dependent. However, an approximate current waveform may be obtained assuming an ideal R-L-C circuit with (constant) parameters whose values are determined by electrical frequency of oscillation. Ideal waveforms for coil current and capacitor voltage, assuming no clamping diode across the capacitor, are sketched in Figure 2-1.

It would be useful to summarize the mathematical relations for these idealized waveforms.

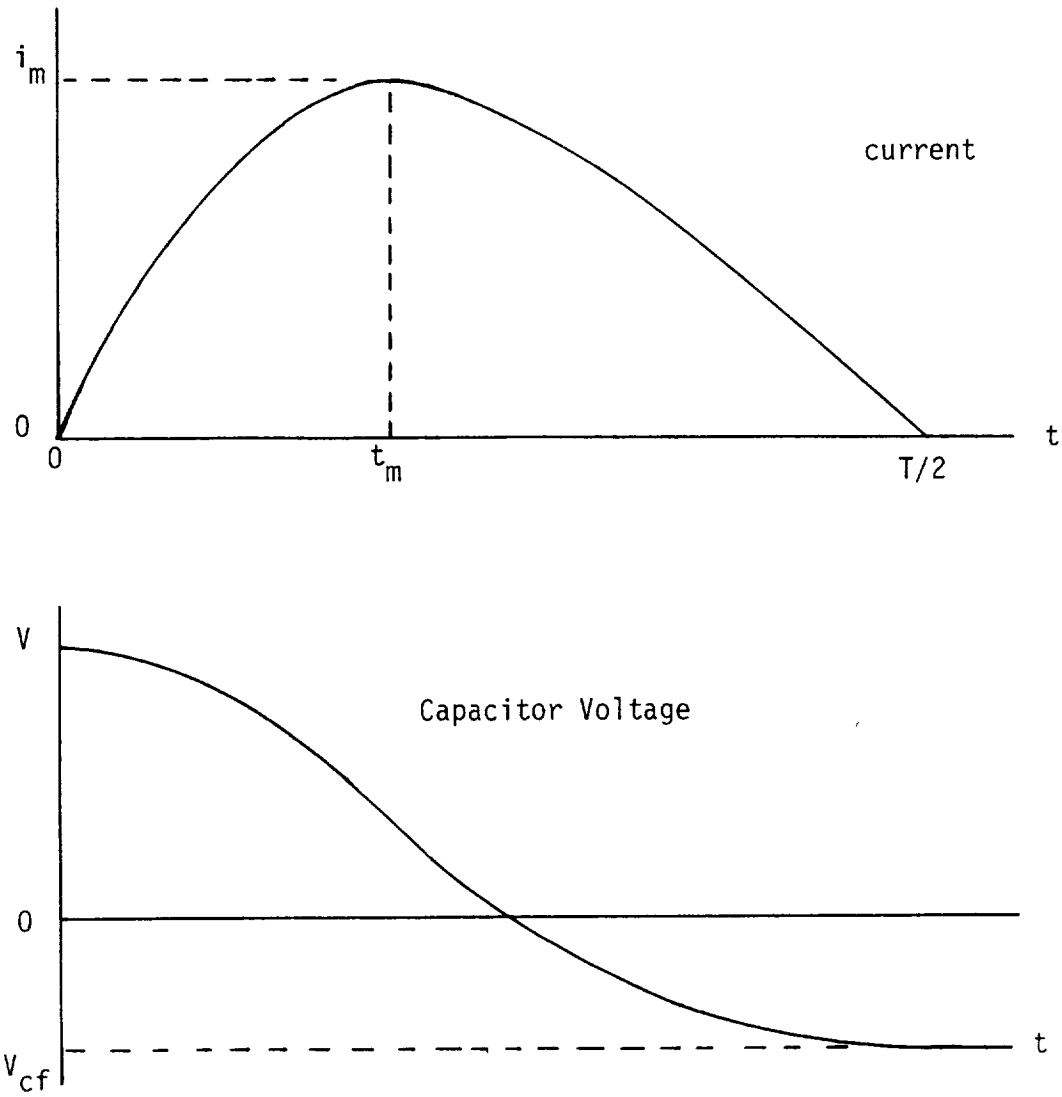

Fig. 2-1 Approximate Waveforms for Coil Current and Capacitor Voltage without a Diode Clamp

If we define a damping parameter by

$$m = \frac{1}{\sqrt{\frac{4L}{R^2C} - 1}} \tag{2-1}$$

then the period of damped oscillation is

$$T = 2\pi\sqrt{LC}\sqrt{m^2 + 1} \tag{2-2}$$

The time for the maximum current can be expressed in alternate forms

$$\begin{aligned} t_m &= \sqrt{LC}\sqrt{m^2 + 1}\ \arctan\left(\frac{1}{m}\right) \\ &= \frac{T}{2\pi}\ \arctan\left(\frac{1}{m}\right) \\ &= \frac{1}{2}RC\frac{m^2+1}{m}\ \arctan\left(\frac{1}{m}\right) \end{aligned} \tag{2-3}$$

If the initial stored energy is W, then the maximum current is

$$i_m = \sqrt{\frac{2W}{L}}\, e^{-m\ \arctan\left(\frac{1}{m}\right)} \tag{2-4}$$

Without the clamping diode, the capacitor will become reverse-charged with the final voltage

$$v_{cf} = -Ve^{-\pi m} \tag{2-5}$$

where V is the initial capacitor voltage. Finally, the maximum stored inductor energy and the final re-stored capacitor energy are, respectively,

$$\frac{1}{2}L\ i_m^2 = W\ e^{-2m\ \arctan\left(\frac{1}{m}\right)} \tag{2-6}$$

and

$$\frac{1}{2}C\ v_{cf}^2 = W\ e^{-2\pi m} \tag{2-7}$$

Parameter values for a typical discharge circuit are tabulated below. This circuit consisted of a 600 μF capacitor with a 22 foot cable (Simmonds Energy System), and a 30-turn, 2 inch diameter impulse coil without a metal target. The values in the parameter table were all determined by bridge measurements.

	Capacitance (μF)	Inductance (μH)	Resistance (Ω)
30-Turn 2 Inch Dia. Coil		19.8	.0273 (at 1 kHz)
600μF Capacitor	600.0		.003 (at 1 kHz)
22 ft Cable		1.7	.043
Totals	600.0	21.5	.0733

Discharge waveform data for this same circuit were determined experimentally to be:

$$V = 500 \text{ volts}$$

$$V_{cf} = -260 \text{ volts}$$

$$i_m = 2025 \text{ amps}$$

$$T/_2 = 368 \text{ μsec.}$$

Using these data, it is possible to estimate the effective circuit resistance and inductance by:

$$m = \frac{1}{\pi} \ln\left(\frac{V}{-V_{cf}}\right) = 0.2083$$

$$L_{ckt} = \left(\frac{V}{i_m}\right)^2 C\, e^{-2m \arctan \frac{1}{m}} = 207\mu H$$

$$R_{ckt} = \frac{2\pi Lm}{T/2} = 0.0736\Omega.$$

These inductance and resistance values are in substantial agreement with the values obtained from bridge measurements.

Figure 2-2 is a graph of

$$\frac{i_m}{\sqrt{2W/L}}$$

vs $R\sqrt{C/L}$, based on ideal R-L-C circuit theory. It can be used to estimate the degradation in peak current due to coil and cable resistance.

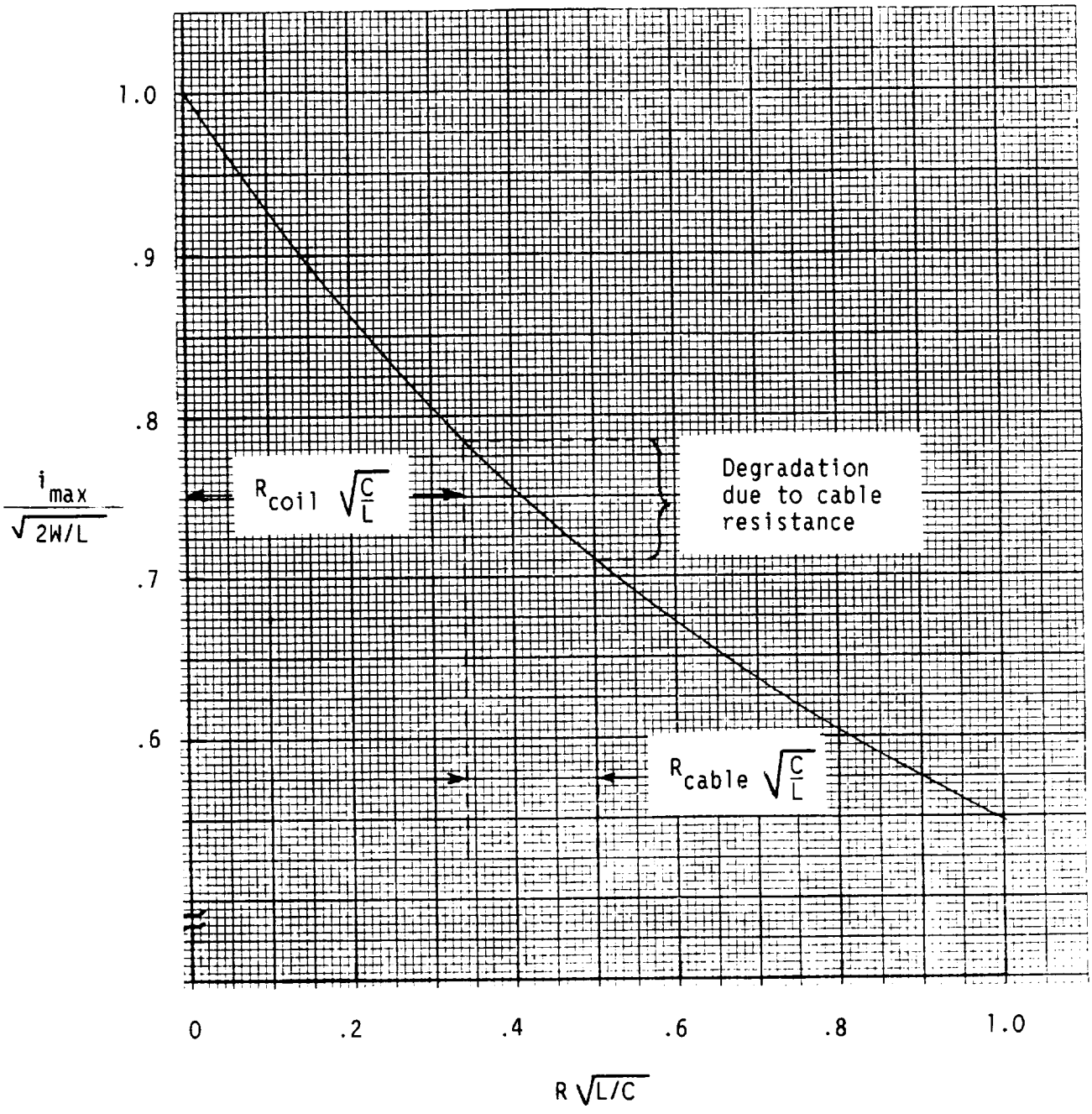

Fig. 2-2 Graph Showing Loss of Peak Current Due to Coil and Cable Resistance

III. Ballistic Pendulum Studies

A ballistic pendulum was constructed and utilized to study the effects of parameter variations on impulse production. A schematic drawing of the apparatus is shown in Fig. 2-3. The maximum pendulum swing (θ_{max}) was measured by an electrical output from the precision potentiometer, and the delivered impulse was determined from the formula:

$$\text{Impulse} = \frac{4\pi J}{lT} \sin \frac{\theta_{max}}{2} \text{ lb-sec} \qquad (2\text{-}8)$$

where

J = Moment of inertia of the pendulum = .387 lb-ft-sec^2 (calculated)

l = Pendulum length, pivot to target center = 3.727 ft.

T = Free oscillation period = 2.09 sec (measured)

Numerically, $4\pi J/lT) = 0.624$ lb-sec.

This section describes the various test conditions and the test results. In most cases a "dummy coil" was included in series with the "active coil" to simulate double coil operation. When dummy coils were used, they were always identical to the active coils and were fitted with identical targets (except where noted otherwise).

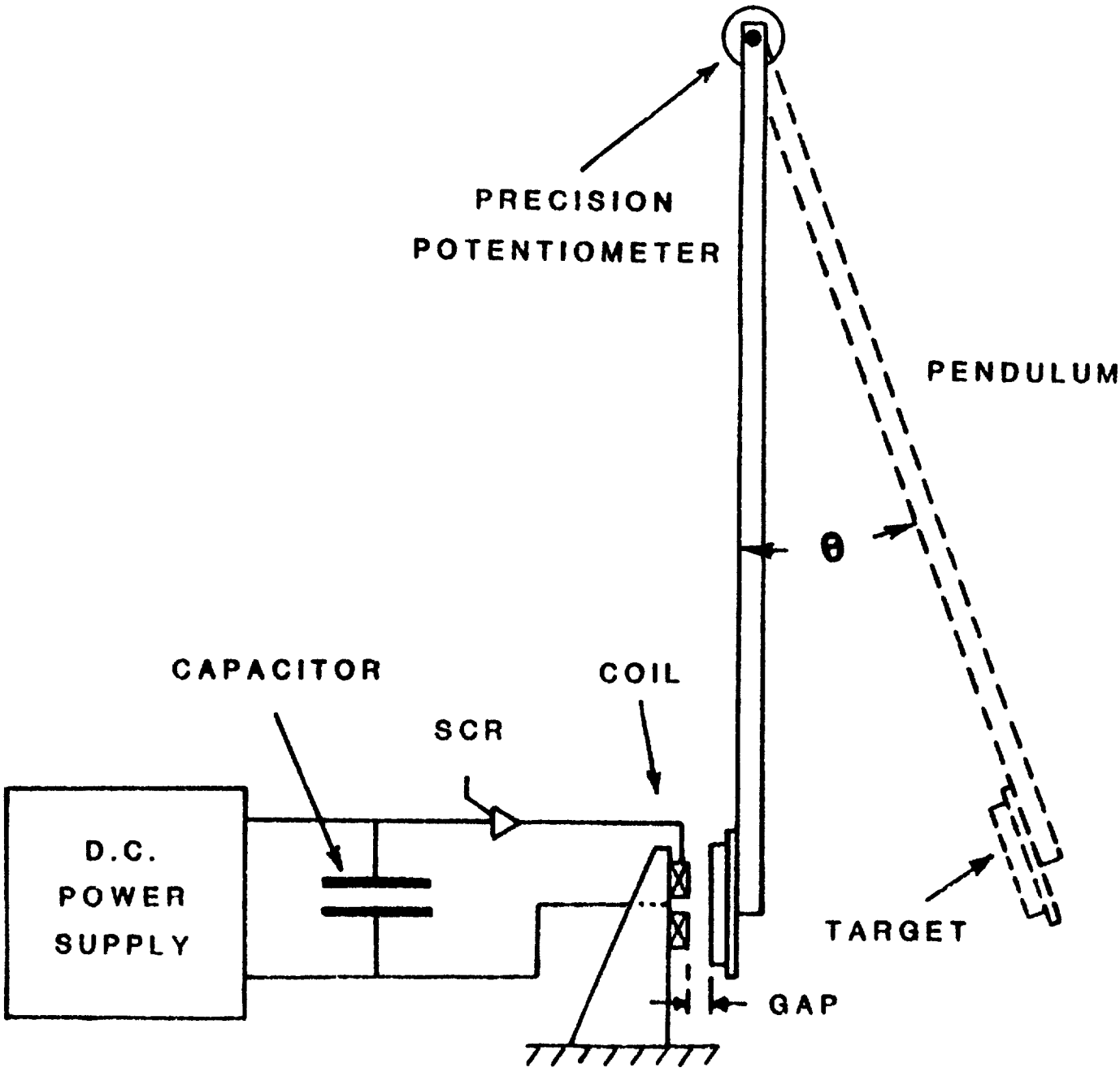

Fig. 2-3 Ballistic Pendulum Apparatus

A. Varying Voltage

Test 1

ELECTRICAL	ACTIVE COIL	DUMMY COIL	TARGET
Volts Var.	Turns 30	Used yes	Mat. Al 2024-T3
μF 600	Dia. 2.0"	With Target	Thickness .032"
Joules Var.	Thickness .188"	no	Gap .50"

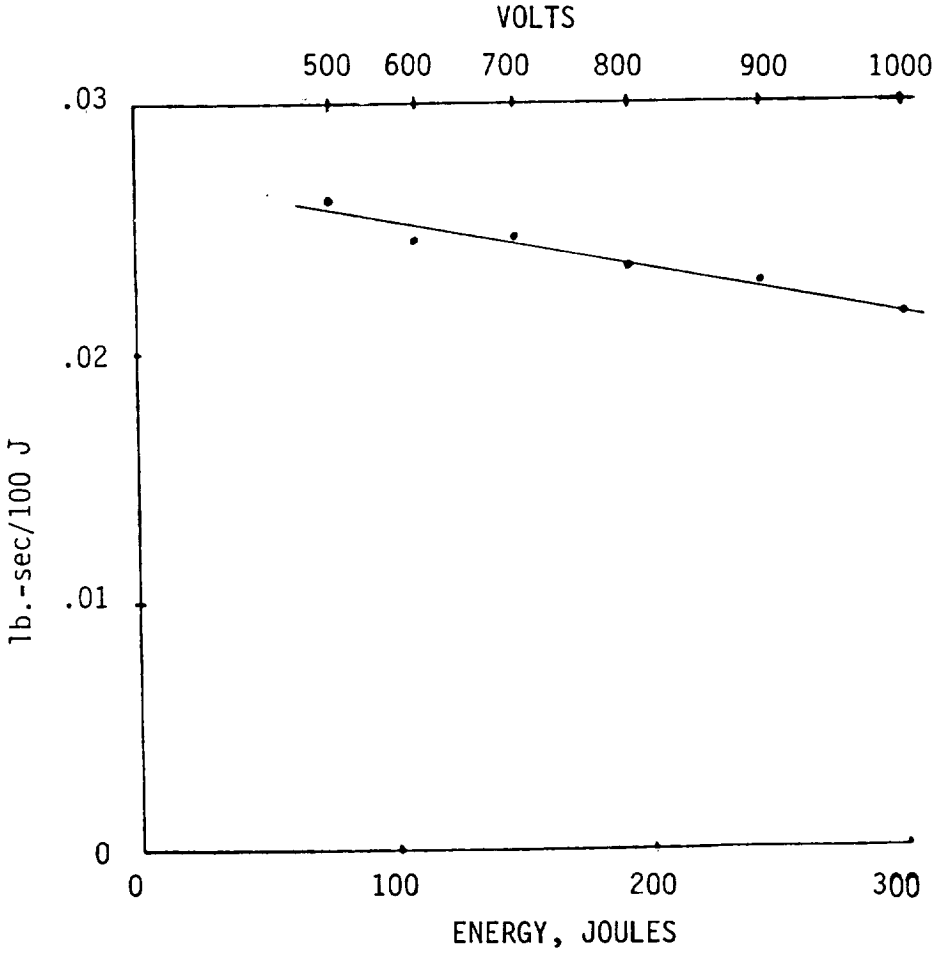

Fig. 2-4 Impulse Per Unit Energy with Voltage Varied

Test 2

ELECTRICAL	ACTIVE COIL	DUMMY COIL	TARGET
Volts Var.	Turns 30	Used yes	Mat. Al 1100
μF 400	Dia. 2.0"	With Target	Thickness .050"
Joules Var.	Thickness .195"	yes	Gap .050"

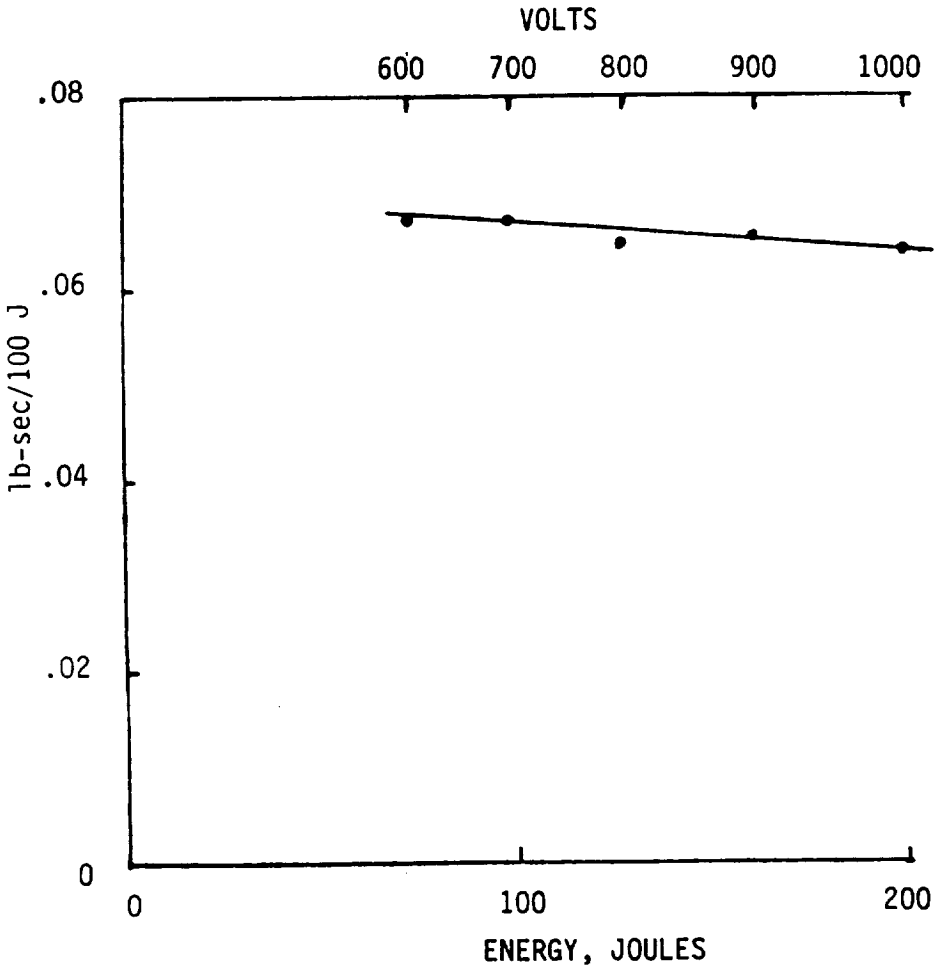

Fig. 2-5 Impulse Per Unit Energy with Voltage Varied

Coil Current Data For Test 2

Volts	i_m(KA)	KA/KV	t_m(μs)
600	1.40	2.33	163
800	1.85	2.31	163
1000	2.31	2.31	163

Comments: This test was intended to verify that the impulse is proportional to the square of the capacitor voltage. The experimental data show some small deviation from a proportionality, both for a thin poor-conductivity target and a thicker good-conductivity target. This deviation is relatively inconsequential. Impulse values can still be extrapolated with fair accuracy from one voltage to another by assuming proportionality to V^2.

B. Varying Capacitance, Fixed Energy

Test 3

ELECTRICAL	ACTIVE COIL	DUMMY COIL	TARGET
Volts Var.	Turns 30	Used yes	Mat. Al 2024-T3
F Var.	Dia. 2.0"	With Target	Thickness .032"
Joules 150	Thickness .188"	no	Gap .050"

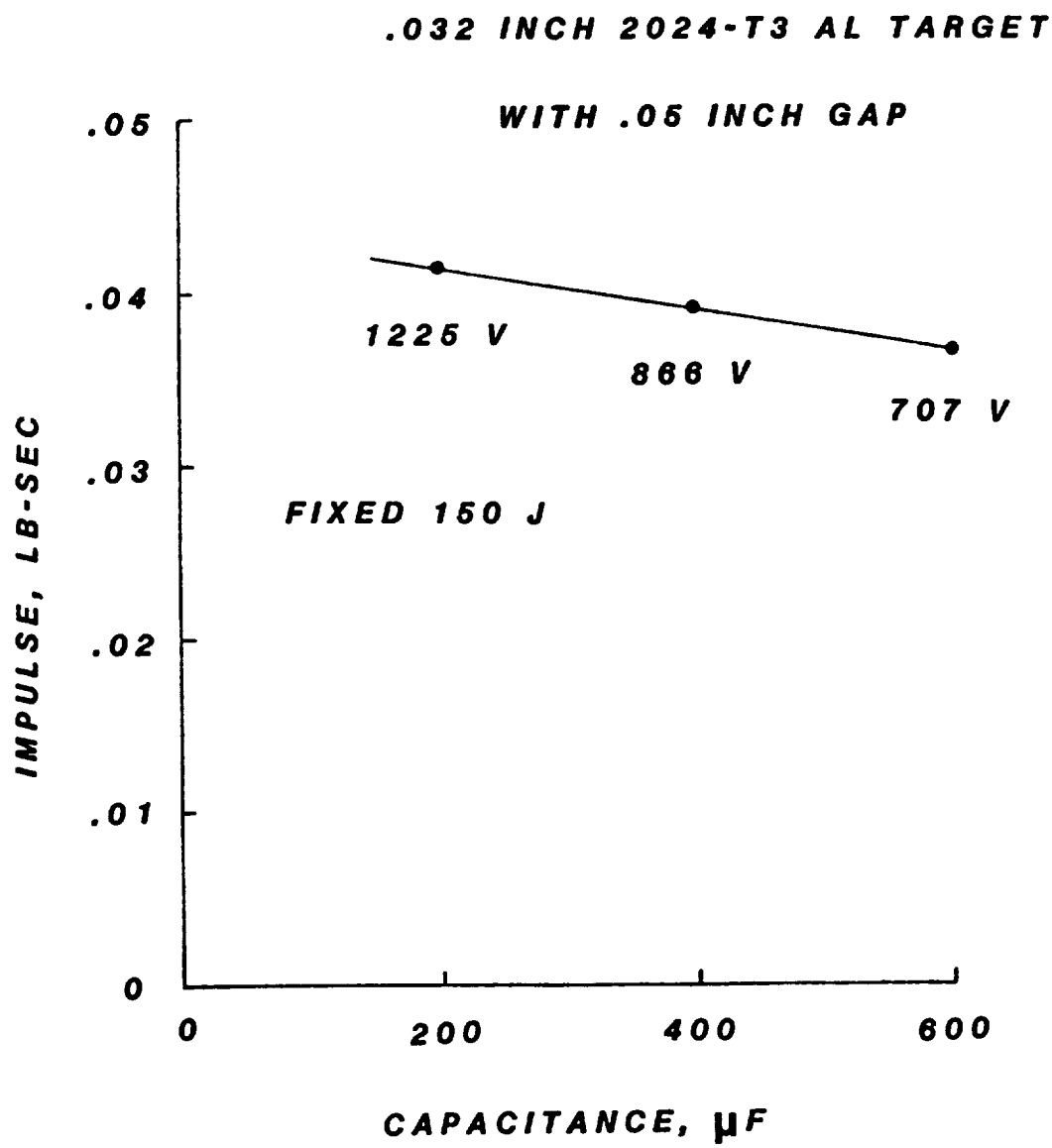

Fig. 2-6 Impulse vs Capacitance with Fixed Energy

Test 4

ELECTRICAL	ACTIVE COIL	DUMMY COIL	TARGET
Volts Var.	Turns 40	Used yes	Mat. Al 1100
μF Var.	Dia. 2.28"	With Target	Thickness .050"
Joules 120	Thickness .195"	yes	Gap .050"

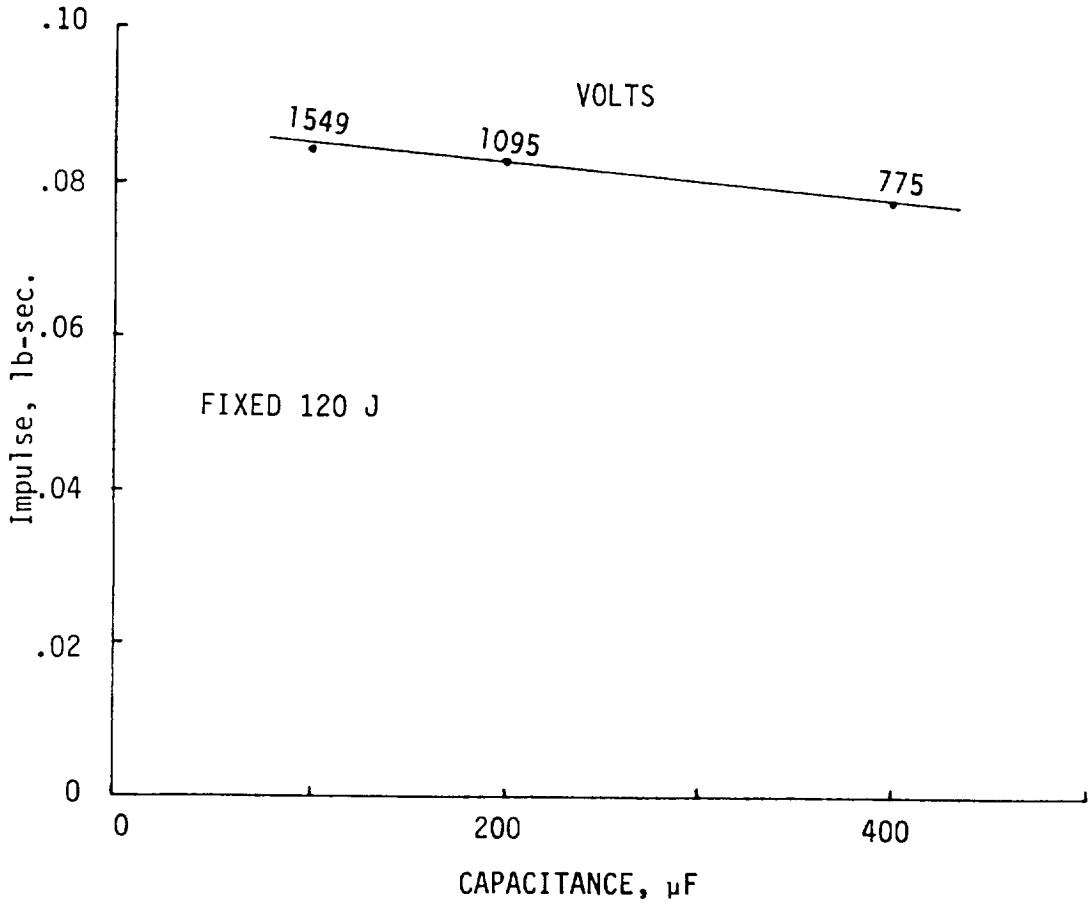

Fig. 2-7 Impulse vs. Capacitance with Fixed Energy

Coil Current Data For Test 4

μF	Volts	i_m(KA)	t_m(μs)
100	1549	2.18	80
200	1095	2.00	115
400	775	1.79	163

Comments: This test explored the relative effectiveness of different capacitance - voltage combinations with fixed energy. Both tests (3) and 4) showed small advantaged of high voltage - low capacitance combinations.

C. Varying Coil-to-Target Gap

Test 5

ELECTRICAL	ACTIVE COIL	DUMMY COIL	TARGET
Volts 800	Turns 30	Used yes	Mat. Al 2024-T3
μ F 600	Dia. 2.0"	With Target	Thickness .032"
Joules 192	Thickness .188"	no	Gap Var.

See Figure 2-8 on following page.

Test 5 (continued)

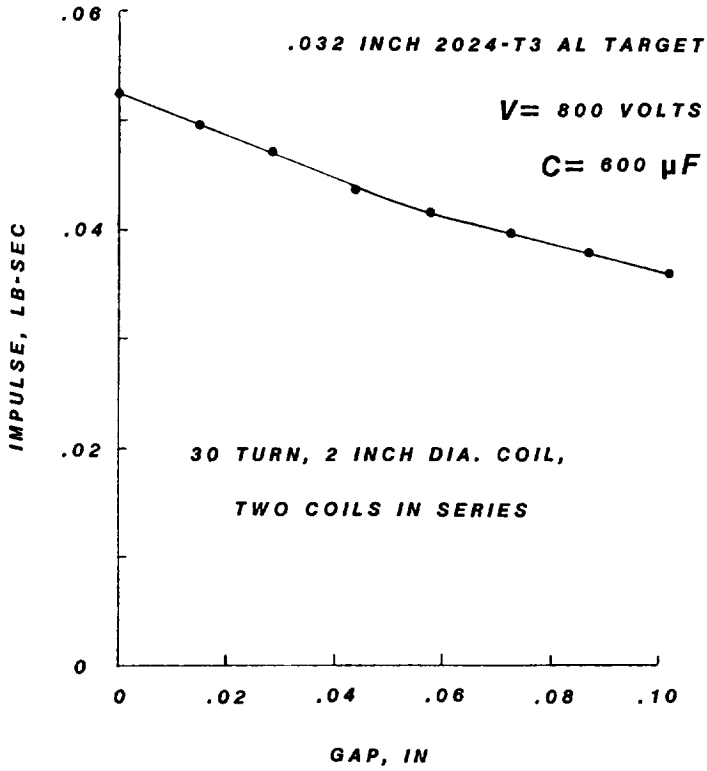

Fig. 2-8 Impulse vs Coil-to-Target Gap

Comments: As expected, the delivered impulse decreased with increased coil-to-target gap. This reduction was about 20 percent for the gap increase from zero to 0.05 inch.

D. Varying Target Material and Thickness

Test 6

ELECTRICAL	ACTIVE COIL	DUMMY COIL	TARGET
Volts 800	Turns 30	Used yes	Mat. Var.
μF 600	Dia. 2.0"	With Target	Thickness Var.
Joules 192	Thickness .188"	no	Gap .050"

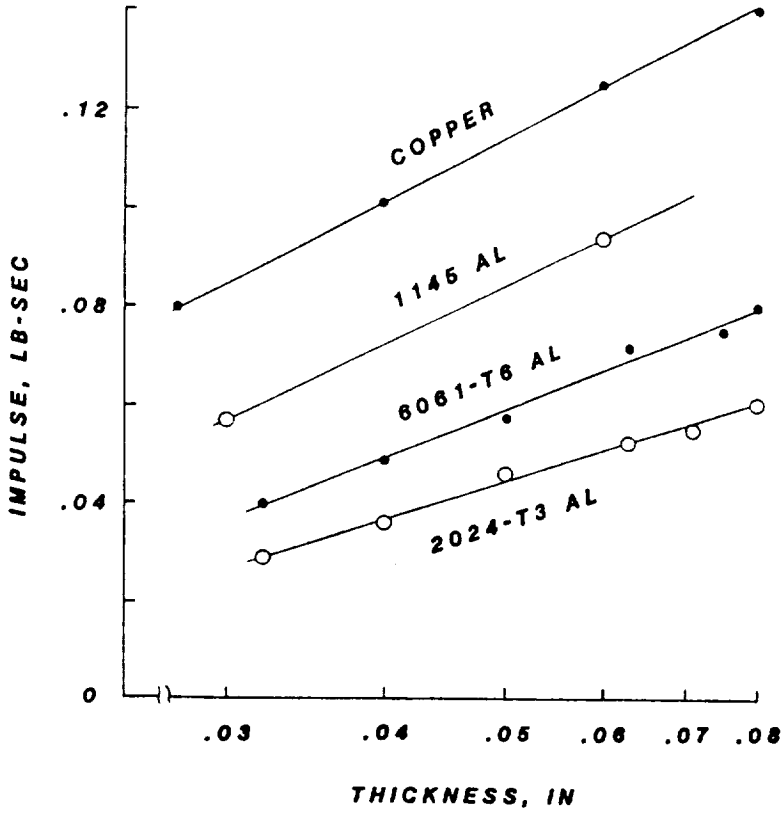

Fig. 2-9 Impulse vs Target Material and Thickness

Comments: These data show large gains in impulse performance when high electrical conductivity targets are used. The published conductivities in percent of annealed copper for the three aluminum types are:

1145 - 62%
6061-T6 - 43%
2024-T3 - 30%

Increasing the target thickness also increases the impulse, but with diminishing returns.

E. Varying Target Thickness

Test 7

ELECTRICAL	ACTIVE COIL	DUMMY COIL	TARGET
Volts 800	Turns 30	Used yes	Mat. Cu
F 600	Dia. 2.0"	With Target	Thickness Var.
Joules 192	Thickness .188"	no	Gap 0

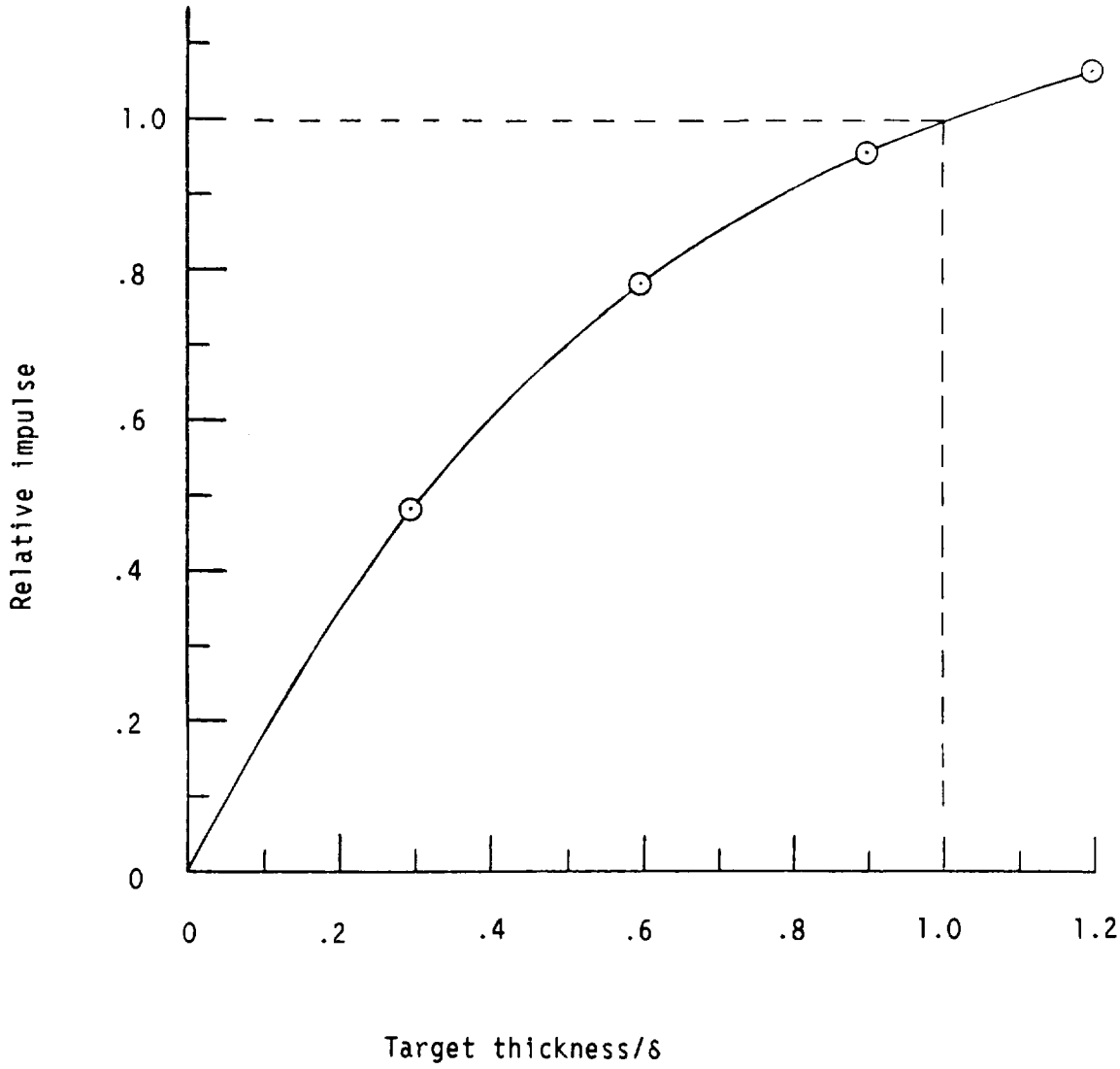

Fig. 2-10

Comments: This test also studied the effect of target thickness, but careful measurements were made for peak current times, so that the target thickness could be compared with the electrical skin depth. An often stated rule of thumb criterion is that the desired target thickness, from the standpoint of impulse production, should be about one electrical skin depth calculated from the formula

$$\delta = \frac{1}{\pi f \mu_o \sigma}$$

where σ is the electrical conductivity of the target in mhos/meter, $\mu_o = 4\pi \times 10^{-7}$, and f is the resonant frequency (Hertz) of the electrical circuit. Figure 2-10 may be used to judge the consequences of operating with targets thinner than one electrical skin depth.

F. Varying Coil Diameter and Turns

Test 8

ELECTRICAL	ACTIVE COIL	DUMMY COIL	TARGET
Volts 600	Turns Var.	Used no	Mat. Cu
μF 600	Dia. Var.	With Target	Thickness .021"
Joules 108	Thickness .188"	n/a	Gap .050"

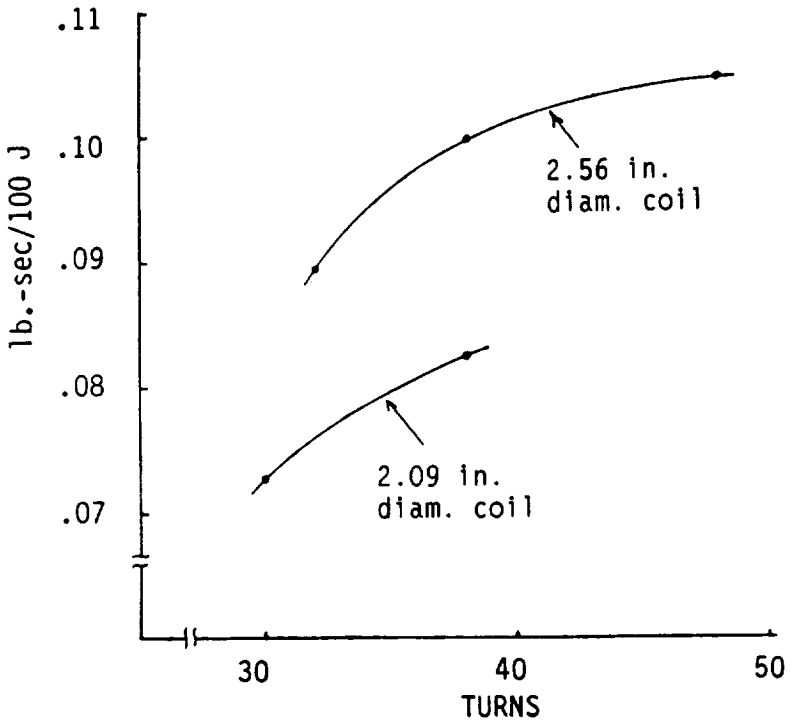

Fig. 2-11 Impulse Per Unit Energy with Two Coil Diameters and Variable Turns

COIL CURRENT DATA

For Test 8

Coil Dia. (In)	Turns	i_m (KA)	t_m (μs)
2.09	30	3.58	117
2.09	38	2.83	137
2.56	32	3.18	137
2.56	38	2.78	146
2.56	48	2.14	174

Comments: This test measured the relative effectiveness of five coil designs for which the number of turns and the outer diameters were varied. A greater number of turns for a given coil diameter was achieved by rolling the ribbon wire thinner.

No dummy coils were used in the impulse tests. Voltage and capacitance were held fixed, so the energy was also fixed. In general, the data showed that given diameter coils produced more impulse as turns were increased, and that coils with a given number of turns produced more impulse as the diameter was increased.

Test 9

ELECTRICAL	ACTIVE COIL	DUMMY COIL	TARGET
Volts Var.	Turns 40	Used yes	Mat. Al 1100
μF 400	Dia. 2.28"	With Target yes	Thickness .050"
Joules Var.	Thickness Var.		Gap .050"

Current Data at V = 800 Volts

Coil Thickness (In)	i_m (KA)	t_m (μs)
.195	1.85	163
.150	1.79	158
.100	1.66	146

Comments: For this test, six identical 40-turn coils were constructed. Each had a thickness of 0.195" (the ribbon wire width after the rolling operation). Then one pair was milled to a reduced thickness of 0.150", and another pair to 0.100". Finally, the various pairs (one active, the other dummy) were installed into the ballistic pendulum apparatus for tests.

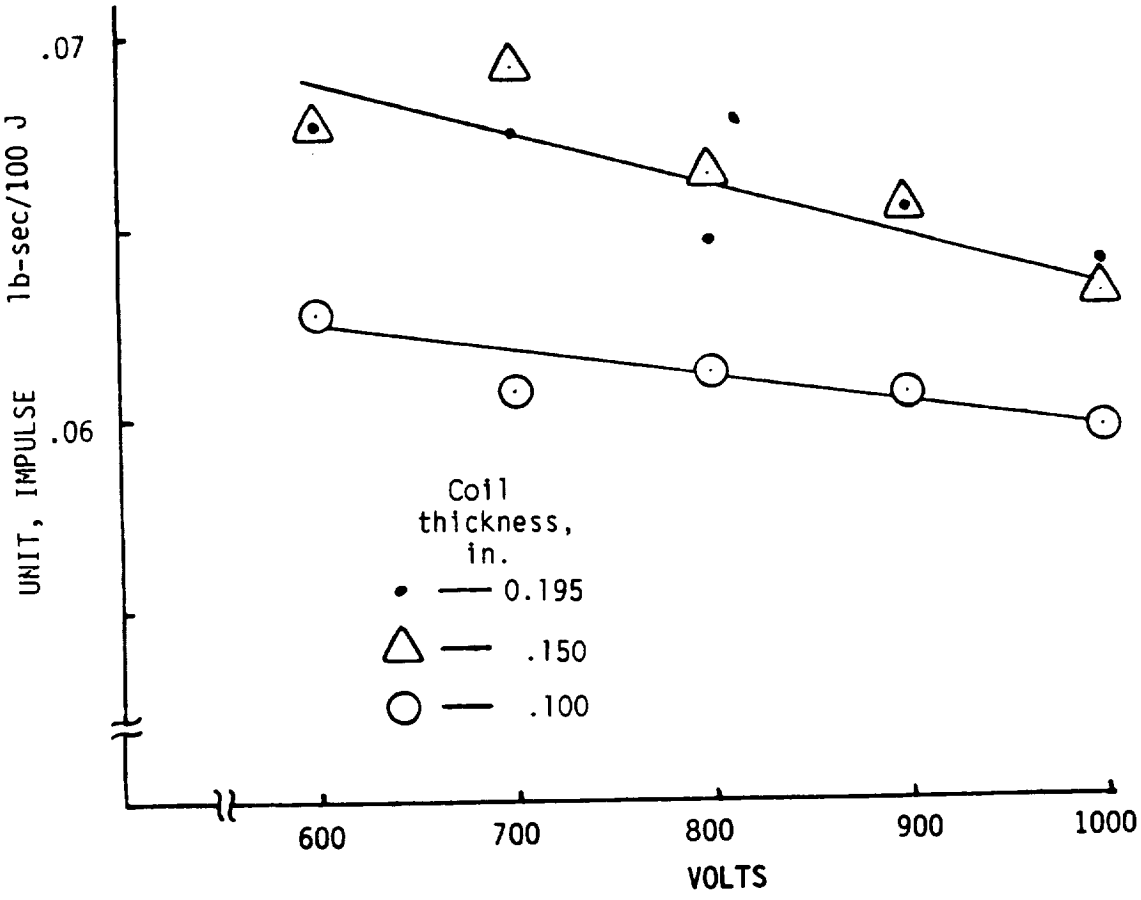

Fig. 2-12 Impulse Per Unit Energy with Three Coil Thickness

The results show no detectable degradation in performance for the 0.105" thick coil, but an approximately 7 percent impulse reduction for the 0.100" thick coil (relative to the 0.195" thick coil). The performance loss for the thinnest coil was presumably, due to its excessive resistance. Data on resistance values were as follows:

	d.c. ohms
0.195" thick coils	.035 each
0.150" thick coils	.045 each
0.100" thick coils	.068 each
Supply cable	.043

G. Series vs Parallel Coils

Test 10

ELECTRICAL	ACTIVE COIL	DUMMY COIL	TARGET
Volts Var.	Turns 40	Used yes	Mat. Al 1100
μF Var.	Dia. 2.28"	With Target	Thickness .050"
Joules 60/Coil	Thickness .195"	yes	Gap .050

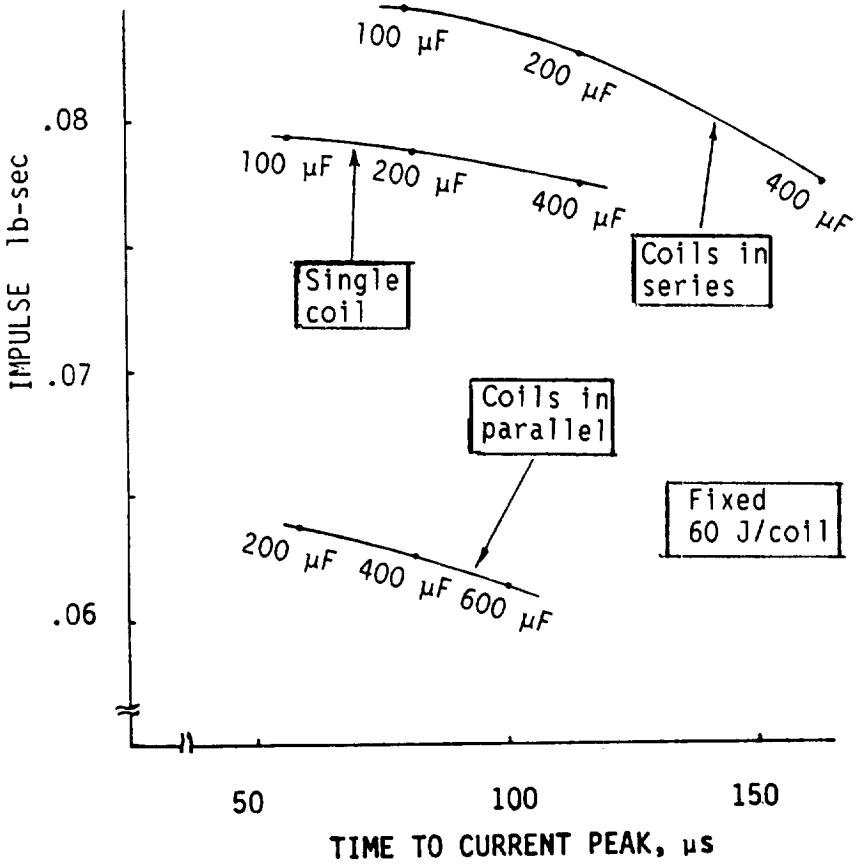

Fig. 2-13 Impulse vs Time to Current Peak, with Series and Parallel Coil Operation Compared

(Test 10 - continued)

Peak Currents For t_m = 80μs

		KA
Series Coils	(C = 100 μF)	1.55
Single Coil	(C = 200 μF)	1.49
Parallel Coils	(C = 400 μF)	1.34/coil

Comments: This test utilized the two 0.195" thick coils from Test 9. The object of the experiment was to compare impulse production with coils (active and dummy) placed in series, to that with the coils in parallel, to that for single operation. Various capacitance values were used, with voltage adjusted for fixed 60 Joules/coil.

Relative to single coil operation, the series combination showed improved performance while the parallel combination showed substantially worse performance. If the coil currents were identical (same peak values and same time to peak) then the impulse values should be the same. The table above, which lists peak currents with fixed rise times, shows the greatest current for coils in series and least current for coils in parallel. Furthermore, the impulse ratios agree approximately with the ratios of the peak currents squared.

It appears that the explanation for the relative impulse performance lies in the varying degrees of circuit damping. Without resistance in the supply cable, then the damping factors should be the same in all cases. However, the (constant) supply cable resistance causes the damping to be greatest with parallel coil operation.

H. Effect of the Diode Clamp

Some impulse measurements were made with and without the (reverse charge prevention) diode in place. The conditions and results were as follows:

Test 11

ELECTRICAL	ACTIVE COIL	DUMMY COIL	TARGET
Volts Var.	Turns 30	Used no	Mat. Cu
μF Var.	Dia. 2.0"	With Target	Thickness .021"
Joules Var.	Thickness .188"	_____	Gap .050"

RESULTS

(Test 11 - continued)

C(μF)	V(Volts)	Impulse with Diode / Impulse w/o Diode
600	500	.92
400	600	.92
200	800	1.00

Comment: The diode introduces a slight performance degradation, but it is a small penalty to pay for increased capacitor life.

IV. Magnetic Field Diagnostics Experiment

This section describes a magnetic field measurement method for studying the distribution of eddy currents within, and pressure distribution on, a flat metallic plate subjected to an axially symmetric transient magnetic field produced by an pulsed circular coil. The pulsing system, coil and target (including coil-to-target gap) closely simulated conditions that existed during electro-impulse-de-icing tests conducted by Wichita State University. For this experiment, the target was rigidly supported, and reduced voltage was used (energy about 15% of that required for de-icing).

A. Experimental Apparatus

Figure 2-14 shows the energy discharge system, omitting the capacitor charging circuit and the thyristor firing circuit. Two identical pulsing coils were operated in series, because that was the arrangement used in most of the de-icing tests. However, only one of the two coils were located in the coil-target assembly which is detailed in Fig. 2-15. The effective gap between the coil (copper) surface and the near surface of the target was 0.078 inch.

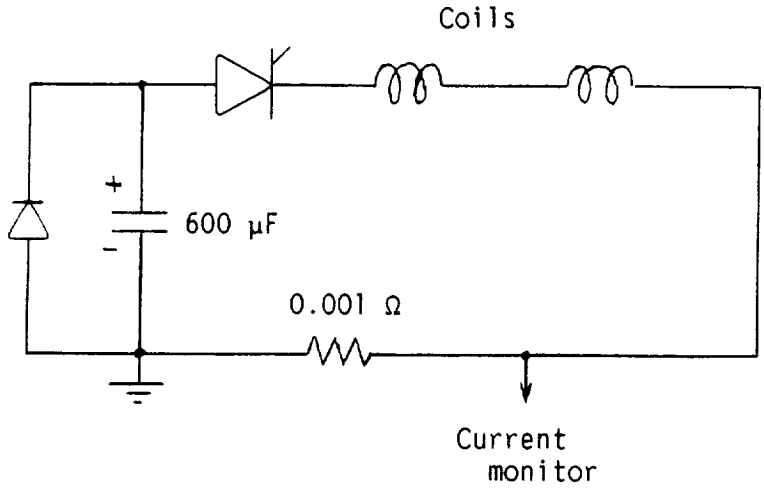

Fig. 2-14 Energy Discharge Circuit

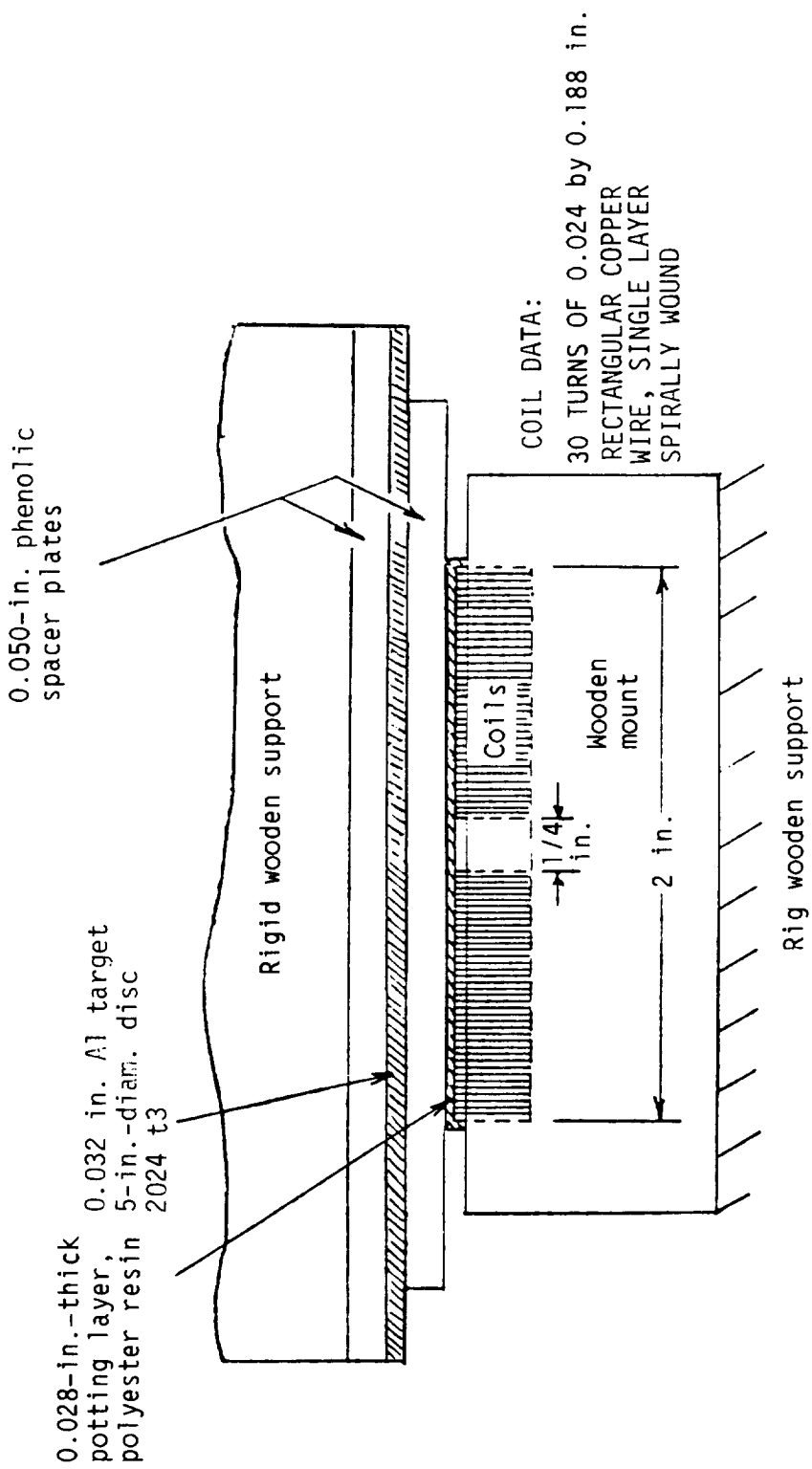

Fig. 2-15 Details of the Coil-Target Assembly

Each coil consisted of 30 turns of 0.024" x 0.188" rectangular copper wire spirally wound in a single layer from an inner radius of 0.125" to an outer radius of 1.00".

The initial capacitor voltage utilized for this experimental study was 400 volts, and the resulting discharge current waveforms are shown in Fig. 2-16. One trace is with the aluminum target removed, the other is with the target in place.

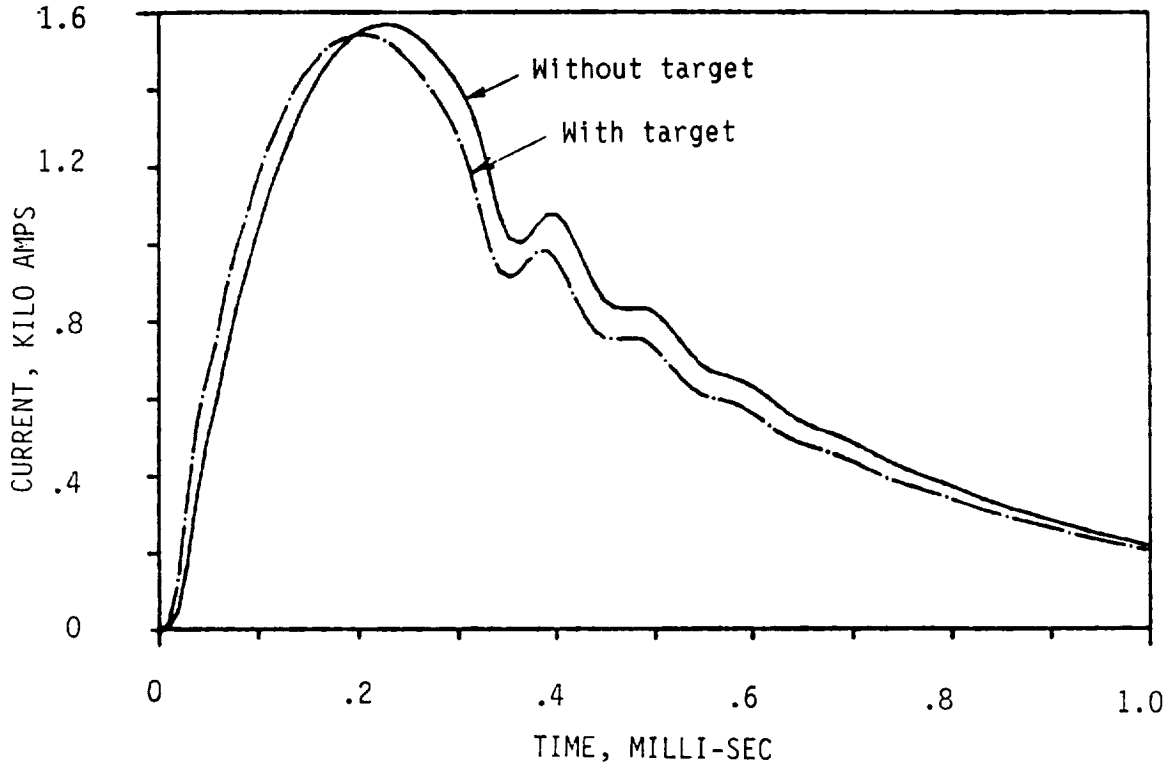

Fig. 2-16 Discharge Current With and Without the Aluminum Target Present

B. Magnetic Field Measurements

A field measuring plate was constructed in a manner illustrated in Fig. 2-17. Shallow concentric grooves were cut into both sides of a 0.050" thick phenolic disc with radius increments of 0.2", starting at r = 0.2" and ending at r = 2.0". Single-turn loops of .006" diameter wire were then cemented into these grooves, and their twisted leads brought out to solder tabs through radial channels. Figure 2-18 is a photograph of the finished plate.

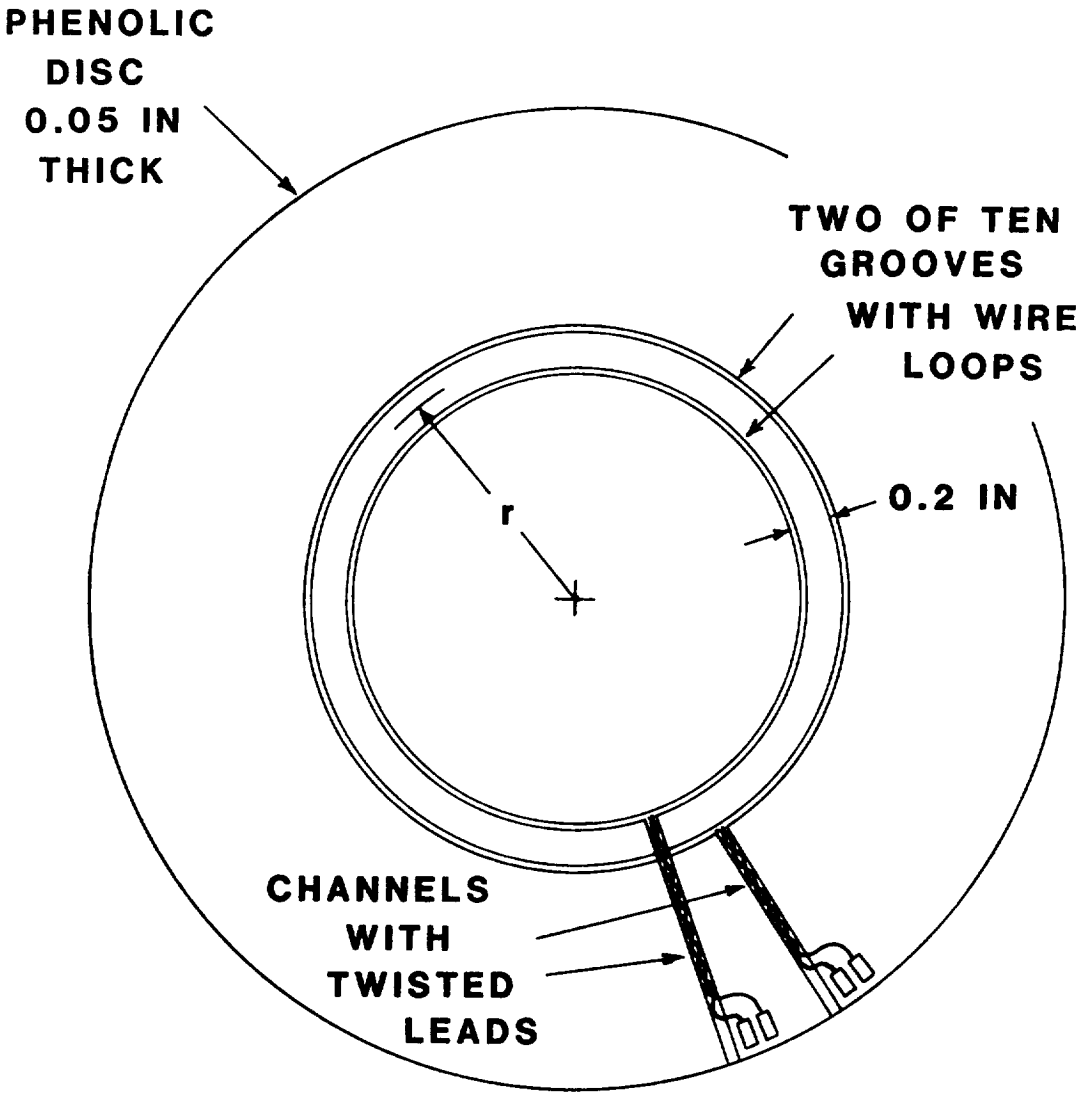

Fig. 2-17 Partial Illustration of the Field Measuring Plate

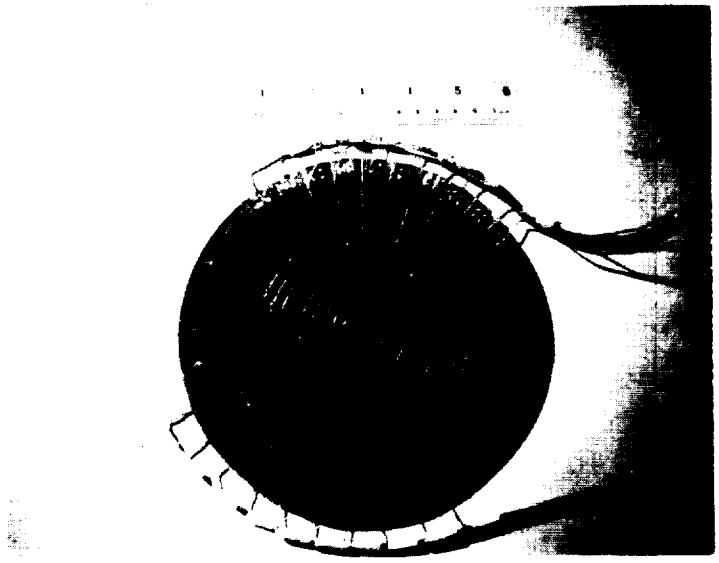

Fig. 2-18 Photograph of the Field Measuring Plate

For measuring the fields on either side of the target, the measuring plate simply substituted for the corresponding spacer plate in Fig. 2-15. A measurement of the flux density component perpendicular to the plate was derived from the induced voltage in any two neighboring loops connected in series opposition. For the two loops illustrated in Fig. 2-17, for example,

$$B_{\perp}(t) = 1550 \frac{\int_0^t v\, dt}{\pi(r_2^2 - r_1^2)} \text{ Teslas} \qquad (2\text{-}9)$$

where r is in inches and v in volts. This value is the average perpendicular flux density over the area between the two induction loops. In deriving further results, we will assume the answer to apply at a radius midway between the two loops.

To measure the tangential (radial) component of flux density at any radius, the front and back loops at that radius are connected in series opposition, and calculations are made from

$$B_r(t) = 1550 \frac{\int_0^t v\,dt}{2\pi rh} \text{ Teslas} \qquad 2\text{-}10$$

where r is the radius of the two induction loops and h is their separation, both in inches.

The specific tests are identified in the following Test Table, and the data appear on Figs. 2-19 through 2-25.

TEST TABLE

Test	Configuration	Measurements Made	Data
1	Target removed, Field Measurement Plate against coil surface	$B_\perp$ on both sides of Meas. Plate	Peak $B_\perp$ vs r (2-19) plotted in Fig.
		B_r	Peak B_r vs r (2-20) plotted in Fig.
2	Target removed, .041" spacer between coil and Meas. Plate	B_r	B_r vs time (2-21) in Fig.
3	Target in place, Meas. Plate between coil and target	$B_\perp$ adjacent to target	$B_\perp$ vs time (2-22) in Fig.
		B_r	B_r vs time (2-23) in Fig.
4	Target in place, Meas. Plate beyond target	$B_\perp$ adjacent to target	$B_\perp$ vs time (2-24) in Fig.
		B_r	B_r vs time (2-25) in Fig.

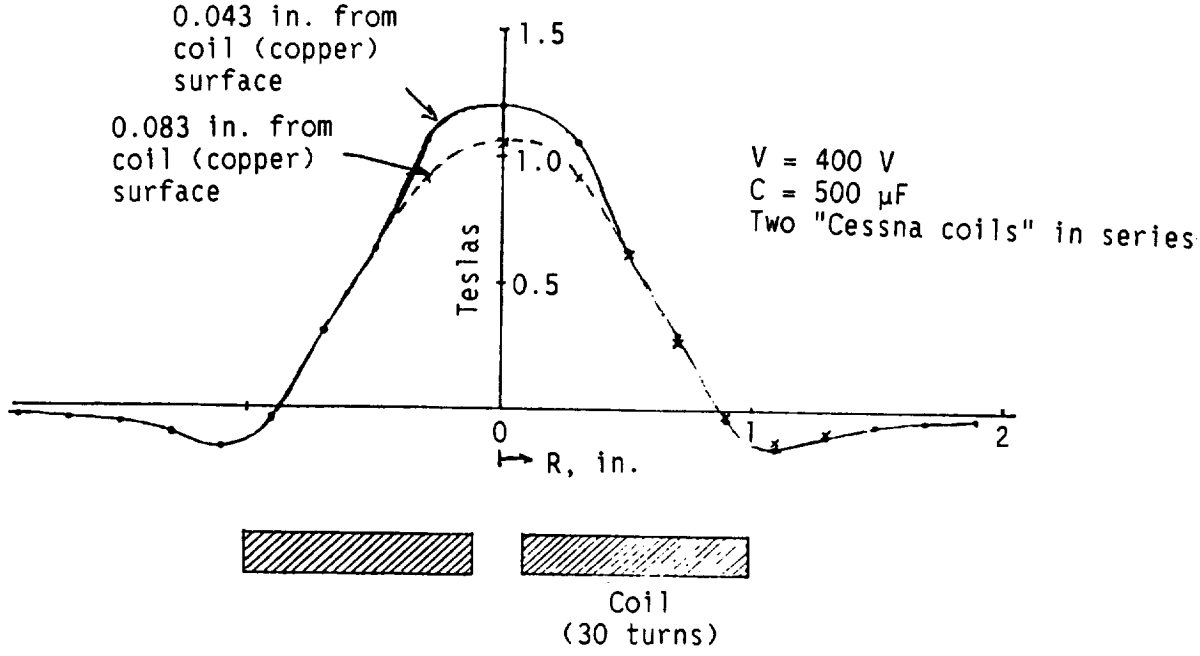

Fig. 2-19 Maximum $B_{\perp}$ vs Radius, no Target Present

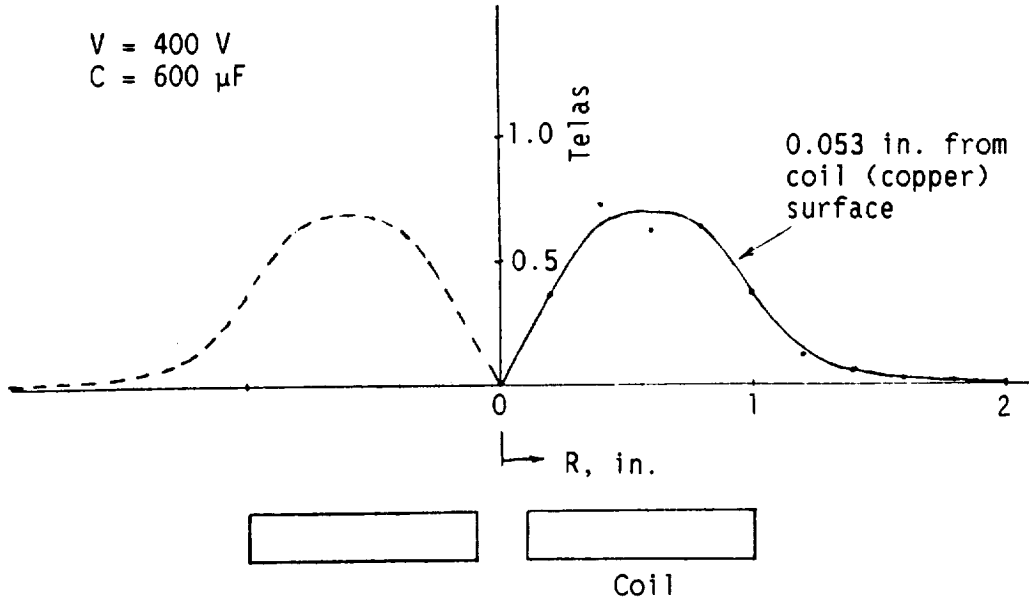

Fig. 2-20 Maximum B_r vs Radius, no Target Present

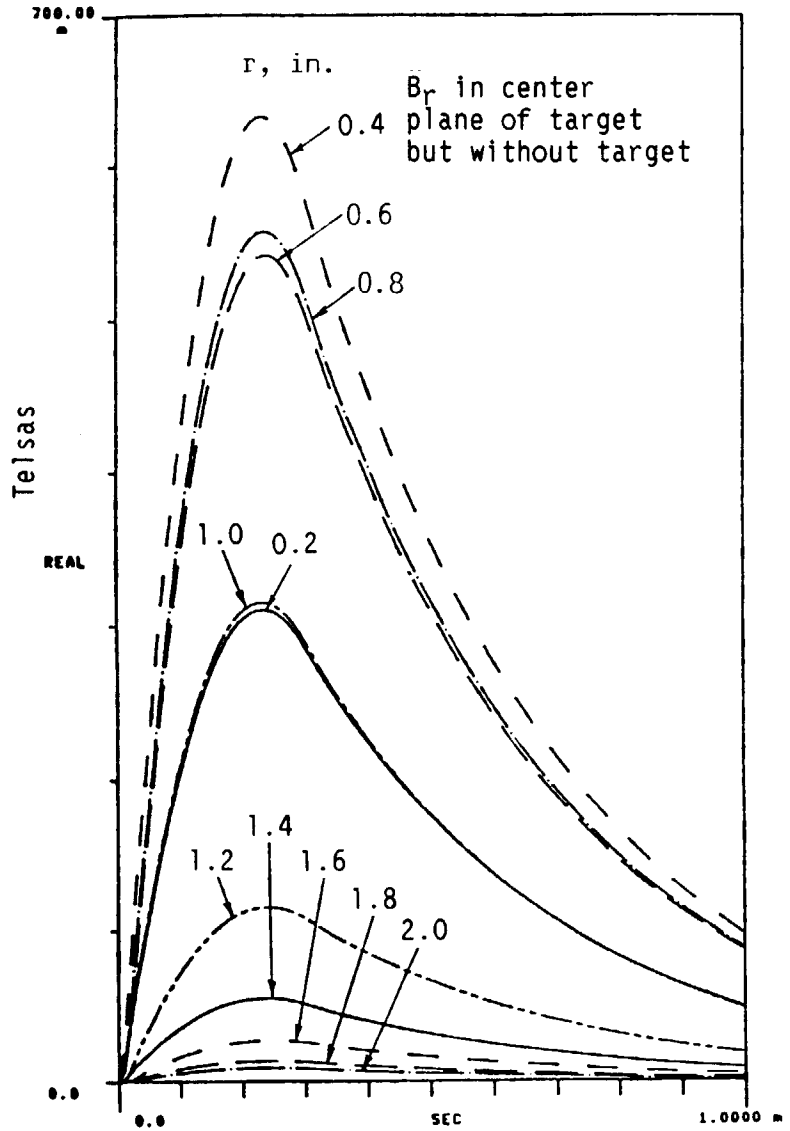

Fig. 2-21 B_r in the Center Plane of the Target but with the Target Removed

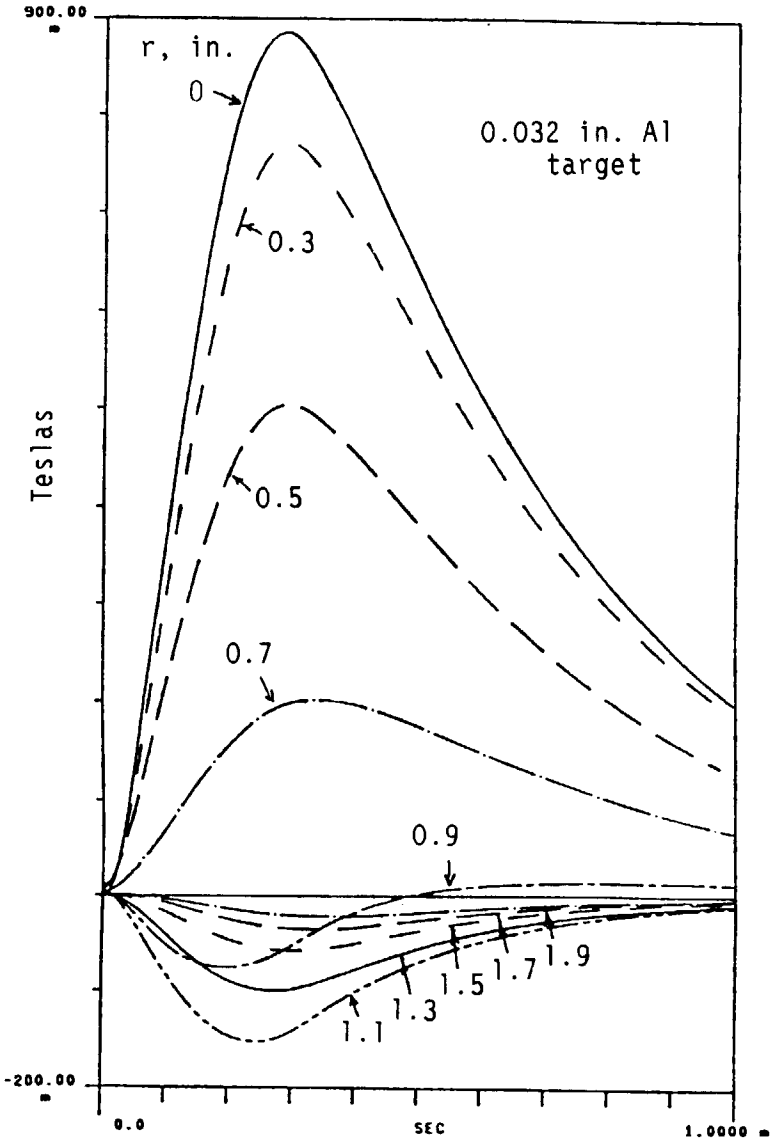

Fig. 2-22 $B_\perp$ on the Near Side

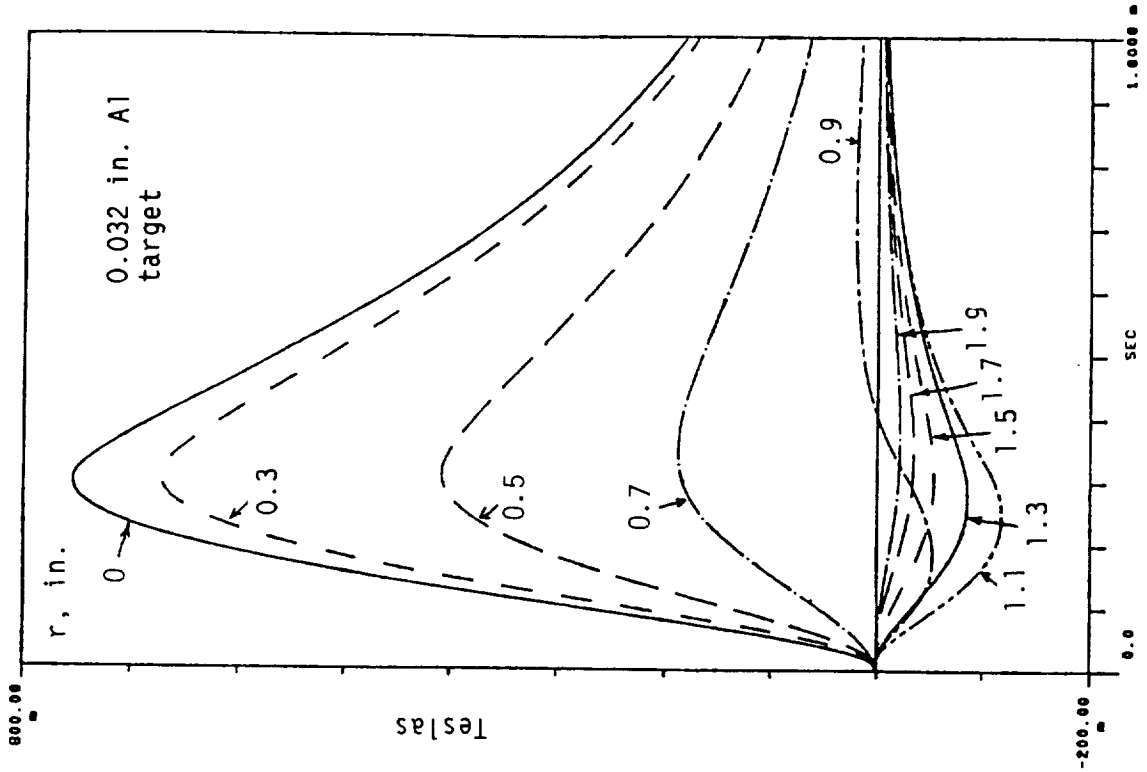

Fig. 2-24 $B_{\perp}$ on the Far Side

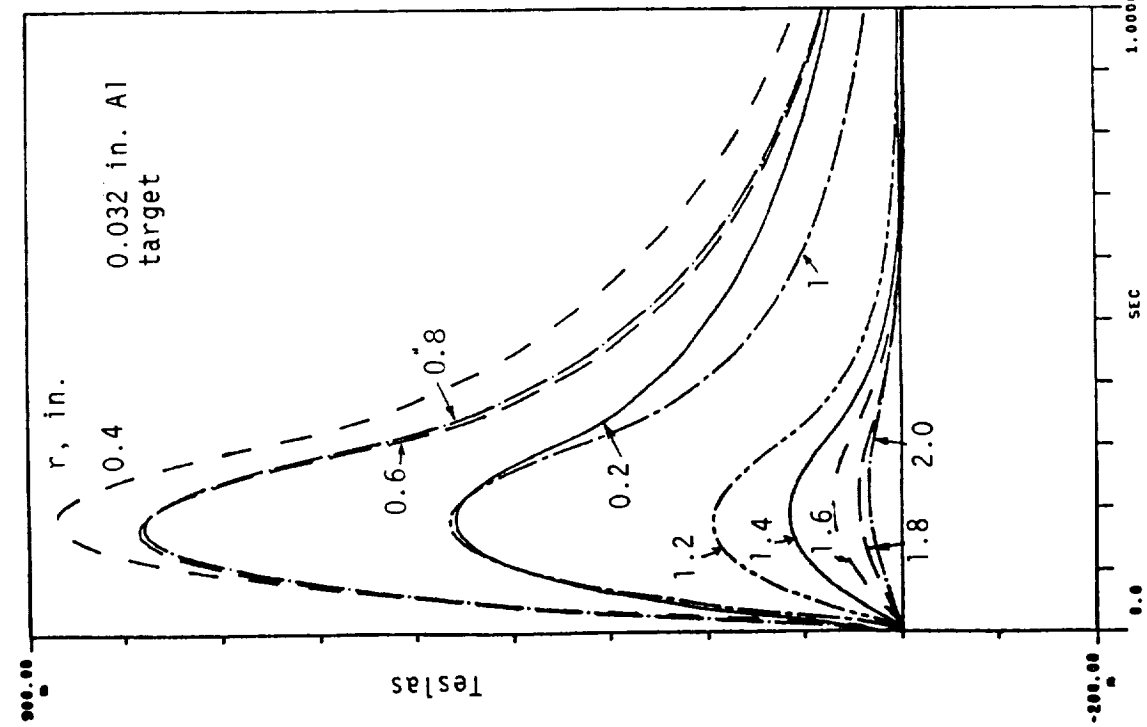

Fig. 2-23 B_r on the Near Side

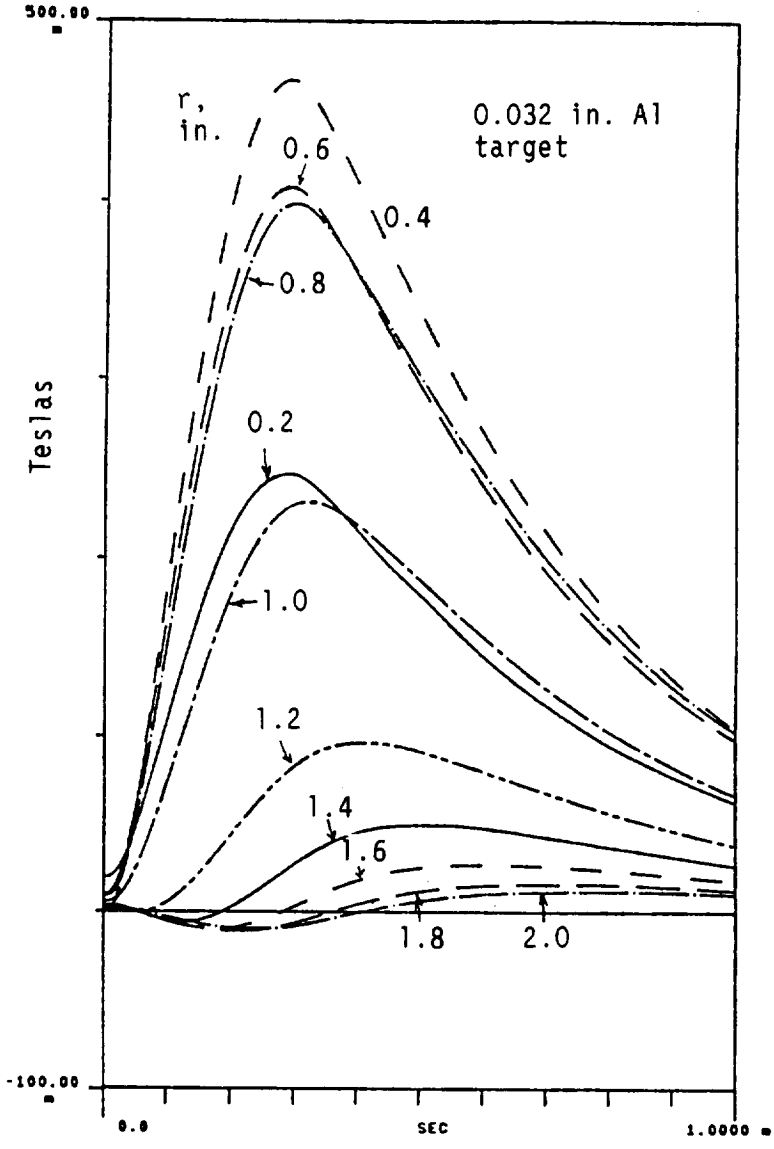

Fig. 2-25 $B_{\perp}$ on the Far Side

The purpose of Test 2 was to obtain B_r data, due to the coil alone, at the mid-plane position of the target to be added for Tests 3 and 4. These data will be used in the pressure calculation.

All B_r data showed an anomolous behavior (irregularities) at r = 0.4 relative to r = 0.6. A separate check was made, in which the plate was reversed (interchanging the two sides). This produced a reversal of the irregularities, so the effect was probably due to an inaccuracy in the construction of the plate.

C. Eddy Currents

Information on the magnitude and distribution of eddy currents in the target was obtained from a finite increment version of Ampere's Law,

$$\Delta I_{eddy} = \frac{1}{\mu_0} \oint \overline{B} \cdot \overline{dL} \qquad (2\text{-}11)$$

One of the circulation paths is illustrated by the dotted rectangle in Fig. 2-26.

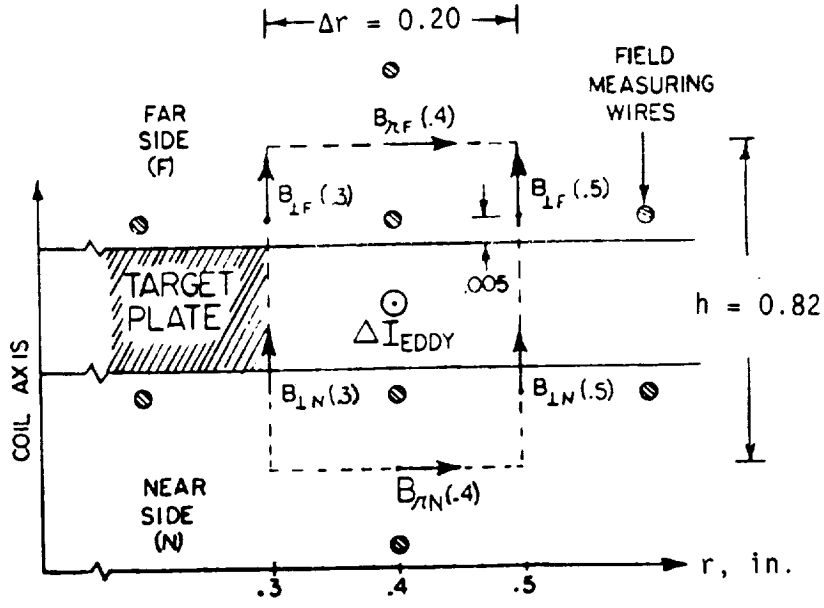

Fig. 2-26 Illustration of a Circulation Path For Evaluating Eddy Currents

It is imagined that the current in the drive coil (below the target) is referenced into the view, and the eddy currents are referenced out of the view. Thus, a counterclockwise circulation is taken, and the result is divided by Δr to obtain the current per inch of radius, assumed to apply a r = 0.4". For the path illustrated in Fig. 26,

$$\Delta I_{eddy} = \frac{1}{\mu_0}\left(\frac{B_{\perp N}(.5) + B_{\perp F}(.5)}{2}\,h - \frac{B_{\perp F}(.3) + B_{\perp N}(.3)}{2}\,h = \left[B_{rN}(.4) - B_{rF}(.4)\right]\Delta r\right) \qquad (2\text{-}12)$$

Numerically,

$$K_{eddy} = \frac{\Delta I_{eddy}}{\Delta r} = 4.14\left[B_{\perp N}(.5) + B_{\perp F}(.5) - B_{\perp F}(.3) - B_{\perp N}(.3)\right] + 20.2\left[B_{rN}(.4) - B_{rF}(.4)\right] \text{ KA/In} \qquad (2\text{-}13)$$

where all B components are in Teslas.

Calculated results for K_{eddy} vs time at various radii are graphed in Fig. 2-27, and plots of K_{eddy} vs radius are shown in Fig. 2-28. The latter figure includes the drive coil current density for comparison. It is observed that a reasonable (about 50%) current transfer efficiency occurs very early in the process, whereas the eddy currents are only about 10% of the drive current at the time of 250 μ s. Eventually, the eddy currents reverse, due to the reversed EMF from the collapsing magnetic field.

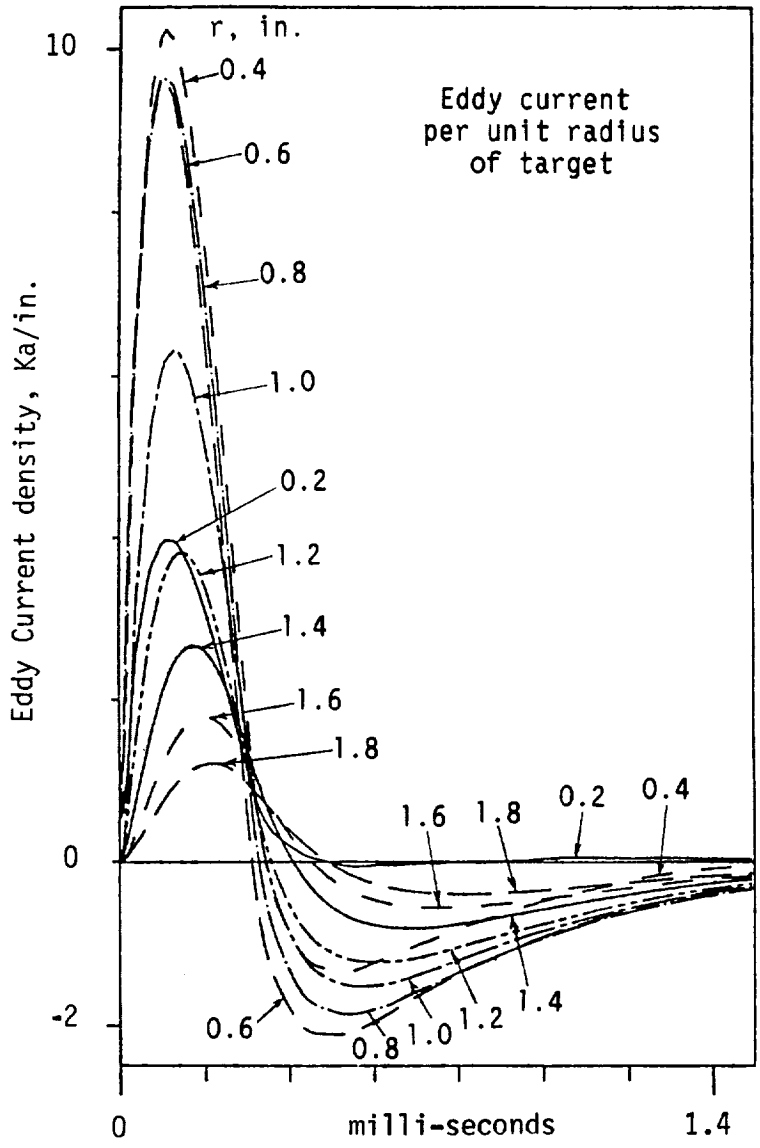

Fig. 2-27 Calculated Eddy Current Densities vs Time, at Various Radii

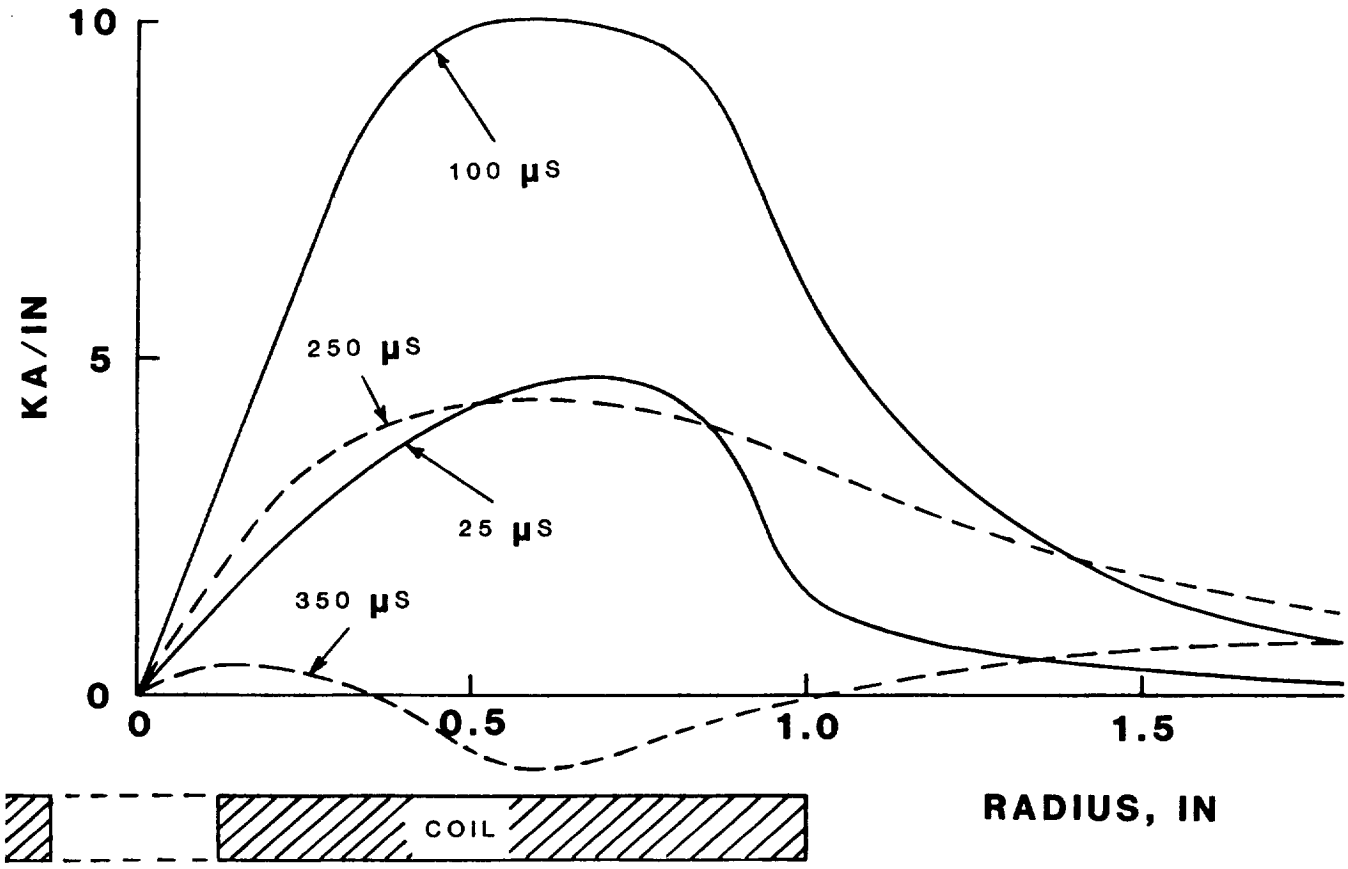

Fig. 2-28 Eddy Current Profiles

D. Pressure on the Target

Having evaluated the eddy currents, the pressure on the target can be found by the "conductor force equation," utilizing data for B_r along the center plane of the target. The B_r data used was that from Test 2, corrected for change in coil current due to the presence of the target. Thus the B_r data from Test 2 were multiplied by the factor

$$\frac{I_{coil}(t) \text{ in Test 3}}{I_{coil}(t) \text{ in Test 2}}$$

The difference in the two currents is small, as seen from Fig. 2-16.

Figure 2-29 illustrates the factors involved in the pressure calculation. The normal force exerted on a typical ring from r to r+ Δ r is

$$\Delta F_{\perp} = B_r \Delta I_{eddy} 2\pi r,$$

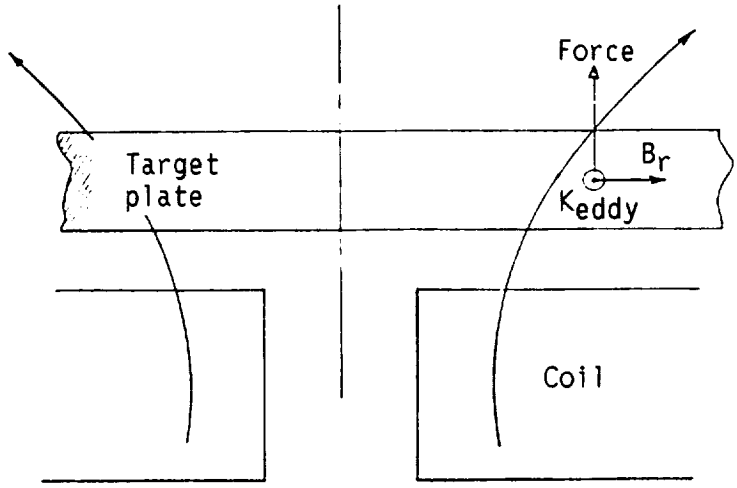

Fig. 2-29 Illustration for Pressure Calculations

yielding the following pressure formula:

$$p = 5.71\ B_r\ K_{eddy}\ PSI \tag{2-14}$$

where K_{eddy} is in KA/in, and B_r in Teslas.

Calculated results for p vs t at various radii are graphed in Fig. 2-30, and pressure "footprints" for several values of time are shown in Fig. 2-31.

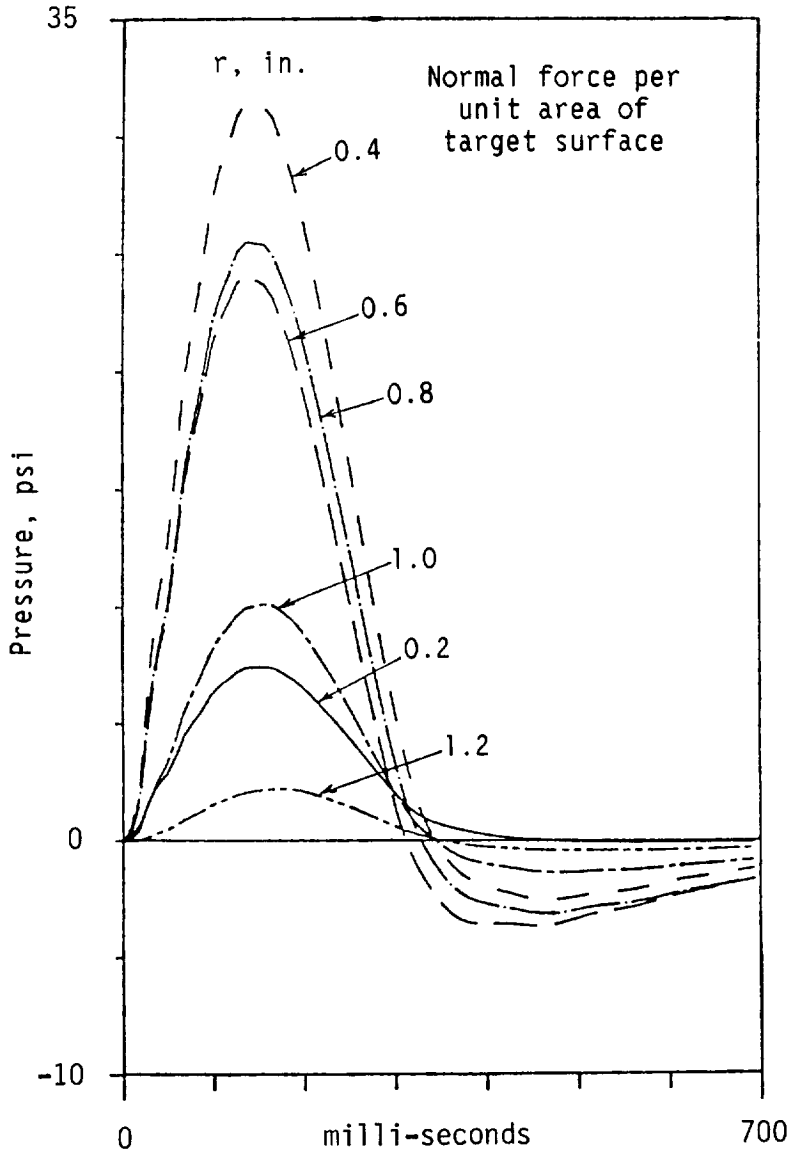

Fig. 2-30 Pressure vs Time at Various Radii

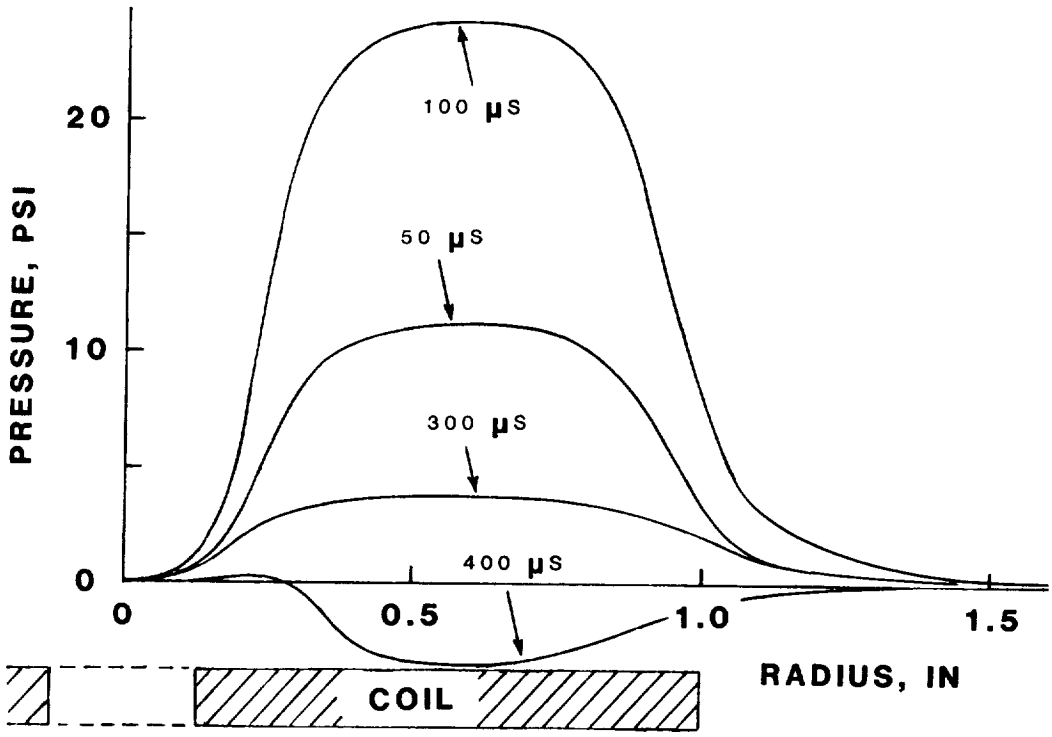

Fig. 2-31 Pressure Distribution with Radius

E. Total Normal Force and Impulse

The total normal force on the target was evaluated by the finite interval version of

$$\text{Force} = \int_{r=0}^{\infty} p\, 2\pi r dr \qquad (2\text{-}15)$$

and is graphed in Fig. 2-32, and its time integral in Fig. 2-33. The latter figure shows an impulse degradation of about 25%, due to the collapsing magnetic field.

An independent measurement of the impulse was made with a ballistic pendulum, and the pendulum value exceeded the 0.0112 lb-sec value on Fig. 2-33 by about 10%.

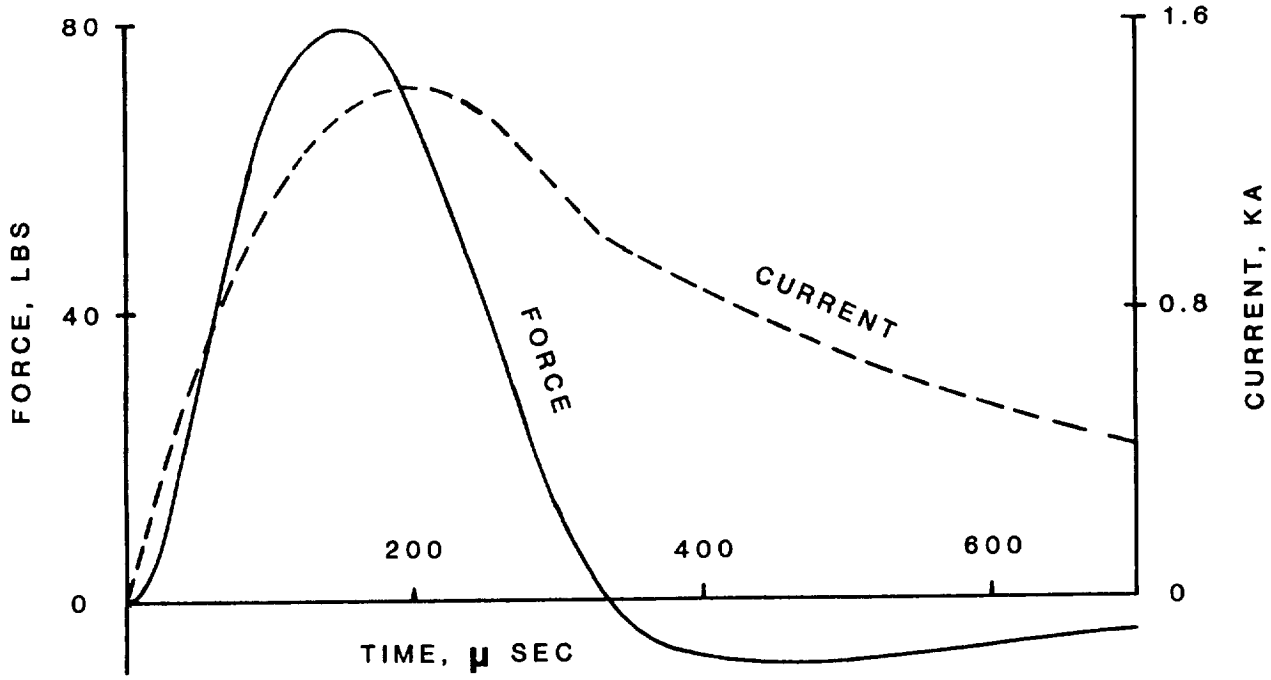

COIL CURRENT AND RESULTING NORMAL FORCE

Fig. 2-32 Total Normal Force vs Time

F. Radial Forces in the Target

If $B_{\perp}$ were used in the force calculation (Fig. 2-29), the result would be the radially acting force tending to compress the target. This force would turn to an expansive force when either $B_{\perp}$ or K_{eddy} become opposite to the reference directions.

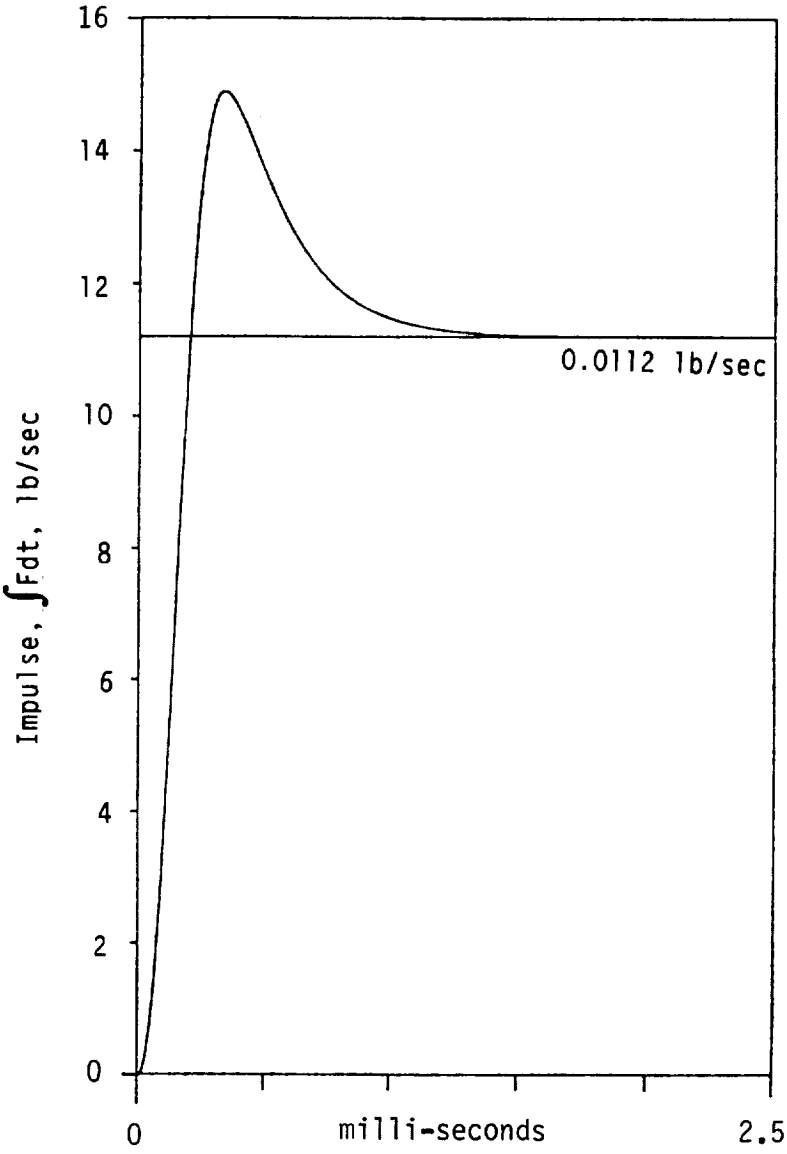

Fig. 2-33 Time Integral of the Total Normal Force

The radial force acting on the incremental target area $r\Delta\phi\Delta r$ is

$$\Delta F_r = -(K_{eddy}\Delta r) r\Delta\phi B_\perp, \tag{2-16}$$

and the force per unit of target (surface) area is

$$p_r = -B_\perp K_{eddy} \tag{2-17}$$

The specific formula, for example, to evaluate p_r at r = 0.6" is

$$p_r(.6) = -1.43 \left[B_{\perp F}(.5) + B_{\perp N}(.5) + B_{\perp F}(.7) + B_{\perp N}(.7) \right] K_{eddy}(.6)_{PSI} \tag{2-18}$$

where the B components are in Teslas, and K_{eddy} in KA/In. $B_{\perp F}$ data are from Test 4 and $B_{\perp N}$ data from Test 3.

Figure 2-34 shows graphs of p_r vs time, at various r locations, and Fig. 2-35 shows p_r vs r at various times. At early stages, the radial forces are compressive at small radii, and expansive at large radii. This action is reversed in later stages.

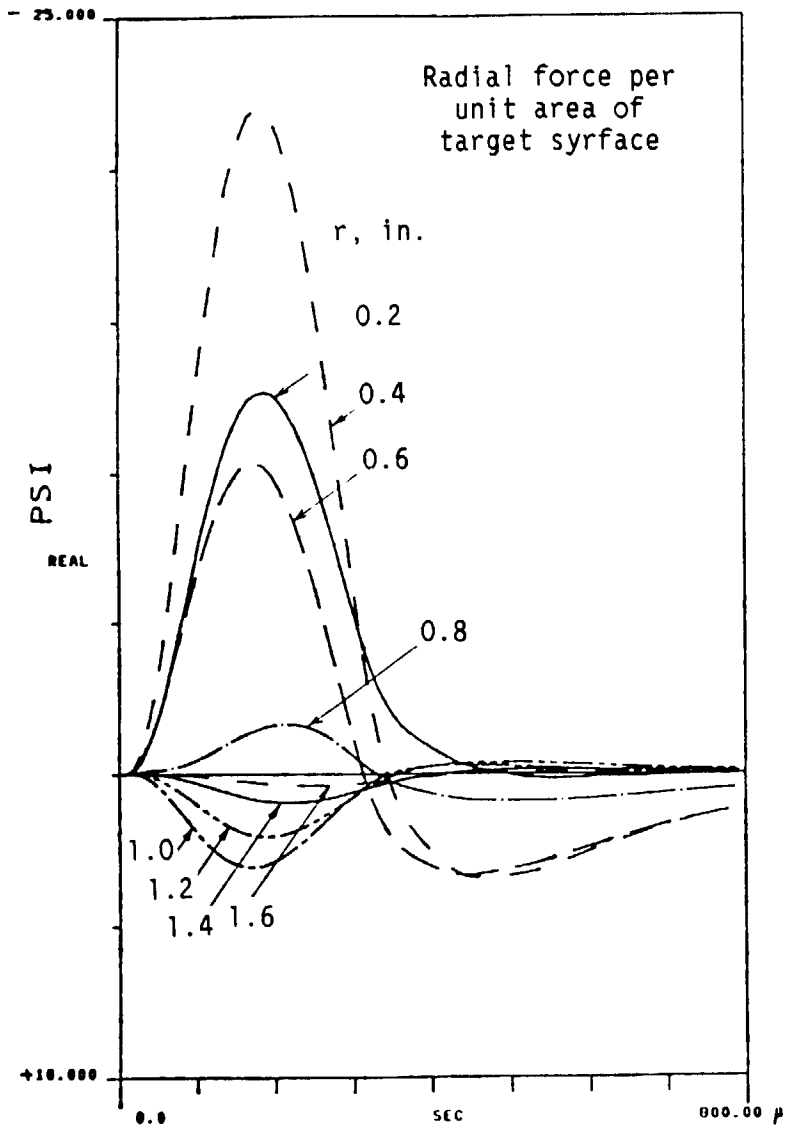

Fig. 2-34 In-Plane Force Per Unit Target Area

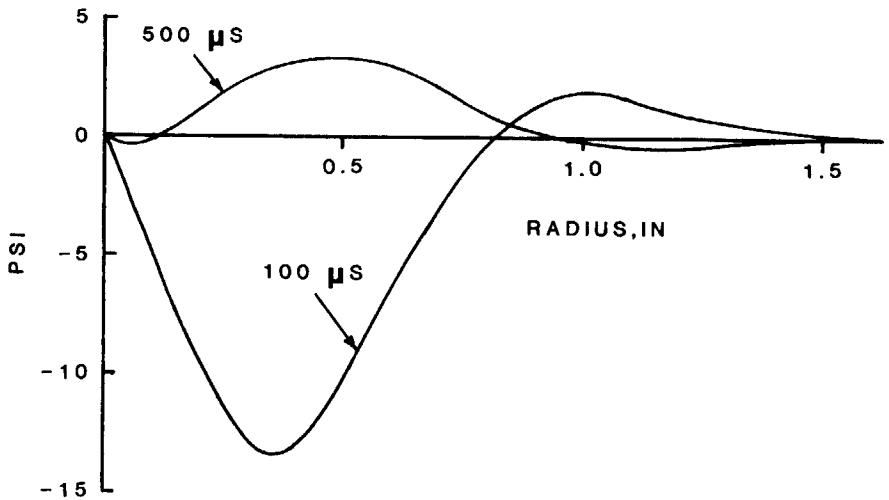

Fig. 2-35 Radial Distribution of In-Plane Force Per Unit Target Area

V. Electrodynamic Modeling

The primary goal of EIDI electrodynamic modeling is to produce a computer code which, given the geometrical details of the coil-target configuration (and circuit information such as the capacitance, voltage, and cable properties) will calculate the temporal and spatial distribution of mechanical pressure on the aircraft skin (target). The model could become extremely complex if goals are not restricted. Examples of possible goal restrictions are:

(a) Coils and metal skins might be restricted to flat geometries.

(b) Coils might be restricted to circular shapes.

(c) Non-uniformities in current distributions over the cross-section of the coil conductors might be ignored.

(d) Aircraft skin movement during the duration of the capacitor discharge might be ignored.

(e) Certain assumptions might be made regarding the discharge current, relieving the computer code of the necessity of solving circuit problem.

A. Summary of Modeling Approaches

(1) El-Markabi, et al (2-1) presented a computer analysis technique for determining the coil impedance and total target force when the coil was energized with a steady a.c. current. A planar target and a circular cylindrical coil were assumed. The technique involved Hankel transforms and transmission line analogies.

(2) R.M. Bowley, et al (2-2), calculated mechanical impulse strengths for assumed discharge current waveforms. Planar stationary targets and circular cylindrical coils were assumed. The method involved Hankel-Laplace transformations. Formulas were presented for calculating currents and fields within the target with comments on their application toward the determination of the spatial distribution of the target forces. There is no direct evidence that such forces were actually

calculated.

(3) G.L. Lewis (2-3), co-author of Ref (2-2), presented further calculated results with greater discussion on EIDI applications. An example of system design was given. The emphasis is still on mechanical impulse.

(4) R. Henderson (2-4) utilized El-Markabi's field modeling technique, and Fourier transforms for handling the time dependence. Again, planar stationary targets and circular cylindrical coils were assumed. The method entailed simultaneous solution to the field problem and the circuit problem (including the effect of the diode clamp). Calculated results included the discharge current, target force vs time and impulse strength. There was also the intent to calculate the pressure distributions, but this has not yet been done. Dr. Henderson's work is detailed in Section V B, and extensive results pertaining to coil impedance are given in Section VI.

(5) J.L. Walsh (2-5) presented a solution for pressure distribution on a planar stationary target, assuming a circular cylindrical coil with a known discharge current. His technique involved B-field calculations by the Biol-Savart Law and the simultaneous solution of eddy currents in many target elements. He did the solution in the frequency domain by Fourier transform methods. There appears to be some discrepancy between calculated results and experimental measurements, and these discrepancies have not been adequately resolved.

(6) Bernhart and Schrag have developed a discrete element solution that differs from Mr. Walsh's approach in that the target is sub-divided in z as well as r, and the solution is carried out in the time domain rather than the frequency domain. Early versions of the Bernhart-Schrag program utilized known coil current as input information. The final version includes a model of the discharge circuit so, like

Henderson's program, it generates its own coil current. The Bernhart-Schrag model is described in Section VC, along with sample results.

B. Details and Results of Henderson's Model

1. The Field Problem

The electromagnetic field portion of the problem was handled by the Hankel transform technique described by El-Markabi, et al (2-1). Figure 2-36 shows the coil target geometry with nomenclature illustrated.

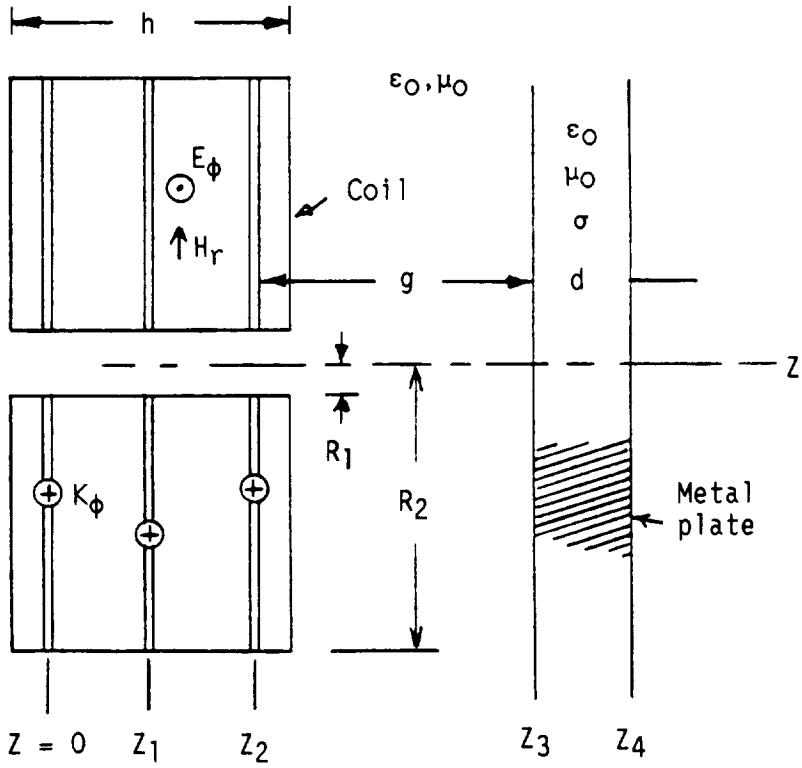

Fig. 2-36 Coil-Target Geometry and Nomenclature

The Hankel transformed fields are defined by

$$\begin{matrix} E_\phi(\lambda,z) \\ H_r^\phi(\lambda,z) \end{matrix} = \int_{r=0}^{\infty} \left\{ \begin{matrix} E_\phi(r,z) \\ H_r^\phi(r,z) \end{matrix} \right\} J_1(\lambda,r)\,r\,dr \qquad (2\text{-}19)$$

These are said to be the fields in "Hankel Space". El-Markabi shows that when Maxwell's Equations for axially symmetrical fields are transformed into Hankel Space, and displacement current ignored, then the resulting equations are analogous to those characterizing one-dimensional transmission lines. Thus, the field problem can be modeled by an equivalent transmission circuit in Hankel Space. El-Markabi's solution assumes the coil current to be sinusoidal, and the fields are then phasors. He also approximates the volume-distributed coil current by several current sheets. A three-sheet approximation is pictured in Fig. 2-36, and is assumed for the equivalent transmission line model pictured in Fig. 2-37.

In the T-line model, $E_\phi(\lambda,\omega)$ is analogous to voltage and $H_r(\lambda,\omega)$ is analogous to current. The model consists of six line sections. The extreme left section $(z<z_0)$ extends to $z = -\infty$, so there is no reflected wave on it. This section may then be replaced by its characteristic impedance Z_a. The same reasoning applies to the section $(z>z_4)$. All other sections have been represented in Fig. 2-37 by their 4-terminal network parameters (A, B, C, D). The three sheet current sources are assumed to be the same. This assumption may be removed in some future work, to account for skin effect. Then the middle source would have a phase delay and reduced amplitude.

Formulas for the characteristic impedances, Z, and for the propagation constants, γ, are:

Air Section

$$Z_a = j\omega\mu_0/\lambda$$

$$\gamma_a = \lambda$$

Metal Plate

$$Z_p = Z_a \left(1 + \frac{j\omega\mu_0\sigma}{\lambda^2}\right)^{-\frac{1}{2}}$$

$$\gamma_p = \frac{\lambda Z_a}{Z_p}$$

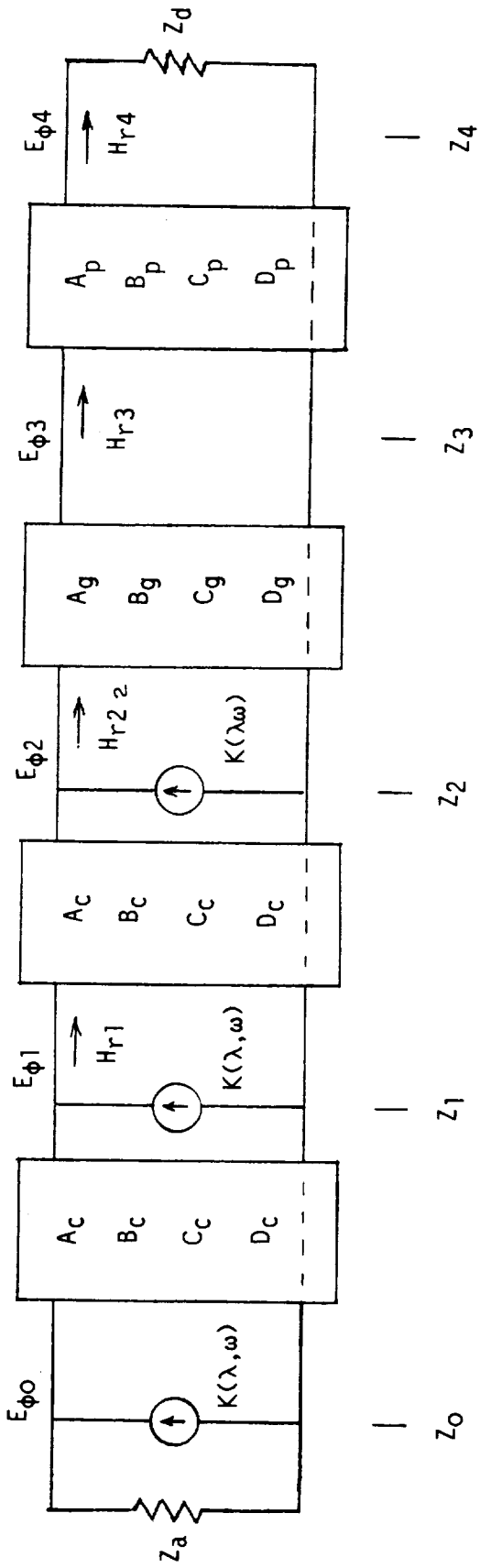

Fig. 2-37 Hankel Space Transmission Model of the Field Problem

Formulas for the 4-terminal network parameters are:

$$
\begin{aligned}
A_c &= D_c = \text{COSH}\ (\lambda h/3) \\
B_c &= Z_a\ \text{SINH}\ (\lambda h/3) \\
C_c &= B_c\ Z_a^{-2} \\
A_g &= D_g = \text{COSH}\ (\lambda g) \\
B_g &= Z_a\ \text{SINH}\ (\lambda g) \\
C_g &= B_g\ Z_a^{-2} \\
A_p &= D_p = \text{COSH}\ (\gamma_p d) \\
B_p &= Z_p\ \text{SINH}\ (\gamma_p d) \\
C_p &= B_p\ Z_p^{-2}
\end{aligned}
$$

The Hankel Space current sources are calculated from

$$K(\lambda,\omega) = \frac{N\ I\ (\omega)}{3(R_2-R_1)} \int_{R_1}^{R_2} J_1(\lambda r) r dr \qquad (2\text{-}20)$$

where N is the number of coil turns, and I (ω) is the Fourier transform of the coil current.

Analysis of the network (Fig. 2-37) is done by a computer. If fields are desired in real space, then the inverse Hankel transformation must be calculated:

$$\begin{Bmatrix} E_\phi(r,z) \\ H_r^\phi(r,z) \end{Bmatrix} = \int_{\lambda=0}^{\infty} \begin{Bmatrix} E_\phi(\lambda,z) \\ H_r^\phi(\lambda,z) \end{Bmatrix} J_1(\lambda r)\lambda d\lambda, \qquad (2\text{-}21)$$

and if they are desired as time functions, then an additional calculation must be performed for the inverse Fourier transform.

2. The Circuit Problem

The electrical circuit can be represented as shown in Figs. 2-38 (a) and (b).

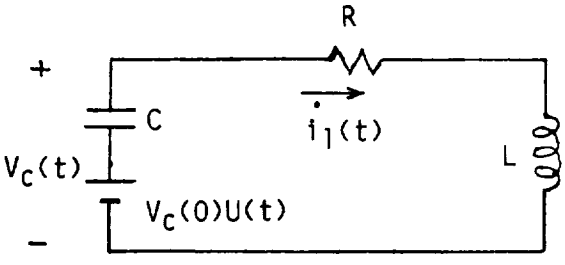

Fig. 2-38 (a)

Applies up to time t_x, when the diode clamp begins to conduct.

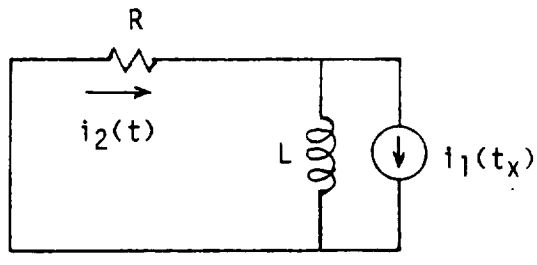

Fig. 2-38 (b)

Applies for $t>t_x$

Both circuits have initial conditions represented as external sources. Direct time-domain solutions for these circuits cannot be written because R and L are functions of frequency.

Figures 2-39 (a) and (b) are the frequency domain circuits. They show a breakdown of elements of the physical circuit. It is assumed that this circuit contains a series-connected dummy coil in free space (no target).

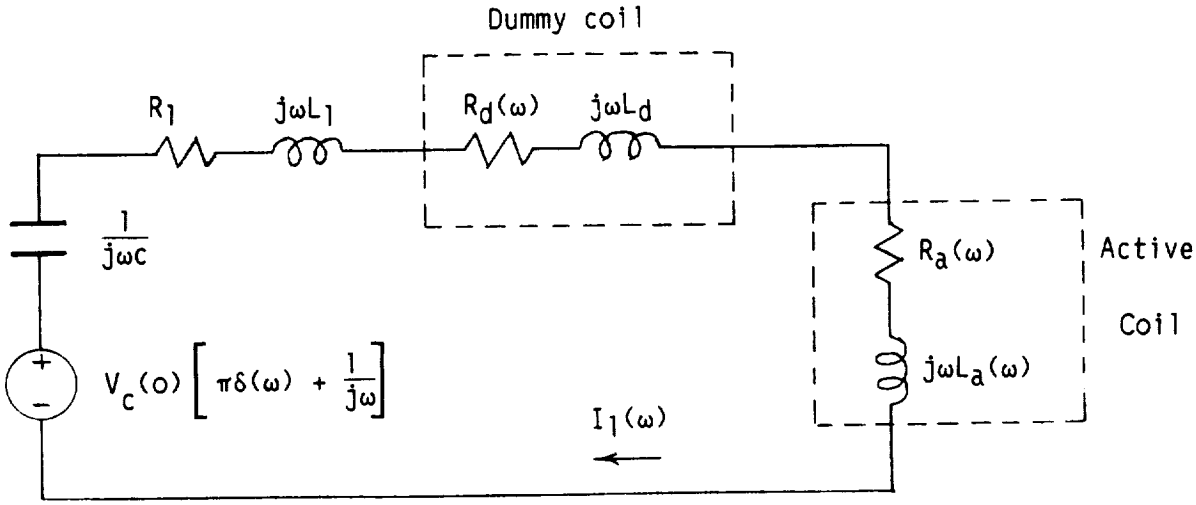

Fig. 2-39 (a) Frequency Domain Circuit ($t<t_x$)

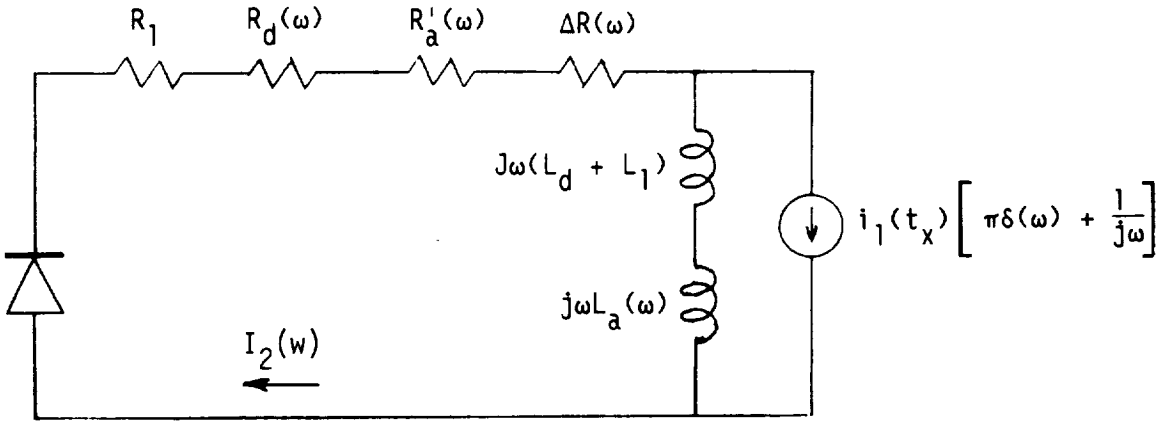

Fig. 2-39 (b) Frequency Domain Circuit ($t>t_x$)

The symbols in Fig. 2-39 represent:

R_1 = Equivalent resistance of the capacitor and the cable.

L_1 = Equivalent inductance of the capacitor and the cable.

$R_d(\omega)$ = A.C. resistance of the dummy coil.

L_d = Inductance of the dummy coil.

$R_a(\omega)$ = Effective resistance of the active coil.

$R_a'(\omega)$ = Portion of $R_a(\omega)$ that is the free-space A.C. resistance.

$\Delta R(\omega)$ = Portion of $R_a(\omega)$ that is field-induced. It is due to the presence of the metal plate.

$L_a(\omega)$ = Inductance of the active coil in the presence of the metal plate.

Data of $R_d(\omega)$ and $R_a^1(\omega)$ can be estimated from the graph in Figure 2-52.

The field-induced impedance of the active coil $Z(\omega) = \Delta R(\omega) + j\omega L_a(\omega)$ must also be found before the circuit problem can be solved. This impedance is defined as the phasor voltage across the coil terminals, resulting from E_ϕ in Fig. 2-36, per ampere of coil current. Thus, a preliminary solution to the field problem must be carried out. The simplest procedure is to set $I(\omega)$ in Eq. 2-20 equal to unity, and then solve the transmission network for E_{ϕ_0} E_{ϕ_1}, and E_{ϕ_2}.

Basing the calculation on the average of these three fields, and following El-Markabi's reasoning, the formula for calculating $Z(\omega)$ becomes

$$Z(\omega) = \frac{2/3\,\pi N}{R_2 - R_1} \int_0^\infty \left\{ \lambda \left[E_{\phi_0}(\lambda) + E_{\phi_1}(\lambda) + E_{\phi_2}(\lambda) \right] \int_{R_1}^{R_2} J_1(\lambda r) r dr \right\} d\lambda. \quad (2\text{-}22)$$

Now the circuit problem can be solved.

$I_1(\omega)$ is first found from the circuit of Fig. 2-39 (a), and its inverse transform, $I_1(t)$, calculated, along with the corresponding $v_{c1}(t)$. The value of t (called t_x in Figs. 2-38 (a) and (b)) for the first zero crossing of $V_{c1}(t)$ is noted. The circuit in Fig. 2-39 (b) is then solved for $i_2(t)$, using $i_1(t_x)$ as the initial condition. The circuit current is finally constructed from the two solution parts by

$$i(t) = i_1(t)\left[1-u(t-t_x)\right] + i_2 u(t-t_x), \tag{2-23}$$

and its Fourier transform $I(\omega)$ found. This is the current spectral information which enters into the Hankel Space current sources (Eq. 2-20).

3. Pressure and Force on the Target

Starting with the equation for the force per unit volume within the target

$$\frac{\overline{F}}{vol} = \overline{J} \times \overline{B} \tag{2-24}$$

where $\overline{J}$ is the local current density, and neglecting displacement current, then the pressure becomes

$$P(r) = \int_{z_3}^{z_4} \left(\frac{F_z}{vol}dz\right) = \frac{-1}{\mu_0} \int_{z_3}^{z_4} B_r \left(\frac{\partial B_r}{\partial z} - \frac{\partial B_z}{\partial r}\right)dz$$

$$= \frac{1}{\mu_0}\left[\frac{B_r^2(z_3)}{2} - \frac{B_r^2(z_4)}{2} + \int_{z_3}^{z_4} B_r \frac{\partial B_z}{\partial r}\, dz\right]. \tag{2-25}$$

Also utilizing $\overline{\nabla} \cdot \overline{B} = 0$, Eq. 2-25 can be further modified into

$$P(r) = \frac{1}{\mu_0}\left[\frac{B_r^2(z_3) - B_z^2(z_3)}{2} - \frac{B_r^2(z_4) - B_z^2(z_4)}{2}\right. \tag{2-26}$$

$$\left. + \int_{z_3}^{z_4} \frac{1}{r} \frac{\partial}{\partial r} (rB_rB_z)\, dz\right].$$

The force contributed by the integral term in Eq. 2-26 is

$$\int_{r=0}^{\infty} 2\pi r \left[\int_{z_3}^{z_4} \frac{1}{r} \frac{\partial}{\partial r} (rB_rB_z)dz\right] dr$$

$$= 2\pi \int_{z_3}^{z_4} \int_{r=0}^{\infty} \frac{\partial}{\partial r} (rB_rB_z)drdz.$$

However,

$$\int_{r=0}^{\infty} \frac{\partial}{\partial r}(rB_rB_z)dr = (rB_rB_z)\Big|_{\text{at } r=\infty} - (rB_rB_z)\Big|_{\text{at } r=0} = 0$$

Thus, while the integral term in Eq. 2-26 may influence the distribution of pressure, it does not contribute to the total force. This total force should then be given by

$$F(t) = \int_{r=0}^{\infty} \frac{2\pi r}{2\mu_0} \left[B_r^2(z_3) - B_z^2(z_3) - B_r^2(z_4) + B_z^2(z_4)\right] dr. \tag{2-27}$$

The calculation for pressure distribution appears to be difficult (no formula has yet been discovered that utilizes only field information at the two surfaces of the target). On the other hand, the force seems to be more readily calculable.

4. Results of Calculations with Henderson's Model

Calculations were made with the problem conditions that existed in the Magnetic Field Diagnostics experiment so that calculated results might be compared with experimental results. A tabulation of the conditions are:

Coils

(Active and Dummy Alike)

$N = 30$ turns, $R_1 = .125$ inch,

$R_2 = 1.00$ inch, $h = .188$ inch,

$R_{dc} = .0235\ \Omega$, $L_d = 22\mu H$.

Target

2024-T3 Aluminum ($\sigma = 3.48 \times 10^7\ \mho/m$),

$d = .032$ inch.

Gap

$g = .1095$ inch

Circuit

$C = 600\mu F$, $R_1 = .054\Omega$

$L_1 = 1\ \mu H$, $V_c(0) = 400$ volts

Figures 2-40 through 2-44 show results pertaining to coil impedance. Fig. 2-40 is plot of the inductance of the active coil at two frequencies, as calculated from Eq. 2-22, as the upper limit on λ is varied. This plot gives an indication of what λ range provides the largest contribution. Figure 2-41 is a similar plot for the real part of Z (ω), which is the field-induced resistance.

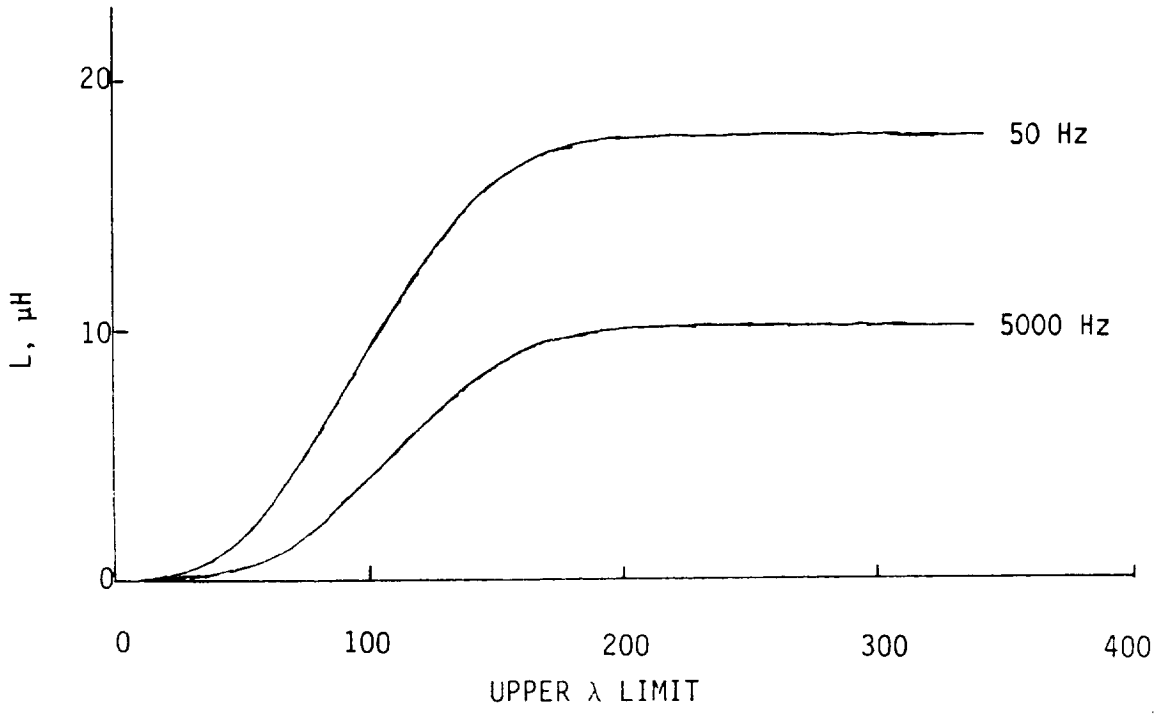

Fig. 2-40 Calculated Coil Inductance, vs Upper λ Limit (Henderson Model)

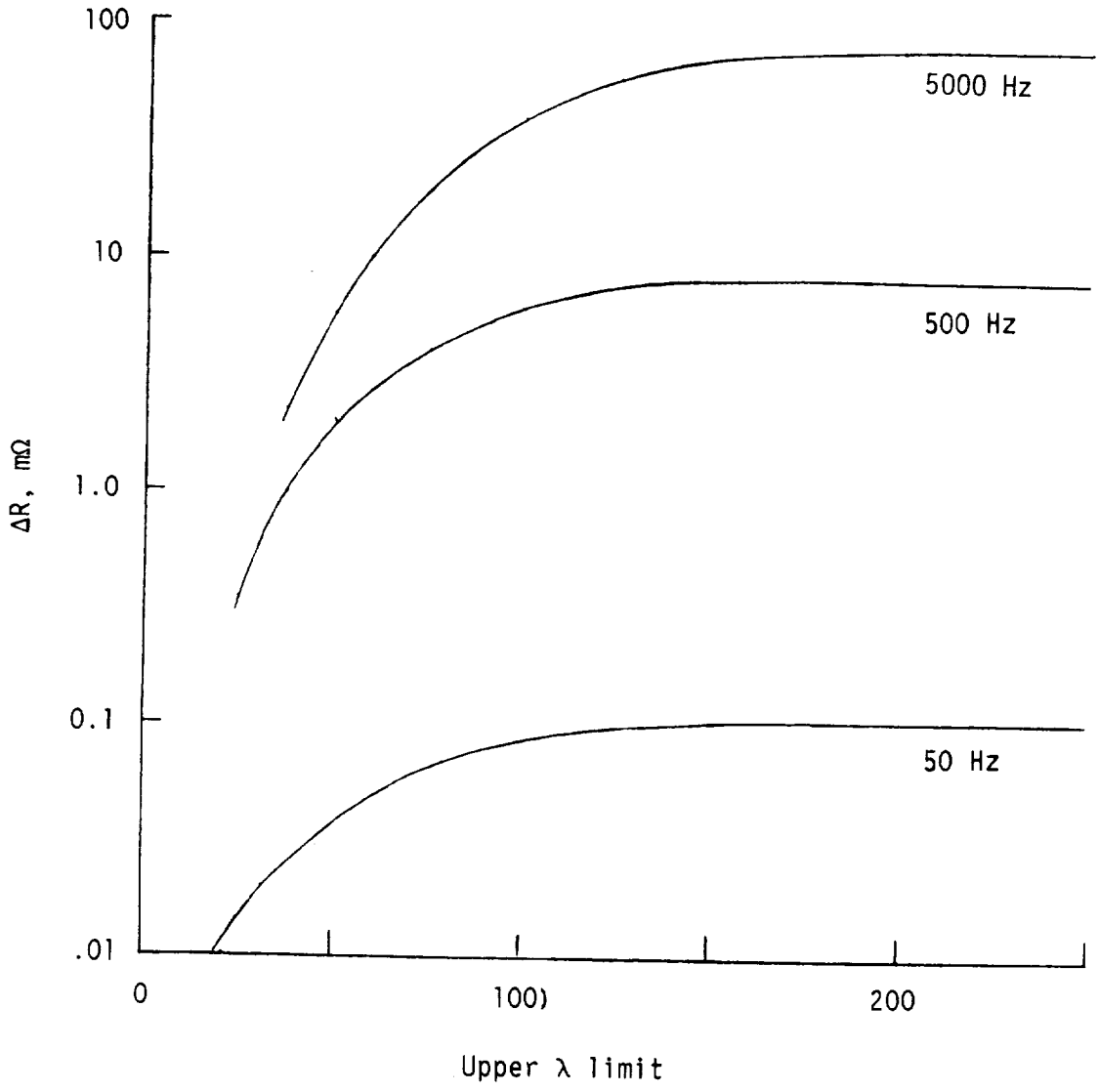

Fig. 2-41 Calculated Coil Resistance Contributed by the Metal Plate vs Upper λ Limit (Henderson Model)

Figure 2-42 is a graph of coil inductance vs frequency, with math model calculations and experimental measurements compared. These comparisons are fair, but could be better.

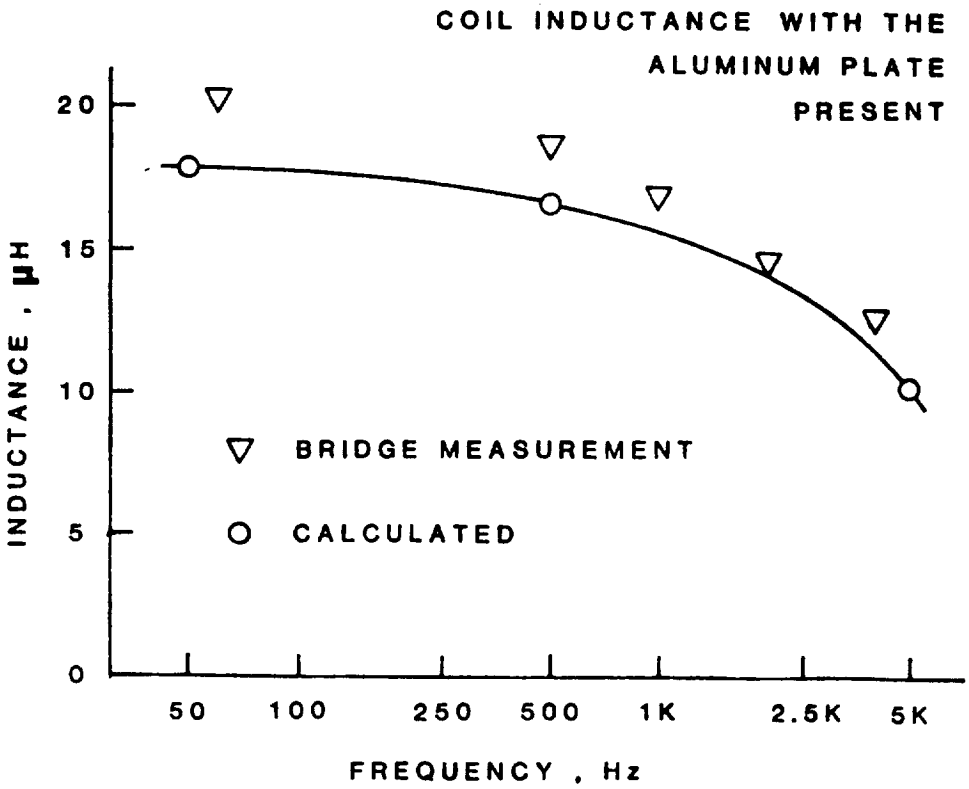

Fig. 2-42 Coil Inductance, Comparative Results (Henderson Model)

Figure 2-43 shows the calculated field-induced resistance as a function of frequency, along with bridge-measured data. The measured values are the difference between the measurement without the target plate and a re-measurement with the target brought into position.

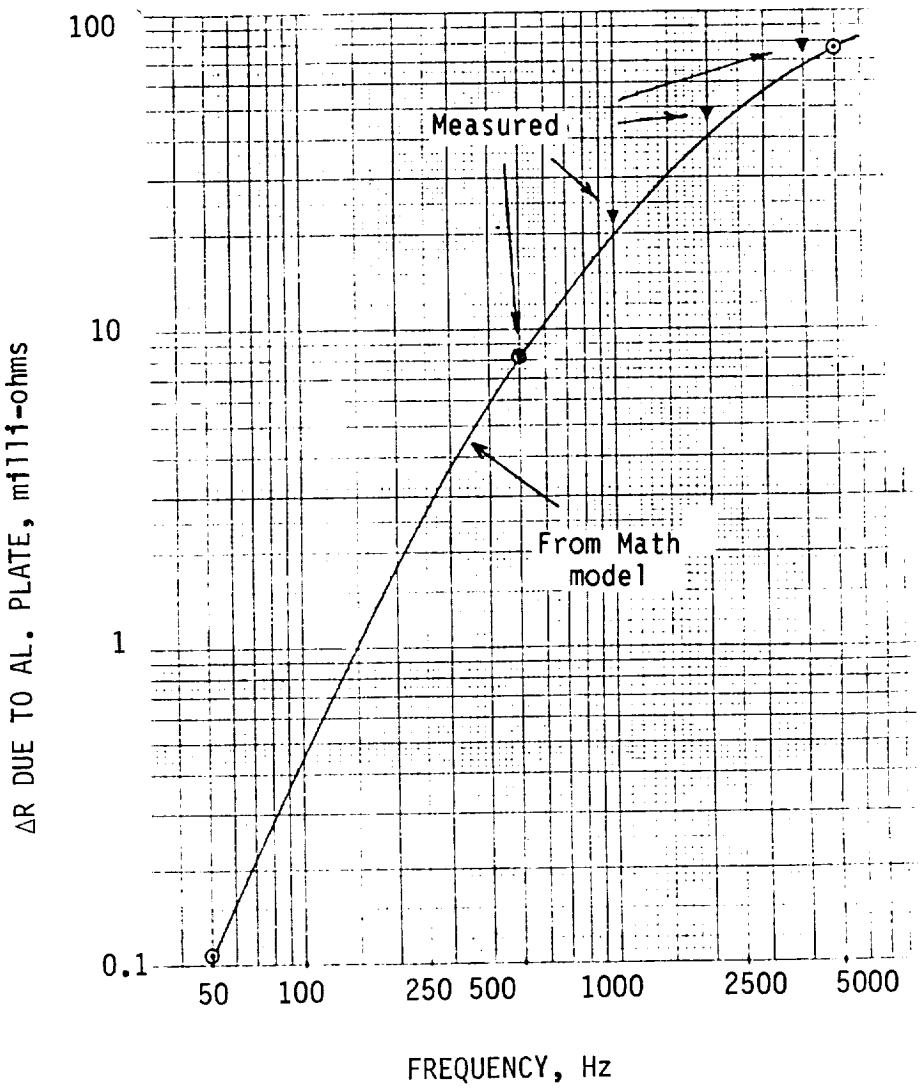

Fig. 2-43 Coil Resistance Due to the Metal Plate vs Frequency (Henderson Model)

Figure 2-44 shows a comparison of the coil current calculated from the math model Eq. 2-23 and the measured current.

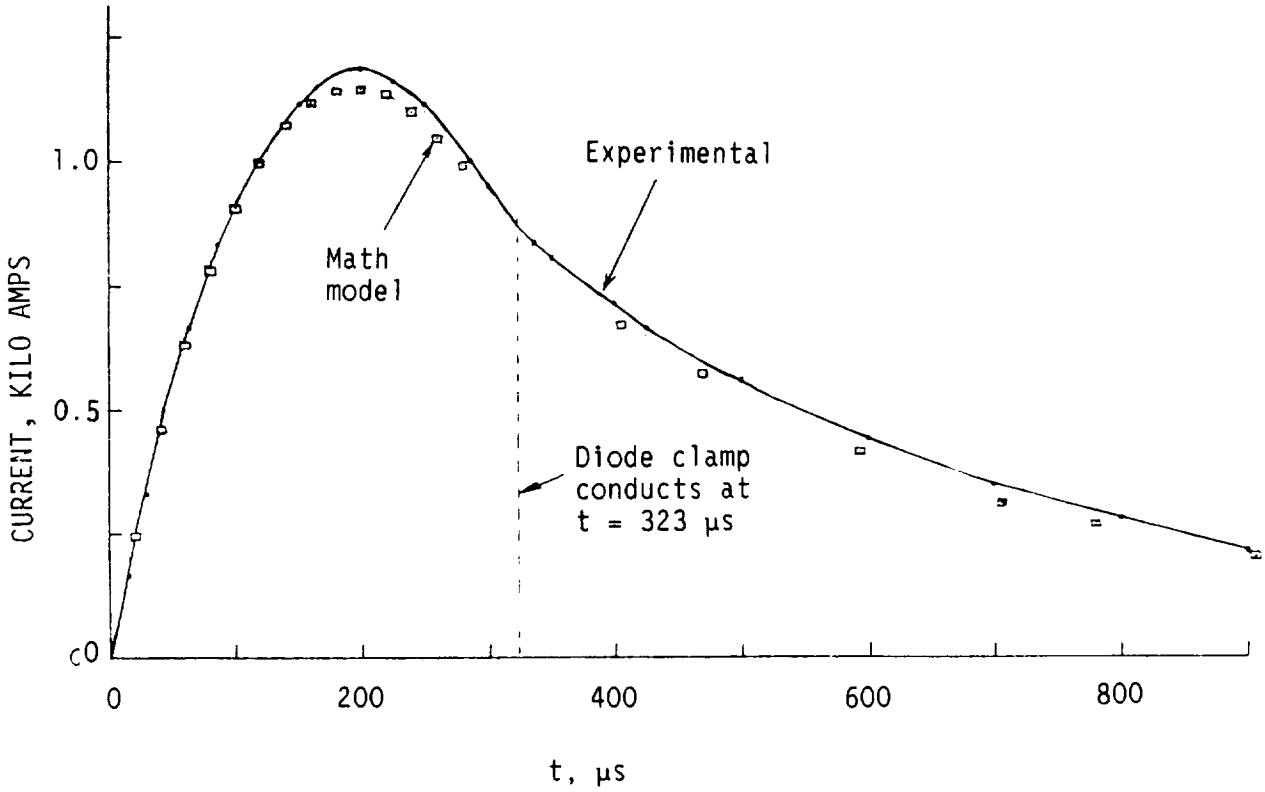

Fig. 2-44 Comparison of Coil Current Calculated from the Math Model with that Measured (Henderson Model)

Figure 2-45 is the Fourier amplitude spectrum for the calculated coil current. There are virtually no contributions beyond 4 KHz. The quantity 1/4tm (the approximate "electrical frequency") is illustrated on the plot.

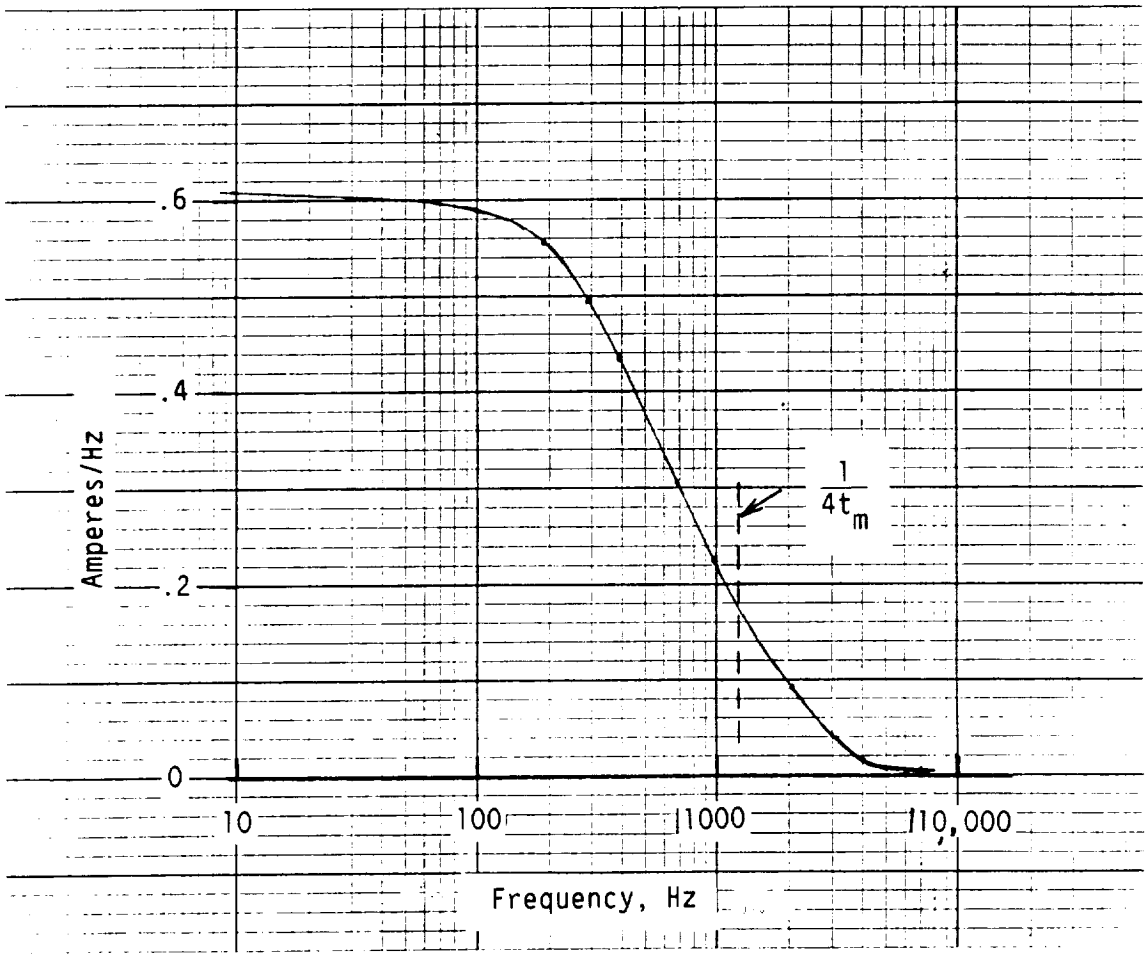

Fig. 2-45 The Calculated Current Spectrum (Henderson Model)

Figures 2-46 through 2-49 are comparisons of calculated B-field components with those measured in the Magnetic Field Diagnostics experiment. The greatest discrepancy appears at the radius 0.4 inch, where it was noted that the experiment yielded anomolous behavior. It should also be recalled that the effective measurement planes were 0.025 inches from the target surfaces, whereas the calculated fields were surface values.

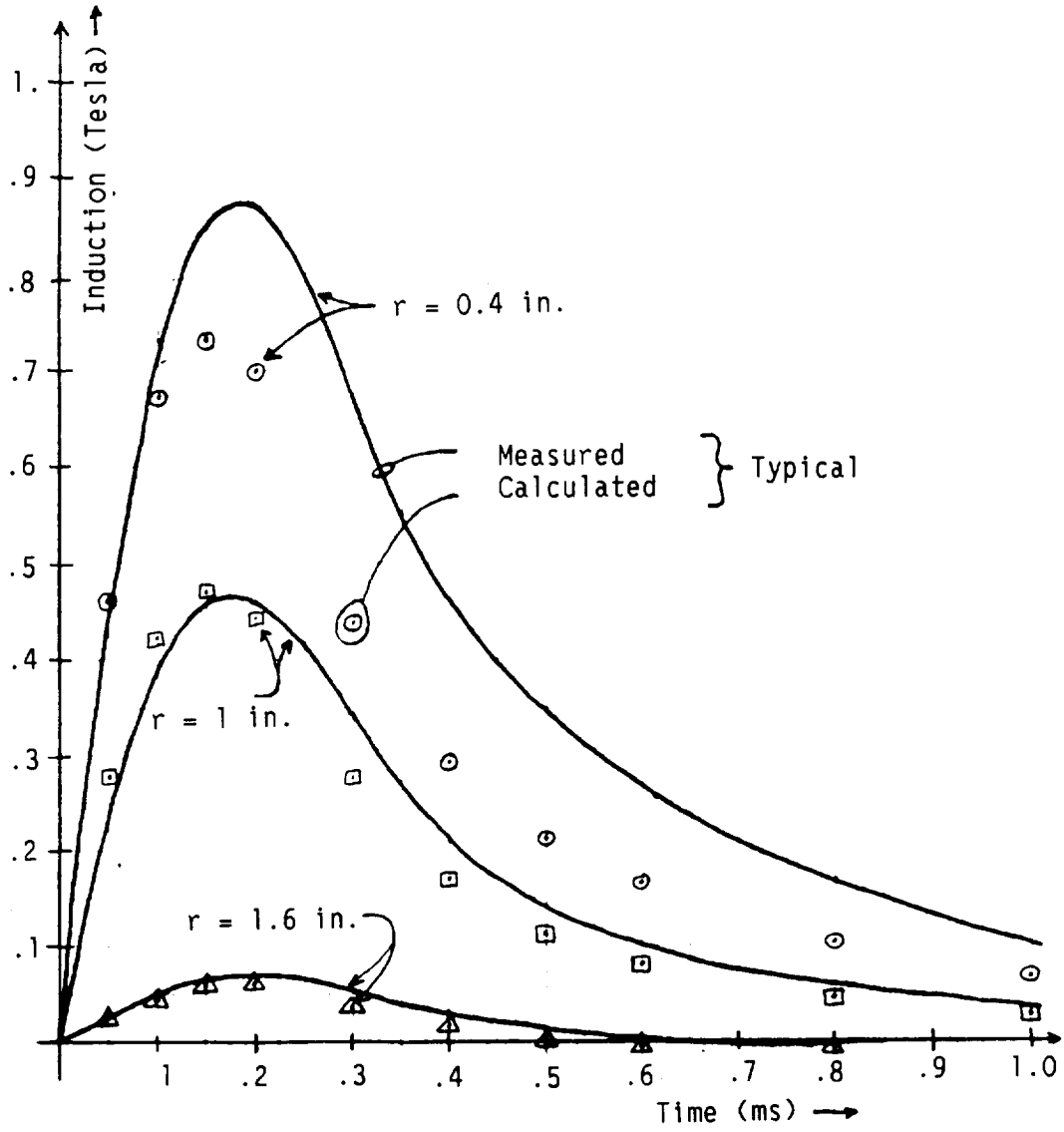

Fig. 2-46
B_r vs Time, Near Side

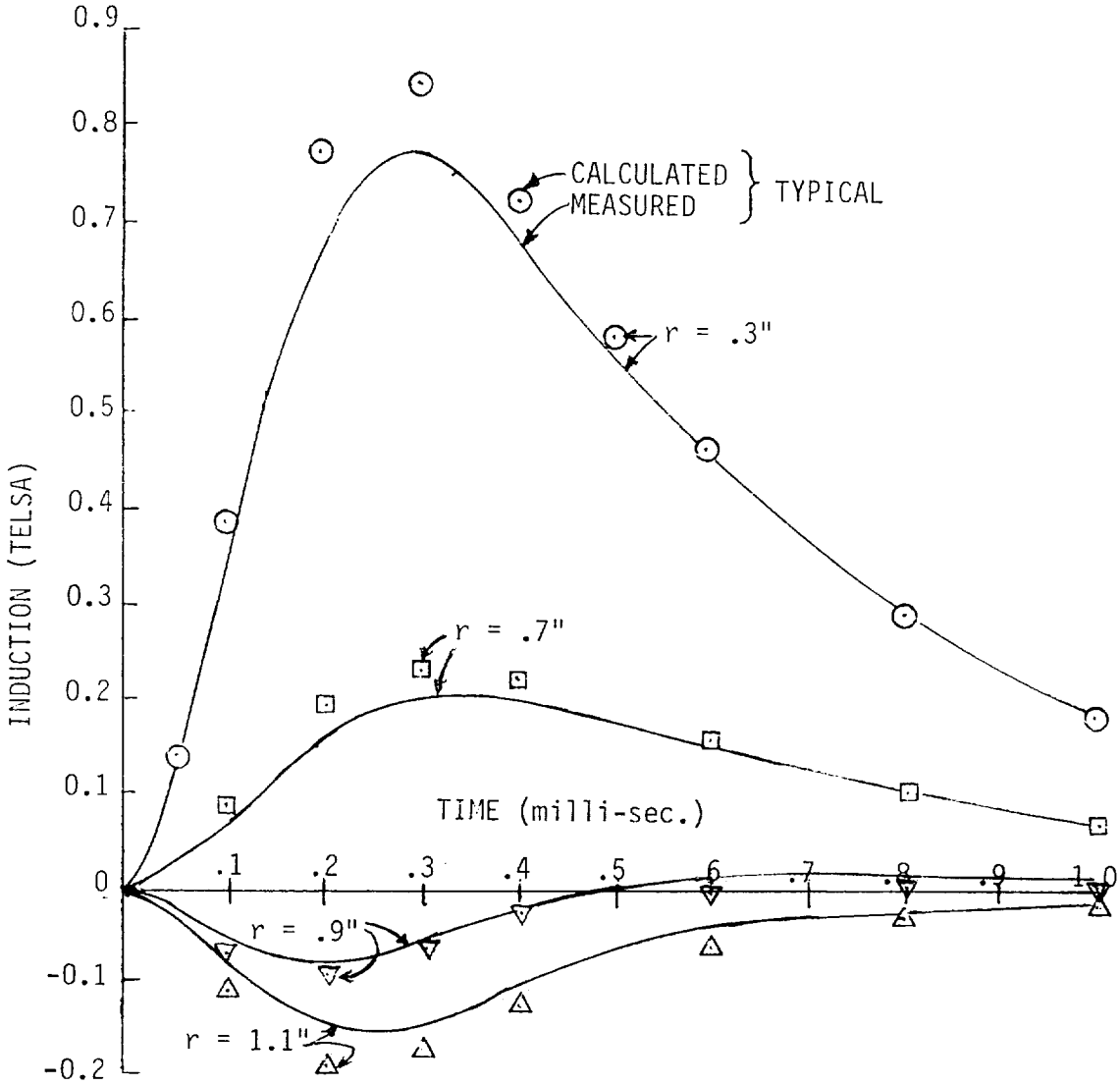

Fig. 2-47
B_z vs Time, Near Side

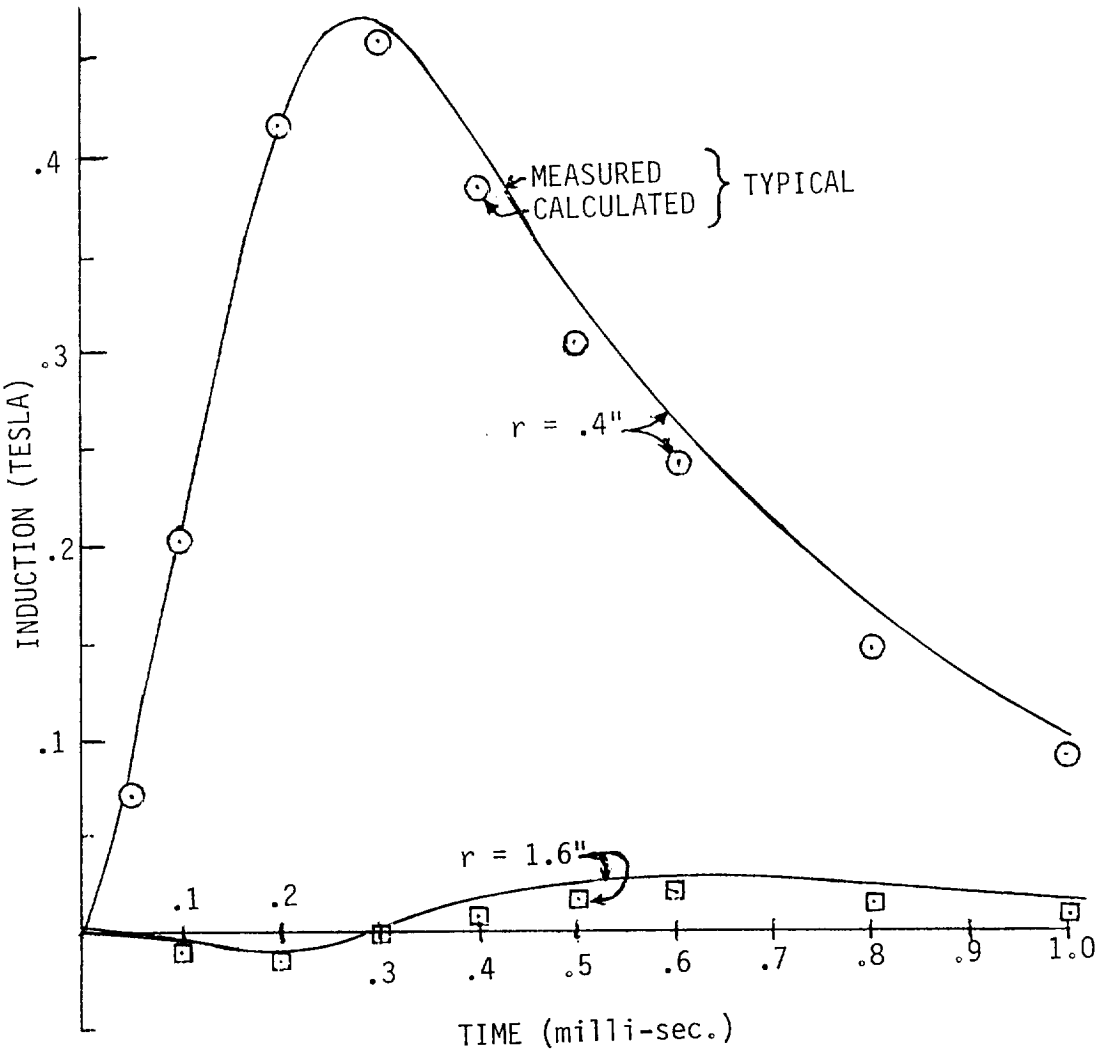

Fig. 2-48
B_r vs Time, Far Side

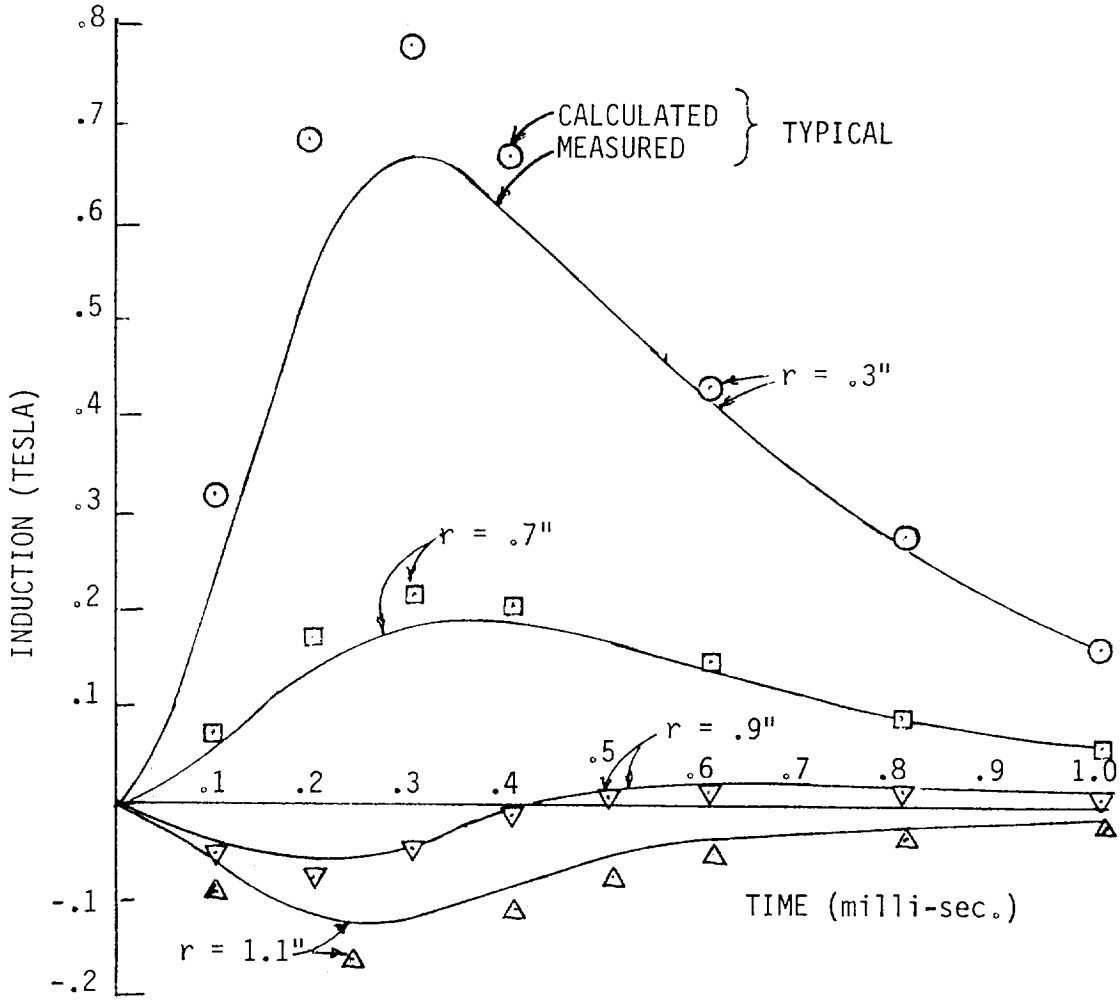

Fig. 2-49

B_z vs Time, Far Side

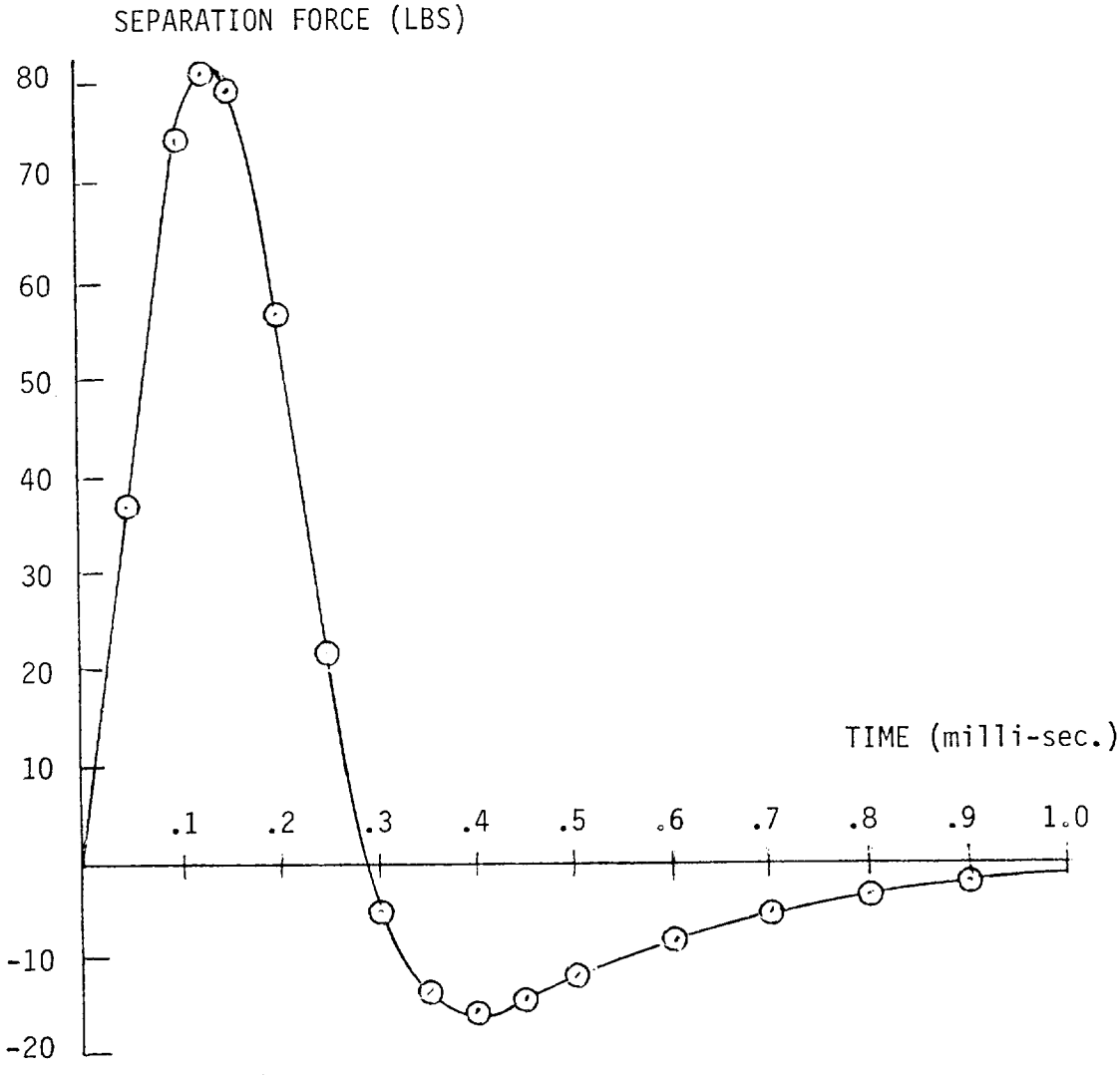

Fig. 2-50
Calculated Force Between Coil and Target

C. Details and Results of the Bernhart-Schrag Model

1. Major Assumptions

Figure 2-51 shows the basic EIDI discharge circuit. The mechanical forces and pressures on the target plate are to be calculated.

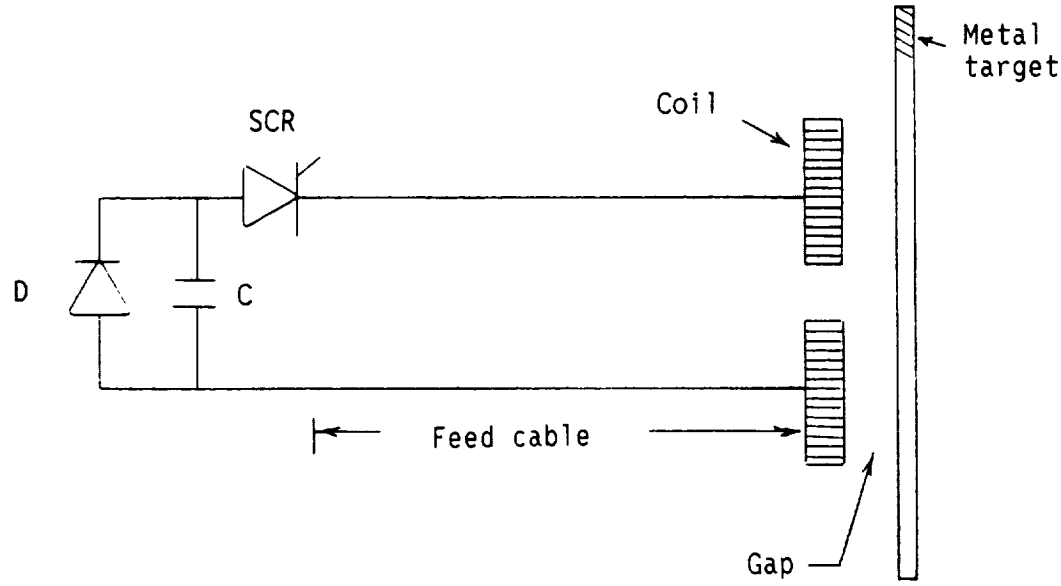

Fig. 2-51 Basic EIDI Circuit

The major assumptions that are made for the purpose of modeling this problem are:

(a) The coil is circular and is wound with rectangular wire. The thickness of the coil is the wide dimension of the rectangular wire.

(b) The target is a flat plate lying parallel to the face of the coil. This target is assumed to be stationary (constant gap).

(c) Several coils may be operated in series or in parallel. Multiple coils are assumed to have identical properties.

(d) It is assumed that the effects of the feed cable can be modeled by a lumped resistance in series with a lumped inductance.

(e) The SCR and the capacitor are assumed to be ideal, although an approximate account of the forward drop in the SCR could be accomplished by a small additional series resistance.

(f) The clamp diode D is assumed to be in the circuit (Some program modifications would be required if the diode were removed). When the diode is in conduction, it is assumed to have a constant voltage drop.

2. Modeling and Behavior Equations

Figure shows the equivalent circuit and a typical capacitor voltage waveform.

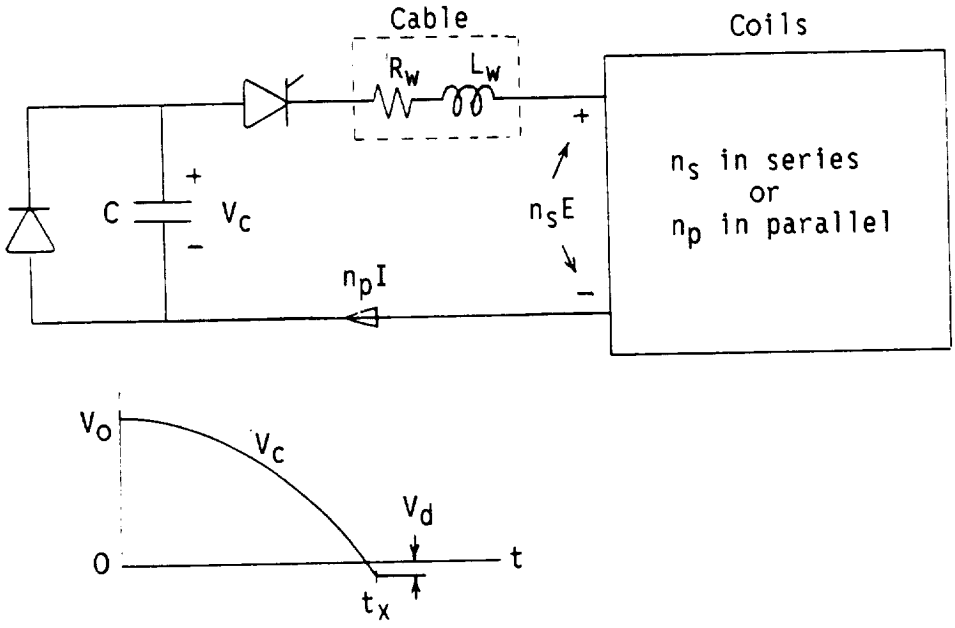

Fig. 2-52 Equivalent Circuit

The governing circuit equation is

$$v_c - R_w(n_p I) - L_w(n_p \dot{I}) = n_s E \qquad (2\text{-}28)$$

and the capacitor equation is

$$V = \begin{cases} V_0 - \frac{1}{C}\int_0^t n_s I\,dt & (t < t_1) \\ -V_0 & (t > t_1) \end{cases} \qquad (2\text{-}29)$$

In Eqs. 2-28 and 2-29, n_p is to be set to 1 when coils are operated in series, and n_s is to be set to 1 when coils are operated in parallel.

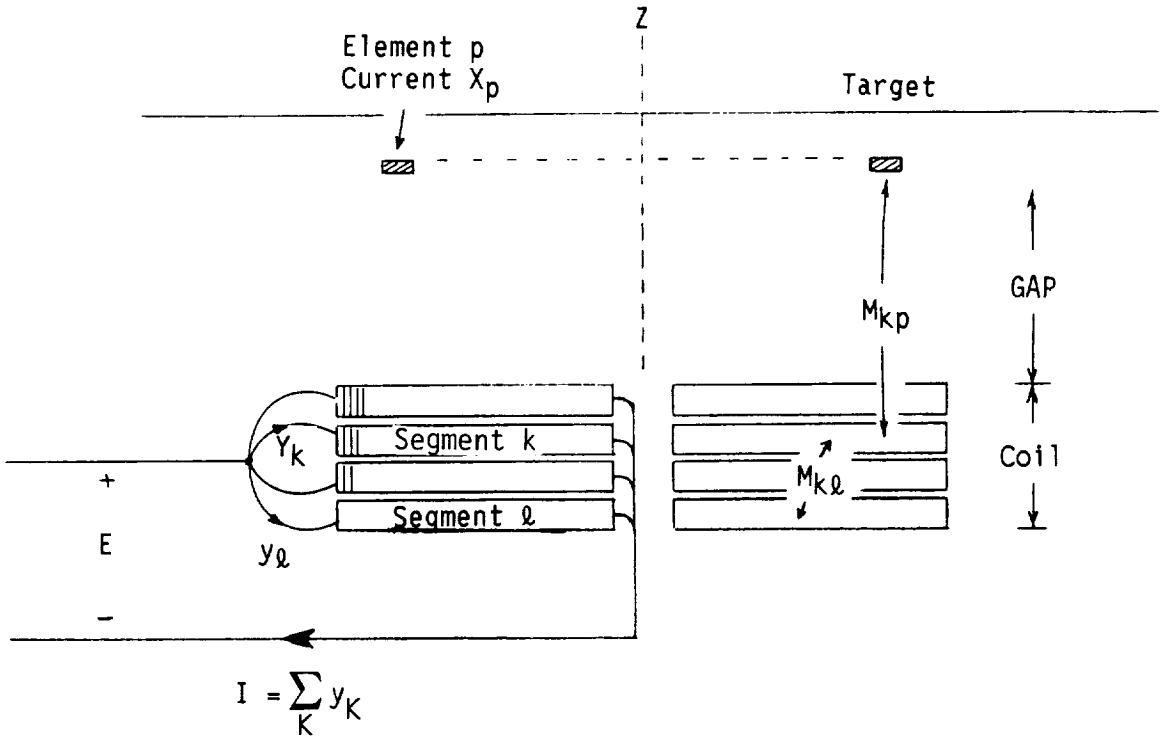

Fig. 2-53 Coil and Target Discretization

Figure 2-53 illustrates the manner in which the coil and target are discretized. Coils are assumed to be segmented in the thickness dimension. Any given coil then consists of several equal thickness segments in parallel, and the current in the k^{th} segment is denoted y_k. All segments

have the same resistance R_c. The segments have both self inductance M_{kk} and mutual inductance M_{kl}. The instantaneous voltage across a coil is denoted $E = E_k = E_l$. The instantaneous coil current is the summation of segment currents.

The target is discretized into "elements" consisting of circular current loops of radius r and cross-sectional area $\Delta r\ \Delta z$. The resistance of the p^{th} target element is ΔR_p, and its current is x_p. Target elements have self inductance and mutual inductance to other elements, M_{pq}. They also have mutual inductance to coil segments, M_{pk}.

The coil equation is given by

$$E_k = y_k \Delta R_c + \sum_l M_{kl} \dot{y}_l + \sum M_{kp} \dot{x}_p \tag{2-30}$$

Figure 2-54 is another coil-target sketch illustrating two target elements. With the aid of this sketch, the target equation is reasoned to be

$$0 = x_p \Delta R_p + \sum_k M_{pk} \dot{y}_k + \sum_q M_{pq} \dot{x}_q \tag{2-31}$$

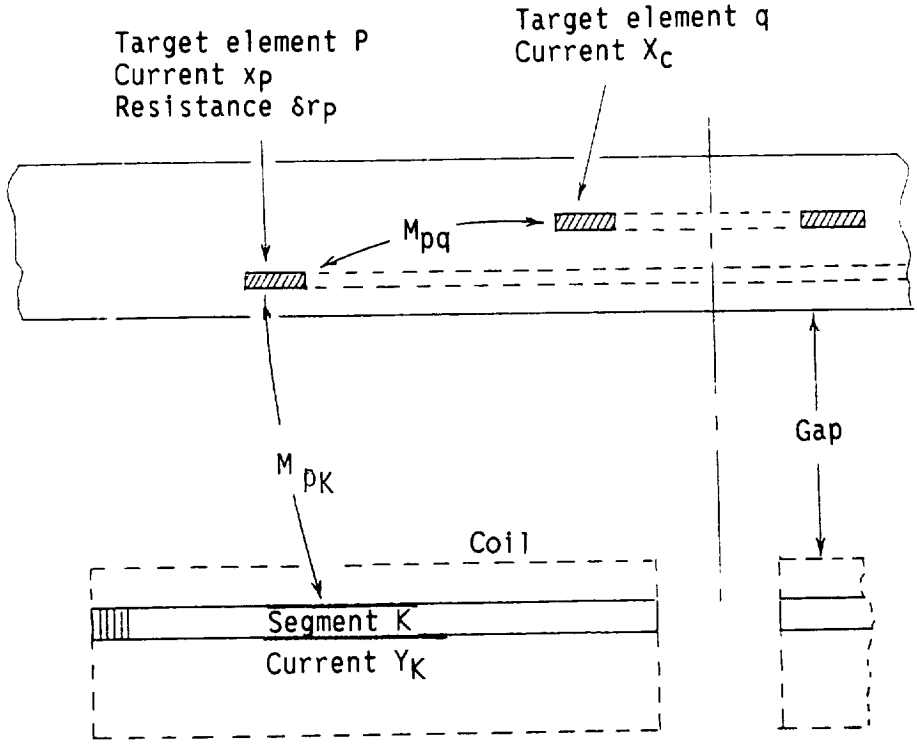

Fig. 2-54 Further Discretization Illustration

Equations 2-28 through 2-31 are to be solved simultaneously for currents in the various coil segments and target elements.

3. State Vector Formulation and Eigenexpansion Solution

State variables will be taken as x, y and v_c. For purposes of illustrating the derivation of the state vector equation, we will imagine only two coil segments. We will first develop the equation that applies prior to diode conduction. For the sake of notation clarity, elements in the inductance matrix for coil segments will be denoted by M, and the entire matrix by $[M_{cc}]$. Elements in the coil-to-target inductance matrix will be called m, and the entire matrix $[M_{ct}]$.

Now Eq. 2-30 may be written as the vector equation

$$\begin{matrix} E_1 \\ E_2 \end{matrix} = \begin{bmatrix} \Delta R_c & 0 \\ 0 & \Delta R_c \end{bmatrix} \begin{bmatrix} y_1 \\ y_2 \end{bmatrix} + \begin{bmatrix} M_{11} & M_{12} \\ M_{21} & M_{22} \end{bmatrix} \begin{bmatrix} \dot{y}_1 \\ \dot{y}_2 \end{bmatrix}$$

$$+ \begin{bmatrix} m_{11} & m_{12} & \cdot & \cdot & \cdot & \cdot & m_{1n} \\ m_{21} & m_{22} & \cdot & \cdot & \cdot & \cdot & m_{2n} \end{bmatrix} \begin{bmatrix} \dot{x}_1 \\ \dot{x}_2 \\ \cdot \\ \cdot \\ \cdot \\ \cdot \\ \cdot \\ \dot{x}_n \end{bmatrix} \qquad (2\text{-}32)$$

Similarly, Eq. 2-28 becomes

$$\begin{bmatrix} n_p L_w & n_p L_w \\ n_p L_w & n_p L_w \end{bmatrix} \begin{bmatrix} \dot{y}_1 \\ \dot{y}_2 \end{bmatrix} + \begin{bmatrix} n_p R_w & n_p R_w \\ n_p R_w & n_p R_w \end{bmatrix} \begin{bmatrix} y_1 \\ y_2 \end{bmatrix}$$

$$- \begin{bmatrix} 1 \\ 1 \end{bmatrix} v_c + \begin{bmatrix} n_s E_1 \\ n_s E_2 \end{bmatrix} = \begin{bmatrix} 0 \\ 0 \end{bmatrix} \qquad (2\text{-}33)$$

Combining Eqs. 2-32 and 2-33, we get

$$\begin{bmatrix} n_p L_w + n_s M_{11} & n_p L_w + n_s M_{12} \\ n_p L_w + n_s M_{21} & n_p L_w + n_s M_{22} \end{bmatrix} \begin{bmatrix} \dot{y}_1 \\ \dot{y}_2 \end{bmatrix}$$

$$+ \begin{bmatrix} n_p R_w + n_s \Delta R_c & n_p R_w \\ n_p R_w & n_p R_w + n_s \Delta R_c \end{bmatrix} \begin{bmatrix} y_1 \\ y_2 \end{bmatrix} \qquad (2\text{-}34)$$

$$+ \begin{bmatrix} n_s m_{11} & n_s m_{12} \ldots n_s m_{1n} \\ n_s m_{21} & n_s m_{22} \ldots n_s m_{2n} \end{bmatrix} \begin{bmatrix} \dot{x}_1 \\ \dot{x}_2 \\ \cdot \\ \cdot \\ \cdot \\ \cdot \\ \cdot \\ \dot{x}_n \end{bmatrix} \qquad \begin{bmatrix} 1 \\ 1 \end{bmatrix} v_c = \begin{bmatrix} 0 \\ 0 \end{bmatrix}$$

which may be abbreviated as

$$[n_p L_w + n_s M_{cc}]\{\ddot{y}\} + [n_p R_w]\{\dot{y}\} + [n_s \Delta R_c]\{y\} + [n_s M_{ct}]\{\ddot{x}\} - [1]v_c = 0 \tag{2-35}$$

Using similar notation, Eq. 2-31 gives

$$[M_{tc}]\{\ddot{y}\} + [M_{tt}]\{\ddot{x}\} + [\Delta R_t]\{x\} = 0 \tag{2-36}$$

Differentiating Eq. 2-29 gives

$$-C\dot{v}_c - [n_p \quad n_p]\begin{bmatrix} y_1 \\ y_2 \end{bmatrix} = -Cv_0\delta(t) \tag{2-37}$$

Finally, Eqs. 2-35, 2-36 and 2-37 may all be incorporated into the following single vector equation:

$$\left[\begin{array}{c|c|c} n_s M_{tt} & n_s M_{tc} & 0 \\ \hline n_s M_{ct} & n_s M_{cc} + n_p L_w & 0 \\ \hline 0 & 0 & \dfrac{-C}{n_p} \end{array}\right] \begin{Bmatrix} \ddot{x} \\ \ddot{y} \\ \dot{v}_c \end{Bmatrix} + \begin{bmatrix} n_s \Delta R_t & 0 & 0 \\ 0 & n_p R_w + n_s \Delta R_c & (-1) \\ 0 & (-1) & 0 \end{bmatrix} \begin{Bmatrix} x \\ y \\ v_c \end{Bmatrix} = \begin{Bmatrix} 0 \\ 0 \\ \dfrac{-CV_0\delta(t)}{n_p} \end{Bmatrix} \tag{2-38}$$

The meanings of the sub-matrices in Eq. 2-18 are reiterated as follows:

$\{M_{tt}\}$ - The self and mutual inductance of and between all discrete target elements. It is a square symmetric array of order N_t, the total number of target elements.

$\{M_{cc}\}$ - The self and mutal inductance of and between all coil segments. It is a square symmetric array of order N_c, the total number of coil segments.

$\{M_{tc}\}$ - The mutual inductance between the N_t target elements and the N_c coil segments. This array is of order (N_t, N_c).

$\{M_{ct}\}$ - The transpose of $\{M_{tc}\}$.

$\{L_w\}$ - The inductance of the external circuit, principally the distribution cables. This is a square array of order N_c. All elements are identical and equal to the scalar inductance L_w.

$\{R_w\}$ - The resistance of the external circuit. This is a square array of order N_c. All elements are identical and equal to the scalar resistance R_w.

$\{\Delta R_t\}$ - The set of resistance values for each discrete target element. It is a square diagonal array of order N_t.

$\{\Delta R_c\}$ - The set of resistance values for each coil segment. It is a diagonal array of order N_c with identical elements.

$\{C\}$ - The scalar capacitance.

Now Eq. (2-38) has the state model form

$$\{A\} * \{\dot{Z}\} + \{B\} * \{Z\} \{f(t)\}, \; Z(o) = o, \tag{2-39}$$

where the state vector $\{Z\}$ consists of the variables

$$\{Z\} = \begin{cases} \{X\} & \text{Eddy currents in } N_t \text{ target elements} \\ \{Y\} & \text{Currents in } N_c \text{ coil segments} \\ \{V_c\} & \text{Capacitor voltage.} \end{cases}$$

The total order for the system is

$$N = N_t + N_c + 1.$$

The solution is obtained by considering the homogeneous form . . .

$$\{A\}\ \{dZ/dt\} + \{B\}\ \{Z\} = \{0\} \tag{2-40}$$

where {A} and {B} are square symmetric arrays. An eigensolution normally utilizes the following form.

$$\{A^{-1}\}\ \{B\}\ \{Z\} = -s\{Z\} \tag{2-41}$$

where $\{A^{-1}\}$ denotes the inverse of the array {A} and (-s) is the desired scalar eigenvalue.

The array {A} is composed of self and mutual inductance terms for both the target and coil. The mutual inductance of an arbitrary target element is very nearly equal to the self inductance of its adjacent element. This creates a very poorly conditioned matrix for inversion purposes. On the other hand, the array {B} is well suited for inversion due to the presence of the normally large diagonal resistance array $\{\Delta R_t\}$. Thus, the following eigenvalue form is used,

$$\{B^{-1}\}\ \{A\}\ \{Z\} = (-1/s)\ \{Z\} \tag{2-42}$$

where $\{B^{-1}\}$ is the inverse of the array {B} and (-1/s) is the eigenvalue. The eigensolution will yield (N-2) real left half plane poles and one pair of complex conjugate poles associated with the oscillatory solution of the (R,L,C) circuit. For each distinct eigenvalue, there is an associated eigenvector, normally expressed as follows,

$$\{Z\} = \{Q\}\ \{q\} \tag{2-43}$$

where the columns of the array {Q} are the eigenvectors and {q} are quite often called generalized coordinates. The properties of {Q} are well known and are repeated below

$$\{Q^T\}\ \{A\}\ \{Q\}\ \{dq/dt\} + \{Q^T\}\ \{B\}\ \{Q\}\ \{q\} = \{Q^T\}\ \{F\} \tag{2-44}$$

where $\{Q^T\}$ is the transpose of the array $\{Q\}$. The quadratic forms $\{Q^T\}$ $\{A\}$ $\{Q\}$ and $\{Q^T\}$ $\{B\}$ $\{Q\}$, are diagonalized during this operation, resulting in the following set of linear first order uncoupled differential equations.

$$\begin{aligned} a_1\, dq_1/dt + b_1\, q_1 &= p_1\,(t) \\ a_2\, dq_2/dt + b_2\, q_2 &= p_2\,(t) \\ a_n\, dq_n/dt + b_n\, q_n &= p_n\,(t) \end{aligned} \qquad (2\text{-}45)$$

These may be reduced to the form

$$dq_i/dt + (b/a)_i q_i = (p/a)_i \&(t) \qquad i=1,2,\ldots n. \qquad (2\text{-}46)$$

Where (b/a) are the eigenvalues of the system, (p/a) are quite often called the modal participation factors, and (t) is the unit impulse function. The solutions are simple exponential growth relations as follows

$$q_i(t) = (p/b)_i\ \{1 - \exp(-b/a)_i t\} \qquad i=1,2,\ldots n. \qquad (2\text{-}47)$$

Once the 'N' values of $\{q(t)\}$ are established, the values of the state vector are obtained from the eigenvector array

$$\{Z(t)\} = \{Q\}\ \{q\}(t)\} \qquad (2\text{-}48)$$

to complete the eigensolution.

This solution prevails until the capacitor voltage reaches zero, or some small negative value, and the diode prevents any large negative voltage across the capacitor. The values of the eddy currents in the N_t target elements and the N_c coil segment currents corresponding to the condition ($v_c = -V_d$) become the initial conditions for a second reduced order homogeneous solution of order $N = N_t + N_c$. The voltage v_c is now stationary, e.g., $v_c = -V_d$, and the system is reduced to an equivalent (R,L) circuit. A second eigen-expansion is employed to define the time domain solution in the exponential decay phase as the poles of the reduced order system are all in the left half plane.

4. Target Pressure

The force on a typical target element is calculated by the "motor force equation". Referring to the p^{th} element illustrated in Fig. 2-55, the normal component (z) of force is

$$F_{zp} = -2\pi r_p x_p \left[\sum_k B_{rpk} - \sum_q B_{rpq} \right] \qquad (2\text{-}49)$$

where

$$B_{rpk} = -\frac{y_k}{2\pi r_p} \frac{\partial M_{pk}}{\partial z} \qquad (2\text{-}50)$$

$$B_{rpq} = -\frac{x_q}{2\pi r_p} \frac{\partial M_{pq}}{\partial z} \qquad (2\text{-}51)$$

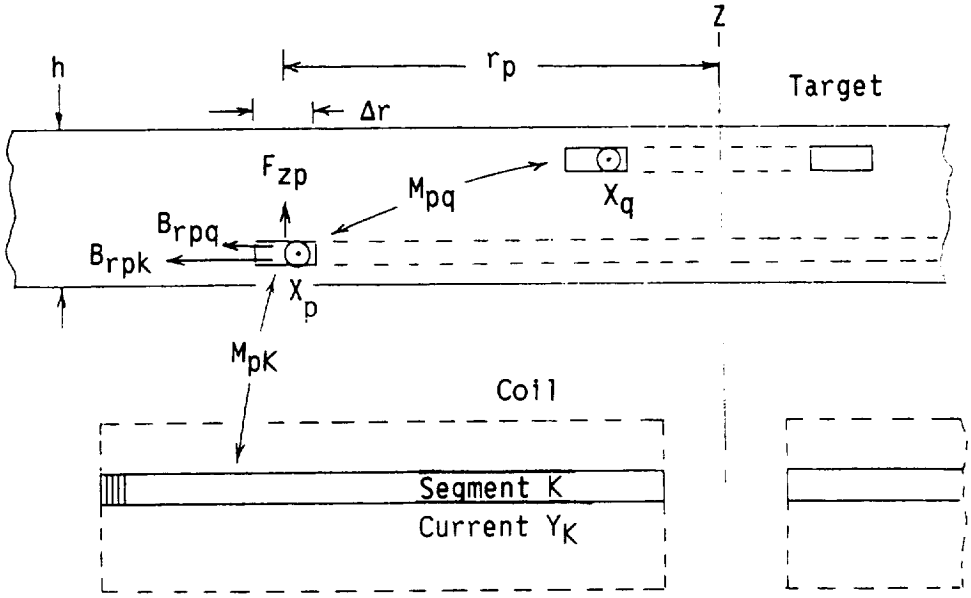

Fig. 2-55

Illustration For Formulating Normal Target Pressure

When F_{zp} is summed across the target thickness for calculating pressures, it is found that B_r from other target elements provide negligible contributions. Thus the last term in (2-49) can be omitted.

The normal pressure at the radius of the p^{th} element is

$$P_N(r_p) = \frac{1}{2\pi r_p \Delta r} \sum_{\text{over}} F_{zp} \tag{2-52}$$

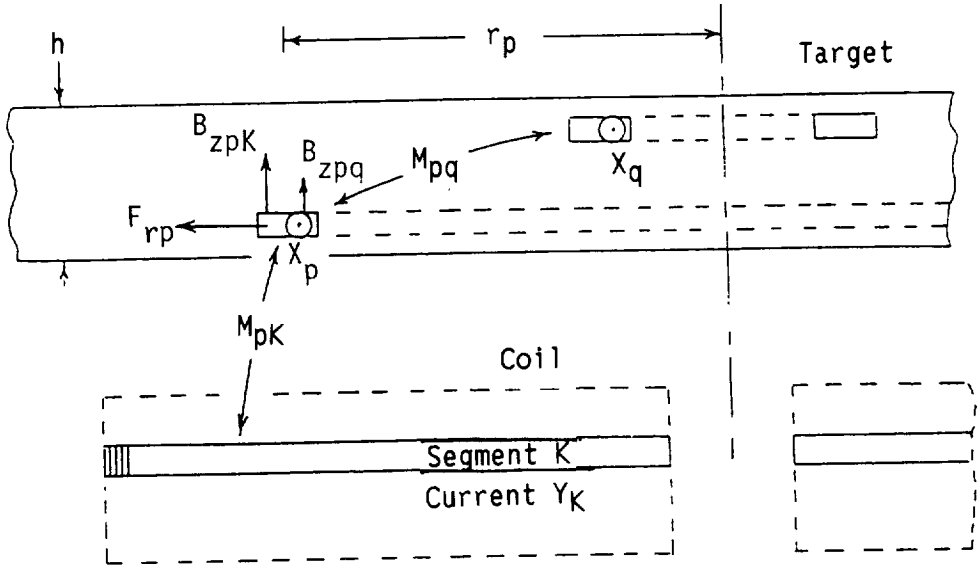

Fig. 2-56

Illustration For Formulating Radial Target Pressure

By similar reasoning from Fig. 2-56, the radial force on the p^{th} target element becomes

$$F_{rp} = 2\pi r_p x_p \left[\sum_k B_{zpk} + \sum_q B_{zpq} \right] \tag{2-53}$$

$$B_{zpk} = \frac{y_k}{2\pi r_p} \frac{\partial M_{pk}}{\partial r} \tag{2-54}$$

$$B_{zpq} = \frac{x_q}{2\pi r_p} \frac{\partial M_{pq}}{\partial r} \tag{2-55}$$

and the corresponding radial pressure is

$$P_r(r_p) = \frac{1}{2\pi r_p h} \sum_{\text{over}} F_{rp} \tag{2-56}$$

h being the target thickness.

5. Further Comments on Discretization

For purposes of bounding the problem, one may ignore electrical effects that come from that portion of the target for which the radius exceeds twice the coil radius. Radial discretization of the target is accomplished by subdividing this twice coil radius into 10 to 30 equal increments. The target thickness is also subdivided into 3 to 6 equal increments, and the coil thickness into 3 to 6 segments. To cite an example, if the target were subdivided into 25 radial divisions and 4 z-divisions, then the number of target elements would be $N_t = 100$. If, in addition the coil is divided into 5 segments ($N_c = 5$), then the total order of the system would be

$$N = 100 + 5 + 1 = 106$$

It will be acknowledged later that the specific computer code that has been developed is limited to a system order of 130.

6. Calculation of the Inductance Arrays

We will first list some basic inductance formulas, and then their applications to the calculation program will be identified. We start with the formula for mutual inductance between two filamentary coaxial circular loops (see Fig. 2-57).

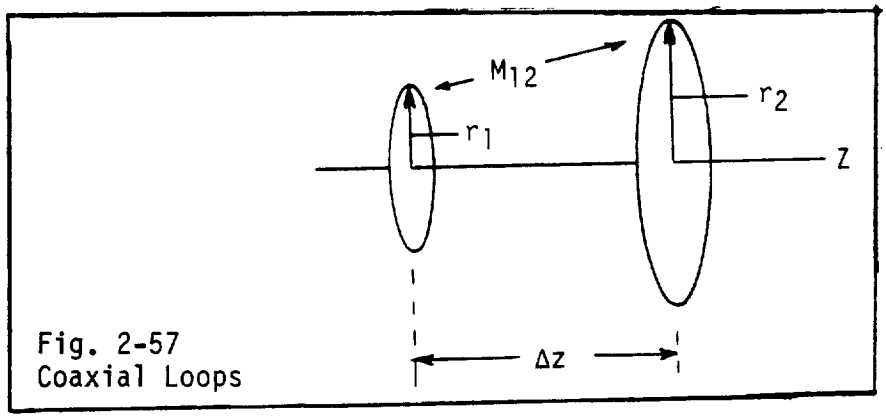

Fig. 2-57
Coaxial Loops

$$M_{12} = \mu_0 \sqrt{(r_1 + r_2)^2 + \Delta z^2} \left[\left(1 - \frac{\alpha}{2} \right) K(\alpha) - E(\alpha) \right] \qquad (2\text{-}57)$$

where

$$\alpha = \frac{4 r_1 r_2}{(r_1 + r_2)^2 + \Delta z^2}$$

and $K(\alpha)$ and $E(\alpha)$ are complete elliptic integrals of the first and second kinds.

The self inductance of a circular loop of wire with loop radius r and wire radius "a" (see Fig. 2-58) is

$$L = \mu_0 r \sqrt{1 - \frac{a}{r}} \frac{2}{\sqrt{a}} \left[\left(1 - \frac{a}{2} \right) K(a) - E(a) \right]$$

where now $$a = \frac{4r(r-a)}{(2r-a)^2} \qquad (2\text{-}58)$$

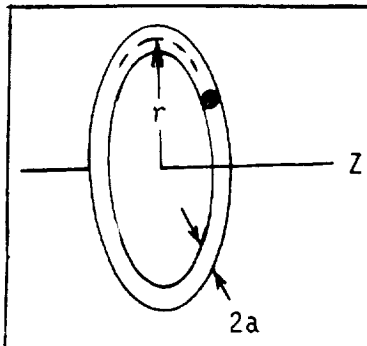

Fig. 2-58
Circular Wire Inductance Loop

Formula 2-58 ignores "internal inductance".

The Weinstein formula (Ref. 2-6) for self inductance of a circular loop of wire having rectangular cross-section (see Fig. 2-59) is

$$L = 4\pi(a\lambda + \mu) \qquad (2\text{-}59)$$

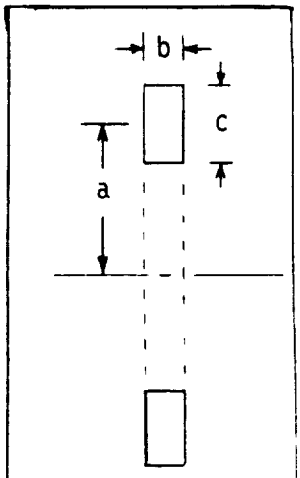

Fig. 2-59
Rectangular Wire Inductance Loop

where, if x = b/c, then

$$\lambda = \log \frac{8a}{c} + \frac{1}{12} - \frac{\pi x}{3} - \frac{1}{2}\log\left(1 + x^2\right)$$

$$+ \frac{1}{12}x^2 \log\left(1 + x^2\right) + \frac{1}{12}x^2 \log\left(1 + \frac{1}{x^2}\right)$$

$$+ \frac{2}{3}\left(x - \frac{1}{x}\right)\tan^{-1} x,$$

and

$$\mu = \frac{c^2}{96a}\left[\left(\log\left(\frac{8a}{c} - \frac{1}{2}\log\left(1 + x^2\right)\right)\right)\left(1 + 3x^2\right) + 3.45x^2 + \frac{221}{60}\right.$$

$$\left. - 1.6\pi x^3 + 3.2x^3 \tan^{-1} x - \frac{1}{10x^2}\log\left(1 + x^2\right) + \frac{1}{2}x^4 \log\left(1 + \frac{1}{x^2}\right)\right]$$

The Rayleigh formula (Ref. 2-6) for the mutual inductance between two circular loops having rectangular cross-sections is written as combinations of mutual inductances between (circular) filament pairs (see Fig. 2-60):

$$M_{AB} = \frac{1}{6}\left(M_{a5} + M_{a6} + M_{a7} + M_{a8} + M_{b1} + M_{b2} - M_{b3} + M_{b4} - 2M_{ab} \right) \qquad (2\text{-}60)$$

We will not elaborate on the specific procedures that have been employed to calculate the various inductance terms.

A coil segment is considered to be sub-divided in radius by the individual turns. Thus a 30-turn coil would have 30 elements in any segment (Fig. 2-61). The self inductance is then evaluated by

$$L_x = \sum_{\alpha} \sum_{\beta} M_{\alpha\beta} \qquad (2\text{-}61)$$

where $M\alpha\beta$ is calculated by the Rayleigh formula (2-60) when $\beta \neq \alpha$, and by the Weinstein formula (2-59) when $\beta = \alpha$.

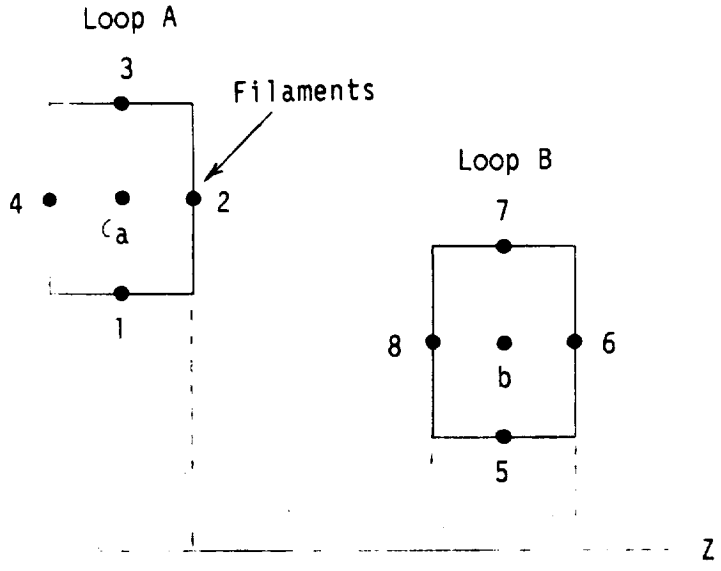

Fig. 2-60
Rectangular Wires in Concentric Loops

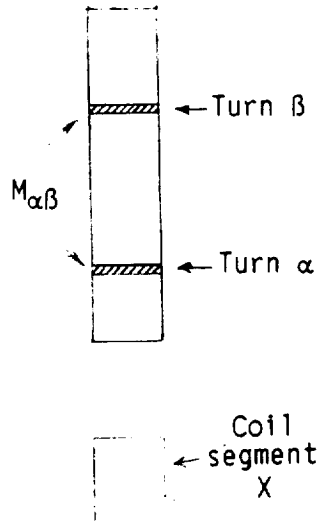

Fig. 2-61
Self Inductance of a Coil Segment

The mutual inductance between two coil segments (Fig. 2-62) is

$$M_{AB} = \sum_{\alpha} \sum_{\beta} M_{\alpha\beta} \qquad (2\text{-}62)$$

where $M_{\alpha\beta}$ is calculated by the Rayleigh formula (2-60).

The mutual inductance between a coil segment and a target element (Fig. 2-63) is

$$M_{Ax} = \sum_{\alpha} M_{\alpha x} \qquad (2\text{-}63)$$

where $M_{\alpha\beta_x}$ is calculated by the Rayleigh formula (2-60).

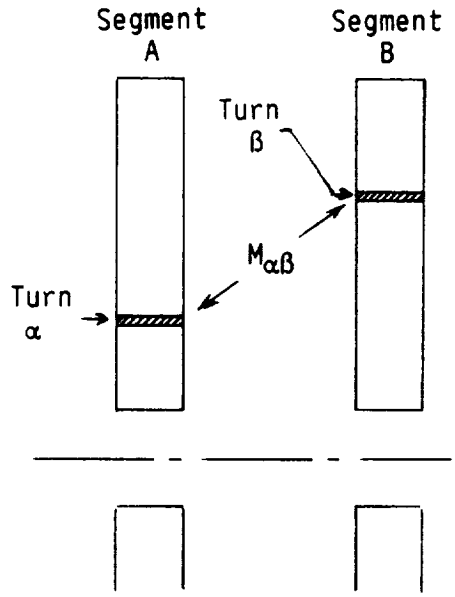

Fig. 2-62
Mutual Inductance Between
Two Coil Segments

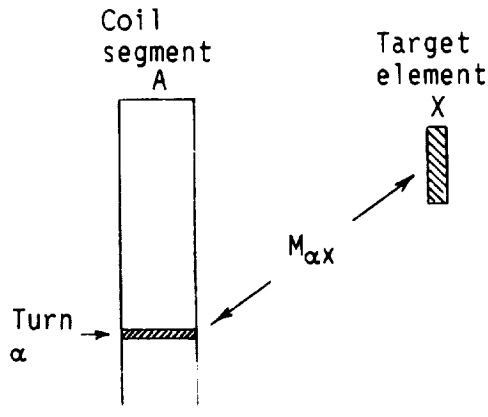

Fig. 2-63
Mutual Inductance Between
a Coil Segment and a Target Element

Target elements are broken up into N_x sub-elements, each being roughly square. Then the self inductance is evaluated from (Fig. 2-64)

$$L_x = \frac{1}{N_x^2}\sum_{\alpha}\sum_{\beta} M_{\alpha\beta} \qquad (2\text{-}64)$$

where $M\alpha\beta$ is calculated by the single filament pair formula (2-57) when $\beta \neq \alpha$, and by (2-58) when $\beta = \alpha$.

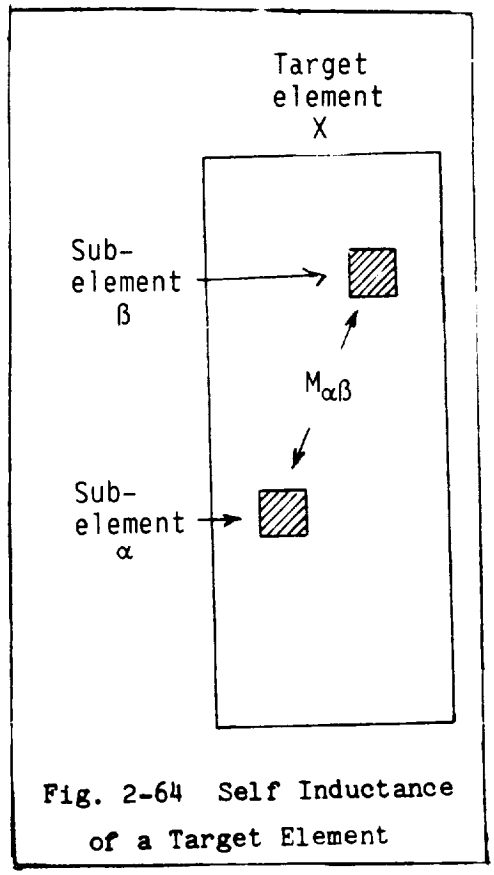

Fig. 2-64 Self Inductance of a Target Element

The procedure here depends on the degree of proximity between the elements. Referring to Fig. 2-65, suppose we want the mutual inductance between Element x and any other Element y. If Element y lies in Region 1, then both elements are sub-divided and the inductance calculated by

$$M_{xy} = \frac{1}{N_x N_y}\sum_{\alpha}\sum_{\beta} M_{\alpha\beta} \qquad (2\text{-}65)$$

where N_x and N_y are the number of sub-elements taken for Elements x and y, respectively, and $M\alpha\beta$ is calculated by the single filament pair formula (2-57).

If Element y lies in Region 2, then M_{xy} is calculated by the Rayleigh formula (2-60).

If Element y is remote (Region 3), then the single filament pair formula (2-57) is employed.

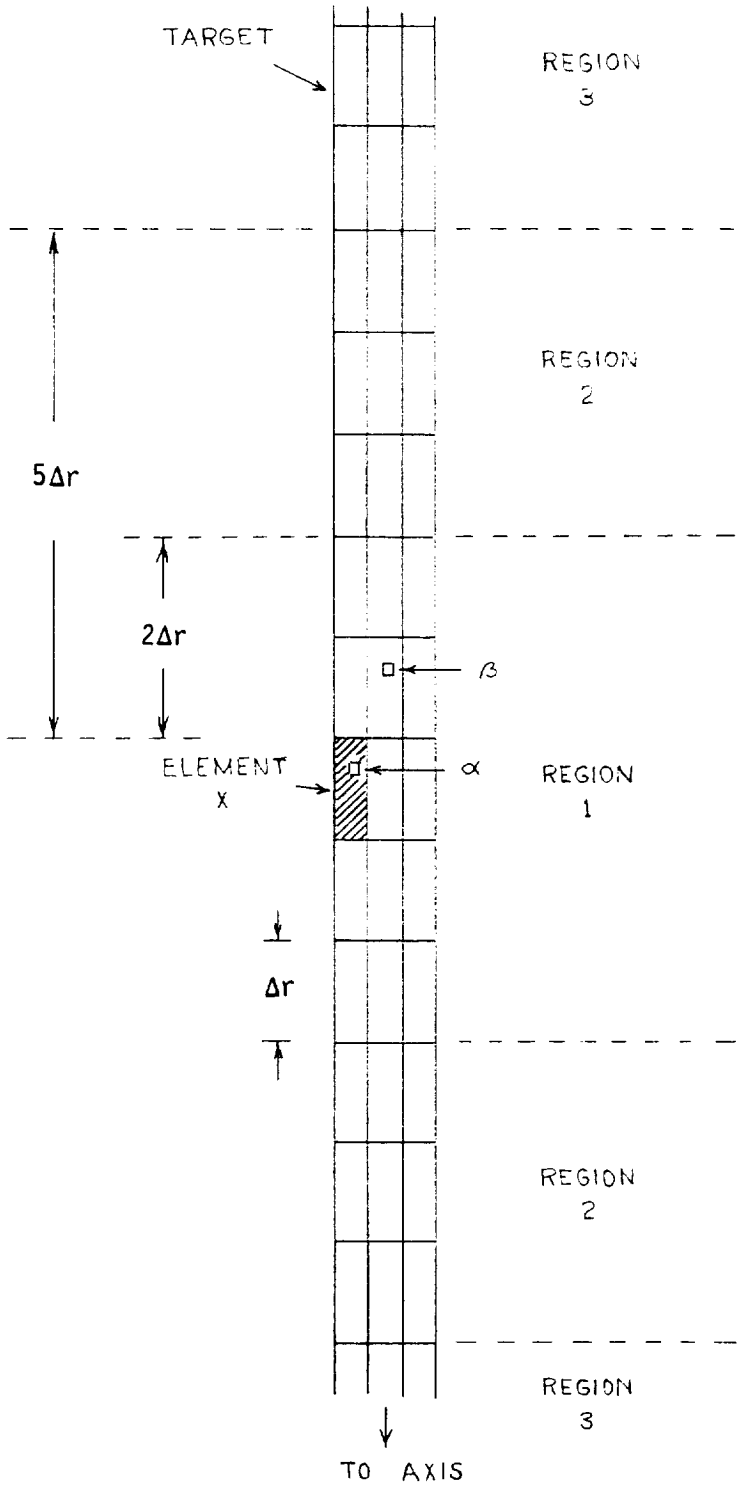

Fig. 2-65 Mutual Inductance Between Target Elements

7. Resistances of Coil Segments and Target Elements

The following formulas are used:

For the coil segments:

$$\Delta R_c = \frac{2\pi \frac{R_o - R_i}{2} N}{\sigma_{cu} \frac{t_c}{N_c}\left(\frac{R_o - R_i}{N} - g\right)} \qquad (2\text{-}66)$$

where
R_o = Outer radius of the coil
R_i = Inner radius of the coil
t_c = Coil (bare wire) thickness
g = Twice the insulation thickness
N = Number of coil turns
N_c = Number of coil segments

For target elements:

$$\Delta R_t = \frac{2\pi}{\sigma_t \Delta z \ln\left(\frac{r_2}{r_1}\right)} \qquad (2\text{-}67)$$

where
Δz = z-dimension of the element
r_2 = outer radius of the element
r_1 = Inner radius of the element
σ_t = Conductivity of the target

8. Comments on the Computer Program

The computer program which Dr. Bernhart developed consists of approximately 1500 lines of FORTRAN IV code in 23 distinct subroutines. It utilizes the EISPACK eigenanalysis subprogram library certified at Argonne National Laboratories. As written, the program is limited to a total system order of 130. Typical runs on an IBM-3081 for a 30 turn coil and a 100 element target take about two minutes of virtual cpu time, and a core size of 1400 of kiobytes.

The program calls for the following inputs:

Target: Thickness, gap, and conductivity.
Coil: Number of turns, minimum and maximum radius, width and thickness of the ribbon wire, number of coils in series or parallel.
Circuit: Initial voltage, capacitance, and the resistance and inductance of the power cables.

The program then yields the following information for selected time intervals:

(a) Capacitor voltage and coil current.
(b) Eddy currents at 80-120 radial and z-positions in the target.
(c) Normal and tangential pressures at 20-50 radial positions on the target.
(d) The normal force on the target and the corresponding impulse strength.

9. Program Verification - Comparison with Henderson's Program.

The Bernhart-Schrag analysis was applied to Henderson's problem which was described in Section B. This was done prior to the time that the circuit model was incorporated into the program. Thus the coil current that Henderson calculated was used as input data. Magnetic fields at the near and far surfaces were calculated and compared with those calculated by Henderson. The coil was divided into 4 segments and the target was divided into 4 divisions in z, 20 divisions in r. These comparisons are shown in Figs. 2-66 through 2-69. The dots are the data calculated by the Bernhart-Schrag program, and the crosses are Henderson's calculations. The greatest disagreement, a few percent, was for the near-side B_z calculation at r = 0.7 inch (see Fig. 2-68). Figures 2-66 and 2-68 also show the field contributions coming from the coil alone. This was included to give a visual indication of how well the target's effect is being modeled.

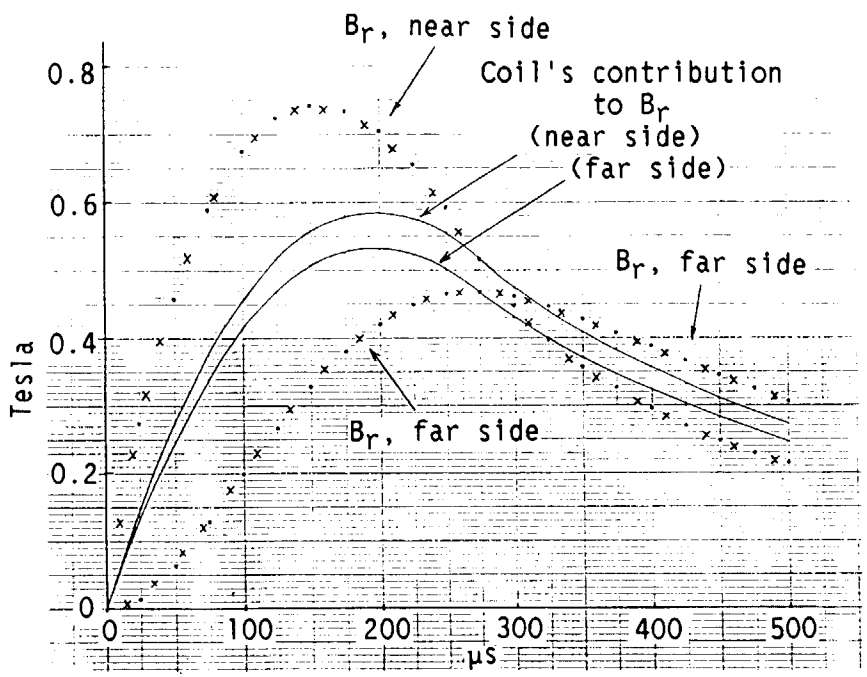

Henderson Problem; See Section V-B.4
X- Henderson Program; Bernhart Program .-

Fig. 2-66
Comparison of Magnetic Field
Strength Computation Methods
at Radius = 0.4 Inches

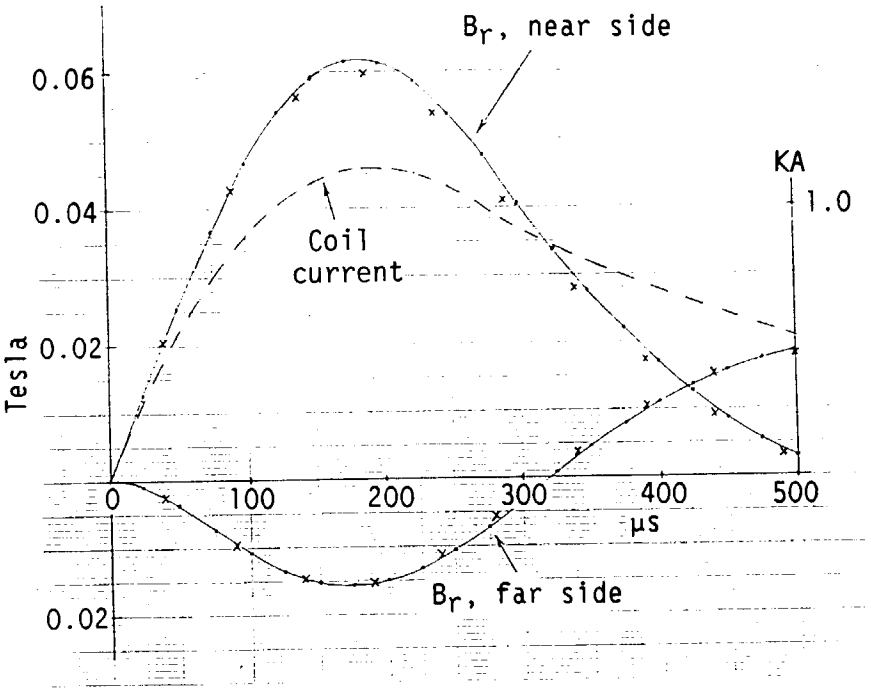

Henderson Probelm; See Section V-B.4
X- Henderson Program; Bernhart Program .-

Fig. 2-67
Comparison of Magnetic Field
Strength Computation Methods
at Radius = 1.6 Inches

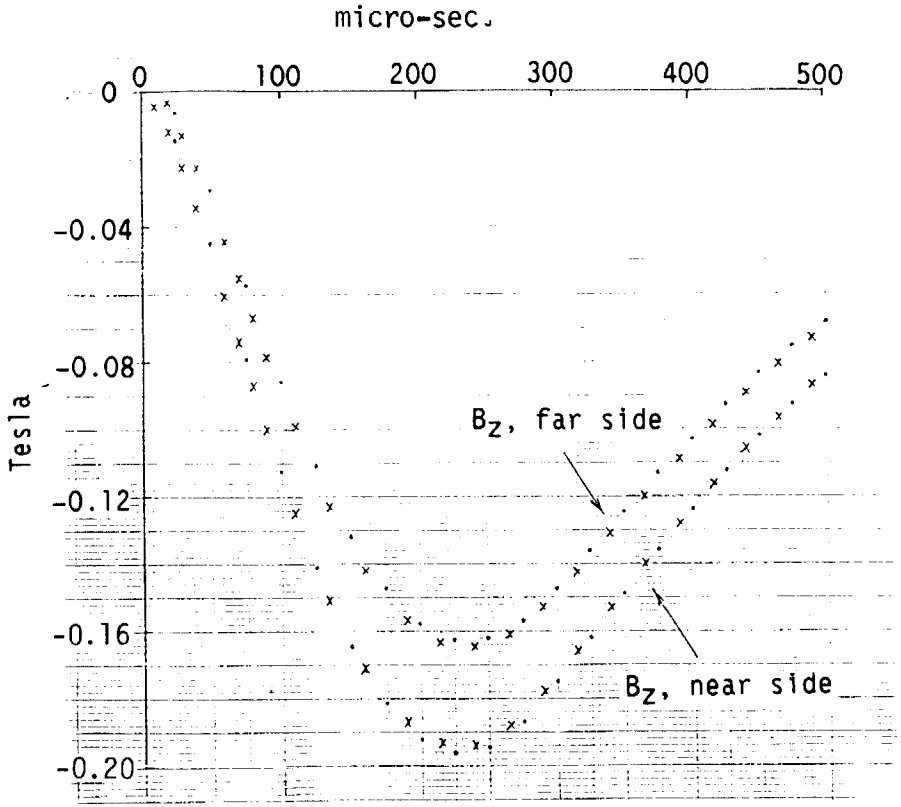

Henderson Problem; See Section V-B.4
X- Henderson Program; Bernhart Program .-

Fig. 2-68
Comparison of Magnetic Field
Strength Computation Methods
at Radius = 0.7 Inches

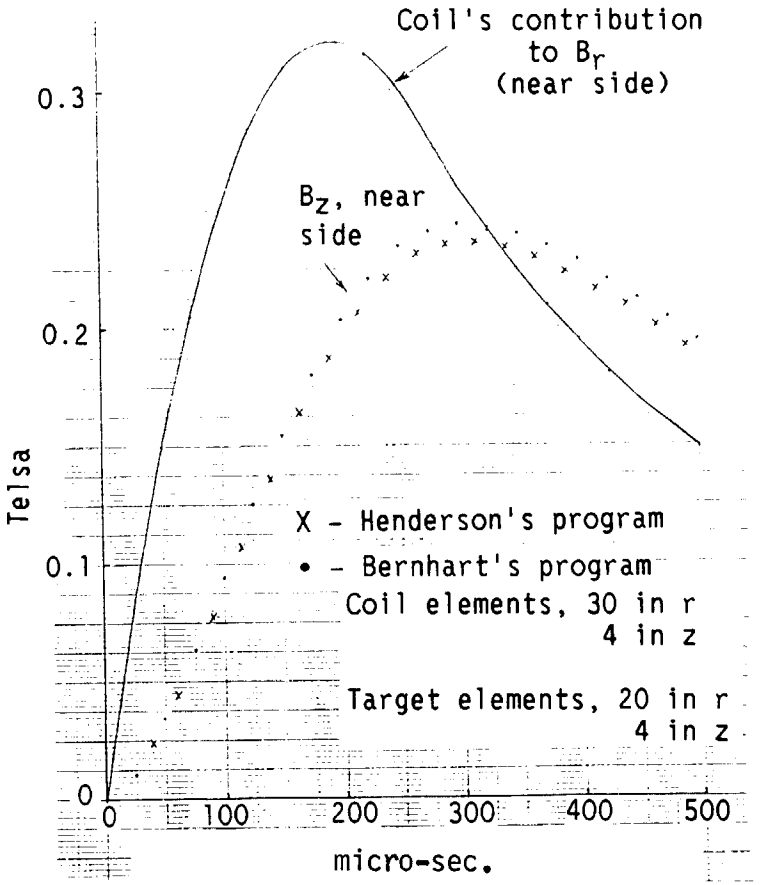

Henderson Problem; See Section V-B.4
X- Henderson Program; Bernhart Program .-

Fig. 2-69
Comparison of Magnetic Field
Strength Computation Methods
at Radius = 1.1 Inches

When the circuit solution was incorporated into the program, the coil current was then computed for the Henderson problem. The problem was modified, however, in one respect. Henderson accounted for a frequency-dependent resistance for the idler coil, where-as Bernhart's program assumes constant external circuit parameters. Thus the idler coil was assigned a resistance that corresponds to 1000 H_z. Figure 2-70 shows the coil current comparisons. Again, the dots are Bernhart's calculations, the crosses are the data from Henderson's program.

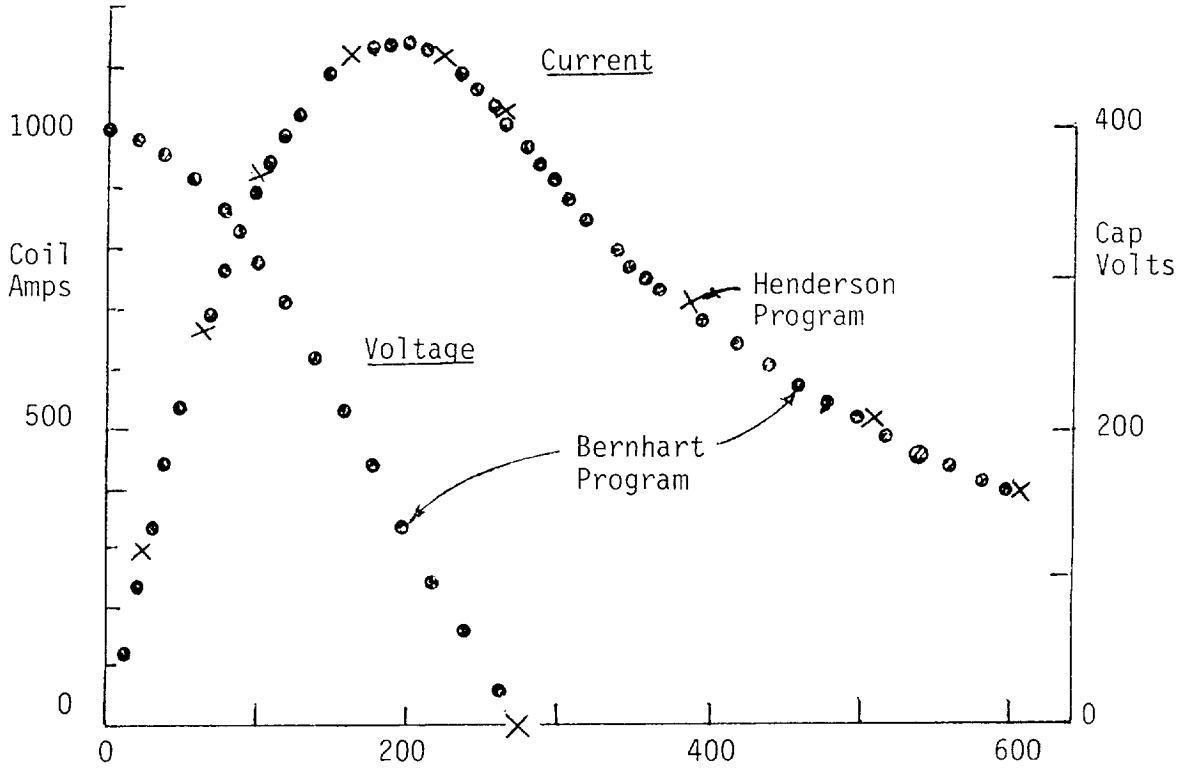

Henderson Problem; See Section V-B.4

Fig. 2-70
Comparison of Circuit Voltage and Current
Histories by Two Computational Methods

Finally, the target force was calculated, and that result is compared with Henderson's calculations in Fig. 2-71.

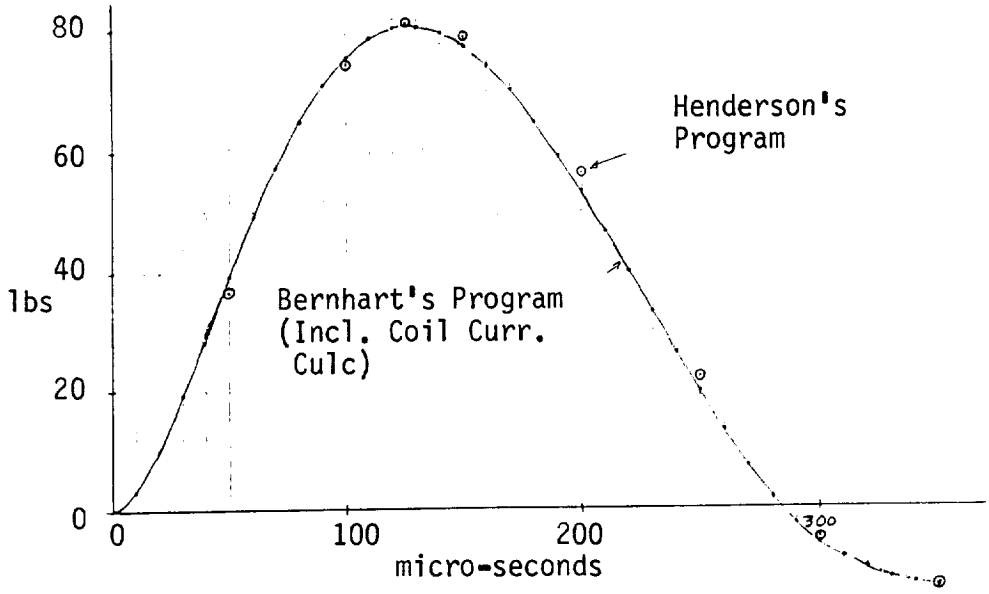

Henderson Problem; See Section V-B.4

Fig. 2-71 Comparisons of Force vs. Time by Two Computational Methods

It is emphasized that the approaches employed by Henderson and by Bernhart-Schrag are radically different. The closeness of agreement add confidence to the validity of both.

10. Program Verification - Calculated Impulse Compared with Values Reported by Lewis

G. L. Lewis (Ref. 2-3) reported impulse calculations for the system defined in Fig. 2-72. He assumed a damped sinusoidal coil current (full cycle):

$$I_{coil} = A e^{-\alpha t} \sin \omega t$$

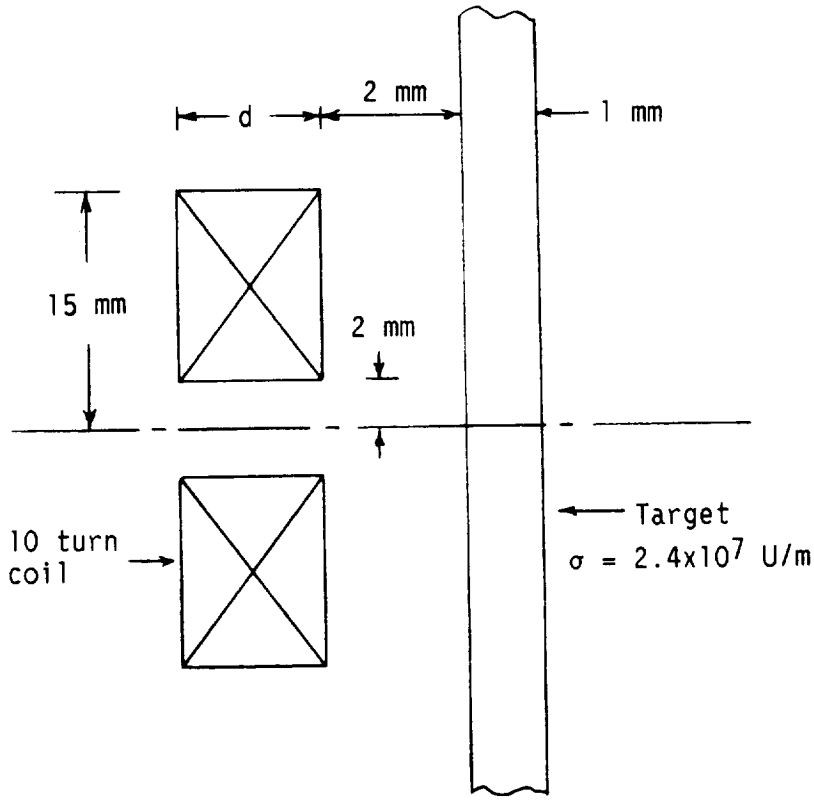

Fig. 2-72 EIDI Geometry for G.L. Lewis Problem

By Lewis' analysis, α and ω corresponding to two coil thicknesses were:

d (mm)	α (sec^{-1})	ω (rad/s)
2	7274.1	81020.5
5	3841.7	82741.2

Lewis presented results in the form of specific impulse, and those values have been converted to actual impulse for A = 1000 Amps.

The problem was solved with Bernhart's program, using the given analytical coil current as input data. The comparisons between Bernhart's and Lewis' results are:

d (mm)	Lewis' calculated Impulse (Lb.-Sec)	Bernhart's Calculated Impulse (Lb-Sec.)
2	0.0003392	0.0003379
5	0.0002725	0.0002717

11. Program Verification - Comparisons Between Calculated Coil Currents and Measured Currents

This series of comparisons was intended to further check the degree to which the program properly computes coil current. Careful measurements were made on the laboratory EIDI (exclusive of an impulse coil) to determine its circuit constants as accurately as possible. The findings are indicated in Fig. 2-73.

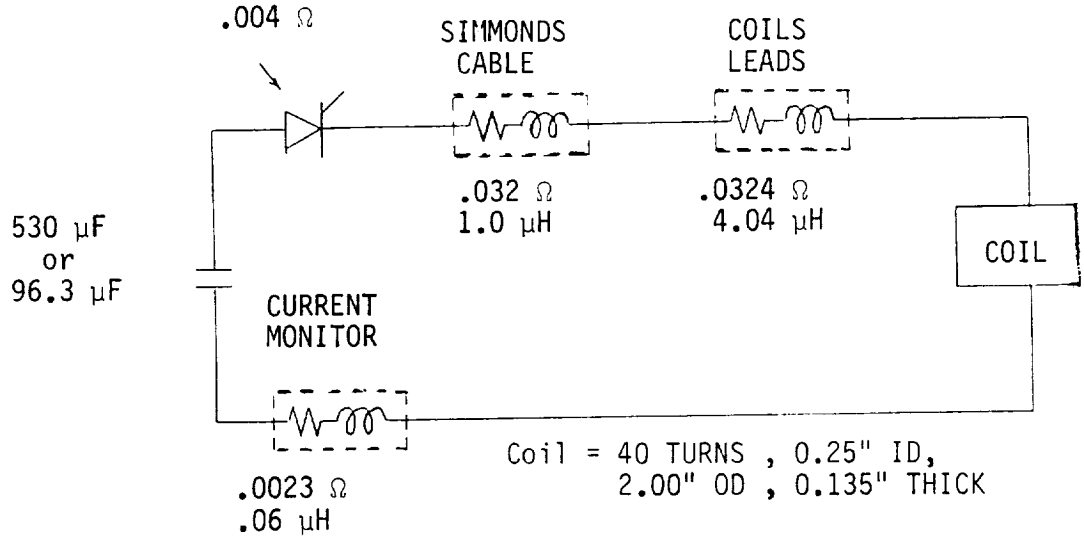

Fig. 2-73 Circuit Characterization for Lewis Experiment

Then the following coil was inserted in the circuit (no target): Turns = 40, Outer radius = 1 Inch, and Thickness = 0.135 Inch. The capacitor voltage and current were measured with an initial capacitor voltage of 400 volts. The voltage and current were also computed by the computer program. Figures 2-74 through 2-77 show the comparisons.

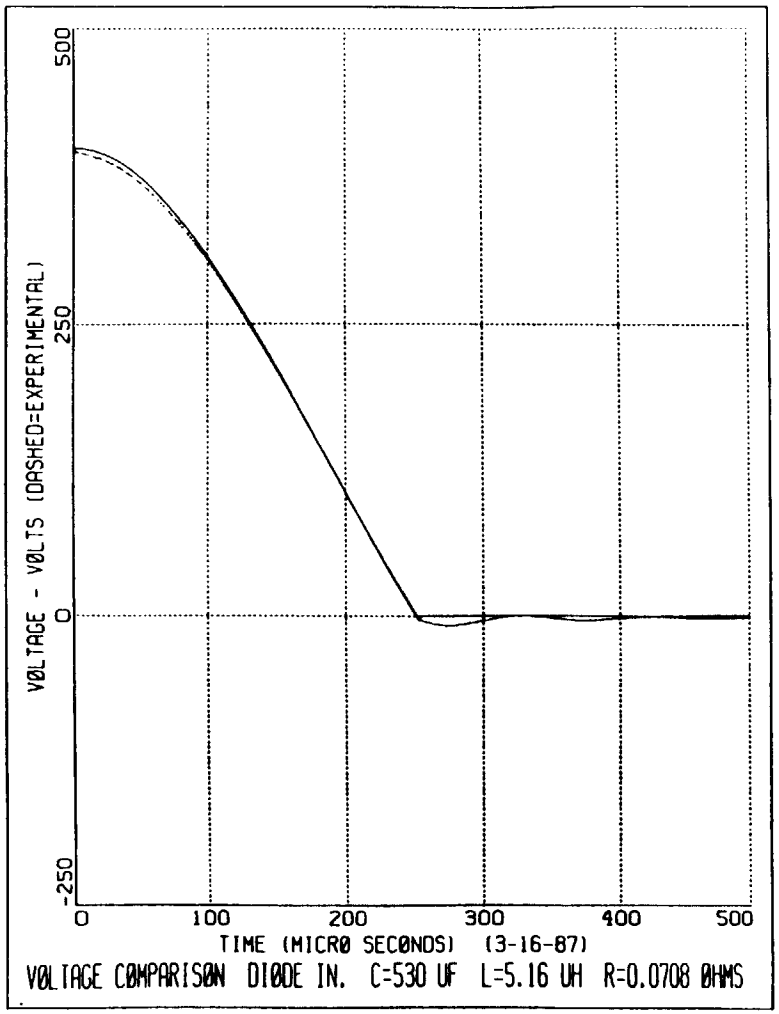

Fig. 2-74 Experimental vs Calculated Voltage History with High Capacitance

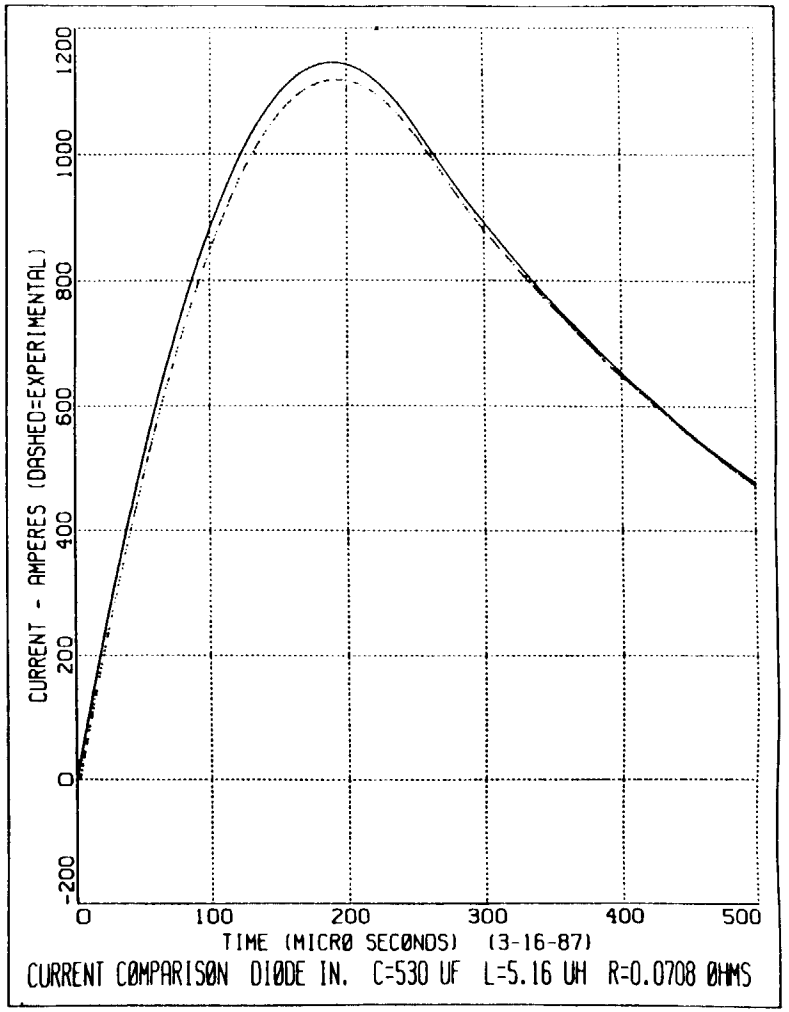

Fig. 2-75 Experimental vs Calculated Current History with High Capacitance

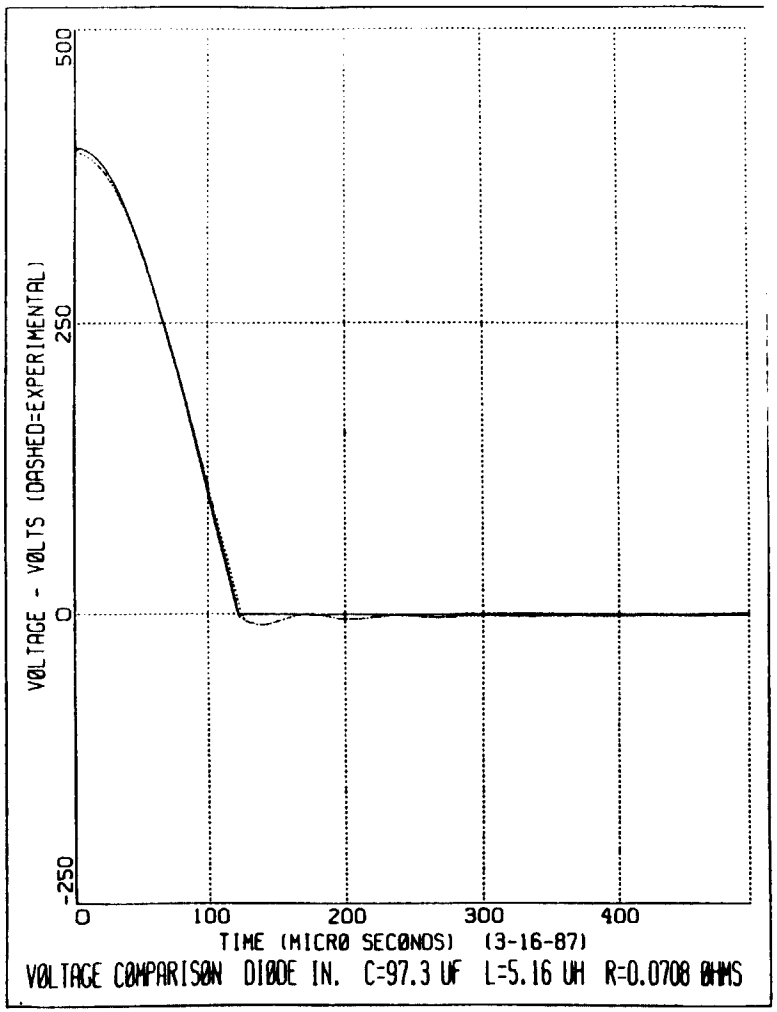

Fig. 2-76 Experimental vs. Calculated Voltage History with Low Capacitance

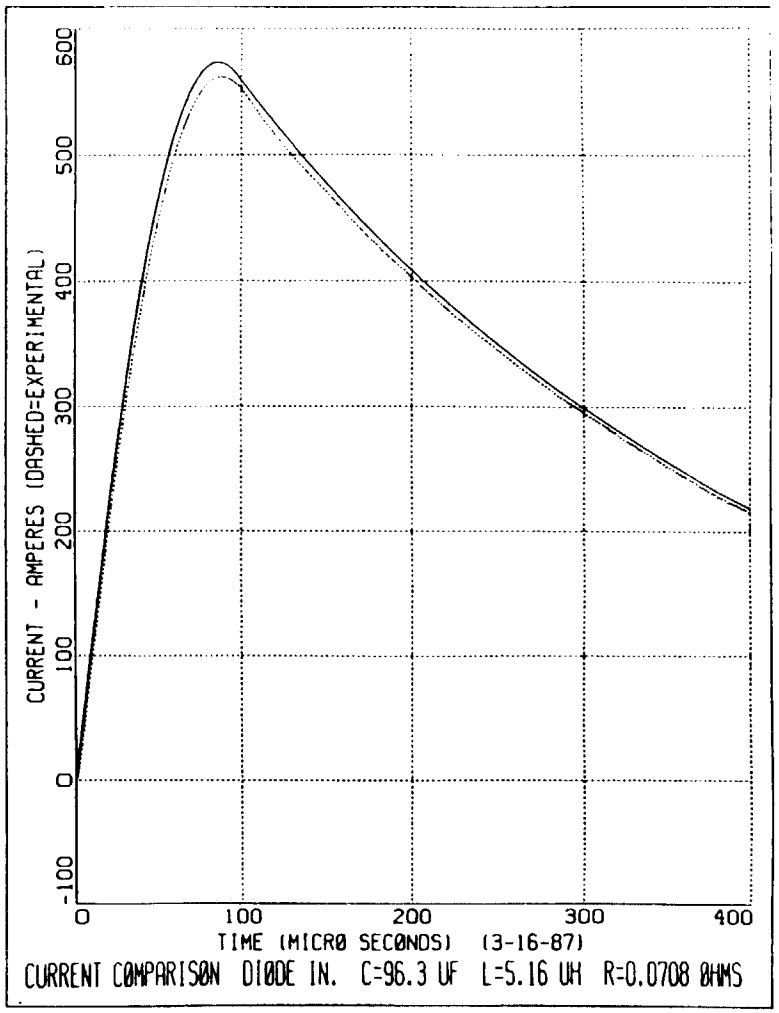

Fig. 2-77 Experimental vs. Calculated Current History with Low Capacitance

Finally tests were conducted with targets present. The conditions were:

Coil - 40 turns, 2 Inch O.D., 0.135 Inch thick

Gaps - 0.01 Inch and 0.08 Inch

Targets - Various: No target, 0.025 Inch 2024-T3 Al, 0.040 Inch 2024-T3 Al, and 0.065 Inch Cu.

Capacitance - 530μF

Initial Capacitor Voltage - 400 volts.

Figure 2-78 shows the comparison between calculated and measured coil current features.

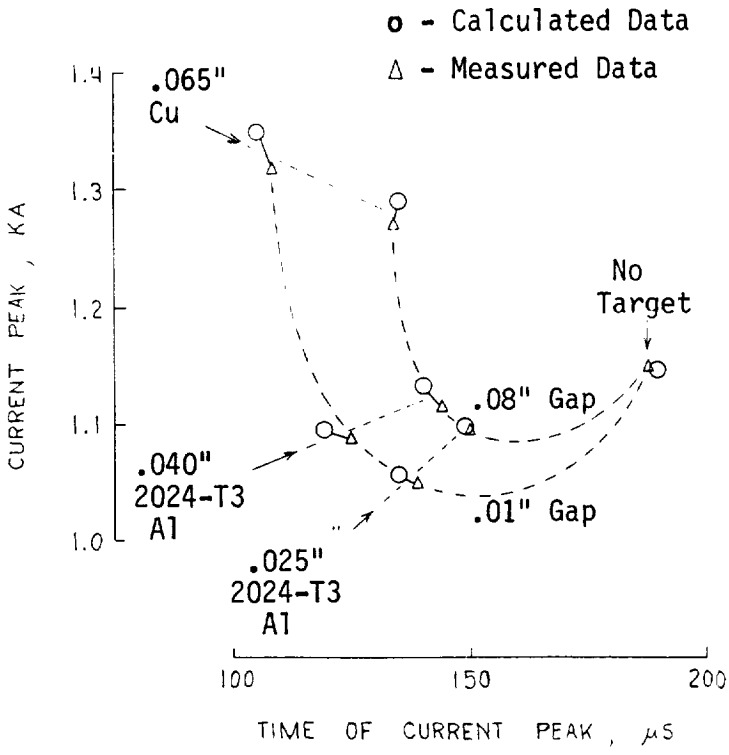

Fig. 2-78 Comparison of Current Peak, Calculated and Measured, for Two Gap Values and Several Targets.

Similar tests were made with three other coils having widely different number of turns and sizes. Details and comparative results are listed in Fig. 2-79.

EXTERNAL CIRCUIT: 96.3 μF, 400v, 5 μH, 0.07 Ω

COIL TURNS	COIL DIAMETER	t when $V_C = 0$	t when I = max.	Value of I_{max}
30	3.5"	1.04	1.05	0.95
35	2.5"	1.00	1.01	0.98
85	4.5"	1.01	1.01	1.00

EXTERNAL CIRCUIT: 530 μF, 400 v, 5μH, 0.07Ω

COIL TURNS	COIL DIAMETER	t when $V_C = 0$	t when I = max.	Value of I_{max}
30	3.5"	1.00	1.04	0.99
35	2.5"	0.97	1.01	1.03
85	4.5"	1.00	1.01	0.99

Fig. 2-79 Ratio of Measured to Calculated Values for Coil and Circuit with No Target

12. Detailed Calculated Results For A Fast Risetime EIDI Problem

Having gained confidence in the validity of the program, we then applied it to a problem that was designed for relatively fast risetime. The problem details are:

Coil - 29 Turns, 0.25 Inch I.D., 2.00 Inch O.D. 0.15 Inch thick

Gap - 0.075 Inch

Target - 0.065 Inch, 30% conductivity

Circuit - single coil operation, no cable resistance or inductance, 100 μF capacitance, and 1000 volts initial capacitor voltage.

For this problem, the coil was discretized into 6 segments and the target into 25 divisions in r (out to r = 2.5 Inches) and 4 divisions in z.

The calculated coil current (not shown here) had a peak value of 2917 amps at t = 40 μs. Some selected plots related to coil and eddy currents are shown in Figs. 2-80 and 2-81. Figure 2-80 shows coil current densities plotted across the coil thickness at three instances of time, and eddy current densities plotted across the target thickness at the same three time values. The magnetic diffusion process is clearly discernible. Figure 2-81 is a plot of the linear eddy current density (target Amps per unit of radial increment) as a function of r for 5 values of time.

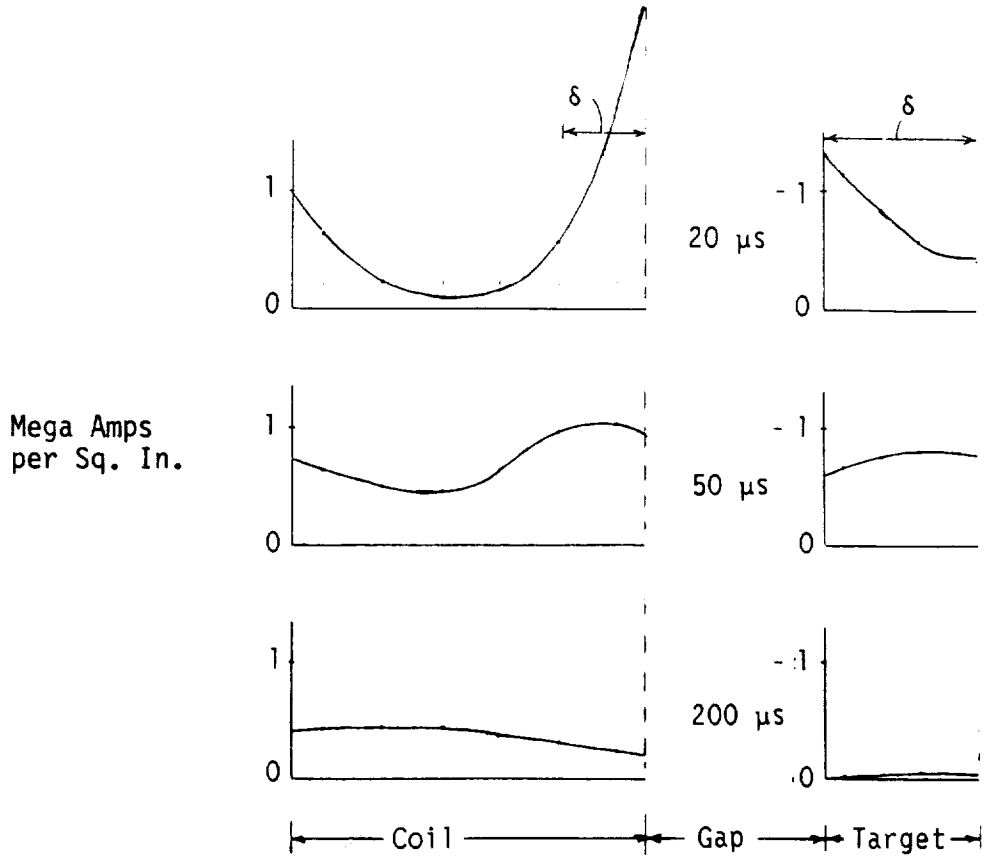

Fig. 2-80 Current Distributions Across the Coil and Target Thicknesses at r = 0.6 Inch.

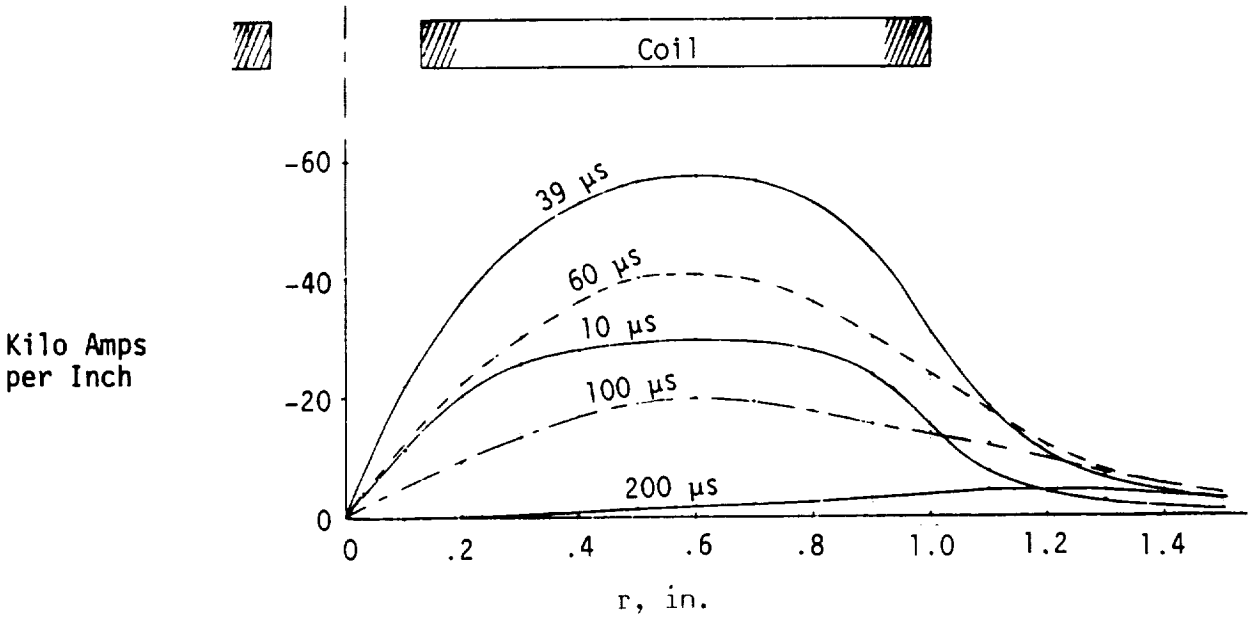

Fig. 2-81 Eddy Current Density, dI/dr

Figure 2-82 shows the calculated pressure distributions on the target at 4 time values, and Figure 2-83 is a plot of the total normal force vs time. The dotted lines in Fig. 2-83 identify the time values for which the pressure profiles (Fig. 2-82) are shown.

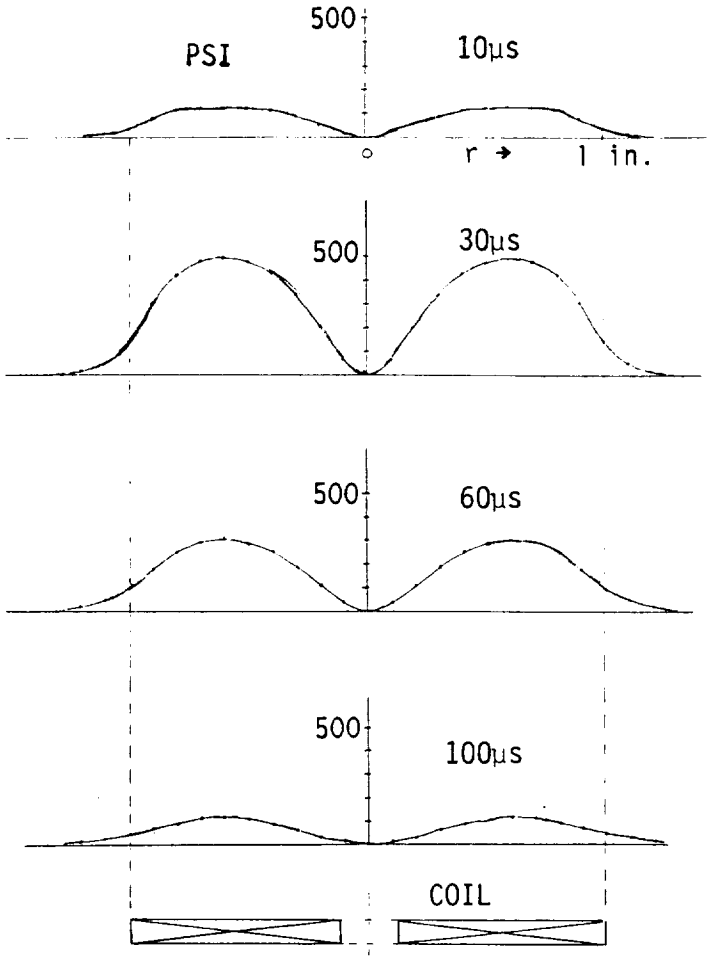

Fig. 2-82 Calculated Pressures on a Target at Four Times

The normal force on a given target element is proportional to the current in that element and to B_r at the location of the element. This B_r has contributions from both the coil and all other target elements. Figure 2-84 shows separate plots of element force contributions coming from the coil's B_r and from the target's B_r. Forces on each of the 4 target elements at r = 0.6 Inch and at t = 50μs are shown. Observe that the component of force coming from the target's B_r produces an expected "pinch effect", but a negligible contribution to target pressure. For this reason, the final computer program ignores the target's B_r in the computation of normal pressures. However, the target's B_z must be included for the computation of radial pressures.

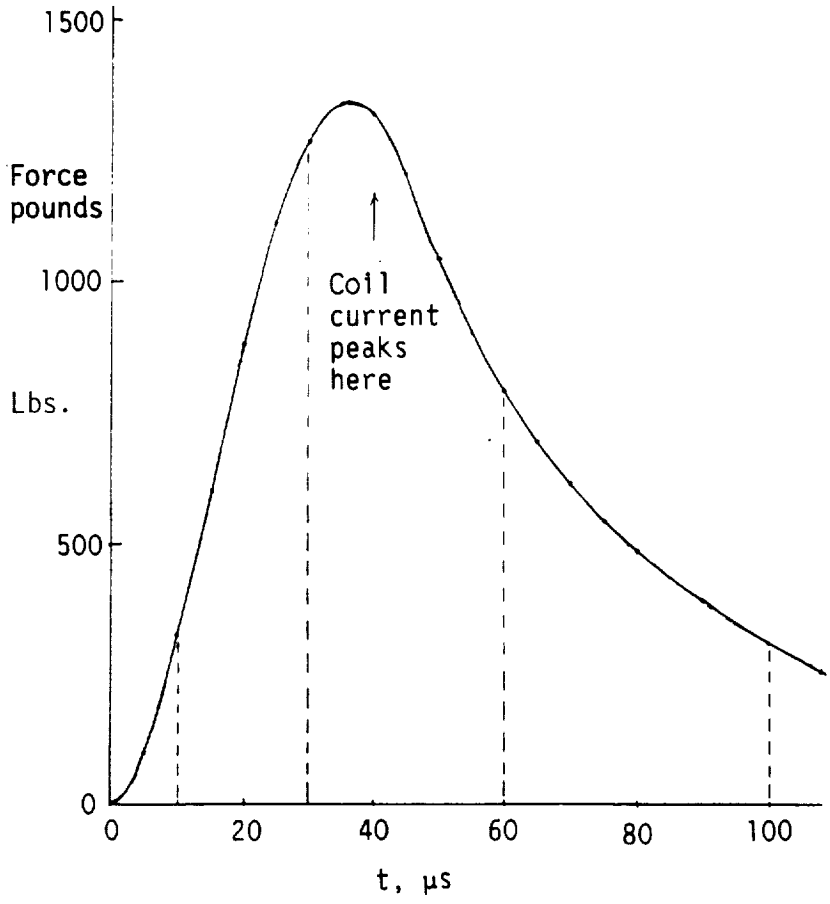

Fig. 2-83 Calculated Normal Force on a Target

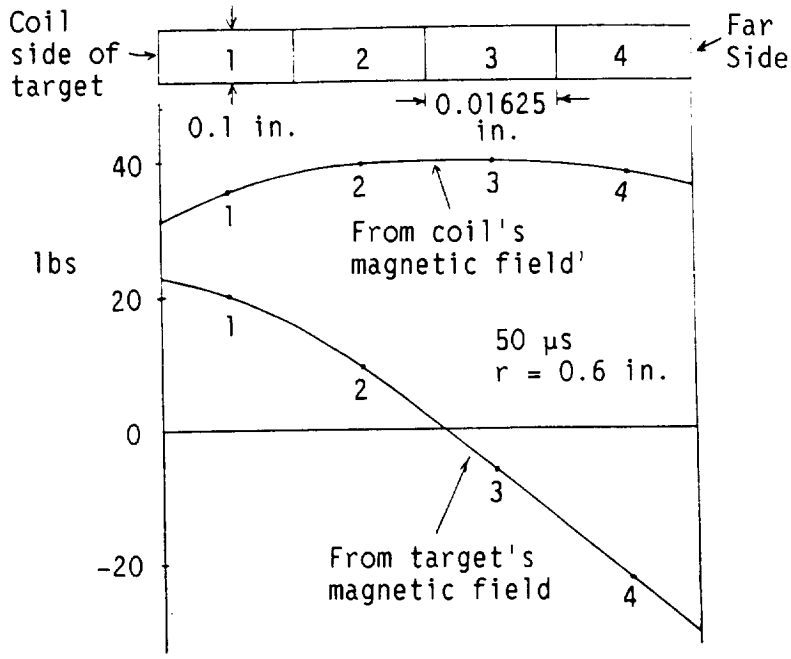

Fig. 2-84 Comparison of Force Contributions on Target Elements

13. Application of the Bernhart - Schrag Model to the Moving Target Problem

In the real EIDI problem, some target (leading edge skin) motion exists during the production of the force. If the electrical period is excessive, then target motion effects may appreciably influence the driving pressure and even the coil current.

A limited study of the moving target problem was made, assuming the target to be backed by a simple harmonic mechanical oscillator (see Fig. 2-85).

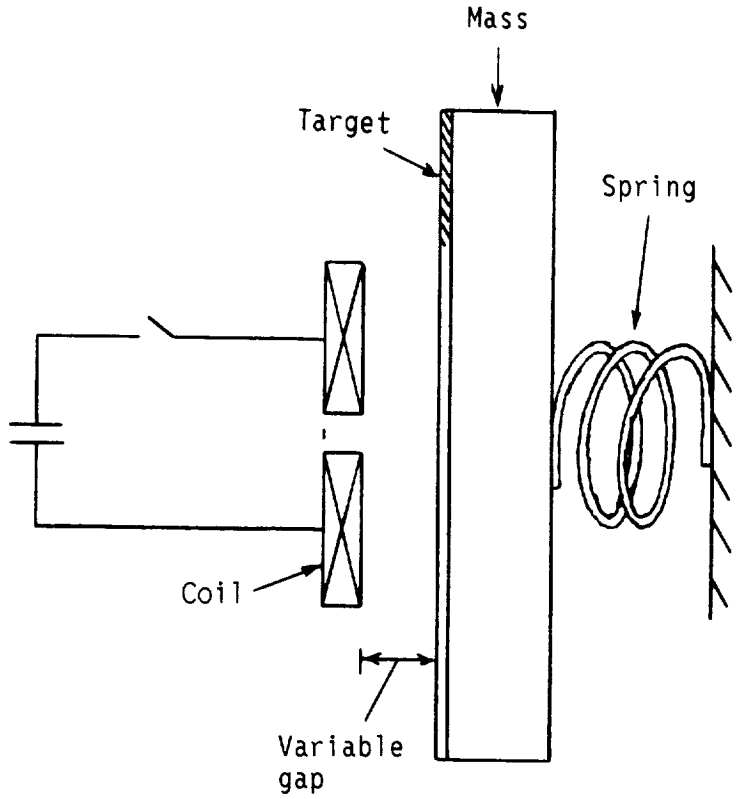

Fig. 2-85 A Basic Moving Target Problem

In addition to accounting for gap changes in the computation of the sub-array $\{M_{tc}\}$, the analysis must incorporate the phenomenon of motional induction. Induced voltage around a target element has a new contribution that is proportional to target velocity, and the induced voltage in a coil segment due to a target element has a new contribution that is also proportional to the target velocity. These effects can be included by modifying array {B} in Eq. (2-39). For the case of single-coil operation, that array becomes

$$\begin{bmatrix} \Delta R_t & \dot{z}M'_{tC} & 0 \\ \dot{z}M'_{tC} & R_w + \Delta R_C & (-1) \\ 0 & (-1) & 0 \end{bmatrix} \tag{2-68}$$

where $\dot{z}$ is the target velocity, and primes mean derivatives with respect to z. Of course, information on the variable gap and on target velocity is derived from Newton's acceleration law applied to the mechanical oscillator.

A solution was obtained by Euler's Method, using the forward difference approximation

$$\frac{\partial z}{\partial t} \doteq \frac{z(t+\Delta t) - z(t)}{\Delta t} \tag{2-69}$$

Thus the state model Eq. (2-39) becomes

$$\{z(t+\Delta t)\} = \{z(t)\} + \left\{A^{-1}\right\}\{f(t) - \Delta t\{B\}\{z(t)\}\} \tag{2-70}$$

where both {A} and {B} are time dependent because both sub-arrays M_{tc} and $\dot{z}$ M'_{tc} vary with time. However, this time variation is approximated by discrete steps at the regular time intervals Δt.

In the two examples that will be described, the basic integration time interval was 0.2 s, and the updating interval (Δt) was 2 μs.

Example 1

Coil: 36 turns, 0.25 inch I.D., 1.829 inch O.D., 0.15 inch thick.

Circuit: No cable resistance, or inductance, C=200μF, Initial voltage = 1414.2 volts.

Gap: 0.075 inch initially.

Target: 0.045 inch thick, 30% conductivity.

Mechanical Oscillator: Mass = 0.0004 Lb-Sec^2/Inch, Frequency = 1400 Hz

For this problem, the coil was divided into 3 segments, the target into 12 radial divisions and 2 z-divisions. Figures 2-86 and 2-87 show calculated results. The dotted curve in Fig. 2-86 is the target motion.

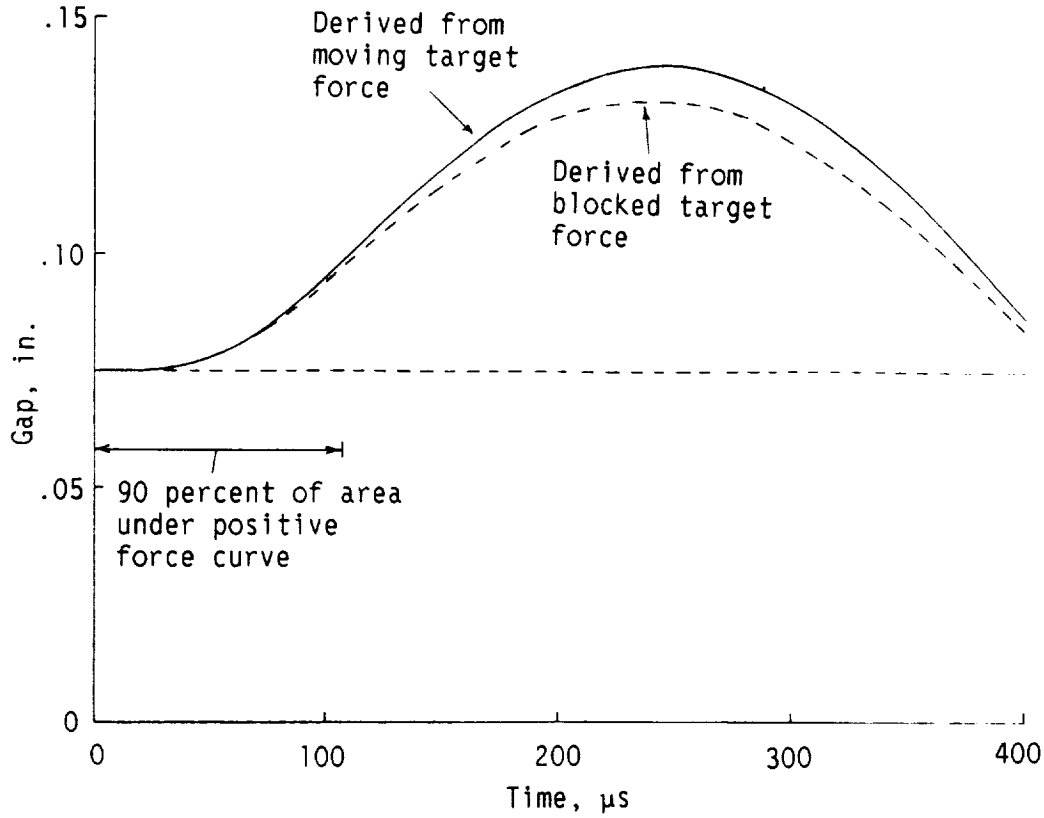

Fig. 2-86 Calculated Target Movement for Example 1.

The solid curve is the target motion that would result from the force that is calculated for a stationary target (fixed 0.075 inch gap). The figure also indicates the time span for 90 percent of the area under the force curve. Figure (2-87) is the calculated coil current (dotted curve), along with the current corresponding to a blocked target.

As can be noted from these figures, the target dynamics is only mildly affected by the analysis refinements for the inclusion of variable gap and motional induction. The coil current is even less affected. It is an interesting fact that this example represents the case where*

$$f_{Elec} = 2.0\ f_{MECH}$$

*The electrical frequency is $\omega/2\pi$, where ω is the imaginary part of the single complex root in the list of calculated eigenvalues.

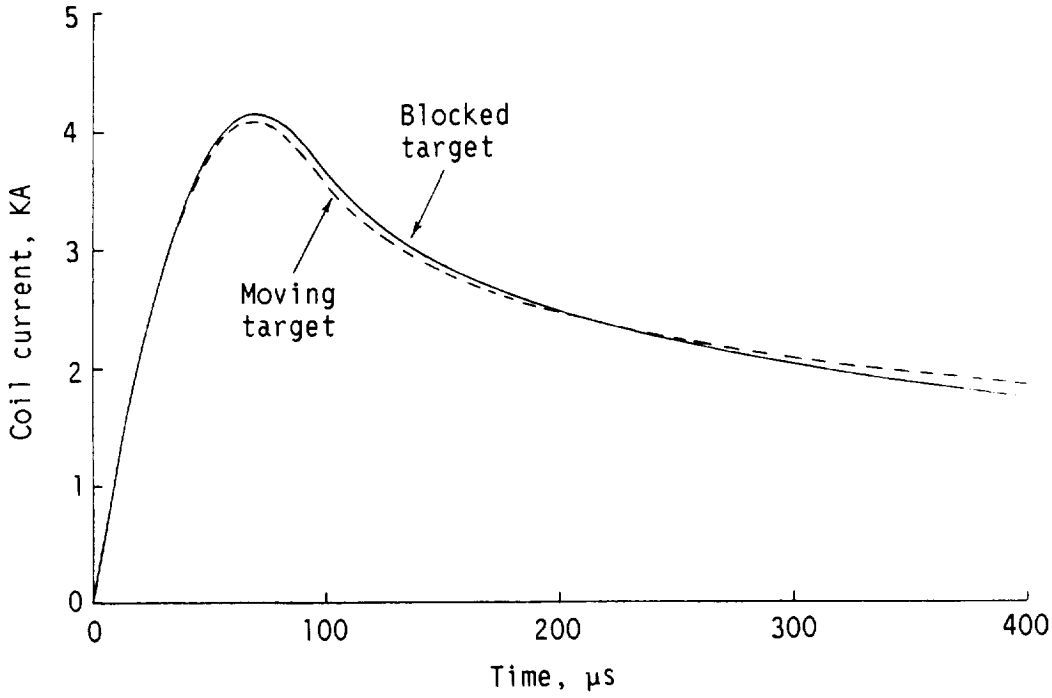

Fig. 2-87 Calculated Coil Current
For Example 1

Example 2

Coil: 50 turns, 0.25 inch I.D., 2.445 inch O.D., 0.15 inch thick.

Circuit: No cable resistance or inductance, C = 600uF, Initial voltage = 1700 volts.

Gap: 0.075 inch initially.

Target: 0.045 inch thick, 30% conductivity.

Mechanical Oscillator: Mass = 0.0004 Lb-Sec2/Inch, Frequency = 3200 Hz

Compared with Example 1, we have lowered the electrical frequency (more coil turns and more capacitance), and raised the mechanical frequency. In fact, it is now found that

$$f_{Elec} = 0.27\, f_{Mech.}$$

The same coil and target discretizations were used as in Example 1. Figures 2-88, 2-89 and 2-90 show the calculated results. Figure 2-88 is the target force (dotted curve), along with that for a blocked target (fixed 0.075 inch gap), and for the moving target but with motional induction omitted. Obviously, motional induction is an important contributing factor.

Figure 2-89 shows the target displacement, together with the displacement that would result from blocked target force calculations. This figure also shows the time span occupied by 90% of the positive blocked-target force curve. Obviously the pulse of drive force is too long, extending even into the target return region. Figure 2-90 shows how the coil current is affected by the target motion, the effect being considerably more pronounced than in Example 1.

We would conclude form these two examples that the advice to make the electrical frequency about twice the structural frequency is sound, and that then errors in determining the structural dynamics from stationary-target force calculations are not great.

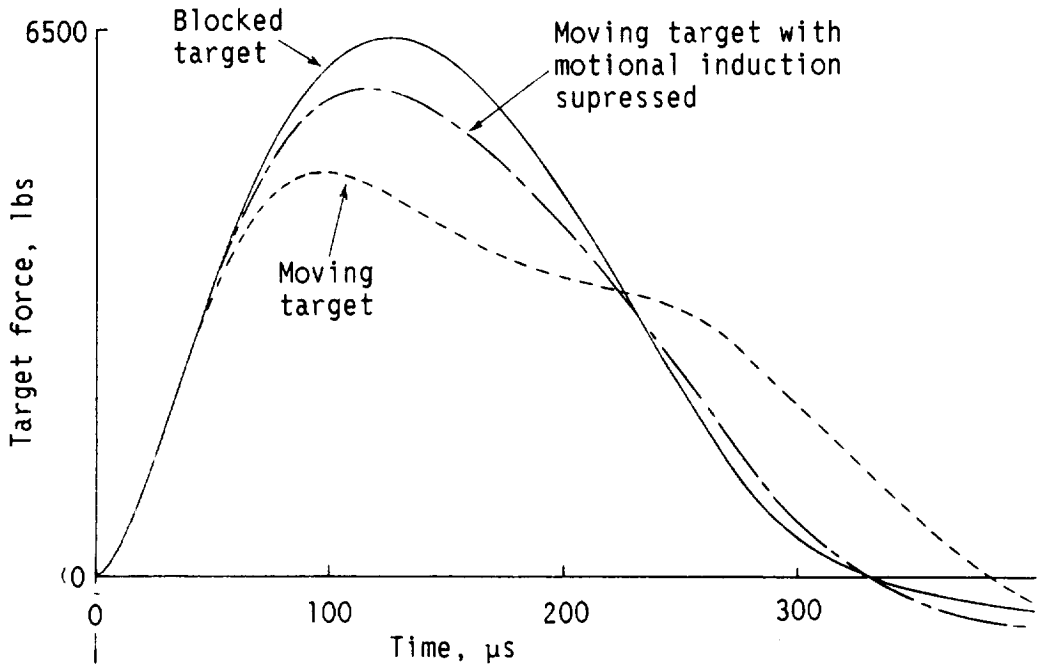

Fig. 2-88 Target Force For Example 2

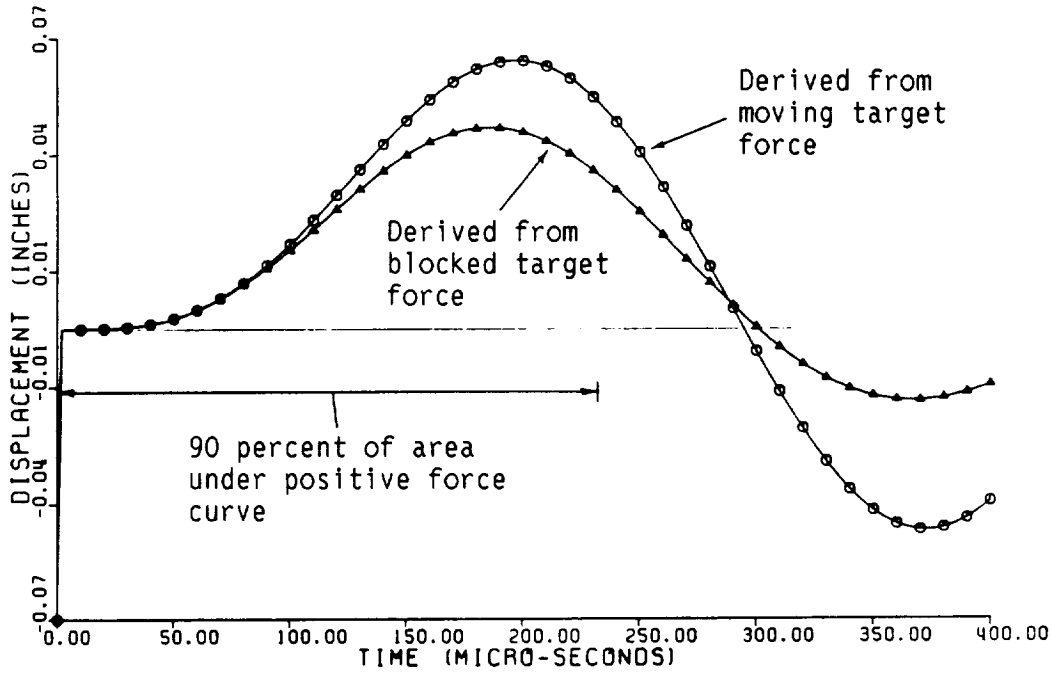

Fig. 2-89 Target Motion For Example 2

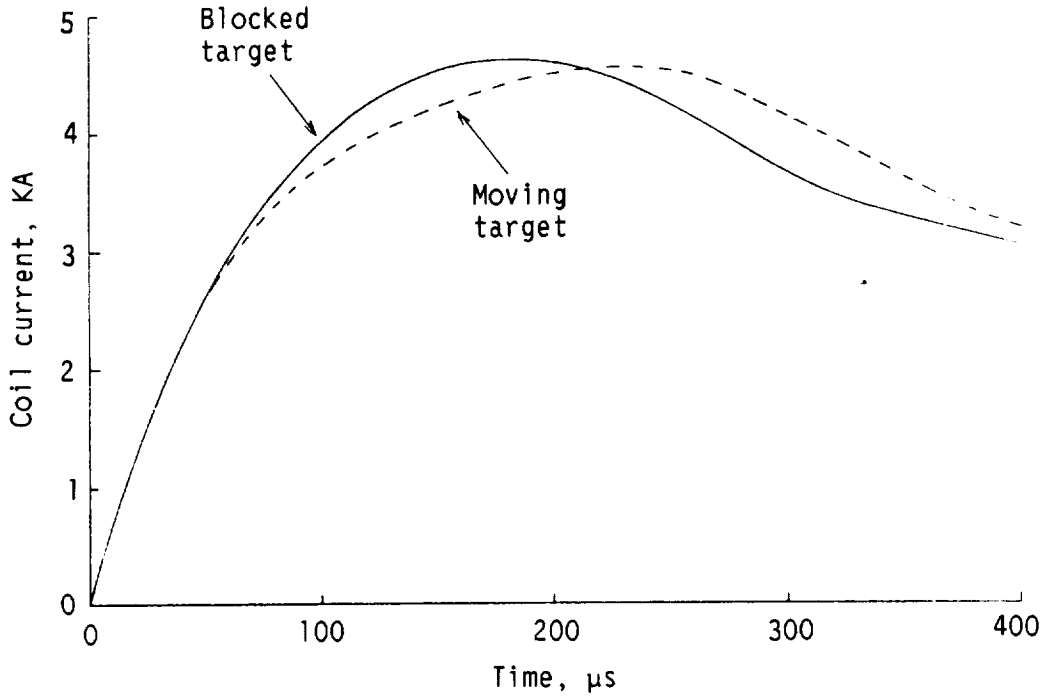

Fig. 2-90 Coil Current For Example 2

Experimental measurements were made on a 30-turn, 2 inch diameter coil. The a.c. resistance was determined by an impedance bridge, and the d.c. resistance by the ammeter-voltmeter method. The data are shown plotted in Figure 2-91, along with results calculated from Eq. 2-71 interpreting the "h" dimension as the coil thickness. There is excellent agreement out to at least 6 KHz. The single data point at 16 KHz suggests that more complicated phenomena are coming into play.

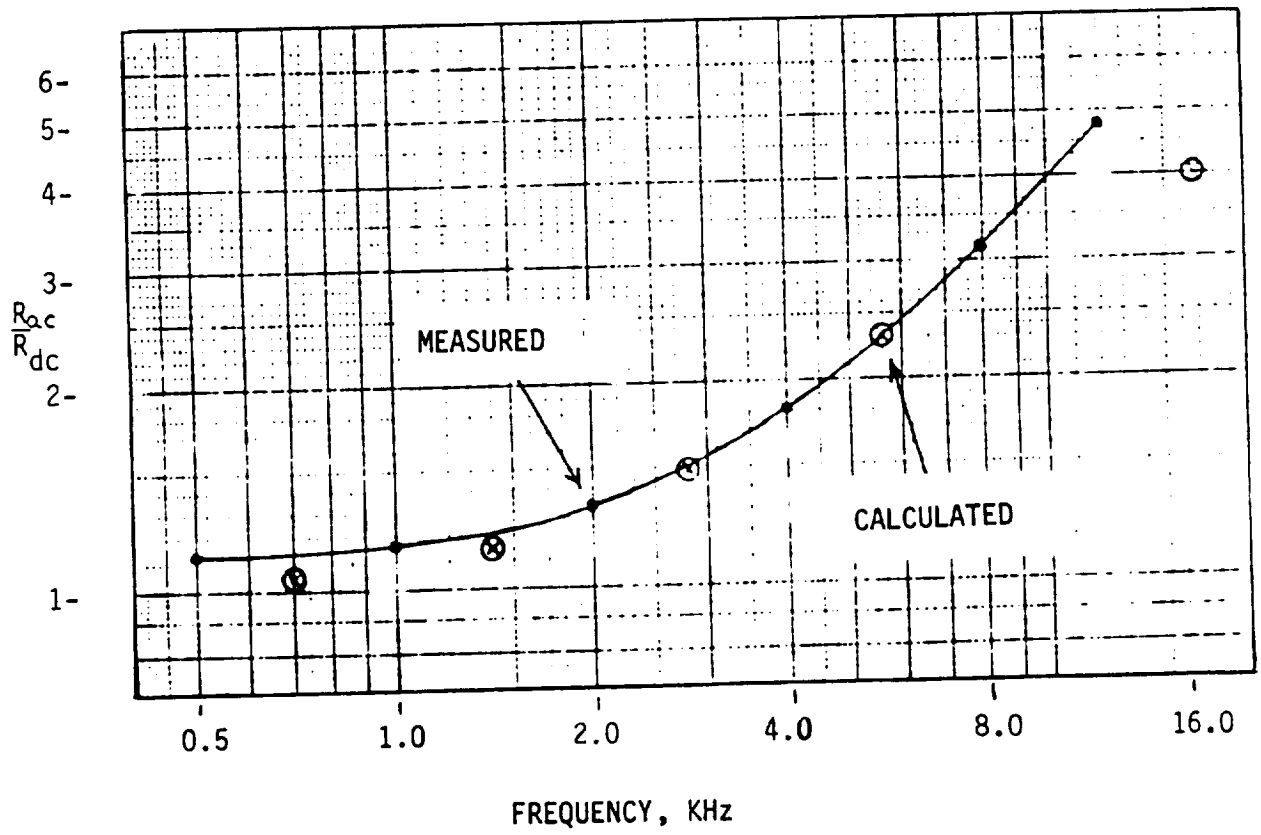

Fig. 2-91 Coil Resistance vs Frequency

Figure 2-92 is a plot of R_{ac}/R_{dc} vs. the ratio of coil thickness to skin depth, as calculated from Eq. 2-69.

VI. Coil Impedance Data

A. Skin Effect Within The Coil

Experimental bridge measurements on an isolated impulse coil show progressively larger effective resistance as the frequency is increased. This is due to skin effect within the coil, and can be approximately accounted for by a formula given below.

Assuming a plate conductor of thickness "h" with symmetrical a.c. excitation on both surfaces, one can derive the following formula for the ratio of a.c. resistance to d.c. resistance:

$$\frac{R_{a.c.}}{R_{d.c.}} = \mathrm{Re}\left[\frac{\frac{\tau h}{2}}{\tanh\left(\frac{\tau b}{2}\right)}\right] \qquad (2\text{-}71)$$

where $\tau = (1 + j)/\delta$

and δ is the skin depth given by

$$\delta = \sqrt{2/\omega\mu\sigma}$$

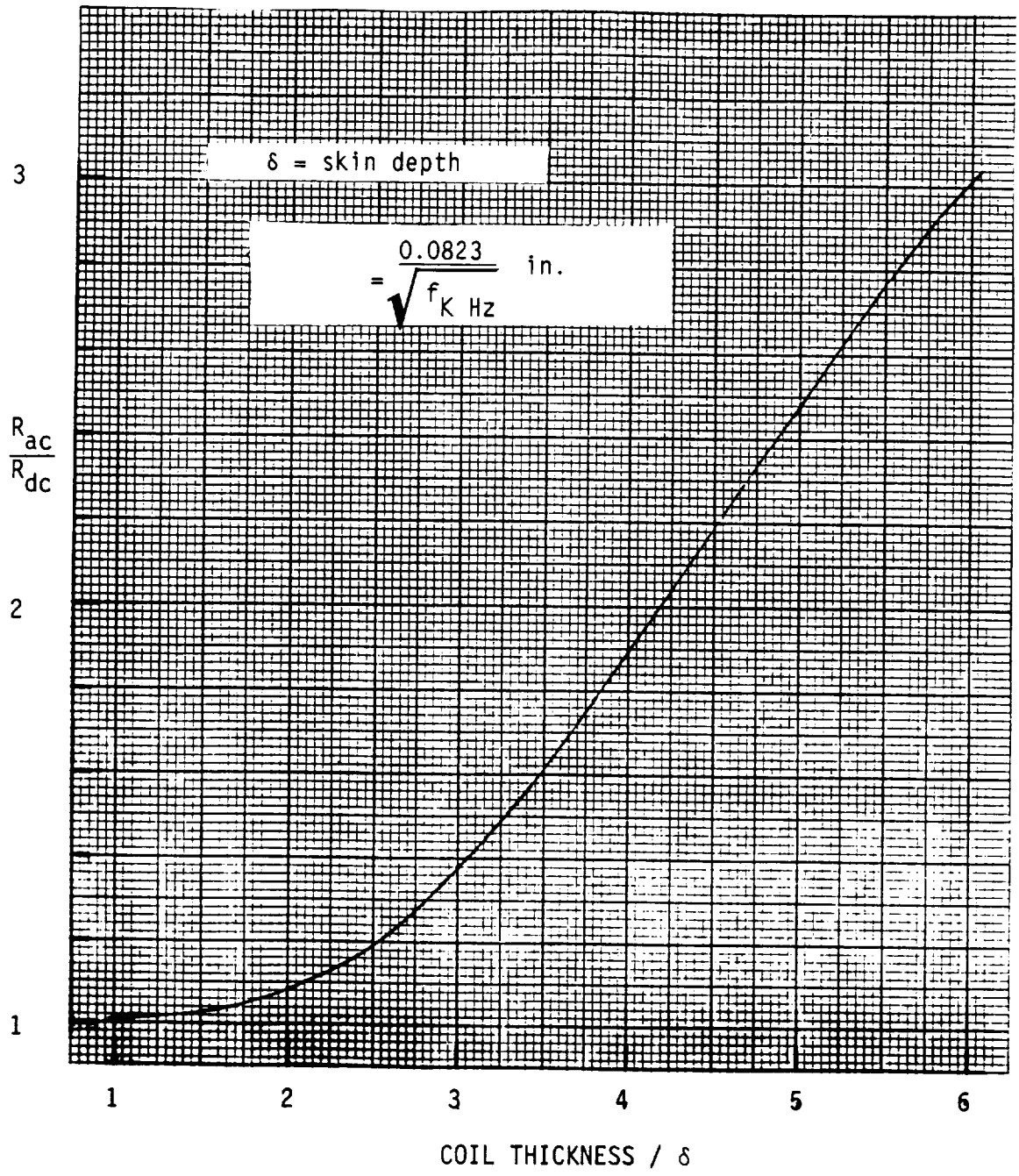

Fig. 2-92 Skin Effect on Round Single Layer Coils Spirally Wound With Rectangular Copper Wire

B. Coil Inductance Tables and Graphs

The inductance of impulse coils were calculated by Dr. Henderson, using the procedure outlined in Sec. B-2, (Eq. 2-22). The calculations assume a uniform current distribution, and this current is replaced by three sheet currents, as was explained in the discussion of Figure 2-36. All calculations assumed a 100-turn coil for which the inductance value is being denoted as L^1. Correction to any other number of turns N, is accomplished by multiplying L^1 by $(N/100)^2$. Also, all calculations assume an inner coil diameter of 0.25 inch.

Several tables (and accompanying graphs) are presented, and each assumes certain fixed design parameters. Information on fixed and variable parameters is summarized on the page preceding each set of tables. Tables 2-2a through 2-2c were intended primarily for design purposes. The corresponding graphs, prepared from the tables, are expecially helpful when interpolations with frequency are required. The abscissa on these graphs is the ratio of the target thickness to electrical skin depth, that is, t/δ. Here δ is calculated from the formula

$$\delta = \frac{0.0823}{\sqrt{f_{KHz}\sigma_u}} \text{ inch} \qquad (2\text{-}72)$$

where σ_u is the electrical conductivity of the target divided by the conductivity of copper. The use of the graphs is illustrated in Section VII, where design examples are considered.

Table 2-1, Graph 2-1

Isolated Coil (No Target)

By Henderson's Model

Coil Thickness Variable, 0.1 to 0.4 Inch

Coil Diameters Variable, 1.5 to 3.5 Inches

COIL OUTER DIAMETER = 1.5 INCH
COIL-TARGET GAP = 0.075 INCH
TARG THICKNESS = 0.025 INCH
TARGET CONDUCTIVITY = 0 PER CENT OF 5.8E7 MHOS/M

CALCULATED INDUCTANCES IN MICROHENRIES ARE:

COIL THICK	FREQUENCY .5KHZ	1KHZ	3KHZ	10KHZ
0.100 INCH	168.19	168.19		
0.150 INCH	160.64	160.64		
0.200 INCH	153.80	153.80		
0.300 INCH	141.88	141.88		
0.400 INCH	131.90	131.90		

COIL OUTER DIAMETER = 2.0 INCH
COIL-TARGET GAP = 0.075 INCH
TARG THICKNESS = 0.025 INCH
TARGET CONDUCTIVITY = 0 PER CENT OF 5.8E7 MHOS/M

CALCULATED INDUCTANCES IN MICROHENRIES ARE:

COIL THICK	FREQUENCY .5KHZ	1KHZ	3KHZ	10KHZ
0.100 INCH	211.25	211.25		
0.150 INCH	203.79	203.79		
0.200 INCH	196.89	196.89		
0.300 INCH	184.52	184.52		
0.400 INCH	173.79	173.79		

COIL OUTER DIAMETER = 2.5 INCH
COIL-TARGET GAP = 0.075 INCH
TARG THICKNESS = 0.025 INCH
TARGET CONDUCTIVITY = 0 PER CENT OF 5.8E7 MHOS/M

CALCULATED INDUCTANCES IN MICROHENRIES ARE:

COIL THICK	FREQUENCY .5KHZ	1KHZ	3KHZ	10KHZ
0.100 INCH	254.67	254.67		
0.150 INCH	247.27	247.27		
0.200 INCH	240.33	240.33		
0.300 INCH	227.65	227.65		
0.400 INCH	216.38	216.38		

COIL OUTER DIAMETER = 3.0 INCH
COIL-TARGET GAP = 0.075 INCH
TARG THICKNESS = 0.025 INCH
TARGET CONDUCTIVITY = 0 PER CENT OF 5.8E7 MHOS/M

CALCULATED INDUCTANCES IN MICROHENRIES ARE:

COIL THICK	FREQUENCY .5KHZ	1KHZ	3KHZ	10KHZ
0.100 INCH	298.37	298.36		
0.150 INCH	290.99	290.99		
0.200 INCH	284.00	284.00		
0.300 INCH	271.10	271.10		
0.400 INCH	259.43	259.43		

COIL OUTER DIAMETER = 3.5 INCH
COIL-TARGET GAP = 0.075 INCH
TARG THICKNESS = 0.025 INCH
TARGET CONDUCTIVITY = 0 PER CENT OF 5.8E7 MHOS/M

CALCULATED INDUCTANCES IN MICROHENRIES ARE:

COIL THICK	FREQUENCY .5KHZ	1KHZ	3KHZ	10KHZ
0.100 INCH	342.20	342.20		
0.150 INCH	334.84	334.84		
0.200 INCH	327.82	327.82		
0.300 INCH	314.73	314.73		
0.400 INCH	302.76	302.76		

Table 2-1a

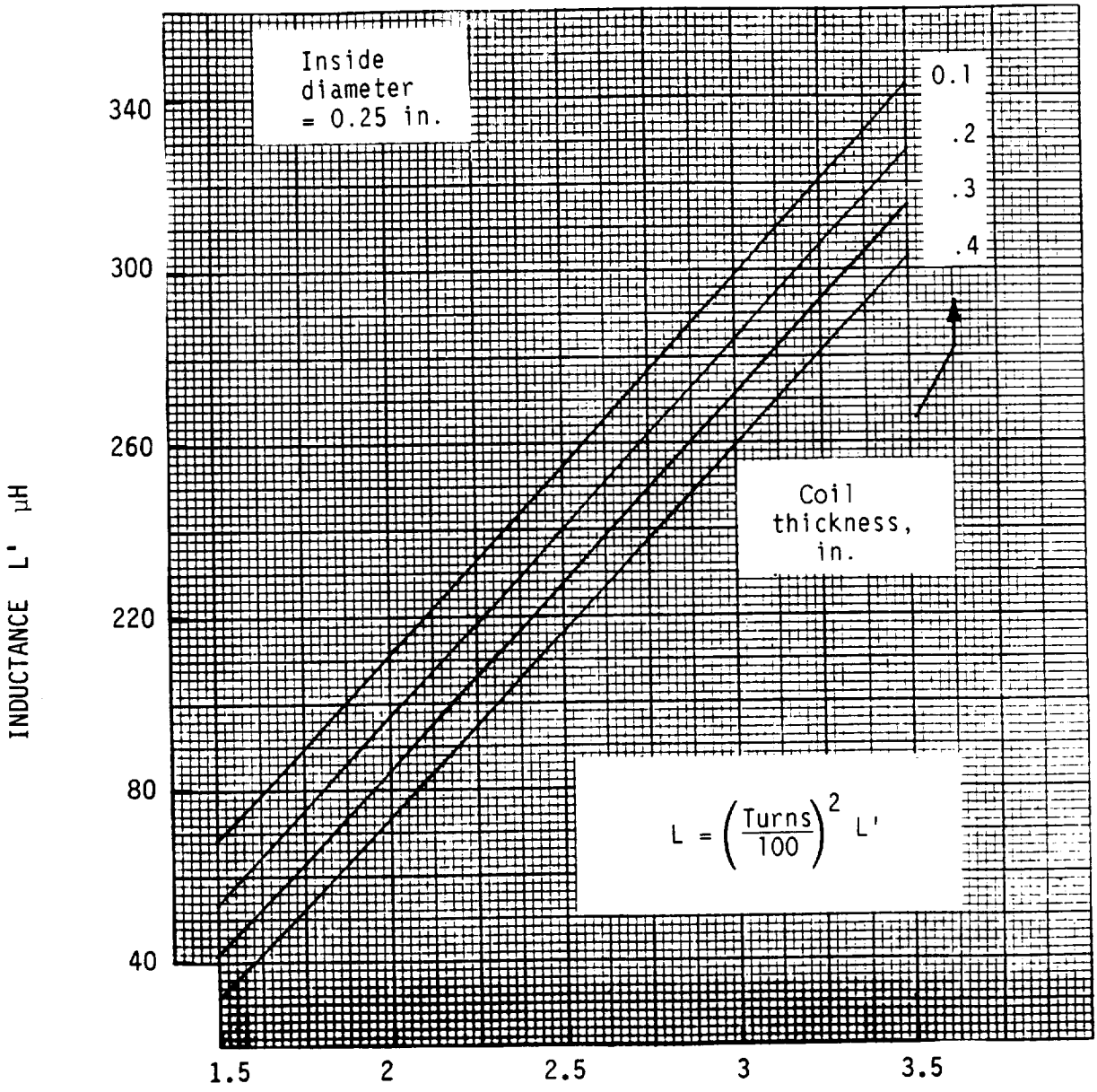

Graph 2-1a Inductance of a Pancake Shaped Coil Without a Nearby Metal Plate

Table 2-2, Graph 2-2

Main Design Data

By Henderson's Model

Coil Thickness 0.15 Inch

Coil Diameters Variable, 1.5 to 3.5 Inches

Coil-Target Gap 0.075 Inch

Target Thicknesses Variable, 0.025 to 0.065 Inch

Target Conductivity σ_u Variable, 30% to 100%

COIL OUTER DIAMETER = 1.5 INCH
COIL-TARGET GAP = 0.075 INCH
COIL THICKNESS = 0.15 INCH

COIL THICKNESS = 0.15 INCH
TARGET CONDUCTIVITY = 30 PER CENT OF 5.8E7 MHOS/M

CALCULATED INDUCTANCES IN MICROHENRIES ARE:

TARGET THICK	FREQUENCY .5KHZ	1KHZ	3KHZ	10KHZ
0.025 INCH	156.20	148.07	120.91	97.32
0.035 INCH	153.28	141.83	113.03	96.18
0.045 INCH	150.26	136.38	108.60	96.29
0.055 INCH	147.34	131.85	106.17	96.80
0.065 INCH	144.59	128.18	104.90	97.38

TARGET CONDUCTIVITY = 40 PER CENT OF 5.8E7 MHOS/M

CALCULATED INDUCTANCES IN MICROHENRIES ARE:

TARGET THICK	FREQUENCY .5KHZ	1KHZ	3KHZ	10KHZ
0.025 INCH	153.65	142.46	113.15	95.17
0.035 INCH	149.47	134.86	106.74	94.95
0.045 INCH	145.42	128.82	103.69	95.46
0.055 INCH	141.69	124.20	102.32	96.10
0.065 INCH	138.39	120.74	101.82	96.66

TARGET CONDUCTIVITY = 50 PER CENT OF 5.8E7 MHOS/M

CALCULATED INDUCTANCES IN MICROHENRIES ARE:

TARGET THICK	FREQUENCY .5KHZ	1KHZ	3KHZ	10KHZ
0.025 INCH	150.90	137.18	107.88	94.09
0.035 INCH	145.60	128.84	102.90	94.34
0.045 INCH	140.74	122.74	100.88	95.00
0.055 INCH	136.50	118.41	100.20	95.64
0.065 INCH	132.90	115.40	100.17	96.10

TARGET CONDUCTIVITY = 60 PER CENT OF 5.8E7 MHOS/M

CALCULATED INDUCTANCES IN MICROHENRIES ARE:

TARGET THICK	FREQUENCY .5KHZ	1KHZ	3KHZ	10KHZ
0.025 INCH	148.07	132.37	104.24	93.47
0.035 INCH	141.83	123.75	100.44	93.98
0.045 INCH	136.38	117.91	99.16	94.69
0.055 INCH	131.85	114.04	98.93	95.28
0.065 INCH	128.18	111.53	99.17	95.63

TARGET CONDUCTIVITY = 100 PER CENT OF 5.8E7 MHOS/M

CALCULATED INDUCTANCES IN MICROHENRIES ARE:

TARGET THICK	FREQUENCY .5KHZ	1KHZ	3KHZ	10KHZ
0.025 INCH	137.18	117.98	97.32	92.50
0.035 INCH	128.84	110.56	96.18	93.30
0.045 INCH	122.74	106.63	96.29	93.89
0.055 INCH	118.41	104.60	96.80	94.15
0.065 INCH	115.40	103.63	97.38	94.19

Table 2-2a

COIL THICKNESS = 0.15 INCH
COIL - TARGET GAP = 0.075 INCH
t = TARGET THICKNESS, INCH
δ = SKIN DEPTH, INCH
σ = TARGET CONDUCTIVITY, RATIO TO COPPER

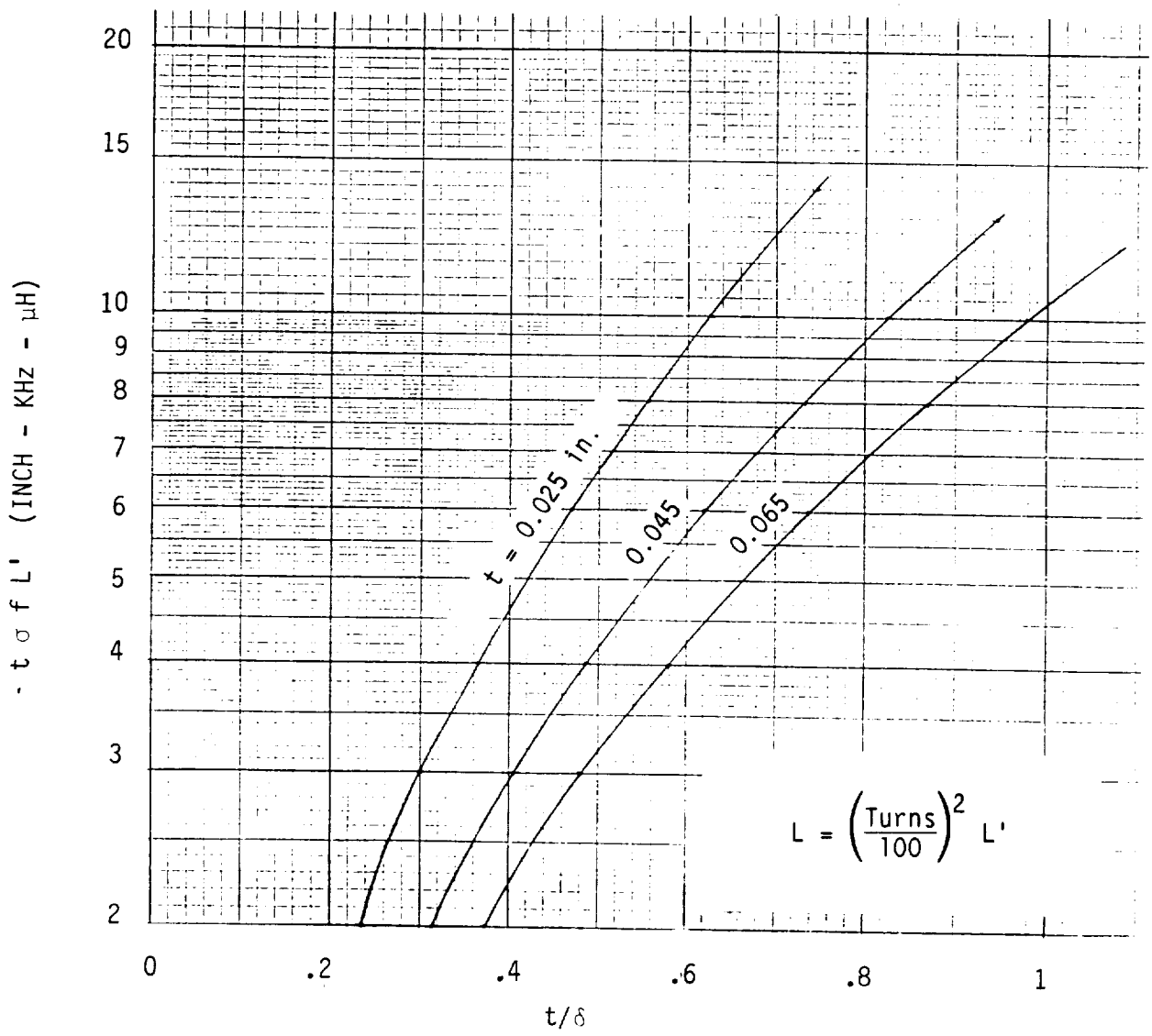

Graph 2-2a Inductance Curves for a 1.5 Inch Diameter Coil

COIL OUTER DIAMETER = 2.0 INCH
COIL-TARGET GAP = 0.075 INCH
COIL THICKNESS = 0.15 INCH
TARGET CONDUCTIVITY = 30 PER CENT OF 5.8E7 MHOS/M

CALCULATED INDUCTANCES IN MICROHENRIES ARE:

TARGET THICK	FREQUENCY .5KHZ	1KHZ	3KHZ	10KHZ
0.025 INCH	193.86	177.41	132.38	103.61
0.035 INCH	187.69	165.75	121.76	102.73
0.045 INCH	181.56	156.20	116.39	103.13
0.055 INCH	175.80	148.69	113.71	103.90
0.065 INCH	170.57	142.90	112.48	104.70

COIL OUTER DIAMETER = 2.0 INCH
COIL-TARGET GAP = 0.075 INCH
COIL THICKNESS = 0.15 INCH
TARGET CONDUCTIVITY = 40 PER CENT OF 5.8E7 MHOS/M

CALCULATED INDUCTANCES IN MICROHENRIES ARE:

TARGET THICK	FREQUENCY .5KHZ	1KHZ	3KHZ	10KHZ
0.025 INCH	188.49	166.96	121.88	101.45
0.035 INCH	180.06	153.73	114.09	101.53
0.045 INCH	172.24	143.99	110.78	102.31
0.055 INCH	165.36	137.01	109.50	103.18
0.065 INCH	159.47	132.08	109.21	103.91

COIL OUTER DIAMETER = 2.0 INCH
COIL-TARGET GAP = 0.075 INCH
COIL THICKNESS = 0.15 INCH
TARGET CONDUCTIVITY = 50 PER CENT OF 5.8E7 MHOS/M

CALCULATED INDUCTANCES IN MICROHENRIES ARE:

TARGET THICK	FREQUENCY .5KHZ	1KHZ	3KHZ	10KHZ
0.025 INCH	182.93	157.71	115.34	100.39
0.035 INCH	172.66	144.08	109.74	100.93
0.045 INCH	163.73	134.92	107.77	101.85
0.055 INCH	156.32	128.88	107.31	102.68
0.065 INCH	150.32	124.94	107.53	103.27

COIL OUTER DIAMETER = 2.0 INCH
COIL-TARGET GAP = 0.075 INCH
COIL THICKNESS = 0.15 INCH
TARGET CONDUCTIVITY = 60 PER CENT OF 5.8E7 MHOS/M

CALCULATED INDUCTANCES IN MICROHENRIES ARE:

TARGET THICK	FREQUENCY .5KHZ	1KHZ	3KHZ	10KHZ
0.025 INCH	177.41	149.73	111.08	99.79
0.035 INCH	165.75	136.43	107.08	100.58
0.045 INCH	156.20	128.20	105.99	101.53
0.055 INCH	148.69	123.16	106.02	102.27
0.065 INCH	142.90	120.11	106.53	102.71

COIL OUTER DIAMETER = 2.0 INCH
COIL-TARGET GAP = 0.075 INCH
COIL THICKNESS = 0.15 INCH
TARGET CONDUCTIVITY = 100 PER CENT OF 5.8E7 MHOS/M

CALCULATED INDUCTANCES IN MICROHENRIES ARE:

TARGET THICK	FREQUENCY .5KHZ	1KHZ	3KHZ	10KHZ
0.025 INCH	157.71	128.29	103.61	98.86
0.035 INCH	144.08	118.67	102.73	99.89
0.045 INCH	134.92	114.09	103.13	100.62
0.055 INCH	128.89	111.96	103.90	100.94
0.065 INCH	124.94	111.11	104.70	100.99

Table 2-2b

COIL THICKNESS = 0.15 INCH
COIL - TARGET GAP = 0.075 INCH
t = TARGET THICKNESS, INCH
δ = SKIN DEPTH, INCH
σ = TARGET CONDUCTIVITY, RATIO TO COPPER

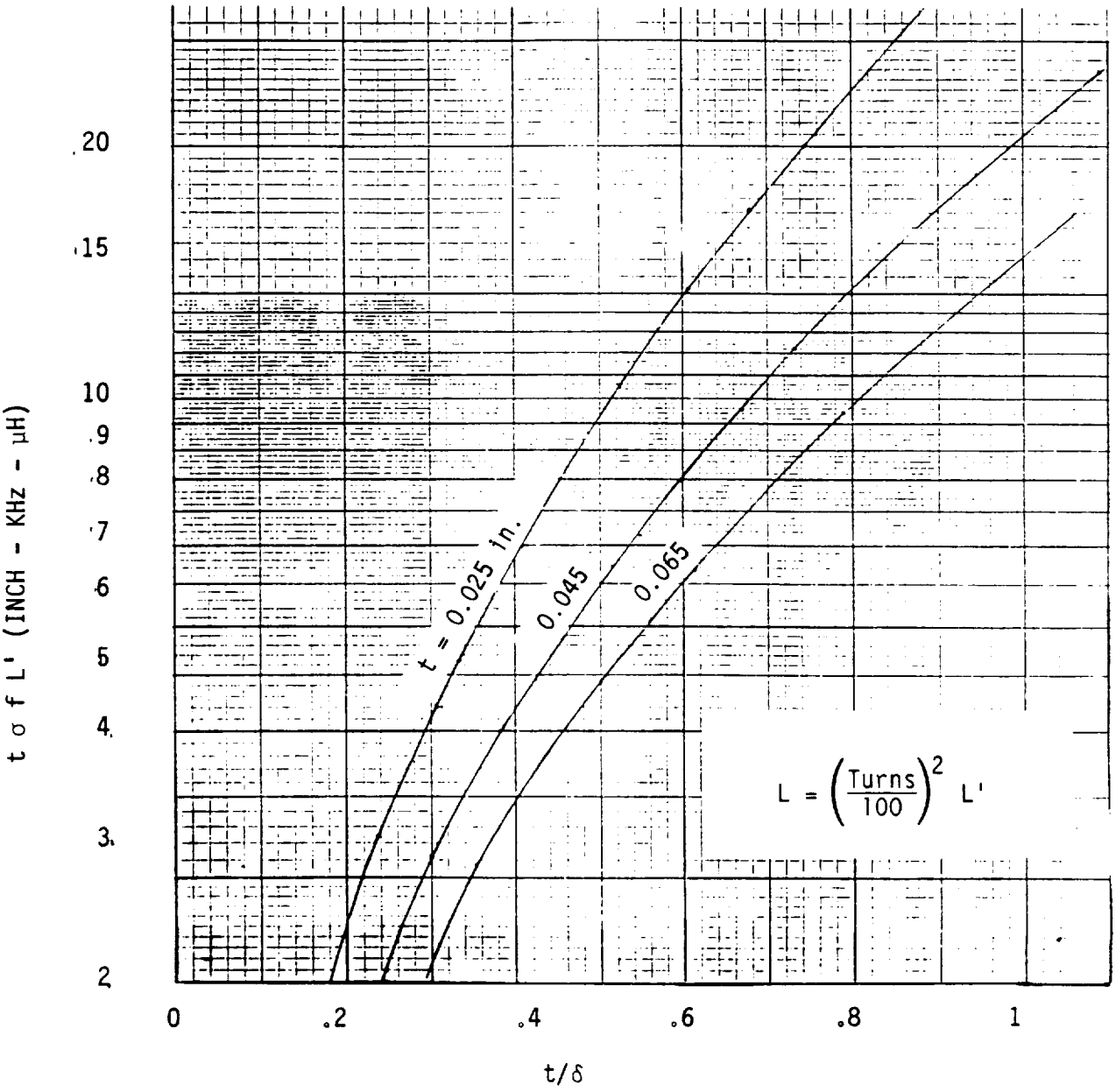

Graph 2-2b Inductance Curves for a 2.0 Inch Diameter Coil

ORIGINAL PAGE IS
OF POOR QUALITY

COIL OUTER DIAMETER = 2.5 INCH
COIL-TARGET GAP = 0.075 INCH
COIL THICKNESS = 0.15 INCH
TARGET CONDUCTIVITY = 30 PER CENT OF 5.8E7 MHOS/M

CALCULATED INDUCTANCES IN MICROHENRIES ARE:

TARGET THICK	FREQUENCY .5KHZ	1KHZ	3KHZ	10KHZ
0.025 INCH	229.03	201.69	139.20	107.93
0.035 INCH	218.39	183.82	126.95	107.36
0.045 INCH	208.21	170.06	121.25	108.02
0.055 INCH	198.96	159.79	118.64	109.00
0.065 INCH	190.82	152.24	117.60	109.98

COIL OUTER DIAMETER = 2.5 INCH
COIL-TARGET GAP = 0.075 INCH
COIL THICKNESS = 0.15 INCH
TARGET CONDUCTIVITY = 40 PER CENT OF 5.8E7 MHOS/M

CALCULATED INDUCTANCES IN MICROHENRIES ARE:

TARGET THICK	FREQUENCY .5KHZ	1KHZ	3KHZ	10KHZ
0.025 INCH	219.80	185.69	126.99	105.86
0.035 INCH	205.84	166.69	118.68	106.22
0.045 INCH	193.51	153.66	115.47	107.23
0.055 INCH	183.11	144.86	114.42	108.28
0.065 INCH	174.54	138.96	114.38	109.14

COIL OUTER DIAMETER = 2.5 INCH
COIL-TARGET GAP = 0.075 INCH
COIL THICKNESS = 0.15 INCH
TARGET CONDUCTIVITY = 50 PER CENT OF 5.8E7 MHOS/M

CALCULATED INDUCTANCES IN MICROHENRIES ARE:

TARGET THICK	FREQUENCY .5KHZ	1KHZ	3KHZ	10KHZ
0.025 INCH	210.56	172.29	119.84	104.86
0.035 INCH	194.22	153.80	114.21	105.66
0.045 INCH	180.79	142.30	112.48	106.78
0.055 INCH	170.17	135.17	112.28	107.76
0.065 INCH	161.93	130.78	112.75	108.44

COIL OUTER DIAMETER = 2.5 INCH
COIL-TARGET GAP = 0.075 INCH
COIL THICKNESS = 0.15 INCH
TARGET CONDUCTIVITY = 60 PER CENT OF 5.8E7 MHOS/M

CALCULATED INDUCTANCES IN MICROHENRIES ARE:

TARGET THICK	FREQUENCY .5KHZ	1KHZ	3KHZ	10KHZ
0.025 INCH	201.69	161.31	115.39	104.29
0.035 INCH	183.82	144.14	111.57	105.32
0.045 INCH	170.06	134.32	110.75	106.45
0.055 INCH	159.79	128.69	111.05	107.31
0.065 INCH	152.24	125.49	111.78	107.82

COIL OUTER DIAMETER = 2.5 INCH
COIL-TARGET GAP = 0.075 INCH
COIL THICKNESS = 0.15 INCH
TARGET CONDUCTIVITY = 100 PER CENT OF 5.8E7 MHOS/M

CALCULATED INDUCTANCES IN MICROHENRIES ARE:

TARGET THICK	FREQUENCY .5KHZ	1KHZ	3KHZ	10KHZ
0.025 INCH	172.29	134.34	107.93	103.42
0.035 INCH	153.80	123.55	107.36	104.63
0.045 INCH	142.30	118.84	108.02	105.47
0.055 INCH	135.17	116.87	109.00	105.83
0.065 INCH	130.78	116.24	109.98	105.89

Table 2-2c

COIL THICKNESS = 0.15 INCH
COIL - TARGET GAP = 0.075 INCH
t = TARGET THICKNESS, INCH
δ = SKIN DEPTH, INCH
σ = TARGET CONDUCTIVITY, RATIO TO COPPER

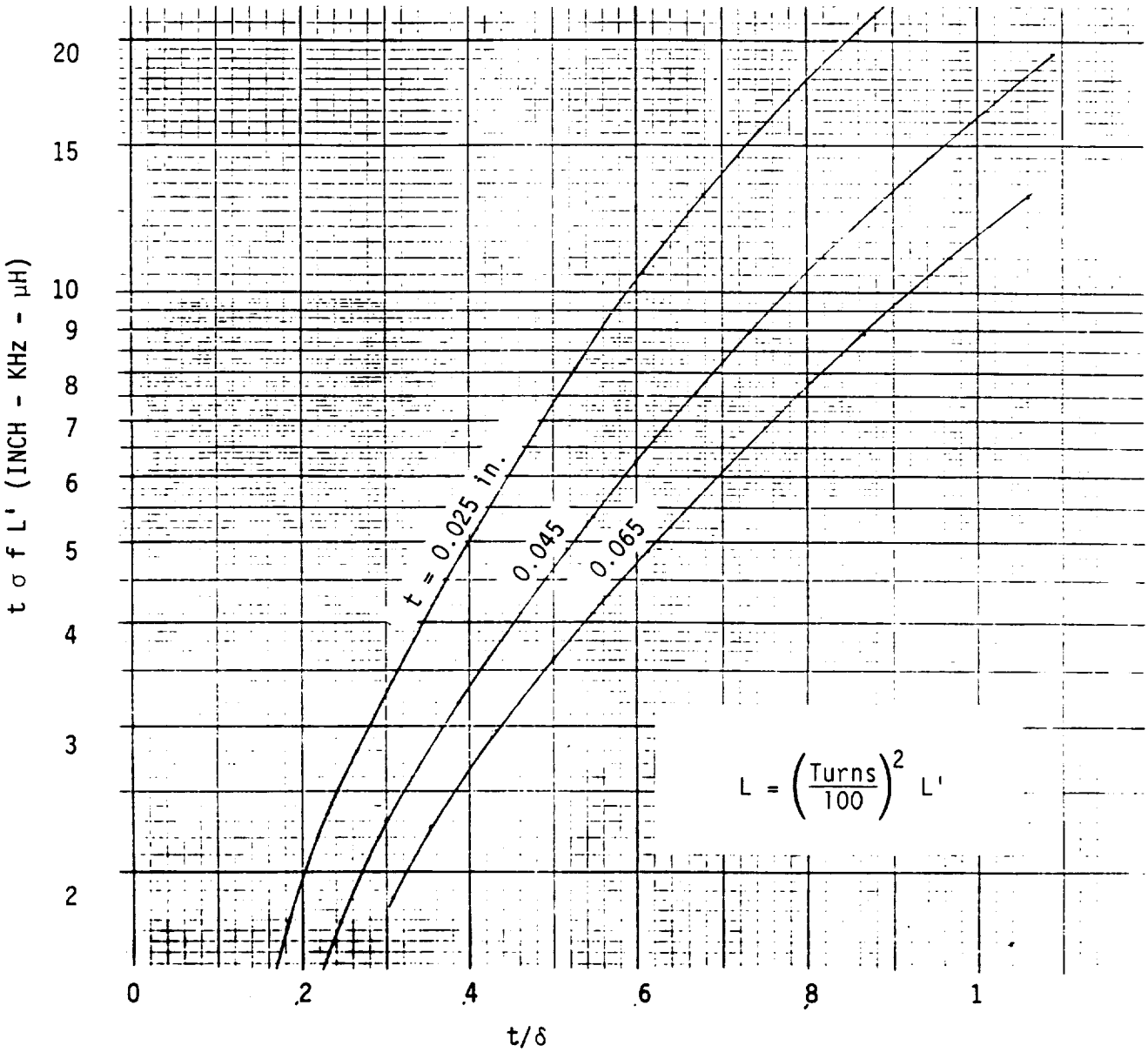

Graphs 2-2c Inductance Curves for a 2.5 Inch Diameter Coil

COIL OUTER DIAMETER = 3.0 INCH
COIL-TARGET GAP = 0.075 INCH
COIL THICKNESS = 0.15 INCH
TARGET CONDUCTIVITY = 30 PER CENT OF 5.8E7 MHOS/M

CALCULATED INDUCTANCES IN MICROHENRIES ARE:

TARGET THICK	FREQUENCY .5KHZ	1KHZ	3KHZ	10KHZ
0.025 INCH	261.45	221.32	143.23	111.15
0.035 INCH	245.29	197.06	130.21	110.87
0.045 INCH	230.40	179.43	124.55	111.74
0.055 INCH	217.33	166.91	122.16	112.90
0.065 INCH	206.18	158.06	121.36	114.02

COIL OUTER DIAMETER = 3.0 INCH
COIL-TARGET GAP = 0.075 INCH
COIL THICKNESS = 0.15 INCH
TARGET CONDUCTIVITY = 40 PER CENT OF 5.8E7 MHOS/M

CALCULATED INDUCTANCES IN MICROHENRIES ARE:

TARGET THICK	FREQUENCY .5KHZ	1KHZ	3KHZ	10KHZ
0.025 INCH	247.44	199.59	130.14	109.19
0.035 INCH	227.09	175.31	121.80	109.80
0.045 INCH	209.92	159.68	118.85	110.99
0.055 INCH	196.02	149.67	118.06	112.18
0.065 INCH	184.98	143.25	118.26	113.15

COIL OUTER DIAMETER = 3.0 INCH
COIL-TARGET GAP = 0.075 INCH
COIL THICKNESS = 0.15 INCH
TARGET CONDUCTIVITY = 50 PER CENT OF 5.8E7 MHOS/M

CALCULATED INDUCTANCES IN MICROHENRIES ARE:

TARGET THICK	FREQUENCY .5KHZ	1KHZ	3KHZ	10KHZ
0.025 INCH	233.90	182.32	122.80	108.25
0.035 INCH	210.95	159.85	117.41	109.27
0.045 INCH	193.06	146.77	115.97	110.55
0.055 INCH	179.53	139.09	116.02	111.65
0.065 INCH	169.45	134.57	116.70	112.41

COIL OUTER DIAMETER = 3.0 INCH
COIL-TARGET GAP = 0.075 INCH
COIL THICKNESS = 0.15 INCH
TARGET CONDUCTIVITY = 60 PER CENT OF 5.8E7 MHOS/M

CALCULATED INDUCTANCES IN MICROHENRIES ARE:

TARGET THICK	FREQUENCY .5KHZ	1KHZ	3KHZ	10KHZ
0.025 INCH	221.32	168.78	118.36	107.73
0.035 INCH	197.06	148.78	114.86	108.95
0.045 INCH	179.43	138.08	114.33	110.22
0.055 INCH	166.91	132.27	114.85	111.18
0.065 INCH	158.06	129.16	115.78	111.73

COIL OUTER DIAMETER = 3.0 INCH
COIL-TARGET GAP = 0.075 INCH
COIL THICKNESS = 0.15 INCH
TARGET CONDUCTIVITY = 100 PER CENT OF 5.8E7 MHOS/M

CALCULATED INDUCTANCES IN MICROHENRIES ARE:

TARGET THICK	FREQUENCY .5KHZ	1KHZ	3KHZ	10KHZ
0.025 INCH	182.32	137.93	111.15	106.91
0.035 INCH	159.85	126.72	110.87	108.26
0.045 INCH	146.77	122.16	111.74	109.19
0.055 INCH	139.09	120.42	112.90	109.58
0.065 INCH	134.57	120.05	114.02	109.64

Table 2-2d

COIL THICKNESS = 0.15 INCH
COIL - TARGET GAP = 0.075 INCH
t = TARGET THICKNESS, INCH
δ = SKIN DEPTH, INCH
σ = TARGET CONDUCTIVITY, RATIO TO COPPER

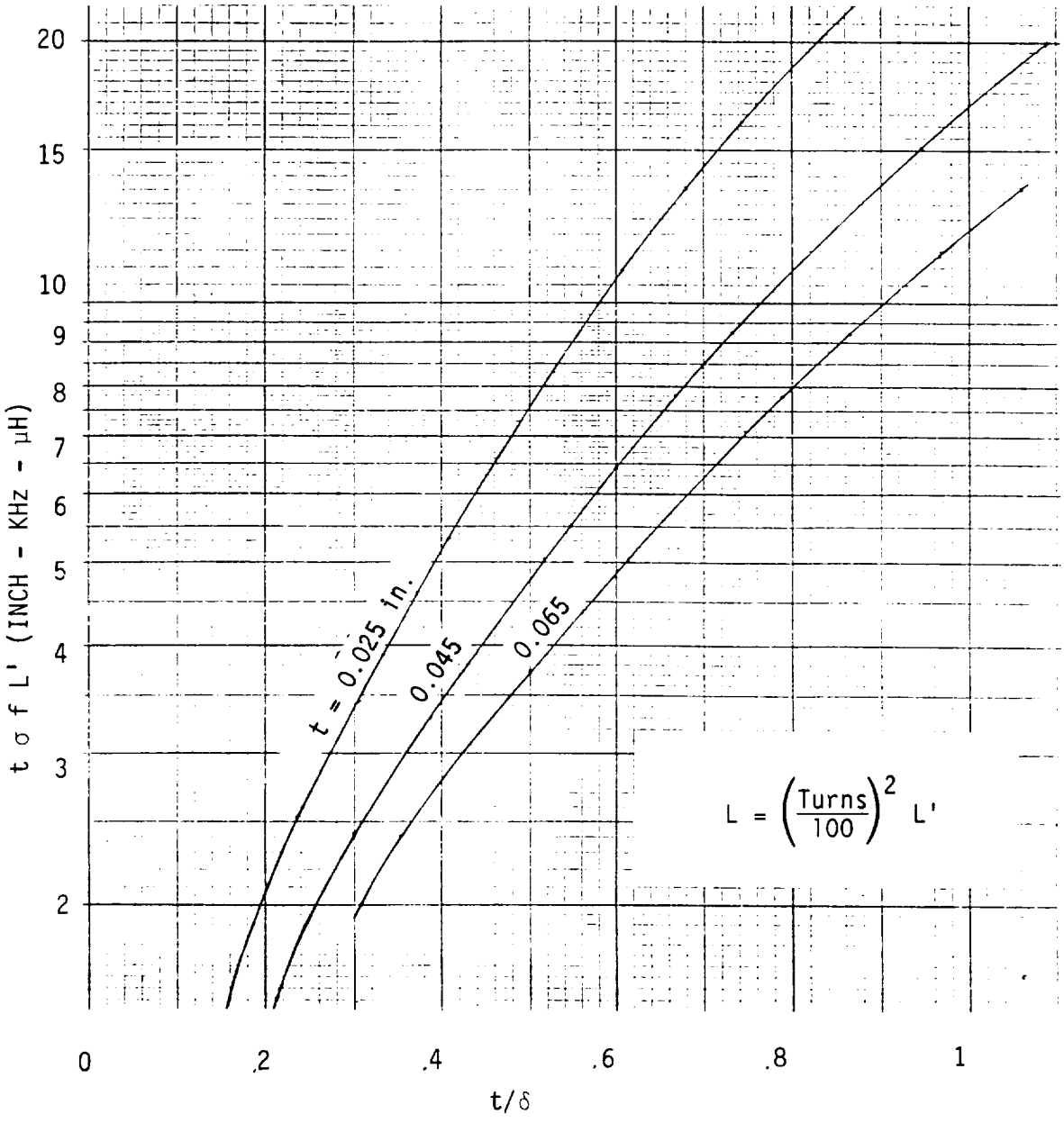

Graph 2-2d Inductance Curves for a 3.0 Inch Diameter Coil

ORIGINAL PAGE IS
OF POOR QUALITY

COIL OUTER DIAMETER = 3.5 INCH
COIL-TARGET GAP = 0.075 INCH
COIL THICKNESS = 0.15 INCH
TARGET CONDUCTIVITY = 30 PER CENT OF 5.8E7 MHOS/M

CALCULATED INDUCTANCES IN MICROHENRIES ARE:

TARGET THICK	FREQUENCY .5KHZ	1KHZ	3KHZ	10KHZ
0.025 INCH	290.97	236.81	145.59	113.64
0.035 INCH	268.48	206.46	132.35	113.62
0.045 INCH	248.49	185.54	126.92	114.67
0.055 INCH	231.54	171.31	124.79	115.97
0.065 INCH	217.49	161.63	124.23	117.20

COIL OUTER DIAMETER = 3.5 INCH
COIL-TARGET GAP = 0.075 INCH
COIL THICKNESS = 0.15 INCH
TARGET CONDUCTIVITY = 40 PER CENT OF 5.8E7 MHOS/M

CALCULATED INDUCTANCES IN MICROHENRIES ARE:

TARGET THICK	FREQUENCY .5KHZ	1KHZ	3KHZ	10KHZ
0.025 INCH	271.46	209.59	132.14	111.80
0.035 INCH	244.23	180.81	124.06	112.61
0.045 INCH	222.24	163.31	121.41	113.95
0.055 INCH	205.11	152.59	120.88	115.26
0.065 INCH	191.96	145.97	121.29	116.31

COIL OUTER DIAMETER = 3.5 INCH
COIL-TARGET GAP = 0.075 INCH
COIL THICKNESS = 0.15 INCH
TARGET CONDUCTIVITY = 50 PER CENT OF 5.8E7 MHOS/M

CALCULATED INDUCTANCES IN MICROHENRIES ARE:

TARGET THICK	FREQUENCY .5KHZ	1KHZ	3KHZ	10KHZ
0.025 INCH	253.24	188.94	124.85	110.92
0.035 INCH	223.59	163.46	119.82	112.11
0.045 INCH	201.59	149.45	118.67	113.52
0.055 INCH	185.65	141.58	118.94	114.72
0.065 INCH	174.17	137.15	119.81	115.54

COIL OUTER DIAMETER = 3.5 INCH
COIL-TARGET GAP = 0.075 INCH
COIL THICKNESS = 0.15 INCH
TARGET CONDUCTIVITY = 60 PER CENT OF 5.8E7 MHOS/M

CALCULATED INDUCTANCES IN MICROHENRIES ARE:

TARGET THICK	FREQUENCY .5KHZ	1KHZ	3KHZ	10KHZ
0.025 INCH	236.81	173.40	120.52	110.43
0.035 INCH	206.46	151.50	117.38	111.81
0.045 INCH	185.54	140.44	117.11	113.19
0.055 INCH	171.31	134.71	117.83	114.23
0.065 INCH	161.63	131.78	118.93	114.82

COIL OUTER DIAMETER = 3.5 INCH
COIL-TARGET GAP = 0.075 INCH
COIL THICKNESS = 0.15 INCH
TARGET CONDUCTIVITY = 100 PER CENT OF 5.8E7 MHOS/M

CALCULATED INDUCTANCES IN MICROHENRIES ARE:

TARGET THICK	FREQUENCY .5KHZ	1KHZ	3KHZ	10KHZ
0.025 INCH	188.94	140.08	113.64	109.66
0.035 INCH	163.46	128.88	113.62	111.13
0.045 INCH	149.45	124.59	114.67	112.12
0.055 INCH	141.58	123.13	115.97	112.54
0.065 INCH	137.15	122.98	117.20	112.60

Table 2-2e

COIL THICKNESS = 0.15 INCH
COIL - TARGET GAP = 0.075 INCH
t = TARGET THICKNESS, INCH
δ = SKIN DEPTH, INCH
σ = TARGET CONDUCTIVITY, RATIO TO COPPER

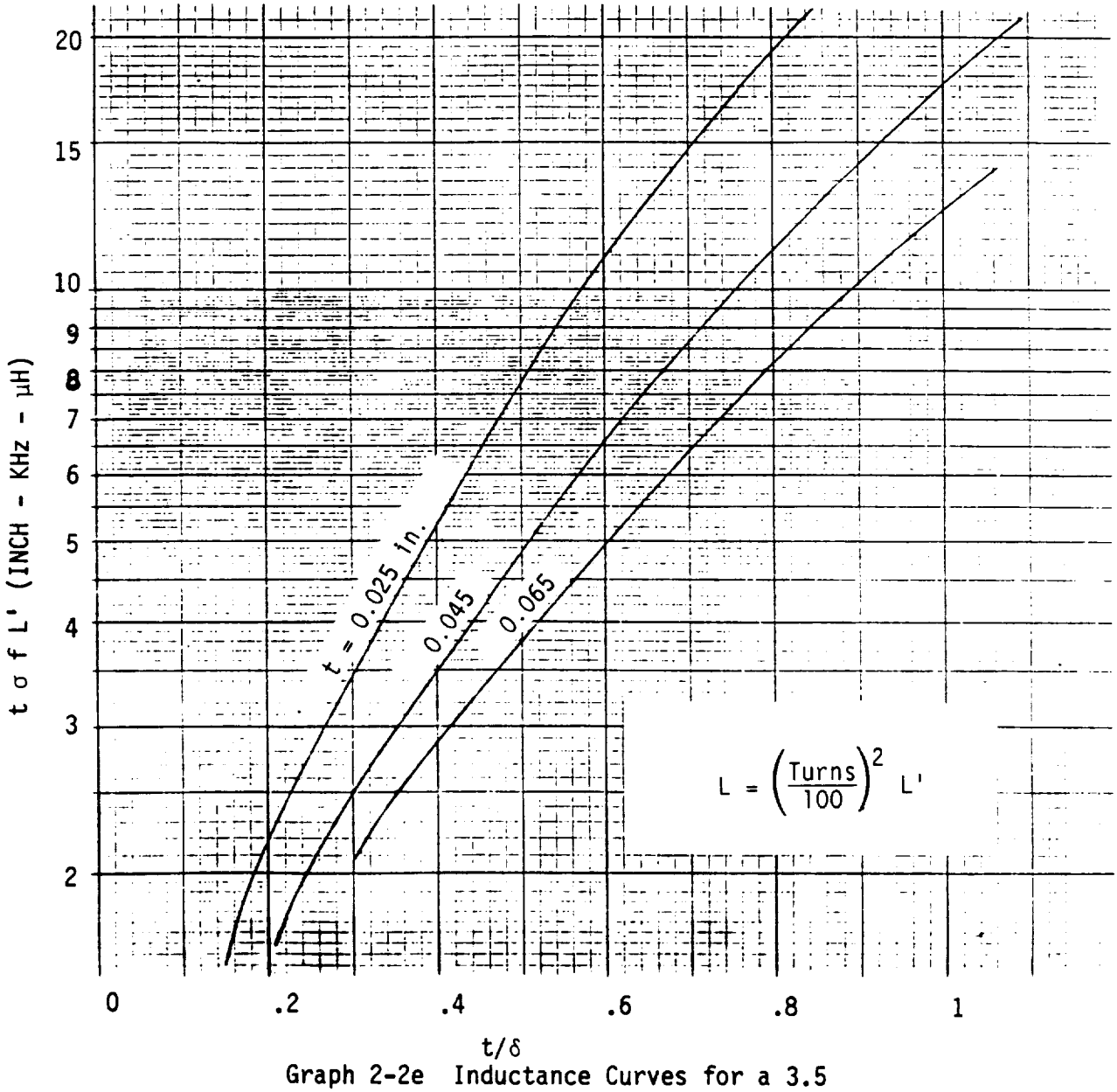

Graph 2-2e Inductance Curves for a 3.5 Inch Diameter Coil

Table 2-3

Effect of Coil-Target-Gap

by Henderson's Model

Coil Thickness 0.15 Inch

Coil Diameters 2.0 and 3.0 Inches

Coil-Target Gap Variable, 0.025 to 0.10 Inch

Target Thickness Variable, 0.025 to 0.065 Inch

Target Conductivity σ_u 60%

COIL OUTER DIAMETER = 2.0 INCH
COIL THICKNESS = 0.150 INCH
TARGET THICKNESS = 0.025 INCH
TARGET CONDUCTIVITY = 60 PER CENT OF 5.8E7 MHOS/M

CALCULATED INDUCTANCES IN MICROHENRIES ARE:

COIL-TARGET GAP	FREQUENCY .5KHZ	1KHZ	3KHZ	10KHZ
0.025 INCH	172.47	138.02	87.73	72.42
0.050 INCH	175.07	144.22	100.18	87.05
0.075 INCH	177.41	149.73	111.08	99.79
0.100 INCH	179.51	154.64	120.65	110.90

COIL OUTER DIAMETER = 2.0 INCH
COIL THICKNESS = 0.150 INCH
TARGET THICKNESS = 0.035 INCH
TARGET CONDUCTIVITY = 60 PER CENT OF 5.8E7 MHOS/M

CALCULATED INDUCTANCES IN MICROHENRIES ARE:

COIL-TARGET GAP	FREQUENCY .5KHZ	1KHZ	3KHZ	10KHZ
0.025 INCH	158.14	121.01	82.31	73.42
0.050 INCH	162.15	129.20	95.53	87.95
0.075 INCH	165.75	136.43	107.08	100.58
0.100 INCH	168.97	142.84	117.20	111.61

COIL OUTER DIAMETER = 2.0 INCH
COIL THICKNESS = 0.150 INCH
TARGET THICKNESS = 0.045 INCH
TARGET CONDUCTIVITY = 60 PER CENT OF 5.8E7 MHOS/M

CALCULATED INDUCTANCES IN MICROHENRIES ARE:

COIL-TARGET GAP	FREQUENCY .5KHZ	1KHZ	3KHZ	10KHZ
0.025 INCH	146.22	110.32	80.77	74.66
0.050 INCH	151.50	119.82	94.23	89.02
0.075 INCH	156.20	128.20	105.99	101.53
0.100 INCH	160.40	135.60	116.28	112.44

COIL OUTER DIAMETER = 2.0 INCH
COIL THICKNESS = 0.150 INCH
TARGET THICKNESS = 0.055 INCH
TARGET CONDUCTIVITY = 60 PER CENT OF 5.8E7 MHOS/M

CALCULATED INDUCTANCES IN MICROHENRIES ARE:

COIL-TARGET GAP	FREQUENCY .5KHZ	1KHZ	3KHZ	10KHZ
0.025 INCH	136.74	103.68	80.74	75.63
0.050 INCH	143.07	114.04	94.25	89.88
0.075 INCH	148.69	123.16	106.02	102.27
0.100 INCH	153.70	131.19	116.33	113.09

COIL OUTER DIAMETER = 2.0 INCH
COIL THICKNESS = 0.150 INCH
TARGET THICKNESS = 0.065 INCH
TARGET CONDUCTIVITY = 60 PER CENT OF 5.8E7 MHOS/M

CALCULATED INDUCTANCES IN MICROHENRIES ARE:

COIL-TARGET GAP	FREQUENCY .5KHZ	1KHZ	3KHZ	10KHZ
0.025 INCH	129.35	99.62	81.36	76.21
0.050 INCH	136.53	110.53	94.80	90.38
0.075 INCH	142.90	120.11	106.53	102.71
0.100 INCH	148.56	128.54	116.78	113.48

Table 2-3a

COIL OUTER DIAMETER = 3.0 INCH
COIL THICKNESS = 0.150 INCH
TARGET THICKNESS = 0.025 INCH
TARGET CONDUCTIVITY = 60 PER CENT OF 5.8E7 MHOS/M

CALCULATED INDUCTANCES IN MICROHENRIES ARE:

COIL-TARGET GAP	FREQUENCY .5KHZ	1KHZ	3KHZ	10KHZ
0.025 INCH	211.75	149.77	88.61	75.33
0.050 INCH	216.72	159.69	104.19	92.32
0.075 INCH	221.32	168.78	118.36	107.73
0.100 INCH	225.57	177.14	131.27	121.73

COIL OUTER DIAMETER = 3.0 INCH
COIL THICKNESS = 0.150 INCH
TARGET THICKNESS = 0.035 INCH
TARGET CONDUCTIVITY = 60 PER CENT OF 5.8E7 MHOS/M

CALCULATED INDUCTANCES IN MICROHENRIES ARE:

COIL-TARGET GAP	FREQUENCY 5KHZ	1KHZ	3KHZ	10KHZ
0.025 INCH	183.34	125.72	84.22	76.78
0.050 INCH	190.48	137.76	100.27	93.65
0.075 INCH	197.06	148.78	114.86	108.95
0.100 INCH	203.13	158.87	128.14	122.84

COIL OUTER DIAMETER = 3.0 INCH
COIL THICKNESS = 0.150 INCH
TARGET THICKNESS = 0.045 INCH
TARGET CONDUCTIVITY = 60 PER CENT OF 5.8E7 MHOS/M

CALCULATED INDUCTANCES IN MICROHENRIES ARE:

COIL-TARGET GAP	FREQUENCY .5KHZ	1KHZ	3KHZ	10KHZ
0.025 INCH	162.48	112.73	83.48	78.31
0.050 INCH	171.31	125.98	99.64	95.04
0.075 INCH	179.43	138.08	114.33	110.22
0.100 INCH	186.91	149.15	127.68	124.00

COIL OUTER DIAMETER = 3.0 INCH
COIL THICKNESS = 0.150 INCH
TARGET THICKNESS = 0.055 INCH
TARGET CONDUCTIVITY = 60 PER CENT OF 5.8E7 MHOS/M

CALCULATED INDUCTANCES IN MICROHENRIES ARE:

COIL-TARGET GAP	FREQUENCY .5KHZ	1KHZ	3KHZ	10KHZ
0.025 INCH	147.52	105.62	84.07	79.47
0.050 INCH	157.63	119.56	100.20	96.10
0.075 INCH	166.91	132.27	114.85	111.18
0.100 INCH	175.42	143.89	128.18	124.88

COIL OUTER DIAMETER = 3.0 INCH
COIL THICKNESS = 0.150 INCH
TARGET THICKNESS = 0.065 INCH
TARGET CONDUCTIVITY = 60 PER CENT OF 5.8E7 MHOS/M

CALCULATED INDUCTANCES IN MICROHENRIES ARE:

COIL-TARGET GAP	FREQUENCY .5KHZ	1KHZ	3KHZ	10KHZ
0.025 INCH	136.90	101.76	85.16	80.14
0.050 INCH	147.94	116.09	101.21	96.71
0.075 INCH	158.06	129.16	115.78	111.73
0.100 INCH	167.35	141.08	129.04	125.38

Table 2-3b

Table 2-4

Effect of Coil Thickness

Computed by Henderson's Model

Coil Thickness Variable, 0.1 to 0.4 Inch

Coil Diameters 2.0 and 3.0 Inches

Coil-Target Gap 0.075 Inch

Target Thickness Variable, 0.075 to 0.065 Inch

Target Conductivity σ_u 60%

COIL OUTER DIAMETER = 2.0 INCH
COIL-TARGET GAP = 0.075 INCH
TARGET THICKNESS = 0.025 INCH
TARGET CONDUCTIVITY = 60 PER CENT OF 5.8E7 MHOS/M

CALCULATED INDUCTANCES IN MICROHENRIES ARE:

COIL THICK	FREQUENCY .5KHZ	1KHZ	3KHZ	10KHZ
0.100 INCH	182.62	151.93	108.20	95.20
0.150 INCH	177.41	149.73	111.08	99.79
0.200 INCH	172.50	147.46	113.15	103.28
0.250 INCH	167.88	145.15	114.57	105.91
0.300 INCH	163.52	142.83	115.47	107.83
0.400 INCH	155.53	138.25	116.12	110.09

COIL OUTER DIAMETER = 2.0 INCH
COIL-TARGET GAP = 0.075 INCH
TARGET THICKNESS = 0.035 INCH
TARGET CONDUCTIVITY = 60 PER CENT OF 5.8E7 MHOS/M

CALCULATED INDUCTANCES IN MICROHENRIES ARE:

COIL THICK	FREQUENCY .5KHZ	1KHZ	3KHZ	10KHZ
0.100 INCH	169.77	137.00	103.60	96.09
0.150 INCH	165.75	136.43	107.08	100.58
0.200 INCH	161.89	135.57	109.66	103.99
0.250 INCH	158.20	134.48	111.51	106.55
0.300 INCH	154.67	133.23	112.78	108.40
0.400 INCH	148.07	130.39	114.00	110.56

COIL OUTER DIAMETER = 2.0 INCH
COIL-TARGET GAP = 0.075 INCH
TARGET THICKNESS = 0.045 INCH
TARGET CONDUCTIVITY = 60 PER CENT OF 5.8E7 MHOS/M

CALCULATED INDUCTANCES IN MICROHENRIES ARE:

COIL THICK	FREQUENCY .5KHZ	1KHZ	3KHZ	10KHZ
0.100 INCH	159.17	127.69	102.32	97.16
0.150 INCH	156.20	128.20	105.99	101.53
0.200 INCH	153.27	128.26	108.72	104.83
0.250 INCH	150.38	127.96	110.70	107.29
0.300 INCH	147.56	127.40	112.08	109.08
0.400 INCH	142.15	125.67	113.46	111.10

COIL OUTER DIAMETER = 2.0 INCH
COIL-TARGET GAP = 0.075 INCH
TARGET THICKNESS = 0.055 INCH
TARGET CONDUCTIVITY = 60 PER CENT OF 5.8E7 MHOS/M

CALCULATED INDUCTANCES IN MICROHENRIES ARE:

COIL THICK	FREQUENCY .5KHZ	1KHZ	3KHZ	10KHZ
0.100 INCH	150.78	121.95	102.33	98.01
0.150 INCH	148.69	123.16	106.02	102.27
0.200 INCH	146.52	123.80	108.77	105.49
0.250 INCH	144.30	124.01	110.76	107.88
0.300 INCH	142.06	123.88	112.14	109.60
0.400 INCH	137.61	122.85	113.53	111.53

COIL OUTER DIAMETER = 2.0 INCH
COIL-TARGET GAP = 0.075 INCH
TARGET THICKNESS = 0.065 INCH
TARGET CONDUCTIVITY = 60 PER CENT OF 5.8E7 MHOS/M

CALCULATED INDUCTANCES IN MICROHENRIES ARE:

COIL THICK	FREQUENCY .5KHZ	1KHZ	3KHZ	10KHZ
0.100 INCH	144.29	118.47	102.88	98.50
0.150 INCH	142.90	120.11	106.53	102.71
0.200 INCH	141.34	121.12	109.22	105.88
0.250 INCH	139.65	121.65	111.17	108.23
0.300 INCH	137.87	121.78	112.52	109.91
0.400 INCH	134.17	121.18	113.85	111.77

Table 2-4a

COIL OUTER DIAMETER = 3.0 INCH
COIL-TARGET GAP = 0.075 INCH
TARGET THICKNESS = 0.025 INCH
TARGET CONDUCTIVITY = 60 PER CENT OF 5.8E7 MHOS/M

CALCULATED INDUCTANCES IN MICROHENRIES ARE:

COIL THICK	FREQUENCY .5KHZ	1KHZ	3KHZ	10KHZ
0.100 INCH	224.24	167.36	112.08	100.28
0.150 INCH	221.32	168.78	118.36	107.73
0.200 INCH	218.43	169.81	123.70	114.09
0.250 INCH	215.57	170.50	128.24	119.52
0.300 INCH	212.75	170.90	132.09	124.15
0.400 INCH	207.25	170.98	138.04	131.41

COIL OUTER DIAMETER = 3.0 INCH
COIL-TARGET GAP = 0.075 INCH
TARGET THICKNESS = 0.035 INCH
TARGET CONDUCTIVITY = 60 PER CENT OF 5.8E7 MHOS/M

CALCULATED INDUCTANCES IN MICROHENRIES ARE:

COIL THICK	FREQUENCY .5KHZ	1KHZ	3KHZ	10KHZ
0.100 INCH	198.06	145.52	108.19	101.61
0.150 INCH	197.06	148.78	114.86	108.95
0.200 INCH	195.90	151.45	120.55	115.21
0.250 INCH	194.62	153.61	125.39	120.55
0.300 INCH	193.24	155.34	129.50	125.10
0.400 INCH	190.24	157.70	135.90	132.23

COIL OUTER DIAMETER = 3.0 INCH
COIL-TARGET GAP = 0.075 INCH
TARGET THICKNESS = 0.045 INCH
TARGET CONDUCTIVITY = 60 PER CENT OF 5.8E7 MHOS/M

CALCULATED INDUCTANCES IN MICROHENRIES ARE:

COIL THICK	FREQUENCY .5KHZ	1KHZ	3KHZ	10KHZ
0.100 INCH	178.95	133.78	107.57	103.00
0.150 INCH	179.43	138.08	114.33	110.22
0.200 INCH	179.62	141.68	120.09	116.38
0.250 INCH	179.55	144.67	124.99	121.62
0.300 INCH	179.26	147.13	129.15	126.09
0.400 INCH	178.17	150.74	135.63	133.07

COIL OUTER DIAMETER = 3.0 INCH
COIL-TARGET GAP = 0.075 INCH
TARGET THICKNESS = 0.055 INCH
TARGET CONDUCTIVITY = 60 PER CENT OF 5.8E7 MHOS/M

CALCULATED INDUCTANCES IN MICROHENRIES ARE:

COIL THICK	FREQUENCY .5KHZ	1KHZ	3KHZ	10KHZ
0.100 INCH	165.32	127.39	108.12	104.05
0.150 INCH	166.91	132.27	114.85	111.18
0.200 INCH	168.09	136.39	120.58	117.26
0.250 INCH	168.91	139.84	125.46	122.43
0.300 INCH	169.43	142.72	129.59	126.83
0.400 INCH	169.73	147.03	136.02	133.71

COIL OUTER DIAMETER = 3.0 INCH
COIL-TARGET GAP = 0.075 INCH
TARGET THICKNESS = 0.065 INCH
TARGET CONDUCTIVITY = 60 PER CENT OF 5.8E7 MHOS/M

CALCULATED INDUCTANCES IN MICROHENRIES ARE:

COIL THICK	FREQUENCY .5KHZ	1KHZ	3KHZ	10KHZ
0.100 INCH	155.66	123.94	109.13	104.66
0.150 INCH	158.06	129.16	115.78	111.73
0.200 INCH	159.97	133.57	121.44	117.76
0.250 INCH	161.45	137.28	126.25	122.90
0.300 INCH	162.56	140.38	130.33	127.26
0.400 INCH	163.86	145.08	136.66	134.07

Table 2-4b

Table 2-5, Graph 2-5

Double Target Results

By Henderson's Model

Coil Thickness 0.15 Inch

Coil Diameter 2.5 Inches

Coil-Doubler Gap 0.075 Inch

Doubler Thickness Variable, 0.035 to 0.055 Inch

Doubler Conductivity σ_u , 60%

Skin Thickness Variable, 0.015 to 0.045 Inch

Skin Conductivity σ_u 30%

****

COIL OUTER DIAMETER = 2.5 INCH
COIL-DOUBLER GAP = 0.075 INCH
COIL THICKNESS = 0.15 INCH
TARGET CONDUCTIVITY = 30 PER CENT OF 5.8E7 MHOS/M
DOUBLER CONDUCTIVITY = 60 PER CENT OF 5.8E7 MHOS/M

TARGET THICKNESS = 0.015 INCHES

CALCULATED INDUCTANCES IN MICROHENRIES ARE:

	FREQUENCY			
DOUBLER THICK	1KHZ	2KHZ	3KHZ	4KHZ
0.035 INCH	136.41	116.07	110.85	108.83
0.045 INCH	129.90	114.59	110.93	109.50
0.055 INCH	126.18	114.35	111.58	110.43

****
****

COIL OUTER DIAMETER = 2.5 INCH
COIL-DOUBLER GAP = 0.075 INCH
COIL THICKNESS = 0.15 INCH
TARGET CONDUCTIVITY = 30 PER CENT OF 5.8E7 MHOS/M
DOUBLER CONDUCTIVITY = 60 PER CENT OF 5.8E7 MHOS/M

TARGET THICKNESS = 0.025 INCHES

CALCULATED INDUCTANCES IN MICROHENRIES ARE:

	FREQUENCY			
DOUBLER THICK	1KHZ	2KHZ	3KHZ	4KHZ
0.035 INCH	132.91	115.25	110.89	109.20
0.045 INCH	127.91	114.44	111.27	109.99
0.055 INCH	125.08	114.51	112.02	110.91

****
****

COIL OUTER DIAMETER = 2.5 INCH
COIL-DOUBLER GAP = 0.075 INCH
COIL THICKNESS = 0.15 INCH
TARGET CONDUCTIVITY = 30 PER CENT OF 5.8E7 MHOS/M
DOUBLER CONDUCTIVITY = 60 PER CENT OF 5.8E7 MHOS/M

TARGET THICKNESS = 0.035 INCHES

CALCULATED INDUCTANCES IN MICROHENRIES ARE:

	FREQUENCY			
DOUBLER THICK	1KHZ	2KHZ	3KHZ	4KHZ
0.035 INCH	130.35	114.90	111.18	109.70
0.045 INCH	126.48	114.53	111.71	110.51
0.055 INCH	124.33	114.80	112.49	111.37

****
****

COIL OUTER DIAMETER = 2.5 INCH
COIL-DOUBLER GAP = 0.075 INCH
COIL THICKNESS = 0.15 INCH
TARGET CONDUCTIVITY = 30 PER CENT OF 5.8E7 MHOS/M
DOUBLER CONDUCTIVITY = 60 PER CENT OF 5.8E7 MHOS/M

TARGET THICKNESS = 0.045 INCHES

CALCULATED INDUCTANCES IN MICROHENRIES ARE:

	FREQUENCY			
DOUBLER THICK	1KHZ	2KHZ	3KHZ	4KHZ
0.035 INCH	128.51	114.89	111.63	110.28
0.045 INCH	125.49	114.78	112.20	111.02
0.055 INCH	123.85	115.17	112.96	111.78

****

Table 2-5a

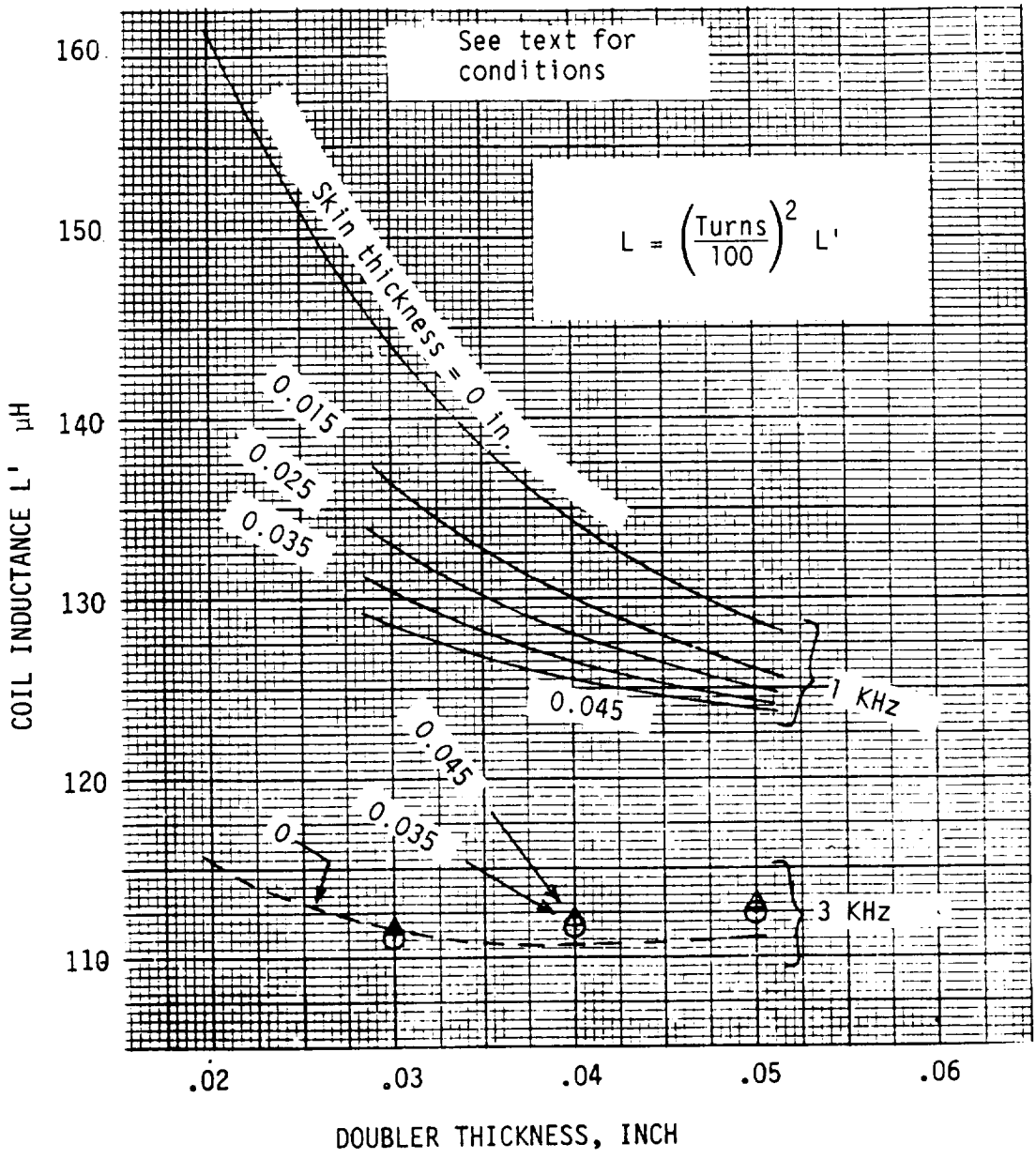

Graph 2-5a Effect of Doubler - Skin Combinations on Coil Inductance

C. Tables and Graphs of the Coil Resistance Contributed by the Target

The increase in coil resistance, due to the presence of the target was calculated by Dr. Henderson, using the procedure outlined in Sec. B-2 (Eq. 2-22). The calculations assume a uniform current distribution, and this current is replaced by three current sheets, as was explained in the discussion of Figure 2-36. All calculations assumed a 100-turn coil for which the resistance increase is being denoted as ΔR^1. Correction to any other number of turns, N, is accomplished by multiplying ΔR^1 by $(N/100)^2$. Also, all calculations assumed an inner coil diameter of 0.25 inch.

Several tables (and accompanying graphs) are presented, and each assumes certain fixed design parameters. Information on the fixed and variable parameters is summarized on the page preceding each set of tables. Tables 2-6a through 2-6e were intended primarily for design purposes. The corresponding graphs, prepared from the tables, are especially helpful when interpolations with frequency are required. The abscissa on the graphs is the ratio of the target thickness to electrical skin depth, that is, t/δ. Here δ is calculated from the formula

$$\delta = \frac{0.0823}{\sqrt{f_{KHz}\sigma_u}} \text{ inch},$$

where σ_u is the electrical conductivity of the target divided by the conductivity of copper. The use of the graphs is illustrated in Section VII, where design examples are considered.

Table 2-6, Graph 2-6

Main Design Data

Coil Thickness 0.15 Inch

Coil Diameters Variable, 1.5 to 3.5 Inches

Coil-Target Gap 0.075 Inch

Target Thickness Variable; 0.025 to 0.065 Inch

Target Conductivity σ_u Variable, 30% to 100%

COIL OUTER DIAMETER = 1.5 INCH
COIL-TARGET GAP = 0.075 INCH
COIL THICKNESS = 0.15 INCH
TARGET CONDUCTIVITY = 30 PER CENT OF 5.8E7 MHOS/M

CALCULATED RESISTANCES IN MILLOHMS ARE:

TARGET THICK	FREQUENCY .5KHZ	1KHZ	3KHZ	10KHZ
0.025 INCH	45.19	146.52	579.42	1058.97
0.035 INCH	57.01	168.63	526.33	799.60
0.045 INCH	65.85	179.01	466.24	653.09
0.055 INCH	72.23	182.00	413.05	570.67
0.065 INCH	76.67	180.50	369.33	527.99

COIL OUTER DIAMETER = 1.5 INCH
COIL-TARGET GAP = 0.075 INCH
COIL THICKNESS = 0.15 INCH
TARGET CONDUCTIVITY = 40 PER CENT OF 5.8E7 MHOS/M

CALCULATED RESISTANCES IN MILLOHMS ARE:

TARGET THICK	FREQUENCY .5KHZ	1KHZ	3KHZ	10KHZ
0.025 INCH	56.31	168.99	544.06	834.72
0.035 INCH	68.82	184.35	463.90	626.11
0.045 INCH	77.11	187.01	395.42	519.85
0.055 INCH	82.24	183.03	342.57	468.99
0.065 INCH	85.07	175.87	303.04	450.43

COIL OUTER DIAMETER = 1.5 INCH
COIL-TARGET GAP = 0.075 INCH
COIL THICKNESS = 0.15 INCH
TARGET CONDUCTIVITY = 50 PER CENT OF 5.8E7 MHOS/M

CALCULATED RESISTANCES IN MILLOHMS ARE:

TARGET THICK	FREQUENCY .5KHZ	1KHZ	3KHZ	10KHZ
0.025 INCH	65.60	182.99	498.09	687.05
0.035 INCH	77.74	190.44	406.96	518.33
0.045 INCH	84.69	186.01	339.16	440.90
0.055 INCH	88.07	176.65	290.95	411.27
0.065 INCH	89.07	165.74	257.18	406.95

COIL OUTER DIAMETER = 1.5 INCH
COIL-TARGET GAP = 0.075 INCH
COIL THICKNESS = 0.15 INCH
TARGET CONDUCTIVITY = 60 PER CENT OF 5.8E7 MHOS/M

CALCULATED RESISTANCES IN MILLOHMS ARE:

TARGET THICK	FREQUENCY .5KHZ	1KHZ	3KHZ	10KHZ
0.025 INCH	73.26	190.85	452.82	584.15
0.035 INCH	84.31	190.61	359.34	446.21
0.045 INCH	89.50	180.40	295.64	390.08
0.055 INCH	91.00	167.29	252.93	375.01
0.065 INCH	90.25	154.19	224.65	378.66

COIL OUTER DIAMETER = 1.5 INCH
COIL-TARGET GAP = 0.075 INCH
COIL THICKNESS = 0.15 INCH
TARGET CONDUCTIVITY = 100 PER CENT OF 5.8E7 MHOS/M

CALCULATED RESISTANCES IN MILLOHMS ARE:

TARGET THICK	FREQUENCY .5KHZ	1KHZ	3KHZ	10KHZ
0.025 INCH	91.49	190.04	317.69	372.52
0.035 INCH	95.22	168.54	239.88	307.37
0.045 INCH	93.00	147.05	195.93	297.27
0.055 INCH	88.32	129.06	171.20	305.36
0.065 INCH	82.87	114.81	158.40	313.54

Table 2-6a

COIL OUTER DIAMETER = 2.0 INCH
COIL-TARGET GAP = 0.075 INCH
COIL THICKNESS = 0.15 INCH
TARGET CONDUCTIVITY = 30 PER CENT OF 5.8E7 MHOS/M

CALCULATED RESISTANCES IN MILLOHMS ARE:

TARGET THICK	FREQUENCY .5KHZ	1KHZ	3KHZ	10KHZ
0.025 INCH	83.78	255.45	847.90	1319.06
0.035 INCH	103.57	282.55	729.80	981.30
0.045 INCH	117.28	289.79	624.64	797.44
0.055 INCH	126.27	286.07	541.13	696.33
0.065 INCH	131.71	276.67	476.73	645.37

COIL OUTER DIAMETER = 2.0 INCH
COIL-TARGET GAP = 0.075 INCH
COIL THICKNESS = 0.15 INCH
TARGET CONDUCTIVITY = 40 PER CENT OF 5.8E7 MHOS/M

CALCULATED RESISTANCES IN MILLOHMS ARE:

TARGET THICK	FREQUENCY .5KHZ	1KHZ	3KHZ	10KHZ
0.025 INCH	102.25	283.74	756.79	1023.30
0.035 INCH	121.52	295.13	615.60	761.41
0.045 INCH	132.67	287.97	510.80	631.32
0.055 INCH	138.19	273.11	435.57	570.56
0.065 INCH	139.92	255.81	381.69	549.72

COIL OUTER DIAMETER = 2.0 INCH
COIL-TARGET GAP = 0.075 INCH
COIL THICKNESS = 0.15 INCH
TARGET CONDUCTIVITY = 50 PER CENT OF 5.8E7 MHOS/M

CALCULATED RESISTANCES IN MILLOHMS ARE:

TARGET THICK	FREQUENCY .5KHZ	1KHZ	3KHZ	10KHZ
0.025 INCH	116.69	296.94	668.70	835.50
0.035 INCH	133.61	293.22	525.25	627.65
0.045 INCH	141.14	275.03	428.86	534.28
0.055 INCH	142.85	253.17	363.86	499.88
0.065 INCH	141.07	231.89	319.77	496.35

COIL OUTER DIAMETER = 2.0 INCH
COIL-TARGET GAP = 0.075 INCH
COIL THICKNESS = 0.15 INCH
TARGET CONDUCTIVITY = 60 PER CENT OF 5.8E7 MHOS/M

CALCULATED RESISTANCES IN MILLOHMS ARE:

TARGET THICK	FREQUENCY .5KHZ	1KHZ	3KHZ	10KHZ
0.025 INCH	127.73	300.38	592.78	707.14
0.035 INCH	141.28	283.94	455.41	539.12
0.045 INCH	144.89	258.13	368.90	472.29
0.055 INCH	143.03	232.39	313.22	455.66
0.065 INCH	138.33	209.56	277.29	461.56

COIL OUTER DIAMETER = 2.0 INCH
COIL-TARGET GAP = 0.075 INCH
COIL THICKNESS = 0.15 INCH
TARGET CONDUCTIVITY = 100 PER CENT OF 5.8E7 MHOS/M

CALCULATED RESISTANCES IN MILLOHMS ARE:

TARGET THICK	FREQUENCY .5KHZ	1KHZ	3KHZ	10KHZ
0.025 INCH	148.47	272.87	395.72	447.97
0.035 INCH	146.61	229.75	294.39	370.49
0.045 INCH	137.52	194.17	239.23	359.70
0.055 INCH	126.59	167.04	208.90	370.50
0.065 INCH	115.95	146.71	193.61	380.81

Table 2-6b

COIL OUTER DIAMETER = 2.5 INCH
COIL-TARGET GAP = 0.075 INCH
COIL THICKNESS = 0.15 INCH
TARGET CONDUCTIVITY = 30 PER CENT OF 5.8E7 MHOS/M

CALCULATED RESISTANCES IN MILLOHMS ARE:

TARGET THICK	FREQUENCY .5KHZ	1KHZ	3KHZ	10KHZ
0.025 INCH	131.95	378.61	1080.06	1510.94
0.035 INCH	159.57	403.00	893.24	1115.41
0.045 INCH	176.96	400.35	746.96	904.38
0.055 INCH	186.91	384.98	638.06	789.85
0.065 INCH	191.56	364.43	557.25	733.16

COIL OUTER DIAMETER = 2.5 INCH
COIL-TARGET GAP = 0.075 INCH
COIL THICKNESS = 0.15 INCH
TARGET CONDUCTIVITY = 40 PER CENT OF 5.8E7 MHOS/M

CALCULATED RESISTANCES IN MILLOHMS ARE:

TARGET THICK	FREQUENCY .5KHZ	1KHZ	3KHZ	10KHZ
0.025 INCH	157.68	405.95	928.78	1162.21
0.035 INCH	182.07	404.21	731.86	861.44
0.045 INCH	193.68	381.33	597.34	714.11
0.055 INCH	197.16	352.39	504.78	646.35
0.065 INCH	195.63	323.54	440.13	624.16

COIL OUTER DIAMETER = 2.5 INCH
COIL-TARGET GAP = 0.075 INCH
COIL THICKNESS = 0.15 INCH
TARGET CONDUCTIVITY = 50 PER CENT OF 5.8E7 MHOS/M

CALCULATED RESISTANCES IN MILLOHMS ARE:

TARGET THICK	FREQUENCY .5KHZ	1KHZ	3KHZ	10KHZ
0.025 INCH	176.32	411.97	801.18	944.96
0.035 INCH	195.10	388.60	613.94	708.60
0.045 INCH	200.09	352.63	495.44	603.76
0.055 INCH	197.47	316.91	417.89	566.11
0.065 INCH	190.90	285.24	366.26	563.44

COIL OUTER DIAMETER = 2.5 INCH
COIL-TARGET GAP = 0.075 INCH
COIL THICKNESS = 0.15 INCH
TARGET CONDUCTIVITY = 60 PER CENT OF 5.8E7 MHOS/M

CALCULATED RESISTANCES IN MILLOHMS ARE:

TARGET THICK	FREQUENCY .5KHZ	1KHZ	3KHZ	10KHZ
0.025 INCH	189.30	405.85	698.94	797.93
0.035 INCH	201.50	366.43	526.73	608.00
0.045 INCH	200.17	322.91	423.09	533.52
0.055 INCH	192.49	284.55	357.89	516.00
0.065 INCH	182.21	252.80	316.44	523.78

COIL OUTER DIAMETER = 2.5 INCH
COIL-TARGET GAP = 0.075 INCH
COIL THICKNESS = 0.15 INCH
TARGET CONDUCTIVITY = 100 PER CENT OF 5.8E7 MHOS/M

CALCULATED RESISTANCES IN MILLOHMS ARE:

TARGET THICK	FREQUENCY .5KHZ	1KHZ	3KHZ	10KHZ
0.025 INCH	205.98	342.64	453.28	503.81
0.035 INCH	194.30	277.96	334.62	417.42
0.045 INCH	176.31	230.09	271.31	406.30
0.055 INCH	158.46	195.55	236.95	419.24
0.065 INCH	142.62	170.51	219.95	431.16

Table 2-6c

COIL OUTER DIAMETER = 3.0 INCH
COIL-TARGET GAP = 0.075 INCH
COIL THICKNESS = 0.15 INCH
TARGET CONDUCTIVITY = 30 PER CENT OF 5.8E7 MHOS/M

CALCULATED RESISTANCES IN MILLOHMS ARE:

TARGET THICK	FREQUENCY .5KHZ	1KHZ	3KHZ	10KHZ
0.025 INCH	187.76	507.94	1273.44	1657.59
0.035 INCH	221.99	521.61	1022.76	1218.29
0.045 INCH	241.12	503.63	841.85	986.72
0.055 INCH	249.93	473.54	712.65	862.10
0.065 INCH	251.90	440.38	619.08	801.21

COIL OUTER DIAMETER = 3.0 INCH
COIL-TARGET GAP = 0.075 INCH
COIL THICKNESS = 0.15 INCH
TARGET CONDUCTIVITY = 40 PER CENT OF 5.8E7 MHOS/M

CALCULATED RESISTANCES IN MILLOHMS ARE:

TARGET THICK	FREQUENCY .5KHZ	1KHZ	3KHZ	10KHZ
0.025 INCH	219.75	527.22	1065.66	1268.60
0.035 INCH	246.60	504.99	821.74	938.36
0.045 INCH	255.88	463.10	663.71	777.99
0.055 INCH	254.96	419.18	557.83	705.02
0.065 INCH	248.41	379.03	485.02	681.95

COIL OUTER DIAMETER = 3.0 INCH
COIL-TARGET GAP = 0.075 INCH
COIL THICKNESS = 0.15 INCH
TARGET CONDUCTIVITY = 50 PER CENT OF 5.8E7 MHOS/M

CALCULATED RESISTANCES IN MILLOHMS ARE:

TARGET THICK	FREQUENCY .5KHZ	1KHZ	3KHZ	10KHZ
0.025 INCH	240.94	520.71	904.23	1028.95
0.035 INCH	257.97	472.43	681.93	770.95
0.045 INCH	257.44	417.56	546.41	657.44
0.055 INCH	248.43	368.56	459.35	617.45
0.065 INCH	235.78	327.58	402.04	615.57

COIL OUTER DIAMETER = 3.0 INCH
COIL-TARGET GAP = 0.075 INCH
COIL THICKNESS = 0.15 INCH
TARGET CONDUCTIVITY = 60 PER CENT OF 5.8E7 MHOS/M

CALCULATED RESISTANCES IN MILLOHMS ARE:

TARGET THICK	FREQUENCY .5KHZ	1KHZ	3KHZ	10KHZ
0.025 INCH	253.97	501.54	780.62	867.68
0.035 INCH	260.81	436.22	581.29	661.11
0.045 INCH	251.81	375.44	464.62	580.87
0.055 INCH	236.77	325.81	392.22	562.79
0.065 INCH	220.19	286.52	346.64	572.12

COIL OUTER DIAMETER = 3.0 INCH
COIL-TARGET GAP = 0.075 INCH
COIL THICKNESS = 0.15 INCH
TARGET CONDUCTIVITY = 100 PER CENT OF 5.8E7 MHOS/M

CALCULATED RESISTANCES IN MILLOHMS ARE:

TARGET THICK	FREQUENCY .5KHZ	1KHZ	3KHZ	10KHZ
0.025 INCH	260.35	399.68	497.28	546.83
0.035 INCH	236.21	315.74	365.49	453.67
0.045 INCH	208.78	257.79	296.02	442.40
0.055 INCH	184.28	217.44	258.63	457.04
0.065 INCH	163.79	188.77	240.36	470.23

Table 2-6d

COIL OUTER DIAMETER = 3.5 INCH
COIL-TARGET GAP = 0.075 INCH
COIL THICKNESS = 0.15 INCH
TARGET CONDUCTIVITY = 30 PER CENT OF 5.8E7 MHOS/M

CALCULATED RESISTANCES IN MILLOHMS ARE:

TARGET THICK	FREQUENCY .5KHZ	1KHZ	3KHZ	10KHZ
0.025 INCH	249.43	637.74	1432.92	1773.31
0.035 INCH	288.31	633.74	1126.23	1299.78
0.045 INCH	306.89	596.78	916.88	1052.13
0.055 INCH	312.49	550.60	771.50	919.64
0.065 INCH	310.08	504.72	667.91	855.54

COIL OUTER DIAMETER = 3.5 INCH
COIL-TARGET GAP = 0.075 INCH
COIL THICKNESS = 0.15 INCH
TARGET CONDUCTIVITY = 40 PER CENT OF 5.8E7 MHOS/M

CALCULATED RESISTANCES IN MILLOHMS ARE:

TARGET THICK	FREQUENCY .5KHZ	1KHZ	3KHZ	10KHZ
0.025 INCH	286.03	642.72	1175.28	1352.77
0.035 INCH	312.24	595.09	892.69	999.43
0.045 INCH	316.53	533.06	716.04	828.83
0.055 INCH	309.32	474.67	599.74	751.83
0.065 INCH	296.55	424.25	520.56	728.15

COIL OUTER DIAMETER = 3.5 INCH
COIL-TARGET GAP = 0.075 INCH
COIL THICKNESS = 0.15 INCH
TARGET CONDUCTIVITY = 50 PER CENT OF 5.8E7 MHOS/M

CALCULATED RESISTANCES IN MILLOHMS ARE:

TARGET THICK	FREQUENCY .5KHZ	1KHZ	3KHZ	10KHZ
0.025 INCH	307.74	619.89	985.79	1095.51
0.035 INCH	319.48	544.38	735.50	820.50
0.045 INCH	311.04	471.26	586.65	700.20
0.055 INCH	294.31	410.35	492.18	658.43
0.065 INCH	275.01	361.43	430.45	657.26

COIL OUTER DIAMETER = 3.5 INCH
COIL-TARGET GAP = 0.075 INCH
COIL THICKNESS = 0.15 INCH
TARGET CONDUCTIVITY = 60 PER CENT OF 5.8E7 MHOS/M

CALCULATED RESISTANCES IN MILLOHMS ARE:

TARGET THICK	FREQUENCY .5KHZ	1KHZ	3KHZ	10KHZ
0.025 INCH	318.87	585.82	844.99	923.02
0.035 INCH	316.87	494.41	624.31	703.36
0.045 INCH	298.39	417.97	497.46	618.62
0.055 INCH	275.30	358.74	419.46	600.17
0.065 INCH	252.36	313.26	370.66	610.79

COIL OUTER DIAMETER = 3.5 INCH
COIL-TARGET GAP = 0.075 INCH
COIL THICKNESS = 0.15 INCH
TARGET CONDUCTIVITY = 100 PER CENT OF 5.8E7 MHOS/M

CALCULATED RESISTANCES IN MILLOHMS ARE:

TARGET THICK	FREQUENCY .5KHZ	1KHZ	3KHZ	10KHZ
0.025 INCH	309.94	446.13	531.99	581.03
0.035 INCH	272.19	345.75	389.93	482.54
0.045 INCH	235.63	279.65	315.64	471.20
0.055 INCH	205.18	234.71	275.89	487.23
0.065 INCH	180.72	203.21	256.66	501.44

Table 2-6e

COIL THICKNESS = 0.15 INCH
COIL - TARGET GAP = 0.075 INCH
t = TARGET THICKNESS, INCH
δ = SKIN DEPTH, INCH
σ = TARGET CONDUCTIVITY, RATIO TO COPPER

ORIGINAL PAGE IS
OF POOR QUALITY

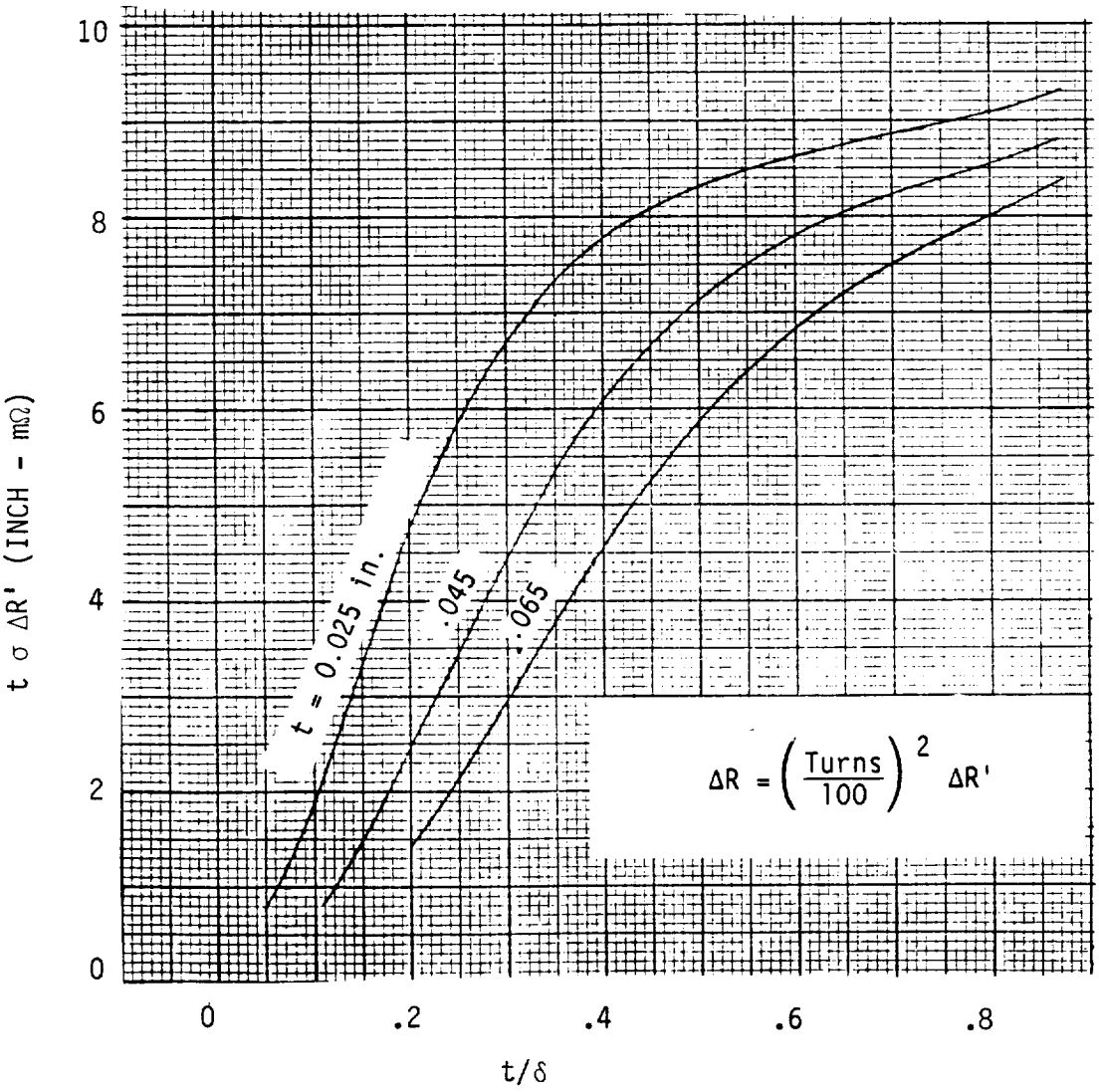

Graph 2-6a Curves for Finding ΔR with a 1.5 Inch Diameter Coil

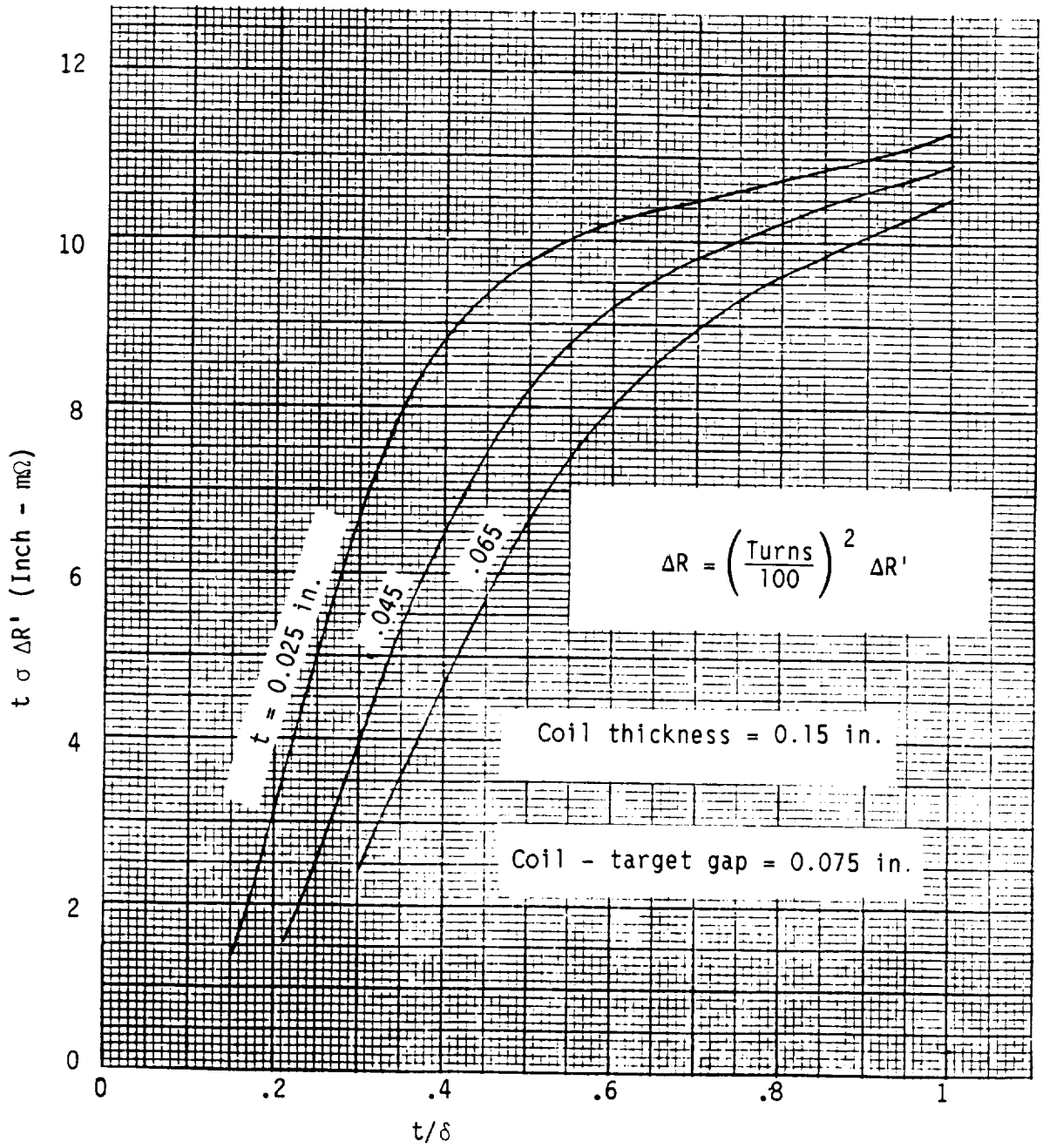

Graph 2-6b Curves for Finding ΔR with a 2.0 Inch Diameter Coil

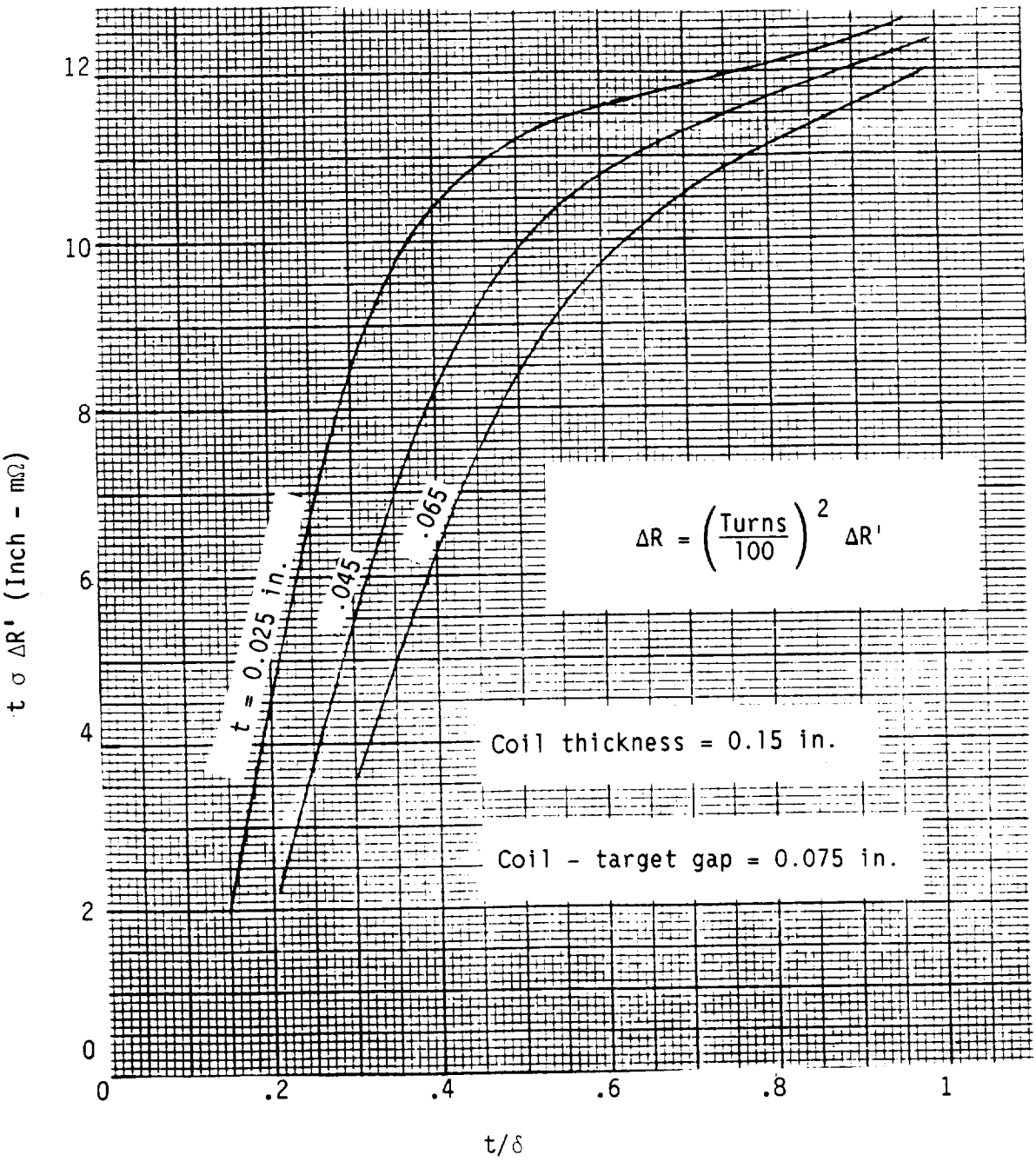

Graph 2-6c Curves for Finding ΔR with a 2.5 Inch Diameter Coil

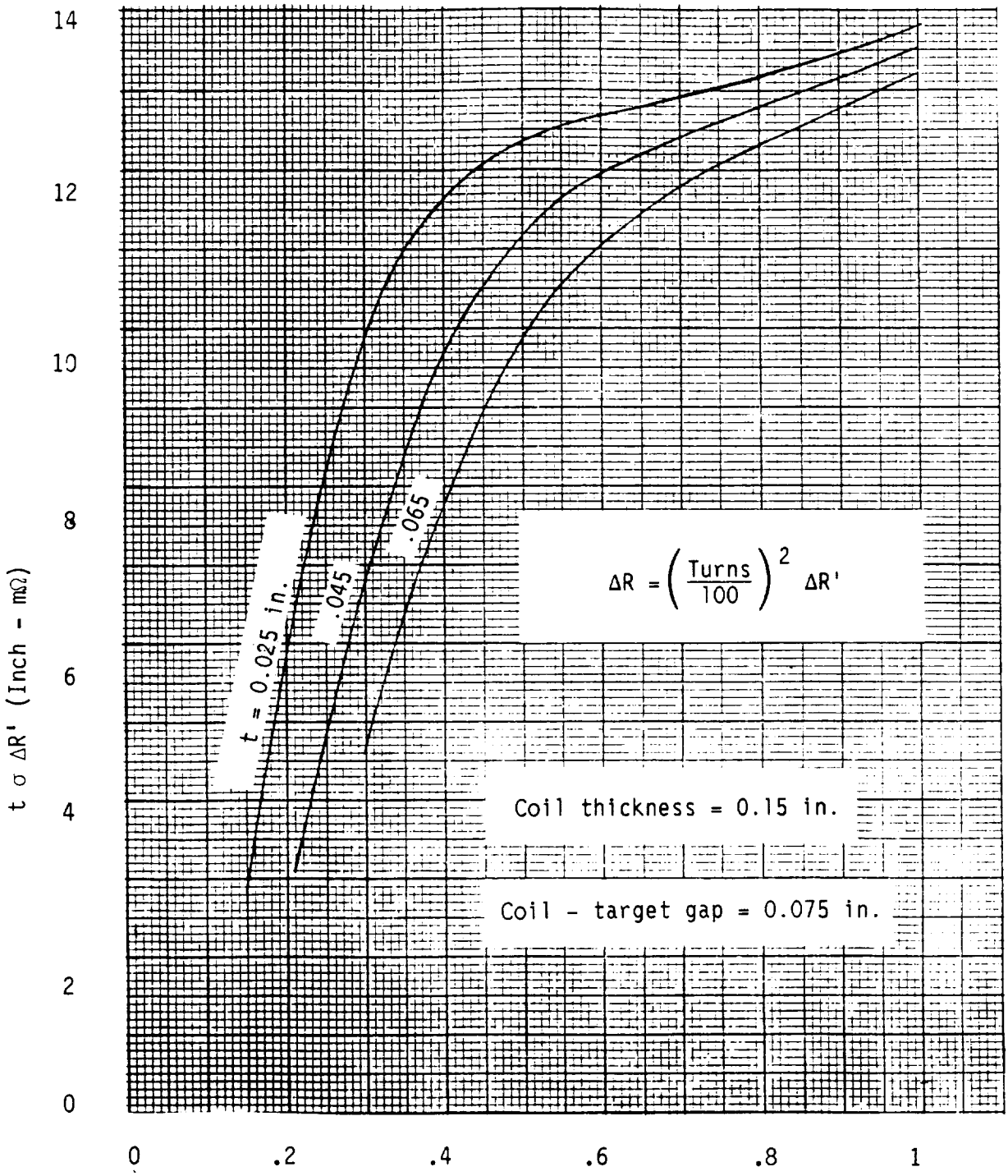

Graph 2-6d Curves for Finding ΔR with a 3.0 Inch Diameter Coil

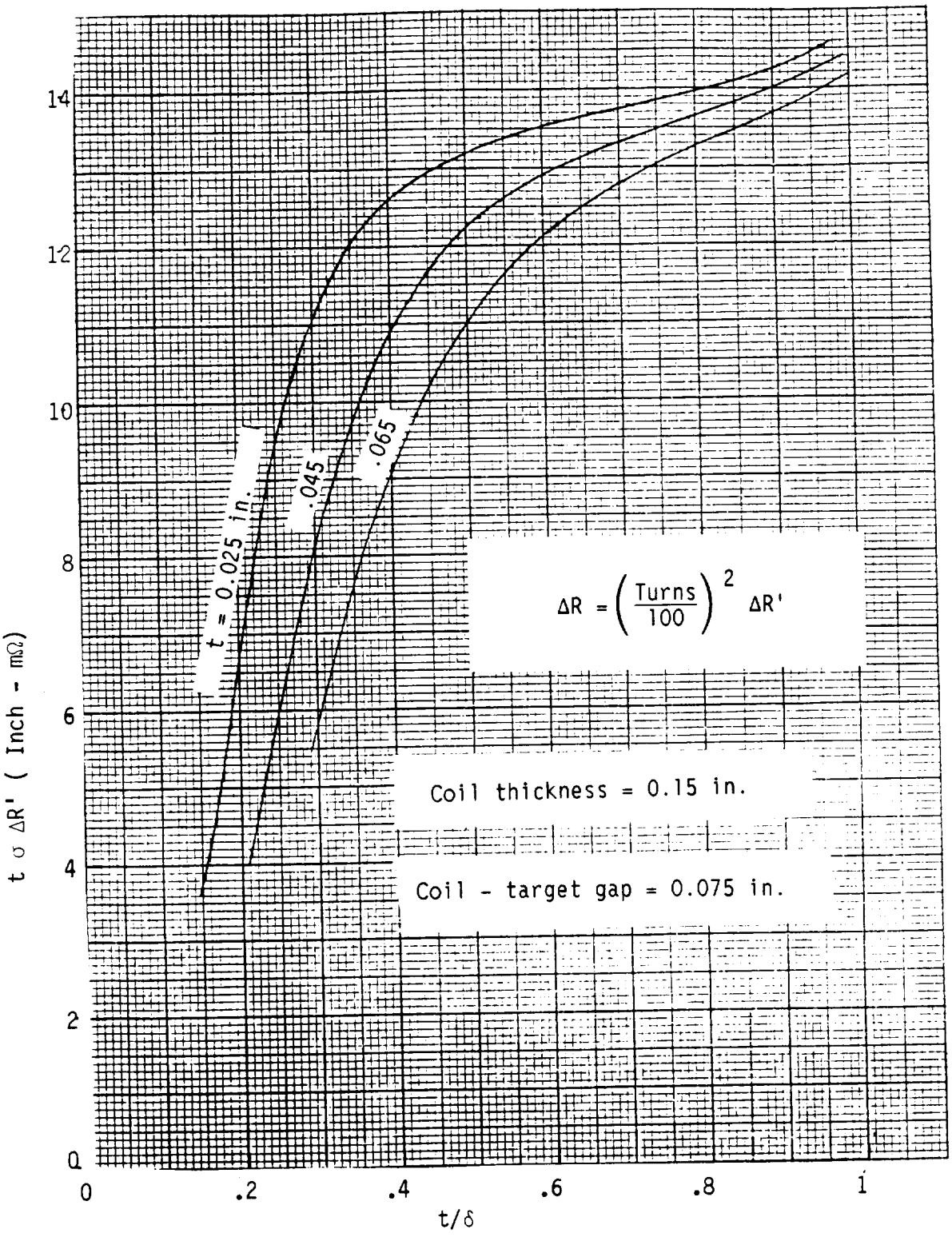

Graph 2-6e Curves for Finding ΔR with a 3.5 Inch Diameter Coil

Table 2-7

Effect of Coil-Target Gap

Coil Thickness 0.15 Inch

Coil Diameters 2.0 and 3.0 Inches

Coil-Target Gap Variable, 0.025 to 0.10 Inch

Target Thickness Variable, 0.025 to 0.065 Inch

Target Conductivity σ_u 60%

COIL OUTER DIAMETER = 2.0 INCH
COIL THICKNESS = 0.150 INCH
TARGET THICKNESS = 0.025 INCH
TARGET CONDUCTIVITY = 60 PER CENT OF 5.8E7 MHOS/M

CALCULATED RESISTANCES IN MILLOHMS ARE:

COIL-TARGET GAP	FREQUENCY .5KHZ	1KHZ	3KHZ	10KHZ
0.025 INCH	158.38	380.71	774.01	935.04
0.050 INCH	142.08	337.81	676.47	811.74
0.075 INCH	127.73	300.38	592.78	707.14
0.100 INCH	115.06	267.67	520.73	617.90

COIL OUTER DIAMETER = 2.0 INCH
COIL THICKNESS = 0.150 INCH
TARGET THICKNESS = 0.035 INCH
TARGET CONDUCTIVITY = 60 PER CENT OF 5.8E7 MHOS/M

CALCULATED RESISTANCES IN MILLOHMS ARE:

COIL-TARGET GAP	FREQUENCY .5KHZ	1KHZ	3KHZ	10KHZ
0.025 INCH	176.83	363.49	597.44	713.24
0.050 INCH	157.89	320.90	520.87	619.00
0.075 INCH	141.28	283.94	455.41	539.12
0.100 INCH	126.67	251.78	399.21	471.00

COIL OUTER DIAMETER = 2.0 INCH
COIL THICKNESS = 0.150 INCH
TARGET THICKNESS = 0.045 INCH
TARGET CONDUCTIVITY = 60 PER CENT OF 5.8E7 MHOS/M

CALCULATED RESISTANCES IN MILLOHMS ARE:

COIL-TARGET GAP	FREQUENCY .5KHZ	1KHZ	3KHZ	10KHZ
0.025 INCH	182.71	332.64	485.09	624.64
0.050 INCH	162.53	292.69	422.40	542.19
0.075 INCH	144.89	258.13	368.90	472.29
0.100 INCH	129.43	228.16	323.05	412.68

COIL OUTER DIAMETER = 2.0 INCH
COIL THICKNESS = 0.150 INCH
TARGET THICKNESS = 0.055 INCH
TARGET CONDUCTIVITY = 60 PER CENT OF 5.8E7 MHOS/M

CALCULATED RESISTANCES IN MILLOHMS ARE:

COIL-TARGET GAP	FREQUENCY .5KHZ	1KHZ	3KHZ	10KHZ
0.025 INCH	181.42	300.83	412.38	602.28
0.050 INCH	160.91	264.09	358.84	522.94
0.075 INCH	143.03	232.39	313.22	455.66
0.100 INCH	127.40	204.96	274.15	398.26

COIL OUTER DIAMETER = 2.0 INCH
COIL THICKNESS = 0.150 INCH
TARGET THICKNESS = 0.065 INCH
TARGET CONDUCTIVITY = 60 PER CENT OF 5.8E7 MHOS/M

CALCULATED RESISTANCES IN MILLOHMS ARE:

COIL-TARGET GAP	FREQUENCY .5KHZ	1KHZ	3KHZ	10KHZ
0.025 INCH	176.28	272.14	365.29	609.74
0.050 INCH	155.99	238.52	317.76	529.58
0.075 INCH	138.33	209.56	277.29	461.56
0.100 INCH	122.93	184.54	242.66	403.52

Table 2-7a

COIL OUTER DIAMETER = 3.0 INCH
COIL THICKNESS = 0.150 INCH
TARGET THICKNESS = 0.025 INCH
TARGET CONDUCTIVITY = 60 PER CENT OF 5.8E7 MHOS/M

CALCULATED RESISTANCES IN MILLOHMS ARE:

COIL-TARGET GAP	FREQUENCY .5KHZ	1KHZ	3KHZ	10KHZ
0.025 INCH	297.15	595.81	943.52	1056.77
0.050 INCH	274.57	546.33	857.50	956.44
0.075 INCH	253.97	501.54	780.62	867.68
0.100 INCH	235.15	460.91	711.69	788.73

COIL OUTER DIAMETER = 3.0 INCH
COIL THICKNESS = 0.150 INCH
TARGET THICKNESS = 0.035 INCH
TARGET CONDUCTIVITY = 60 PER CENT OF 5.8E7 MHOS/M

CALCULATED RESISTANCES IN MILLOHMS ARE:

COIL-TARGET GAP	FREQUENCY .5KHZ	1KHZ	3KHZ	10KHZ
0.025 INCH	307.31	521.41	704.53	805.42
0.050 INCH	282.96	476.63	639.36	728.82
0.075 INCH	260.81	436.22	581.29	661.11
0.100 INCH	240.64	399.71	529.37	600.92

COIL OUTER DIAMETER = 3.0 INCH
COIL THICKNESS = 0.150 INCH
TARGET THICKNESS = 0.045 INCH
TARGET CONDUCTIVITY = 60 PER CENT OF 5.8E7 MHOS/M

CALCULATED RESISTANCES IN MILLOHMS ARE:

COIL-TARGET GAP	FREQUENCY .5KHZ	1KHZ	3KHZ	10KHZ
0.025 INCH	298.24	450.46	563.91	707.49
0.050 INCH	273.90	410.97	511.36	640.29
0.075 INCH	251.81	375.44	464.62	580.87
0.100 INCH	231.75	343.39	422.89	528.04

COIL OUTER DIAMETER = 3.0 INCH
COIL THICKNESS = 0.150 INCH
TARGET THICKNESS = 0.055 INCH
TARGET CONDUCTIVITY = 60 PER CENT OF 5.8E7 MHOS/M

CALCULATED RESISTANCES IN MILLOHMS ARE:

COIL-TARGET GAP	FREQUENCY .5KHZ	1KHZ	3KHZ	10KHZ
0.025 INCH	281.50	391.91	476.39	685.17
0.050 INCH	258.02	357.09	431.82	620.23
0.075 INCH	236.77	325.81	392.22	562.79
0.100 INCH	217.50	297.66	356.90	511.70

COIL OUTER DIAMETER = 3.0 INCH
COIL THICKNESS = 0.150 INCH
TARGET THICKNESS = 0.065 INCH
TARGET CONDUCTIVITY = 60 PER CENT OF 5.8E7 MHOS/M

CALCULATED RESISTANCES IN MILLOHMS ARE:

COIL-TARGET GAP	FREQUENCY .5KHZ	1KHZ	3KHZ	10KHZ
0.025 INCH	262.54	345.25	421.15	696.26
0.050 INCH	240.30	314.29	381.68	630.40
0.075 INCH	220.19	286.52	346.64	572.12
0.100 INCH	201.99	261.56	315.39	520.27

Table 2-7b

Table 2-8

Effect of Coil Thickness

Coil Thickness Variable, 0.1 to 0.4 Inch

Coil Diameters 2.0 and 3.0 Inches

Coil-Target Gap 0.075 Inch

Target Thickness Variable, 0.025 to 0.065 Inch

Target Conductivity σ_u 60%

COIL OUTER DIAMETER = 2.0 INCH
COIL-TARGET GAP = 0.075 INCH
TARGET THICKNESS = 0.025 INCH
TARGET CONDUCTIVITY = 60 PER CENT OF 5.8E7 MHOS/M

CALCULATED RESISTANCES IN MILLOHMS ARE:

COIL THICK	FREQUENCY .5KHZ	1KHZ	3KHZ	10KHZ
0.100 INCH	141.36	335.80	671.42	804.96
0.150 INCH	127.73	300.38	592.78	707.14
0.200 INCH	115.82	269.76	525.82	624.50
0.250 INCH	105.37	243.15	468.45	554.17
0.300 INCH	96.16	219.92	419.03	493.94
0.400 INCH	80.78	181.63	339.07	397.14

COIL OUTER DIAMETER = 2.0 INCH
COIL-TARGET GAP = 0.075 INCH
TARGET THICKNESS = 0.035 INCH
TARGET CONDUCTIVITY = 60 PER CENT OF 5.8E7 MHOS/M

CALCULATED RESISTANCES IN MILLOHMS ARE:

COIL THICK	FREQUENCY .5KHZ	1KHZ	3KHZ	10KHZ
0.100 INCH	157.04	318.84	516.83	613.80
0.150 INCH	141.28	283.94	455.41	539.12
0.200 INCH	127.57	253.90	403.24	476.05
0.250 INCH	115.58	227.92	358.66	422.48
0.300 INCH	105.07	205.34	320.35	376.46
0.400 INCH	87.60	168.34	258.52	302.66

COIL OUTER DIAMETER = 2.0 INCH
COIL-TARGET GAP = 0.075 INCH
TARGET THICKNESS = 0.045 INCH
TARGET CONDUCTIVITY = 60 PER CENT OF 5.8E7 MHOS/M

CALCULATED RESISTANCES IN MILLOHMS ARE:

COIL THICK	FREQUENCY .5KHZ	1KHZ	3KHZ	10KHZ
0.100 INCH	161.61	290.72	419.05	537.63
0.150 INCH	144.89	258.13	368.90	472.29
0.200 INCH	130.41	230.18	326.37	417.09
0.250 INCH	117.79	206.08	290.07	370.13
0.300 INCH	106.74	185.19	258.91	329.92
0.400 INCH	88.49	151.12	208.68	265.30

COIL OUTER DIAMETER = 2.0 INCH
COIL-TARGET GAP = 0.075 INCH
TARGET THICKNESS = 0.055 INCH
TARGET CONDUCTIVITY = 60 PER CENT OF 5.8E7 MHOS/M

CALCULATED RESISTANCES IN MILLOHMS ARE:

COIL THICK	FREQUENCY .5KHZ	1KHZ	3KHZ	10KHZ
0.100 INCH	159.95	262.25	355.96	518.58
0.150 INCH	143.03	232.39	313.22	455.66
0.200 INCH	128.40	206.84	277.00	402.50
0.250 INCH	115.69	184.85	246.10	357.26
0.300 INCH	104.60	165.84	219.59	318.51
0.400 INCH	86.32	134.91	176.90	256.22

COIL OUTER DIAMETER = 2.0 INCH
COIL-TARGET GAP = 0.075 INCH
TARGET THICKNESS = 0.065 INCH
TARGET CONDUCTIVITY = 60 PER CENT OF 5.8E7 MHOS/M

CALCULATED RESISTANCES IN MILLOHMS ARE:

COIL THICK	FREQUENCY .5KHZ	1KHZ	3KHZ	10KHZ
0.100 INCH	155.03	236.81	315.20	525.18
0.150 INCH	138.33	209.56	277.29	461.56
0.200 INCH	123.93	186.27	245.18	407.80
0.250 INCH	111.45	166.27	217.81	362.03
0.300 INCH	100.58	149.00	194.32	322.82
0.400 INCH	82.72	120.95	156.51	259.76

Table 2-8a

COIL OUTER DIAMETER = 3.0 INCH
COIL-TARGET GAP = 0.075 INCH
TARGET THICKNESS = 0.025 INCH
TARGET CONDUCTIVITY = 60 PER CENT OF 5.8E7 MHOS/M

CALCULATED RESISTANCES IN MILLOHMS ARE:

COIL THICK	FREQUENCY .5KHZ	1KHZ	3KHZ	10KHZ
0.100 INCH	273.84	544.61	854.16	952.22
0.150 INCH	253.97	501.54	780.62	867.68
0.200 INCH	235.98	462.85	715.30	793.10
0.250 INCH	219.66	427.99	657.05	726.95
0.300 INCH	204.81	396.52	604.92	668.01
0.400 INCH	178.92	342.17	515.98	567.95

COIL OUTER DIAMETER = 3.0 INCH
COIL-TARGET GAP = 0.075 INCH
TARGET THICKNESS = 0.035 INCH
TARGET CONDUCTIVITY = 60 PER CENT OF 5.8E7 MHOS/M

CALCULATED RESISTANCES IN MILLOHMS ARE:

COIL THICK	FREQUENCY .5KHZ	1KHZ	3KHZ	10KHZ
0.100 INCH	282.14	475.02	636.76	725.59
0.150 INCH	260.81	436.22	581.29	661.11
0.200 INCH	241.56	401.50	532.14	604.26
0.250 INCH	224.15	370.32	488.39	553.84
0.300 INCH	208.36	342.26	449.29	508.92
0.400 INCH	180.96	293.99	382.72	432.68

COIL OUTER DIAMETER = 3.0 INCH
COIL-TARGET GAP = 0.075 INCH
TARGET THICKNESS = 0.045 INCH
TARGET CONDUCTIVITY = 60 PER CENT OF 5.8E7 MHOS/M

CALCULATED RESISTANCES IN MILLOHMS ARE:

COIL THICK	FREQUENCY .5KHZ	1KHZ	3KHZ	10KHZ
0.100 INCH	273.06	409.52	509.23	637.46
0.150 INCH	251.81	375.44	464.62	580.87
0.200 INCH	232.69	345.00	425.14	530.97
0.250 INCH	215.44	317.73	390.03	486.71
0.300 INCH	199.84	293.23	358.68	447.27
0.400 INCH	172.84	251.21	305.35	380.33

COIL OUTER DIAMETER = 3.0 INCH
COIL-TARGET GAP = 0.075 INCH
TARGET THICKNESS = 0.055 INCH
TARGET CONDUCTIVITY = 60 PER CENT OF 5.8E7 MHOS/M

CALCULATED RESISTANCES IN MILLOHMS ARE:

COIL THICK	FREQUENCY .5KHZ	1KHZ	3KHZ	10KHZ
0.100 INCH	257.20	355.78	430.00	617.50
0.150 INCH	236.77	325.81	392.22	562.79
0.200 INCH	218.42	299.09	358.82	514.52
0.250 INCH	201.90	275.19	329.12	471.70
0.300 INCH	186.98	253.74	302.63	433.54
0.400 INCH	161.24	217.02	257.57	368.73

COIL OUTER DIAMETER = 3.0 INCH
COIL-TARGET GAP = 0.075 INCH
TARGET THICKNESS = 0.065 INCH
TARGET CONDUCTIVITY = 60 PER CENT OF 5.8E7 MHOS/M

CALCULATED RESISTANCES IN MILLOHMS ARE:

COIL THICK	FREQUENCY .5KHZ	1KHZ	3KHZ	10KHZ
0.100 INCH	239.51	313.12	380.06	627.65
0.150 INCH	220.19	286.52	346.64	572.12
0.200 INCH	202.87	262.84	317.09	523.13
0.250 INCH	187.30	241.68	290.83	479.65
0.300 INCH	173.26	222.71	267.40	440.89
0.400 INCH	149.08	190.28	227.57	375.06

Table 2-8b

Table 2-9, Graphs 2-9

Double Target Results

Coil Thickness 0.15 Inch

Coil Diameter 2.5 Inches

Coil-Doubler Gap 0.075 Inch

Doubler Thickness Variable, 0.035 to 0.055 Inch

Doubler Conductivity σ_u 60%

Skin Thickness Variable, 0.015 to 0.045 Inch

Skin Conductivity σ_u 30%

****

COIL OUTER DIAMETER = 2.5 INCH
COIL-DOUBLER GAP = 0.075 INCH
COIL THICKNESS = 0.15 INCH
TARGET CONDUCTIVITY = 30 PER CENT OF 5.8E7 MHOS/M
DOUBLER CONDUCTIVITY = 60 PER CENT OF 5.8E7 MHOS/M

TARGET THICKNESS = 0.015 INCHES

CALCULATED RESISTANCES IN MILLOHMS ARE:

	FREQUENCY			
DOUBLER THICK	1KHZ	2KHZ	3KHZ	4KHZ
0.035 INCH	333.75	418.35	445.64	461.36
0.045 INCH	293.84	350.54	372.32	389.45
0.055 INCH	260.43	303.30	325.64	347.76

****
****

COIL OUTER DIAMETER = 2.5 INCH
COIL-DOUBLER GAP = 0.075 INCH
COIL THICKNESS = 0.15 INCH
TARGET CONDUCTIVITY = 30 PER CENT OF 5.8E7 MHOS/M
DOUBLER CONDUCTIVITY = 60 PER CENT OF 5.8E7 MHOS/M

TARGET THICKNESS = 0.025 INCHES

CALCULATED RESISTANCES IN MILLOHMS ARE:

	FREQUENCY			
DOUBLER THICK	1KHZ	2KHZ	3KHZ	4KHZ
0.035 INCH	313.40	382.44	406.50	422.91
0.045 INCH	276.75	325.79	347.71	367.41
0.055 INCH	246.54	286.05	310.35	336.03

****
****

COIL OUTER DIAMETER = 2.5 INCH
COIL-DOUBLER GAP = 0.075 INCH
COIL THICKNESS = 0.15 INCH
TARGET CONDUCTIVITY = 30 PER CENT OF 5.8E7 MHOS/M
DOUBLER CONDUCTIVITY = 60 PER CENT OF 5.8E7 MHOS/M

TARGET THICKNESS = 0.035 INCHES

CALCULATED RESISTANCES IN MILLOHMS ARE:

	FREQUENCY			
DOUBLER THICK	1KHZ	2KHZ	3KHZ	4KHZ
0.035 INCH	294.70	353.05	376.30	395.03
0.045 INCH	261.43	305.53	329.00	352.26
0.055 INCH	234.21	272.05	299.18	328.93

****
****

COIL OUTER DIAMETER = 2.5 INCH
COIL-DOUBLER GAP = 0.075 INCH
COIL THICKNESS = 0.15 INCH
TARGET CONDUCTIVITY = 30 PER CENT OF 5.8E7 MHOS/M
DOUBLER CONDUCTIVITY = 60 PER CENT OF 5.8E7 MHOS/M

TARGET THICKNESS = 0.045 INCHES

CALCULATED RESISTANCES IN MILLOHMS ARE:

	FREQUENCY			
DOUBLER THICK	1KHZ	2KHZ	3KHZ	4KHZ
0.035 INCH	277.76	329.07	353.42	375.83
0.045 INCH	247.76	289.11	315.30	342.86
0.055 INCH	223.30	260.88	291.55	325.59

****

Table 2-9a

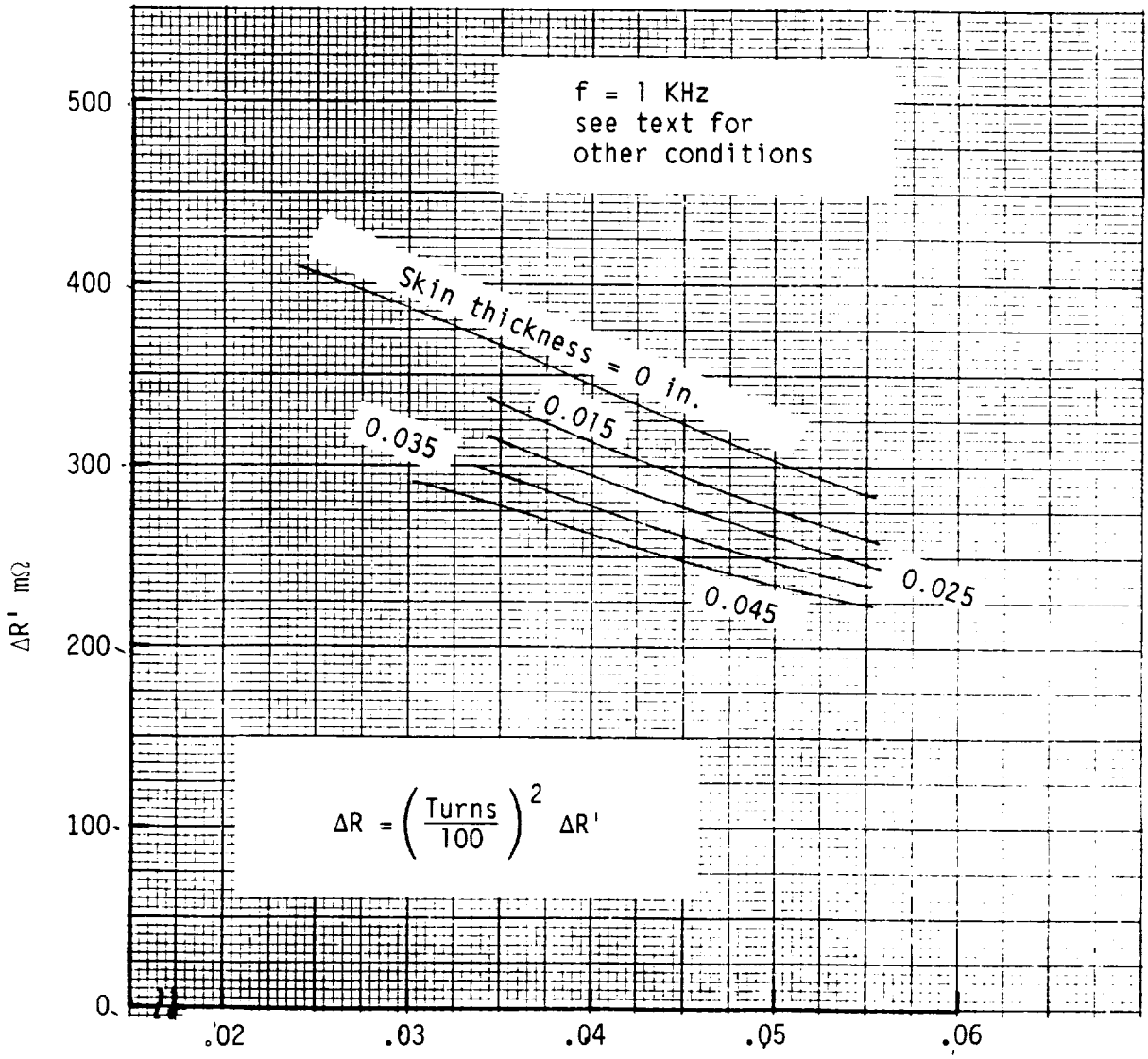

Graph 2-9a Effect of Doubler - Skin Combinations on Coil Resistance

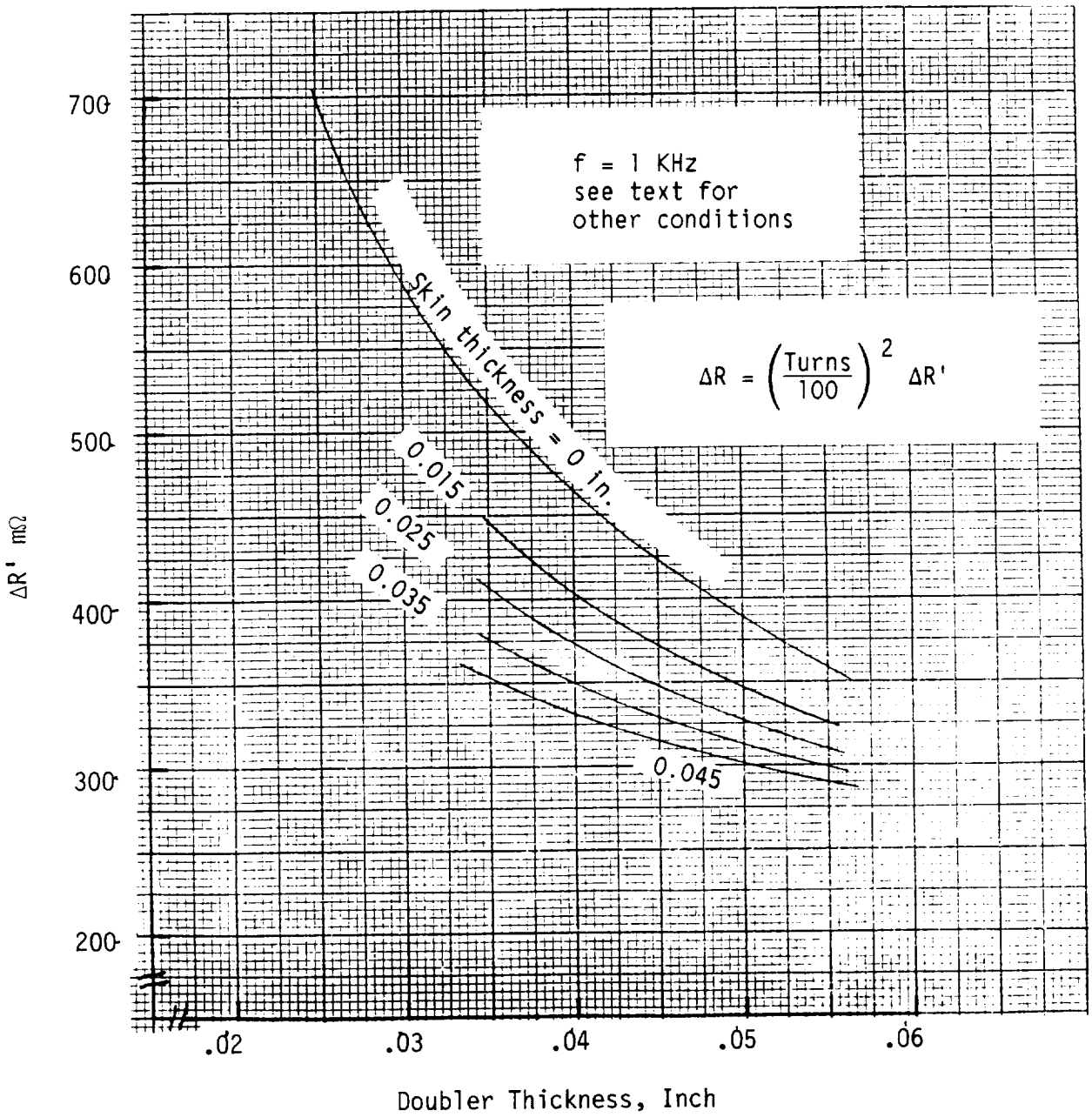

Graph 2-9b Effect of Doubler - Skin Combinations on Coil Resistance

VII. DESIGN EXAMPLES

Two examples of electrical design are given below, one for a relatively thick skin not requiring a doubler; the other for a thin skin-doubler combination. It should be emphazized that the procedure that will be described ignores the possible use of the Bernhart-Schrag analysis code. If that code is available, then calculations can be made with 4 or 5 trials for the number of coil turns, and decisions quickly made on the turns needed by examining the electrical frequency and/or the impulse strength. The code, as written, does not handle the addition of a doubler (dual target conductivities), but it could be extended for such targets.

Example 1

Let the following be known or pre-selected.

* The skin material is 7075-76 aluminum, 0.063 inch thick. Electrical conductivity = 1.914×10^7 mhos/m (33% of the conductivity of copper).
* Two "side coils" are to be used, and operated in series spanwise stations will be pulsed individually).
* The leading edge has a "resonant" mode (suitable for side-coil operation) with a frequency of 1.11 KHz.
* No doubler is to be used.
* The coils are to have 2.5 inch diameters and thicknesses of 0.15 inch, and coil-to-skin gaps are to be 0.075 inch.
* Either a 200 μF or 400 μF discharge capacitor will be used.

(a) Selection of Suitable Risetime:

Using the structural frequency for a risetime criterion, we would design for an electrical resonant frequency of

$$f_{elec} = 2.22 \text{ KHz}$$

which corresponds to a current time-to-peak of

$$t_m = \frac{1}{4 f_{elec}} = 112.6\ \mu s$$

Using electrical skin depth for a risetime criterion, and referring to Fig. 2-10, let us require that the ratio of skin thickness to electrical skin depth be 0.75, which gives an electrical skin depth of

$$\delta = \frac{0.063}{0.75} = .084 \text{ inch.}$$

By formula (with 33% conductivity),

$$\delta = \frac{0.143}{\sqrt{f_{KHz}}} \text{ inch,}$$

yielding $f_{elec} = 2.898$ KHz

and $t_m = 86.3\ \mu s.$

Since the penalty for making

$t_m < 1/(8\ f_{mech})$

is not great, we shall select the risetime

$t_m = 86\ \mu s.$

(b) Number of Turns Required for the Coils

The required coil inductances are found from

$$f_{elec} = 2898 \text{ Hz} = \frac{1}{2\pi\sqrt{LC}} :$$

C	L (Two Coils)	L/Coil
200 μF	15.08 μH	7.54 μH
400 μF	7.54 μH	3.77 μH

Having chosen the ratio of skin thickness to electrical skin depth to be 0.75, then the curves in Graph 2-2C indicate that, for a skin thickness of 0.065 inch, $t\ \sigma_u\ f\ L^1 = 6.8$,

$$\text{so} \quad L^1 = \frac{6.8}{0.065(.33)(2.898)} = 109.4\ \mu H,$$

from which

$$\text{Turns, } N = 100\sqrt{\frac{L}{L1}}$$

Numerically, we get

C	N
200 μF	26.3
400 μF	18.6

(c) Rectangular Wire Thickness and Coil Resistance

The wire thickness (including insulation) is found from

$$t_w = \text{Thickness} = \frac{d_o - d_i}{2} \quad \frac{1}{N}$$

where d_o = Outer coil diameter (2.5 inch)

d_i = Inside coil diameter (0.25)

Also the wire length needed is

$$l = \pi\left(\frac{d_o + d_i}{2}\right) N.$$

Assuming 0.002 inch thick insulation, the d.c. resistance of the coil would be

$$R_{dc} = \frac{1 \times 39.37}{5.8 \times 10'(t_w - 0.0004)(0.15)} \text{ ohms},$$

where 0.15 inch is the width of the rectangular wire, and the factor 39.37 is needed for conversion to metric units. Numerically, we get the results:

C	N	t_w(In)	l(In)	R_{dc}(Ω)
200 μF	26.3	0.0428	113.6	.0132
400 μF	18.6	0.0605	80.3	.0064

The effective operating resistances are greater than R_{dc} because of skin effect within the coils and because of the proximity of the mechanical skin. The former effect is determined from Fig. 2-92, using the (copper) skin depth

$$\delta = \frac{0.0823}{2.898} = .0483 \text{ inch},$$

so $$\frac{\text{coil thickness}}{\delta} = \frac{0.15}{.0483} = 3.10.$$

Thus, from the curve,

$$\frac{R_{ac}}{R_{dc}} = 1.42.$$

The mechanical skin proximity effect is an additional ΔR determined from Graph 2-6C. Using the 0.065 inch skin curve (and skin thickness / of 0.75) gives

$$t \sigma \Delta R^1 = 10.9,$$

so $$\Delta R^1 = \frac{10.9}{(0.065)\ (.33)} = 508 \text{ m}\Omega = 0.508\Omega,$$

and then $$\Delta R = \frac{N^2}{100} \Delta R^1.$$

Again, taking the two capacitance designs, we get the results:

C	N	R_{dc}	R_{ac}	R	$R_{eff}(\Omega)$
200 μF	26.3	.0132	.0187	.0351	.0538
400 μF	18.6	.0064	.0091	.0176	.0267

d. Estimates of Peak Currents and of Cable Requirements

Let us assume that the stored capacitor energy required to de-ice a bay

is W=200 joules. Then the required capacitor voltage is

$$V = \sqrt{\frac{2W}{C}} = \frac{20}{\sqrt{C}} \text{ volts.}$$

The peak currents may be estimated by referring to Fig. 2-2. Take the 200 μF design, for which $R_{coils}\sqrt{\frac{C}{L}} = .1076\sqrt{\frac{200}{15.08}} = 0.392$

Then the graph indicates

$$\frac{I_{max}}{\sqrt{2W/L}} = 0.760$$

Suppose we design feed cables on the basis that they contribute an additional 10% reduction in peak current. Then

$$\frac{I_{max}}{\sqrt{2W/L}} = 0.760\ (.9) = 0.684,$$

so $I_{max} = 0.684\sqrt{\frac{2(200)}{15.08\text{x}10\text{-}6}} = 3{,}523$ Amps

and reading the new abscissa value from the curve (for a 0.684 ordinate) gives $(R_{coils} + R_{cable})\sqrt{\frac{C}{L}} = 0.563$

or $R_{cable} = 0.563\sqrt{\frac{15.08}{200}} - .1076 = 0.0470\Omega$

If, for example, cable lengths are to be 25 feet, and if each cable consists of six wires (three forward wires and three return wires with appropriate bundle construciton to minimize inductance),* then the resistance of each 25 foot wire would be $\frac{0470}{2}(3) = .0705\Omega$

which requires a wire gage having a resistance of 2.82 Ω/1000 ft (Gage 14).

Repeating these steps for the 400 μF case yields the following comparative data:

C	V(volts)	I_{max}(Amps)	$R_{cable}(\Omega)$
200 μF	1414	3523	.0470
400 μF	1000	4982	.0239

It is not surprising that the higher voltage-lower capacitance combination places less stringent demands on the feed cables.

---

* An alternate configuration for a low inductance cable would be two thin flat copper strips separated by a dielectric sheet.

Example 2

We now illustrate a design for the case of a thin skin leading edge requiring a doubler. Let the following be known or pre-selected.

* The skin material is 2024-T3 aluminum, 0.025 inch thick. Electrical conductivity = 1.74 X 10^7 mhos/meter (30% of the conductivity of copper).
* "Nose coils" are to be used, with two coils in series.
* The leading edge has a "resonant" mode (suitable for nose coil operation) with a frequency of 600 Hz.
* The coils are to have 2.5 inch diameters and thicknesses of 0.15 inch, and coil-to-doubler gaps are to be 0.075 inch.
* The discharge capacitor will be 600 μF.

a. Selection of Suitable Risetime

Given the structural frequency of 600 Hz, and assuming that the added doublers do not modify that frequency drastically, we will select the electrical resonant frequency

$$f_{elec} = 1200 \text{ Hz},$$

which corresponds to a current time-to-peak of about

$$t_m = \frac{1}{4f_{elec}} = 208\ \mu s.$$

b. Doubler Design

Let the doublers be made of pure aluminum (approximately 60% conductivity). The corresponding electrical skin depth at 1200 Hz is

$$\delta = \frac{1}{\sqrt{\pi(1200)(4\pi x10^{-7})(0.6x5.8x10^{7})}} = .00246m = .097\ inch$$

Let us design for an electrical thickness of 0.75δ, or 0.073 inch. The leading edge skin will provide a small amount of this electrical thickness. Because of its 30% conductivity, we will estimate its contribution as only one-half the actual skin thickness. Then the required doubler thickness is

$$\text{Doubler Thickness} = .073 - \frac{.025}{2} = .0605\ inch.$$

The doublers should have a diameter of about 1.5 times the coil diameter (3.75 inches in this case).

c. Number of Turns Required for the Coils

Solving the equation $f_{elec} = \frac{1}{2\pi\sqrt{LC}}$ for the required inductance gives

$$L = \frac{1}{600x10^{-6}} \left(\frac{1}{2\pi x1200}\right)^2 = 29.3\ \mu H\ \text{(two coils)},$$

or 14.65 μH / coil.

Let us first ignore the skin's effect on the coil inductance. Then using the inductance curves (Graph 2-2c) with

$$t/\delta = \frac{.0605}{.097} = .624$$

and t = .0605 gives $t\,\sigma_\mu f L^1 = 5.2$,

so $L^1 = \frac{5.2}{.0605(0.6)(1.2)} = 119\ \mu H$

The dual-target results presented in Graph 2-5 happened to have been calculated for a 2.5 inch diameter coil, and so are also useable here. They indicate that with a doubler thickness of .0605 inch, and a skin thickness of .025 inch, then $L^1 = 124\ \mu H$ at 1 KHz. This should drop slightly at 1.2 KHz. Let us pick the value $L^1 = 122\ \mu H$. Then the required number of turns is

$$\text{Turns, } N = 100\sqrt{\frac{L}{L}1} = 100\sqrt{\frac{14.65}{122}} = 34.6$$

d. Rectangular Wire Thickness and Coil Resistance

The needed thickness of the rectangular wire is

$$t_w = \frac{d_o - d_i}{2}\ \frac{1}{N} = \frac{2.5 - 0.25}{2}\ \frac{1}{34.6} = .0325 \text{ inch,}$$

and the wire length is

$$l = \pi\ \frac{d_o + d_i}{2}\ N = \pi\ \frac{2.5 + 0.25}{2}\ (34.6) = 149.5 \text{ inches.}$$

Again, assuming 0.002 inch for insulation thickness, the d.c. resistance of the coil would be

$$R_{dc} = \frac{149.5 \times 39.37}{5.8 \times 10^7(.0325 - .004)(0.15)} = .0237\Omega.$$

The skin depth in copper at 1.2 KHz is

$$\delta = \frac{0.0823}{\sqrt{1.2}} = .0751 \text{ inch,}$$

so $\frac{\text{coil thickness}}{\delta} = \frac{0.15}{.0751} = 2.0$

Then from Fig. 2-92,

$$R_{ac} = 1.08\ (.0237) = .256\Omega,$$

and from Graph 2-9a with the doubler thickness of .0605 inch and the skin thickness of .025 inch, $\Delta R^1 = 230m\Omega$ at 1 KHz

The calculation Table 2-9 shows that for a .055 inch doubler (and .025 skin), ΔR^1 increases by about 40mΩ when the frequency is increased from 1 KHz to 2 KHz. Thus, let the frequency correction for 1.2 KHz be $8_{m\Omega}$, giving $\Delta R^1 = 238m\Omega$, so

$$\Delta R = \left(\frac{N}{100}\right) \Delta R^1 = \left(\frac{34.6}{100}\right)^2 (0.238) = .0285\Omega$$

The effective resistance per coil then becomes

$$R_{eff} = R_{ac} + \Delta R = .0256 + .0285 = .0541\Omega.$$

e. Estimates of Peak Currents and of Cable Requirements

Assume that the de-icing energy requirement is 90 Joules/coil. Then the needed capacitor voltage is $V = \sqrt{\frac{2W}{C}} = \sqrt{\frac{360}{600x10^{-6}}} = 775$ volts.

Also $R_{coils}\sqrt{\frac{C}{L}} = 2 \times .0541 \sqrt{\frac{600}{29.3}} = 0.490$

so Fig. 2-2 shows that $\frac{i_{max}}{\sqrt{2W/L}} = 0.715$

Allowing for a additional 10% reduction in peak current due to cable resistance, then

$$\frac{i_{max}}{\sqrt{2W/L}} = 0.715\ (.9) = .644,$$

so

$$i_{max} = 0.644\sqrt{\frac{360}{29.3x10^{-6}}} = 2257 \text{ Amps},$$

and from Fig 2-2, $(R_{coils} + R_{cable})\sqrt{\frac{C}{L}} = 0.67$

or $R_{cable} = 0.67 \sqrt{\frac{29.3}{600}} - 0.1082 = .040\Omega$

VIII. References

2-1. El-Markabi, M.H.S., et al, "Electromagnetic Properties of a Circular Cylindrical Coil in a Set of Planar Ferromagnetic Regions", IEE Proceedings (London), Vol 129, Part A, No. 8, pp 582-589, Nov. 1982.

2-2. Bowley, R.M., et al, "Production of Short Mechanical Impulses by Means of Eddy Current", IEE Proceedings (London), Vol. 130, Part B, No. 6, pp 415-423, Nov. 1983.

2-3. Lewis, G.L., "The Electrodynamic Operation of Electro-Impulse De-icing Systems", AIAA 24th Aerospace Sciences Meeting, Jan. 6-9, 1986/Reno, Nevada.

2-4. Henderson, R., "Theoretical Analysis of the Electrical Aspects of the Basic Electro-Impulse Problem in Aircraft De-Icing Applications", Ph.D. Dissertation, The Wichita State University, March 1986.

2-5. Walsh, J.L., "Predicting Transient Skin Pressures in Electro-Impulse De-Icing of Airfoils", Masters Thesis, The Wichita State University, May 1986.

2-6. Rosa, E.B., and Cohen, L., "Formula and Tables for the Calculation of Mutual and Self-Inductance", Bulletin of the Bureau of Standards, Vol 5, No. 1, 1908-1909. (Repeated in 1912-1913 Bulletin).

CHAPTER 3. STRUCTURAL DYNAMIC TESTS AND STUDIES

This Chapter is divided into the following sections:

I. Introduction

The structural dynamics associated with electro impulse de-icing has proved to be a difficult and challenging problem. The structural dynamic investigations conducted to date have raised as many new questions as have been answered. The project has been a modest activity from the standpoint of structures personnel and resources. During the first three years of the project, the majority of the resources were utilized in the proof of concept through subjective optimization of the numerous Icing Research Tunnel (IRT) test demonstrations for the participants in the industrial consortium. Eight IRT tests and two flight test demonstrations are summarized in Chapters 5 and 6. The Sections are arranged in chronological order.

The problem of strain measurement in both mild shock environments and strong magnetic fields is treated in Sections II. Methods to minimize the magnetic field effects are examined and applied to a BCAC 767 Leading Edge Slat in Section III.

In Section IV, various concerns and problems associated with structural dynamic modeling of the EIDI system are presented. The first model was a 2.5 inch internal radius semi-cylinder, 66 inches in length. The model was instrumented with strain gages on both the inner and outer surfaces to

separate membrane and bending strains. This model served as a comparative test article in several early IRT investigations. Some representative data for the model is presented in Sections IV.A.

This activity was followed by structural dynamic modeling studies conducted by graduate students at The Wichita State University. These studies were concerned with a comparison of closed form solutions and finite element approximations for the case of a semi-cylindrical shell supported by shear diaphragms. The results of the comprehensive studies are presented in Sections IV.B and IV.C.

The EIDI project began its activities in May 1982 with a single accelerometer, charge amplifier, and a HP-5423A Structural Dynamics Analyzer. During the next three years of IRT tests, this inventory expanded to include numerous transducers and signal conditioning instrumentation, digital oscilloscopes, and PC-micro computers. In October 1984, The Wichita State University acquired the MSC/NASTRAN finite element code. The acquisition of these elements and resources has been encouraging and has prompted some serious attempts to gain a correlation between the analytical and experimental results for a leading edge structure subjected to EIDI pulses. The major unsolved problem was an adequate representation of the spatial and temporal behavior of the coil pulse. This behavior was first shown by Schrag, Ref. 3-1, for a single case of coil size, gap target material, and electrical parameters. The experimental result was conducted with a special magnetic field measuring plate described in Ref. 3-10. This experimental result was generalized into a separated solution of spatial and temporal behavior by Bernhart, Ref. 3-2, and used successfully in a transient response study of a flat rectangular plate subjected to an EIDI pulse.

While this limited study did show favorable agreement with experimental data, it also clearly identified the response sensitivity to both pulse shape and pulse duration. A parallel experimental development designed to measure the temporal behavior of the EIDI pulse was also discussed in Ref. 3-10. This experiment employs fundamental one dimensional wave mechanics in a 48 inch long polycarbonate rod with a propagation time of approximately 860 microseconds. This time delay is adequate to measure the plane wave behavior of the force pulse. Dispersion and attenuation in the rod create uncertainties in the experimental results.

A detailed structural dynamic investigations is treated in Section IV.C for a 2.5 inch inner radius semi-cylinder, 30 inches in length. The temporal force characteristics used in this study were established from the polycarbonate rod experiment. Correlation between experimental and finite element prediction of strains and accelerations were quite favorable. The study also developed several sensitivity factors relating the peak dynamic response to both spatial and temporal parameters in the force model.

Henderson, Ref. 3-12 developed a numerical procedure to evaluate both mechanical and electrical response to a EIDI pulse. The frequency domain solution has unfortunately proved to be computationally intensive and difficult to use for parametric design studies. During the 1986-87 academic year, the project investigators, R. L. Schrag and W. D. Bernhart, were engaged in an intense study which produced a time domain solution of the EIDI process. The EIDI code is both computationally efficient and user friendly and is presented in Chapter 2 and Ref. 3-13. The code can evaluate detailed normal and radial pressure distributions, the normal target force, its peak value and zero crossing, and circuit voltage and current traces. Some results from the EIDI code are discussed in Section V.

Mr. Peter Gien, who is a Ph.D. candidate in Aeronautical Engineering is developing a proposal to conduct a detailed investigation of the total EIDI pulse process. This work will be both a analytical and experimental investigation. The anticipated completion time is December 1988.

II. STRAIN MEASUREMENTS NEAR EIDI COILS

Strain measurements in the magnetic field produced by a EIDI coil has proved to be a difficult problem and the following demonstration problems are intended to portray some of the difficulties. The EIDI coil can generate magnetic flux densities in excess of 10,000 gauss, and the field strength is developed in 100 to 300 microseconds. Any strain gage in the proximity of the coil is subject to transverse magnetic flux which results in induced voltage in the gage. If the resulting induced voltage is not canceled, eliminated or minimized, it obscures the strain signal developed in the gage. Thus, the problem is likened to a signal plus noise phenomena. The typical strain signal is be on the order of 1 to 10 millivolts, whereas the induced or noise voltage may be of the same order and in some cases greater than the strain signal.

Contacts with strain gage manufacturers revealed that the Measurement Group, Inc., (Ref. 3-1) had solved a similar problem for the Princeton University Plasma Physics Laboratory in connection with the Tokamak Fusion Test Reactor. The application involved magnetic flux densities as high as 50,000 gauss and a time duration of approximately one second. A special gage was employed, identified as a "dual element gage," which consists of two identical overlaid grids, laminated in precise alignment with one another, and connected in series such that the current passes through them in opposite directions. The gage is shown in conceptual form in Fig. 3-1. Since the grids are very close together with respect to the field gradients, induced voltage in the grids tend to be equal and of opposite sign, rendering the gages largely immune to magnetic effects. The Measurements

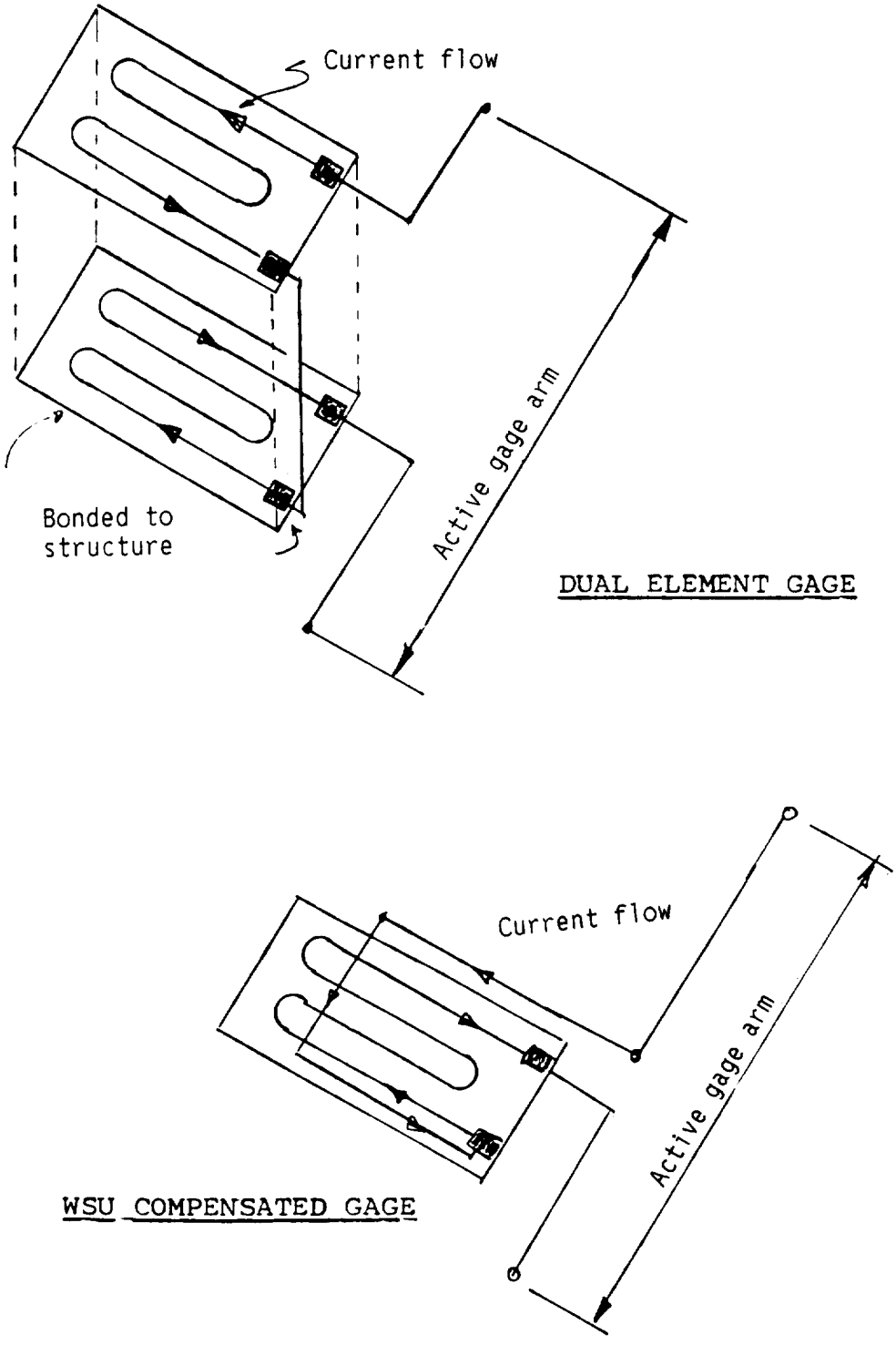

FIGURE 3-1. DUAL ELEMENT GAGE AND WSU COMPENSATED GAGE.

Group also recommends a woven cable product commercially known as Inter-8 Weave to minimize the magnetic noise in the cabling. Several of the "dual element gages" (WK-13-125-WS-700) were obtained and installed on a representative leading edge structure. The lead attachments to the "dual element gages" posed very special soldering problems and several gages were lost during installation. The recommended cabling also proved to be excessive in weight for the relatively light weight structures common to aircraft leading edges.

The first time the "dual element gages" were tested on a EIDI pulsed airfoil, the gages sheared along the bonding plane between the grids and the resulting misalignment rendered them useless to the project. Thus, the EIDI strain gage environment is not only harsh due to the magnetic flux, it is also subject to very high acceleration levels which can reach peak values of 10,000 to 20,000 g's in 100 microseconds or less. This failure prompted Dr. R. L. Schrag to propose a modification to a standard strain gage which is herein identified as a "compensated gage," and is also shown in Fig. 3-1. This modification incorporates the installation of a single loop of 32 gauge enameled wire which serves to partially compensate or minimize the induced magnetic effect. The compensation loop is also bonded to the gage where appropriate. Standard Wheatstone bridges are used in the EIDI project with a complete avoidance of any wire wound potentio-meters or other electrical components. Gage leads consist of twisted pairs of 28 or 32 gauge insulated wire twisted with a drill motor. The leads are both inexpensive and light weight.

Strain measurement must be completed in two steps. After performing a resistance balance of the bridge, the first step is to remove the bridge excitation DC voltage source and pulse the EIDI coil to establish the

induced magnetic effect in the gage. In the second step, the bridge excitation is restored and the EIDI coil is pulsed a second time to establish the induced magnetic effect plus the mechanical strain. Subtracting the two signals yields the desired mechanical strain. This two step operation is of course difficult to achieve in the IRT tests. Some data have been obtained by using a pre-recorded magnetic effect pulse and subtracting it from the pulse data obtained under icing conditions.

The two step process is identified as a DC-bridge measurement by project personnel and has been used with varying levels of success. Figs. 3-2 and 3-3 depict some additional problems for the DC-bridge related to the digital sample time of the transient capture instrumentation. The data contained in the two figures represent strain measurements for a 2.5 inch radius semi-cylinder, 66 inches in length. This simulated leading edge structure contains a single coil located at the mid-length and compensated strain gages placed on the outer and inner surfaces of the 0.040 inch thick skin. The data in Fig. 3-2 represents the two signals for each location and the resulting subtraction when using a HP-5423A Signal Analyzer, whose sample time is approximately 10 microseconds. The desired strain signal is literally obscured during the first 150 microseconds and the establishment of a peak strain is difficult. Fig. 3-3 represents the same data acquired with a two channel Nicolet 3091 Digital Oscilloscope using a 1 microsecond sample time. The figure clearly indicates the desired levels of the two strain signals for a well compensated gage.

A recent improvement in strain measurements has also been developed by Dr. R. L. Schrag. The development is an AC-bridge, wherein the carrier frequency is 100 kilohertz, which is considerably higher than any known strain gage instrumentation. The principal advantage of the instrument is

the single step measurement process. The AC-bridge does require both resistance as well as capacitance balancing and is exceedingly sensitive to lead wire movements during the balancing and pulsing operations. In spite of some of these difficulties, the instrument exhibits great promise. A schematic diagram of the AC-bridge is shown in Fig. 3-4.

Figs. 3-5 through 3-7 are strain measurements for a single gage on the Boeing 767 leading edge slat; details related to the gage location and the slat structure may be found in Section III. Fig. 3-5 is the data for an noncompensated gage and standard strain gage leads using the DC-bridge process; while Fig. 3-6 is the same data with a compensating loop added to the gage with twisted leads. The improvement resulting from the compensating loop is obvious. Fig. 3-7 represents AC-bridge measurements for both the noncompensated and compensated gage. The compensating loop neither adds or detracts from the performance. A brief summary of the peak strain level developed by the four measurements is summarized below. The peak circumferential (chordwise) strain taken as the average of the four measurements is 2070 micro-strain.

Figure 3-5.	1940 micro-strain
Figure 3-6.	1850 micro-strain
Figure 3-7.	2220 micro-strain
Figure 3-7.	2270 micro-strain

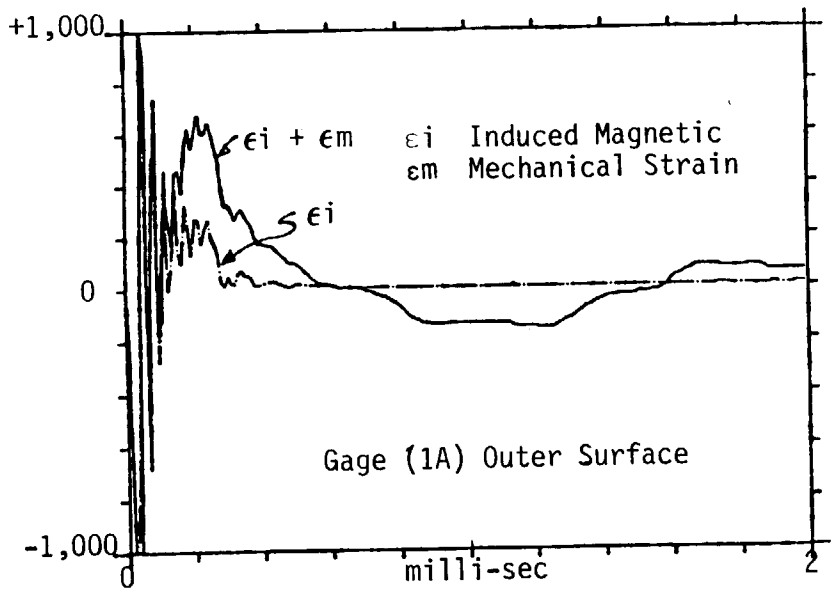

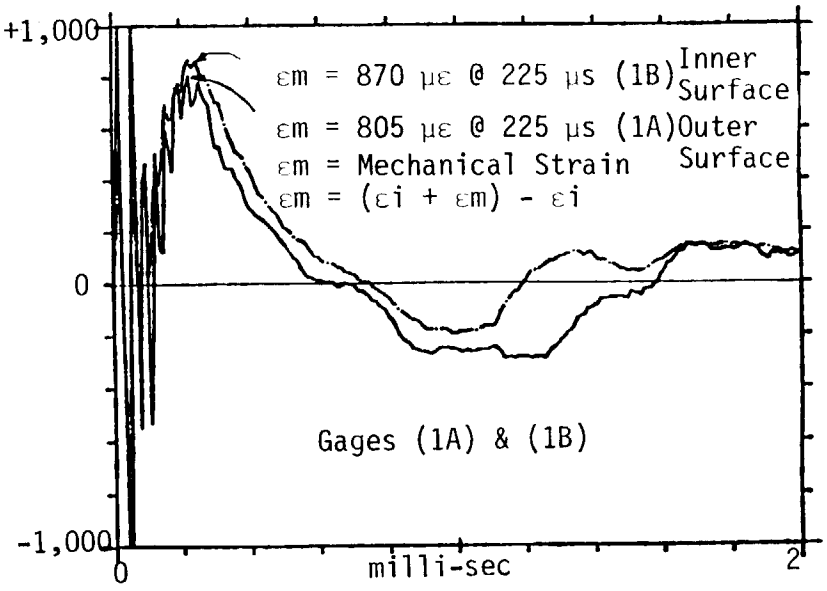

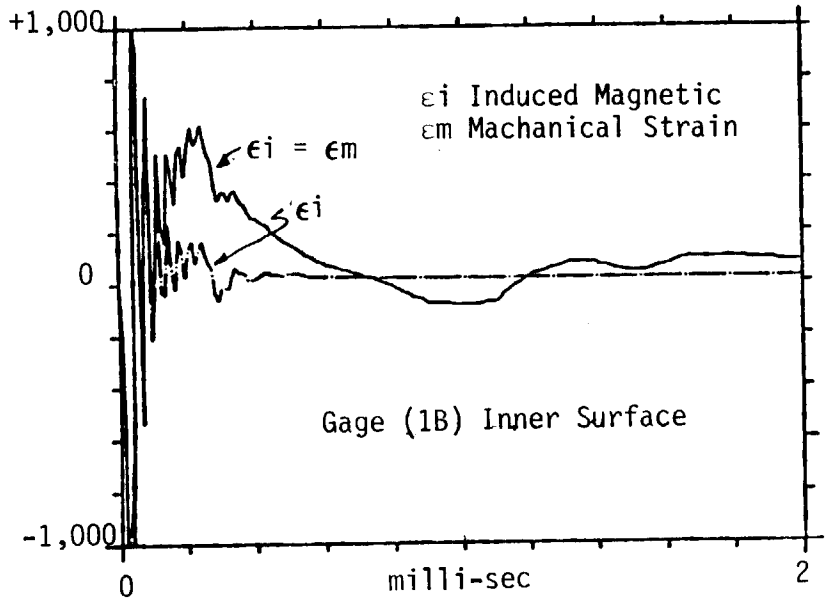

2.5" RADIUS SEMI-CYLINDER (SINGLE COIL).

LONGITUDINAL (SPANWISE) STRAIN: (C=400 V=800 128 JOULES).

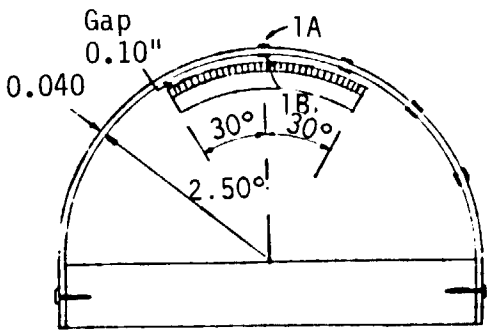

FIGURE 3-2. DC-BRIDGE STRAIN MEASUREMENT (10 MICRO-SECOND SAMPLE TIME).

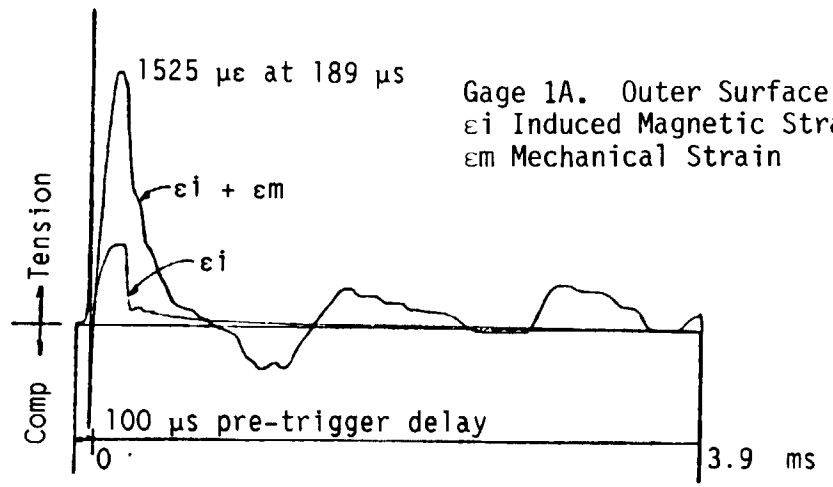

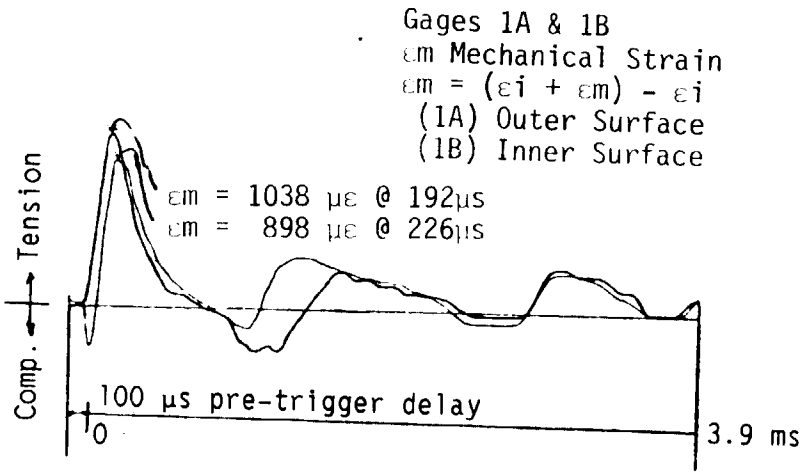

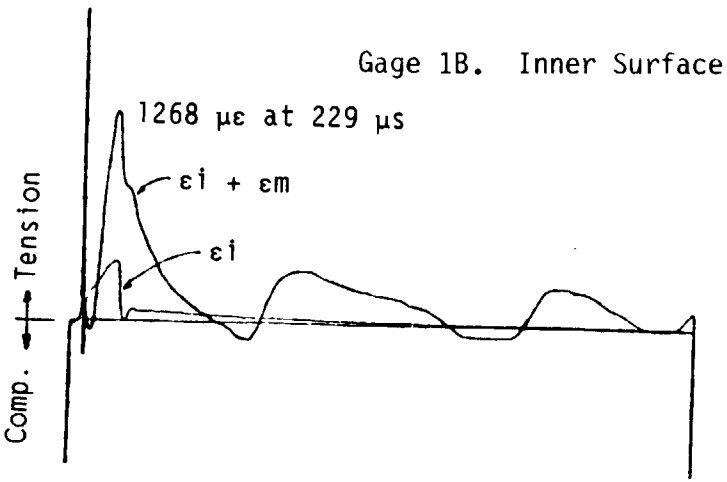

2.5" RADIUS SEMI-CYLINDER (SINGLE COIL).

LONGITUDINAL (SPANWISE) STRAIN: (C=400 V=800 128 JOULES).

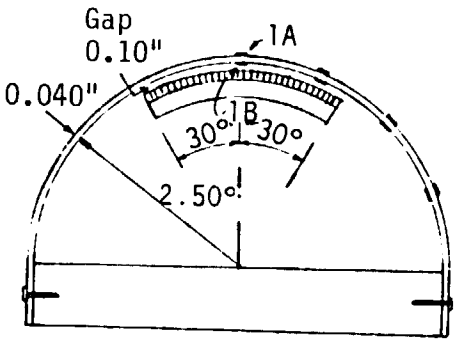

FIGURE 3-3. DC-BRIDGE STRAIN MEASUREMENT (1 MICRO-SECOND SAMPLE TIME).

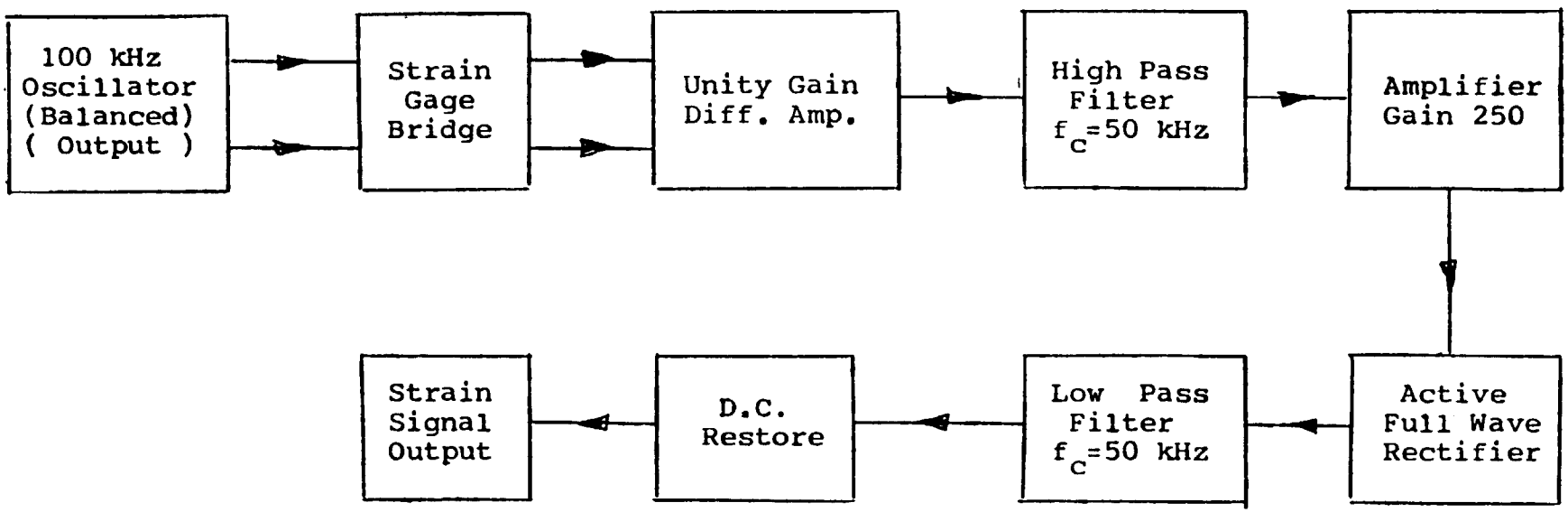

FIGURE 3-4. AC-BRIDGE STRAIN MEASUREMENT SYSTEM.

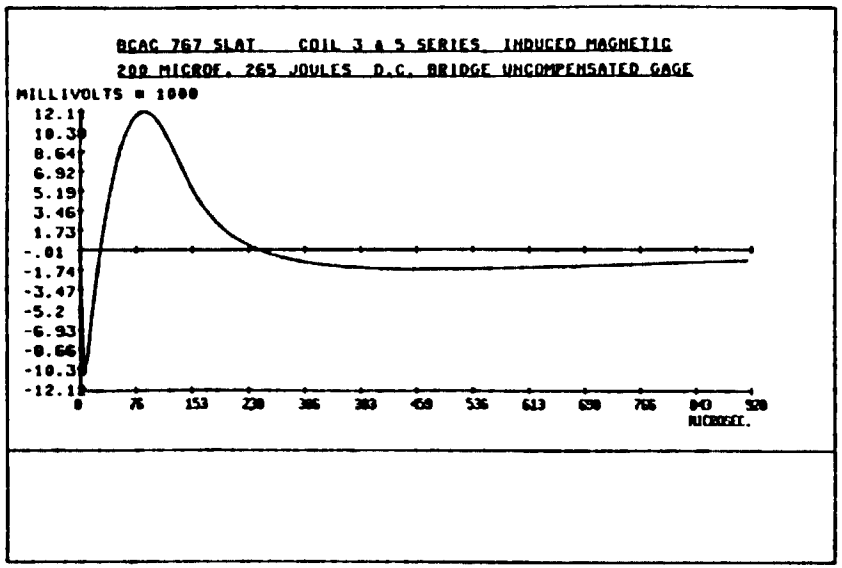

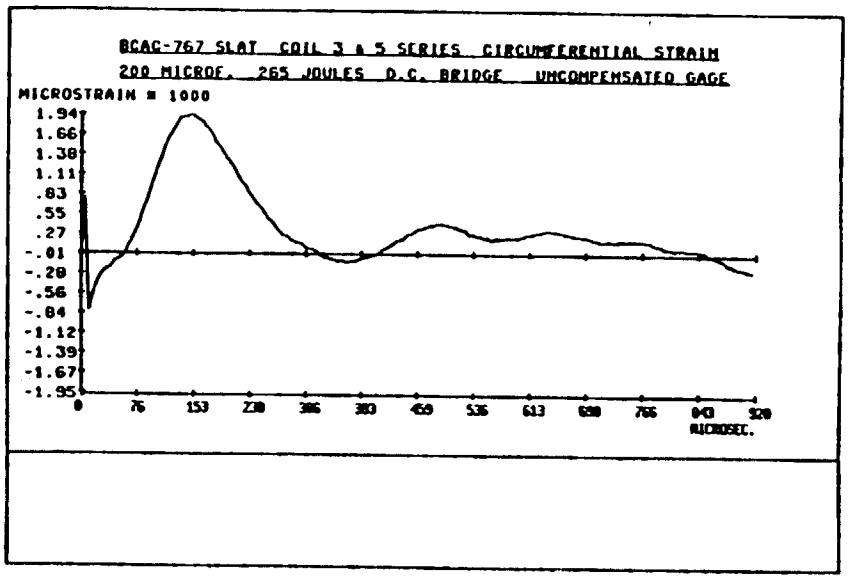

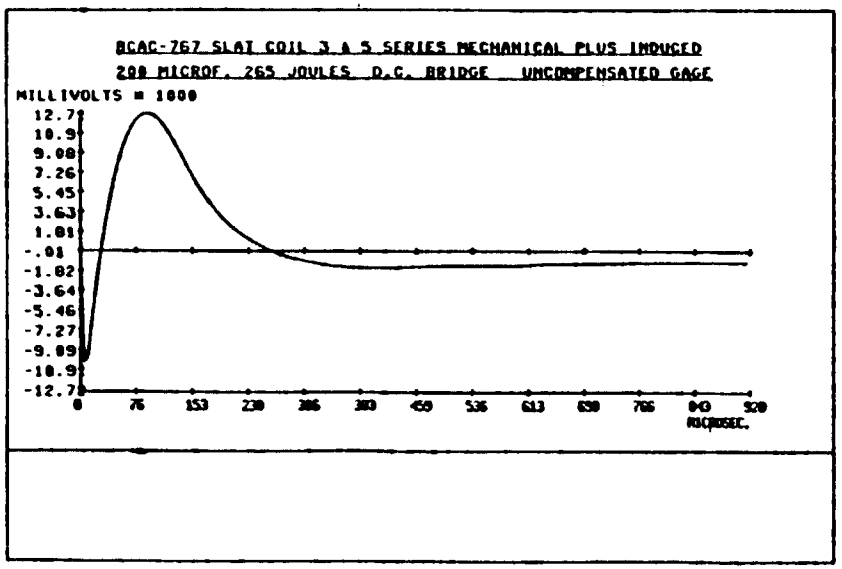

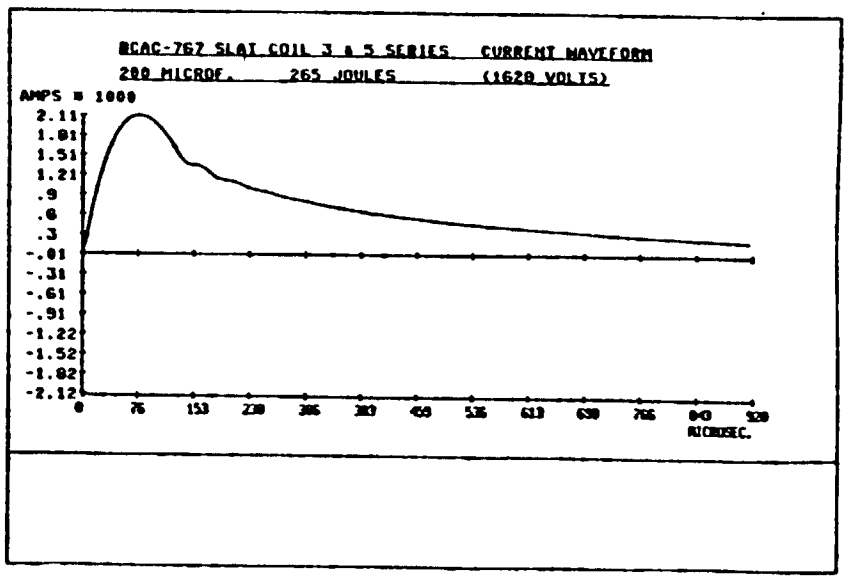

FIGURE 3-5. DC-BRIDGE STRAIN MEASUREMENT (NONCOMPENSATED GAGE).

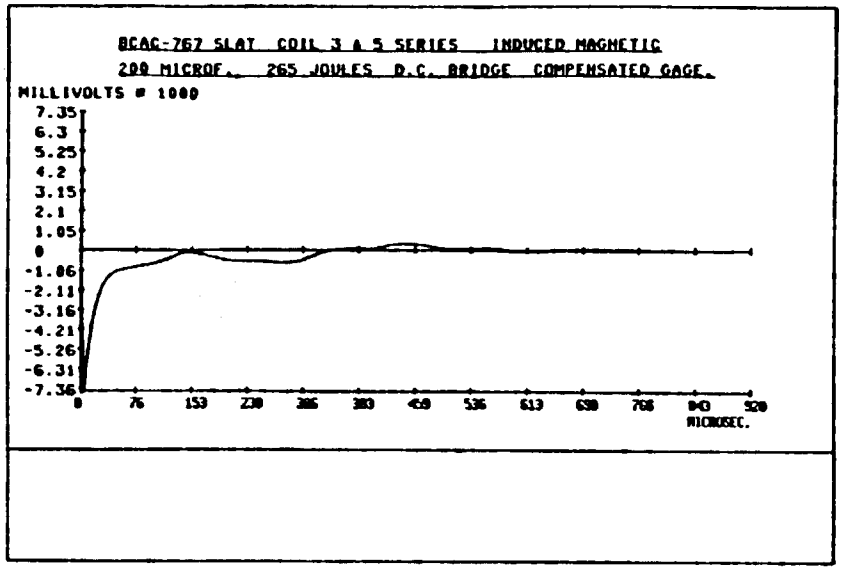

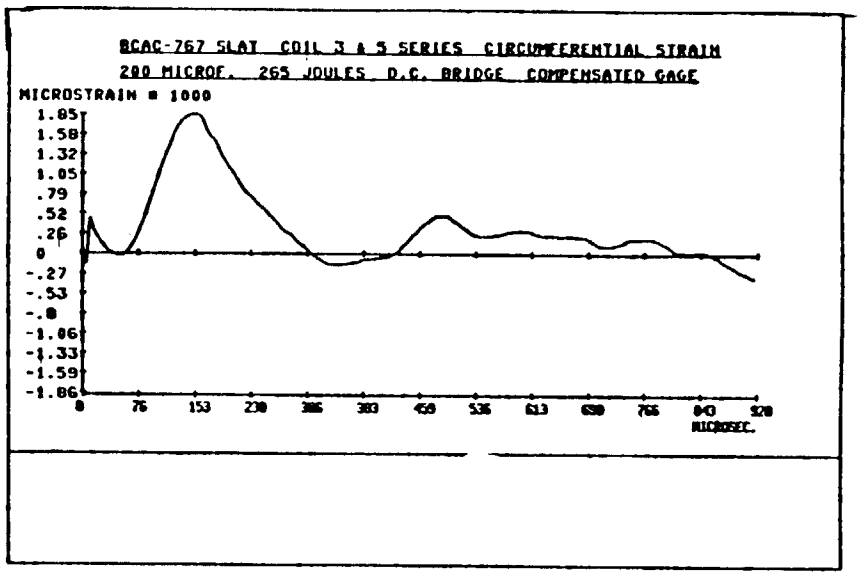

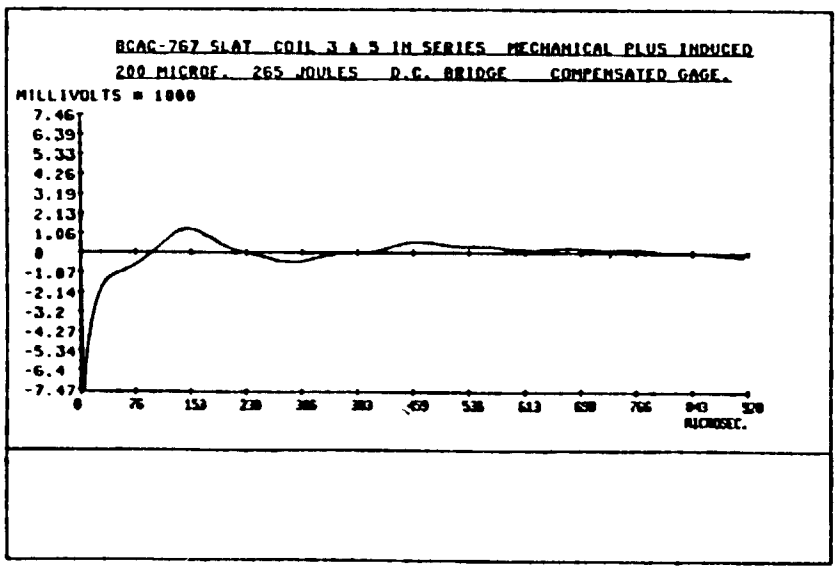

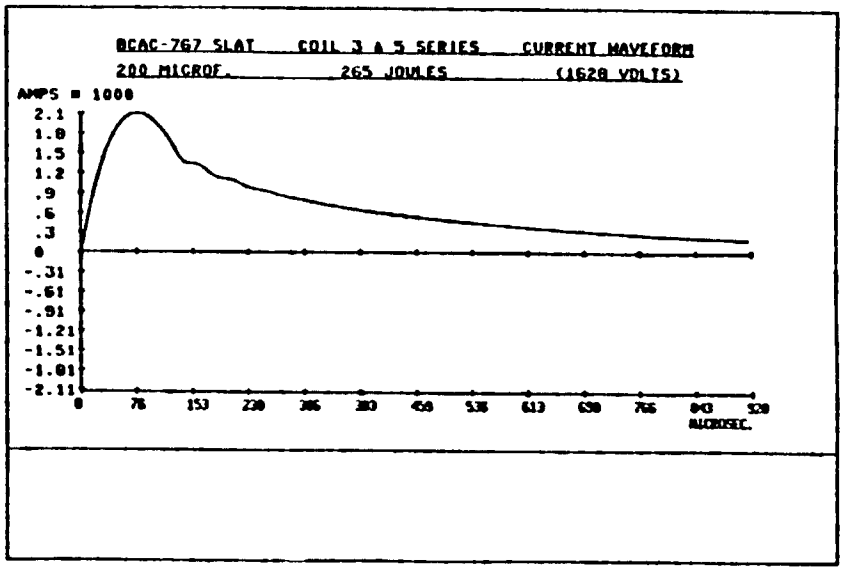

FIGURE 3-6. DC-BRIDGE STRAIN MEASUREMENT (COMPENSATED GAGE).

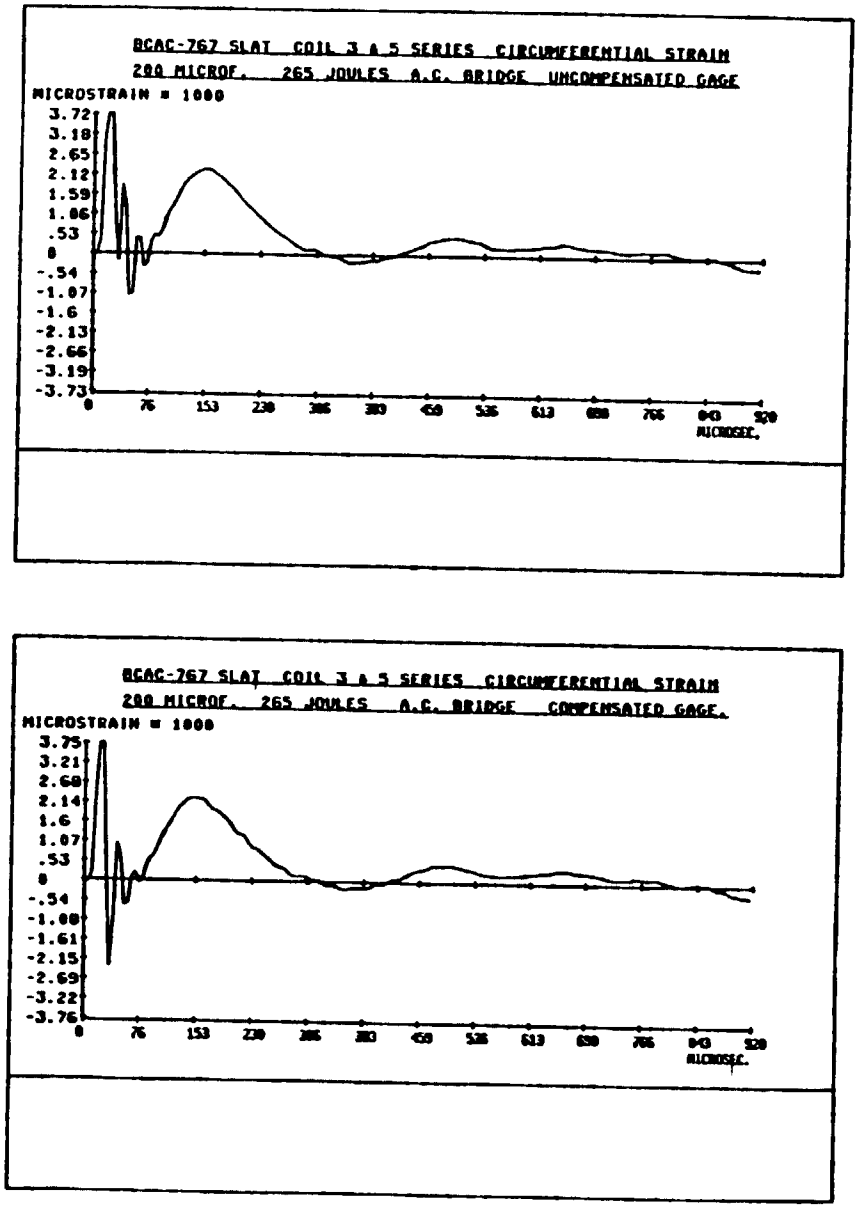

FIGURE 3-7. AC-BRIDGE STRAINS (NONCOMPENSATED AND COMPENSATED GAGE).

III. BOEING (BCAC) 767 LEADING EDGE SLAT STRAIN SURVEY

A 76 inch long section of the BCAC 767 leading edge slat was fitted with EIDI coils and tested in the NASA Lewis IRT on August 13, 14; 1984. A sketch of the leading edge cavity is shown in Fig. 3-8. Prior to the test, this geometric definition was used in a simple two dimensional computer code to approximate the fundamental mode shapes of the leading edge section. The mode shape plots are displayed in Fig. 3-9 and are used in the preliminary design of coil placement in both the upper and lower surfaces. A short 4 inch long section of the leading edge cavity was also dynamically tested to verify the analytically predicted frequencies. The first two frequencies compared favorably with the computer code.

The 76 inch long section is divided into two equal length bays of 38 inches each with ribs on each end and at the center of the span. The selected EIDI coil types and positions used in the IRT test are summarized below.

Coil No.	--Description--	Spanwise Position	Chordwise Position (measured from nose) Lower Sfc	Upper Sfc
1	2 side coils-nose attached	6.3" from lower rib	1.6"	2.5"
2	2 side coils-spar mounted	20.0" from lower rib	3.1"	2.5"
3	2 side coils-spar mounted	32.7" from lower rib	3.1"	2.6"
4	2 side coils-spar mounted	32.7" from upper rib	2.5"	2.5"
5	2 side coils-spar mounted	20.0" from upper rib	2.7"	2.4"
6	2 side coils-skin mounted	6.3" from upper rib	1.4"	1.4"

The coils used in the strain survey were coils 2, 3, and 6. Two strain gages were installed over the upper surface EIDI coils in the circumferential (chordwise) and longitudinal (spanwise) directions. In addition, a

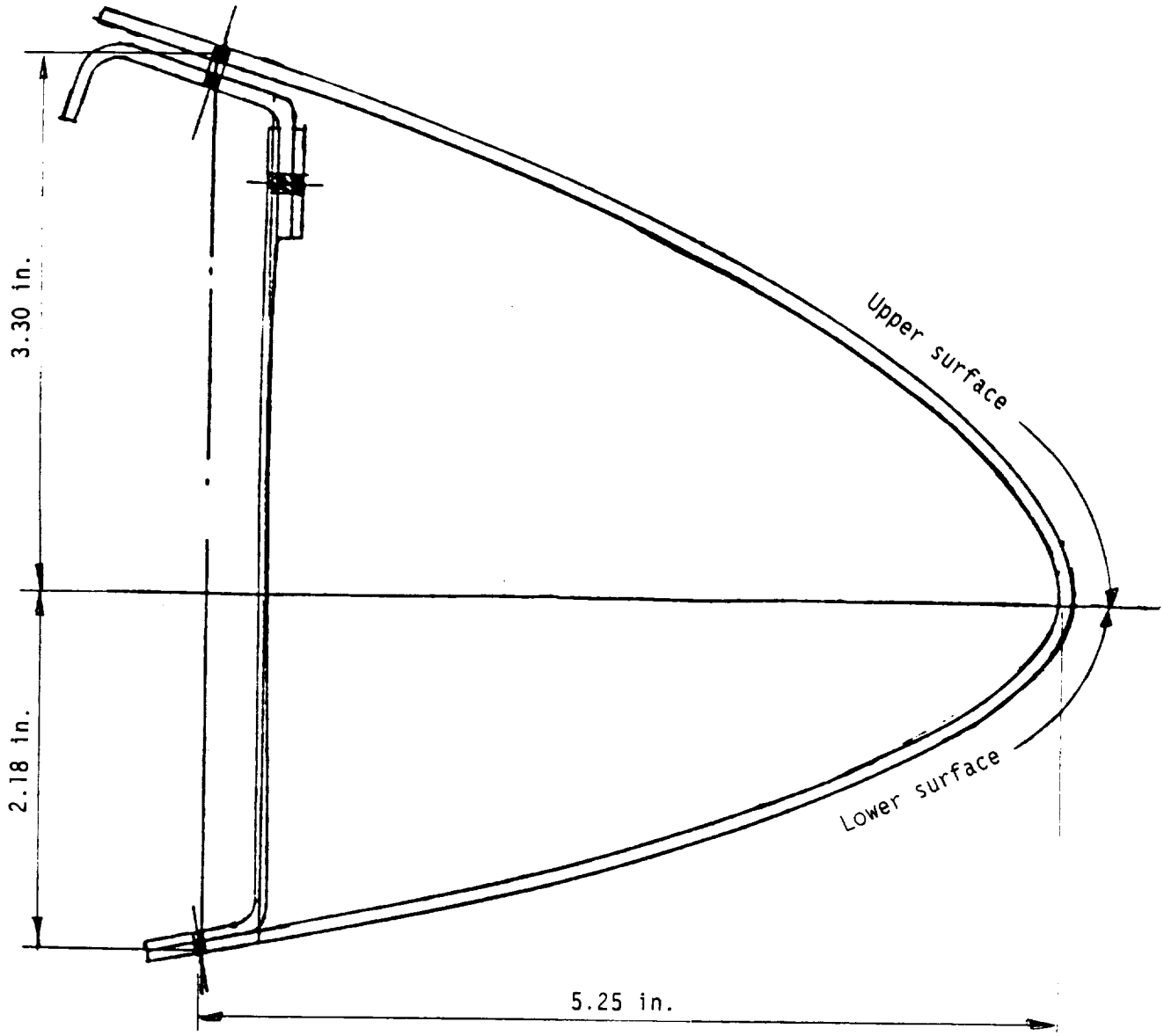

FIGURE 3-8. BOEING (BCAC) 767 LEADING EDGE SLAT CAVITY.

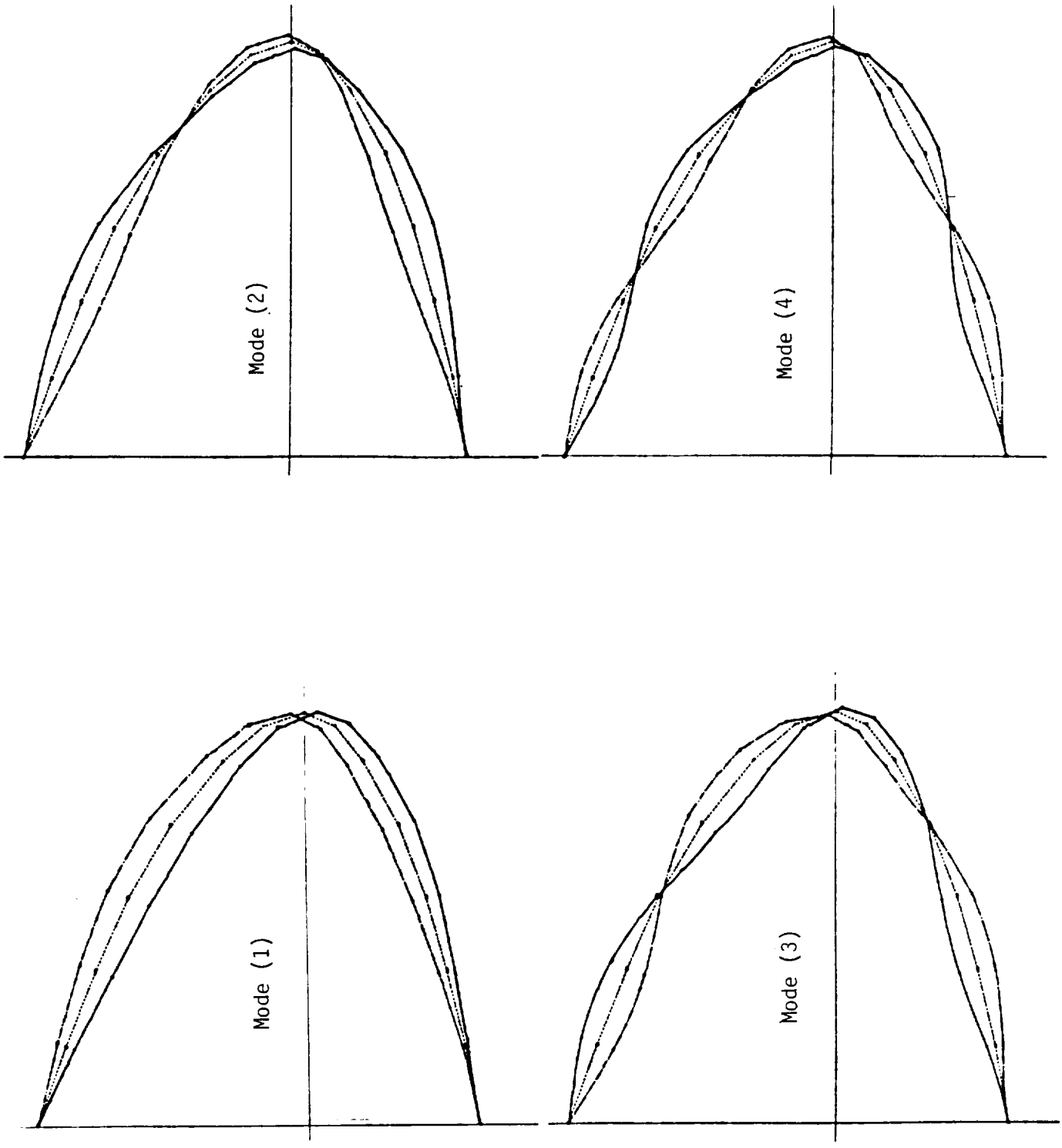

FIGURE 3-9. BCAC-767 L.E. SLAT. COPLANAR MODE SHAPES.

single chordwise gage was utilized on the lower surface over coil 3. The test data are presented in Figs. 3-10 through 3-13.

These three coils were employed in five different IRT test runs. The selected strain measurements correspond to two different sets of electrical parameters for IRT test numbers (4) and (8). Each coil pair was pulsed twice in each test with the sequence; (2,2), (3,3), and (6,6). These two test runs are summarized below.

IRT TEST	COIL (2)	COIL (3)	COIL (6)	Subjective Evaluation
(4)	400UF 900V 162 Joules	400UF 900V 162 Joules	400UF 800V 128 Joules	Fair, some residual ice
(8)	200UF 1250V 156 Joules	200UF 1250V 156 Joules	200UF 1120V 125 Joules	Clean!

The BCAC-767 slat is fabricated from 7075-T6 aluminum sheet 0.062 inches in thickness. The published mechanical properties for this material are; 78,000 psi ultimate strength, 68,000 psi yield strength, and 10,400,000 psi for the modulus of elasticity. From an examination of the strain plots one can conservatively state that the peak chordwise and spanwise strain have nearly identical occurrence times. Thus, the maximum peak stress is predicted on this basis, using a value of 0.30 for Poisson's ratio. In each case, the maximum stress will occur in the chordwise direction. These data are summarized below.

COIL LOCATION NUMBER (2):		
IRT Test (4)	Chordwise Peak:	2,710 micro-strain
162 Joules	Spanwise Peak:	1,820 micro-strain
Upper Sfc.	Maximum Stress:	37,200 psi
IRT Test (8)	Chordwise Peak:	2,520 micro-strain
156 Joules	Spanwise Peak:	1,590 micro-strain
Upper Sfc.	Maximum Stress:	34,300 psi
COIL LOCATION NUMBER (3):		
IRT Test (4)	Chordwise Peak:	2,730 micro-strain
162 Joules	Spanwise Peak:	1,840 micro-strain
Upper Sfc.	Maximum Stress:	37,500 psi
Lower Sfc.	Chordwise Peak:	3,030 Micro-strain

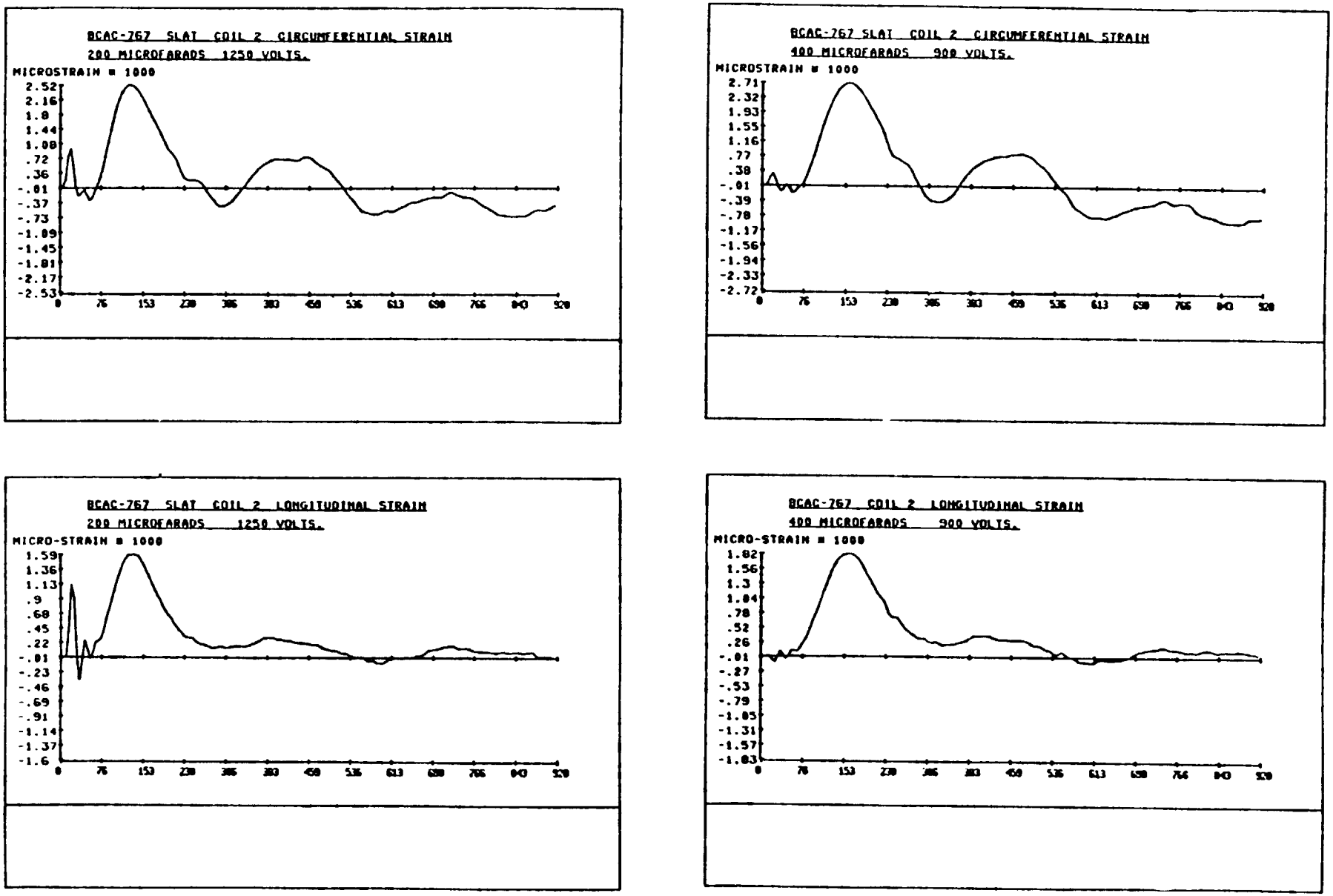

FIGURE 3-10. BCAC -767 L.E. SLAT. STRAINS AT COIL 2 (UPPER SURFACE).

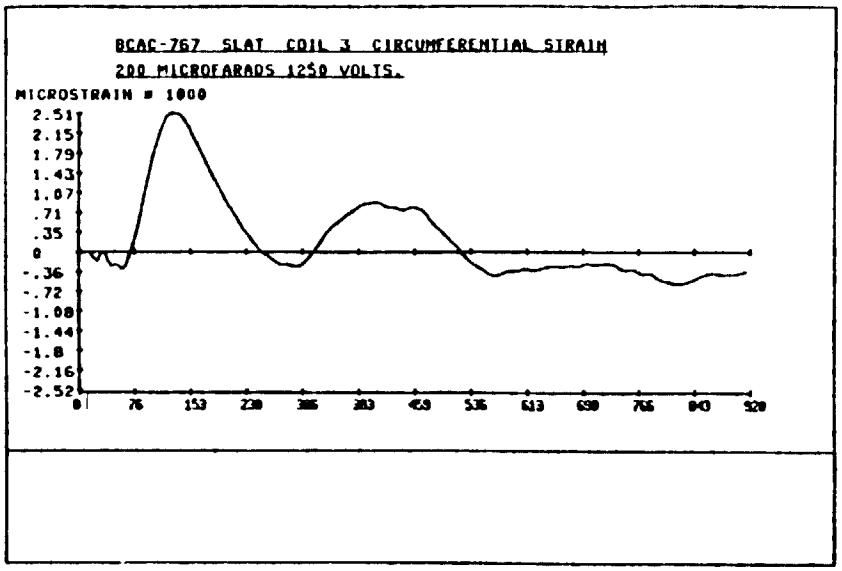

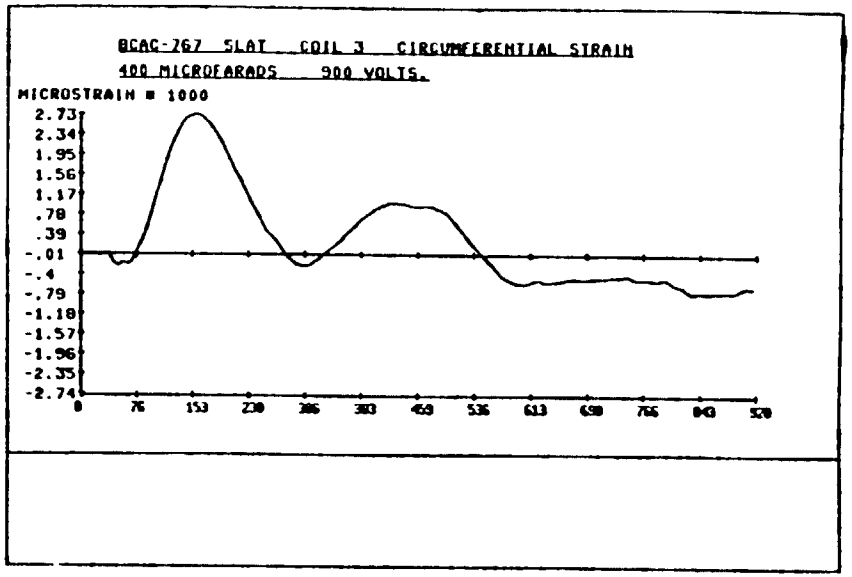

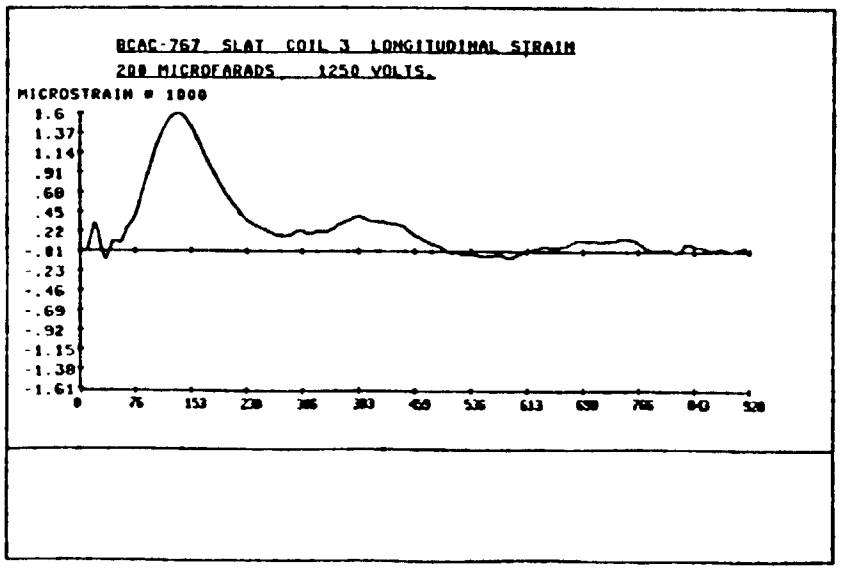

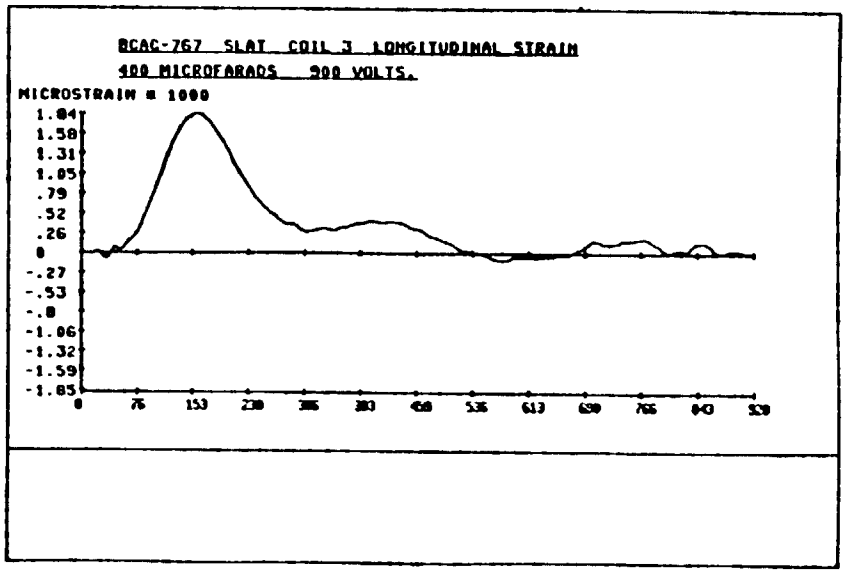

FIGURE 3-11. BCAC -767 L.E. SLAT. STRAINS AT COIL 3 (UPPER SURFACE).

ORIGINAL PAGE IS
OF POOR QUALITY

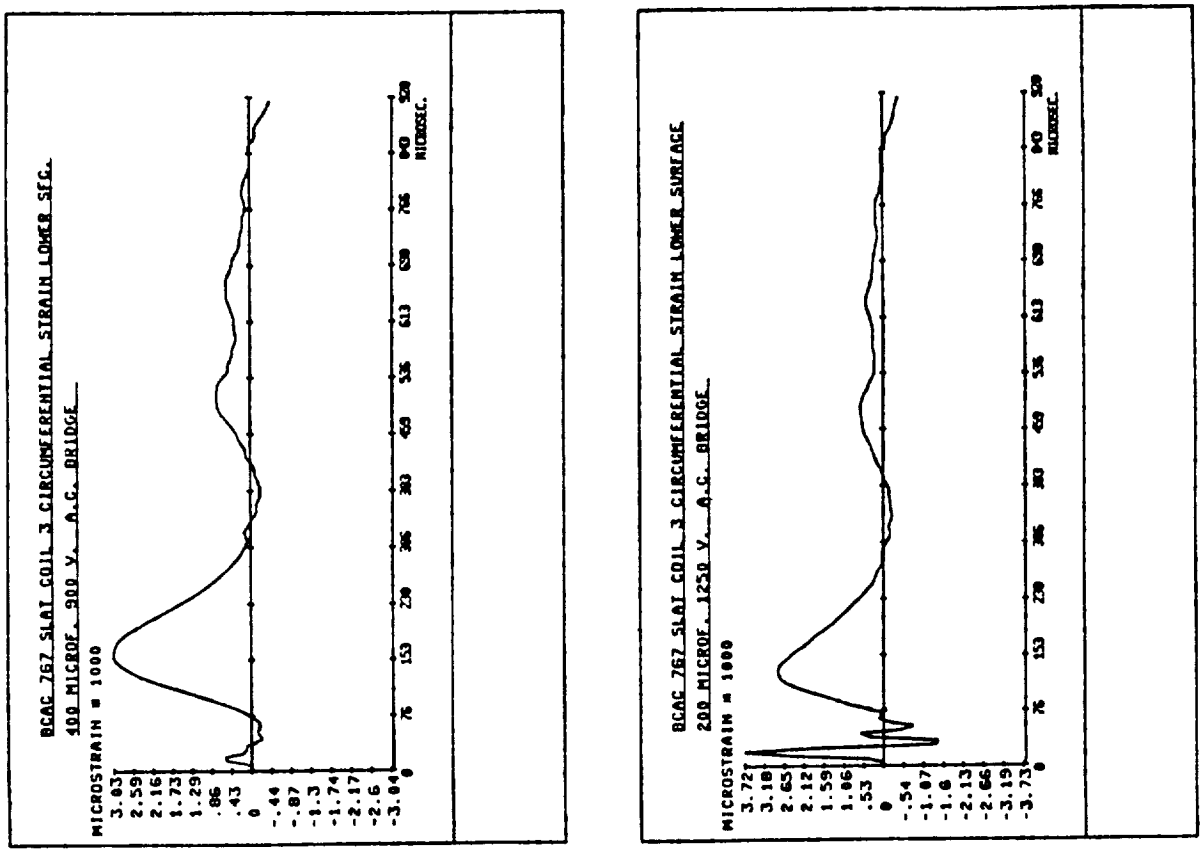

FIGURE 3-12. BCAC-767 L.E. SLAT. STRAINS AT COIL 3 (LOWER SURFACE).

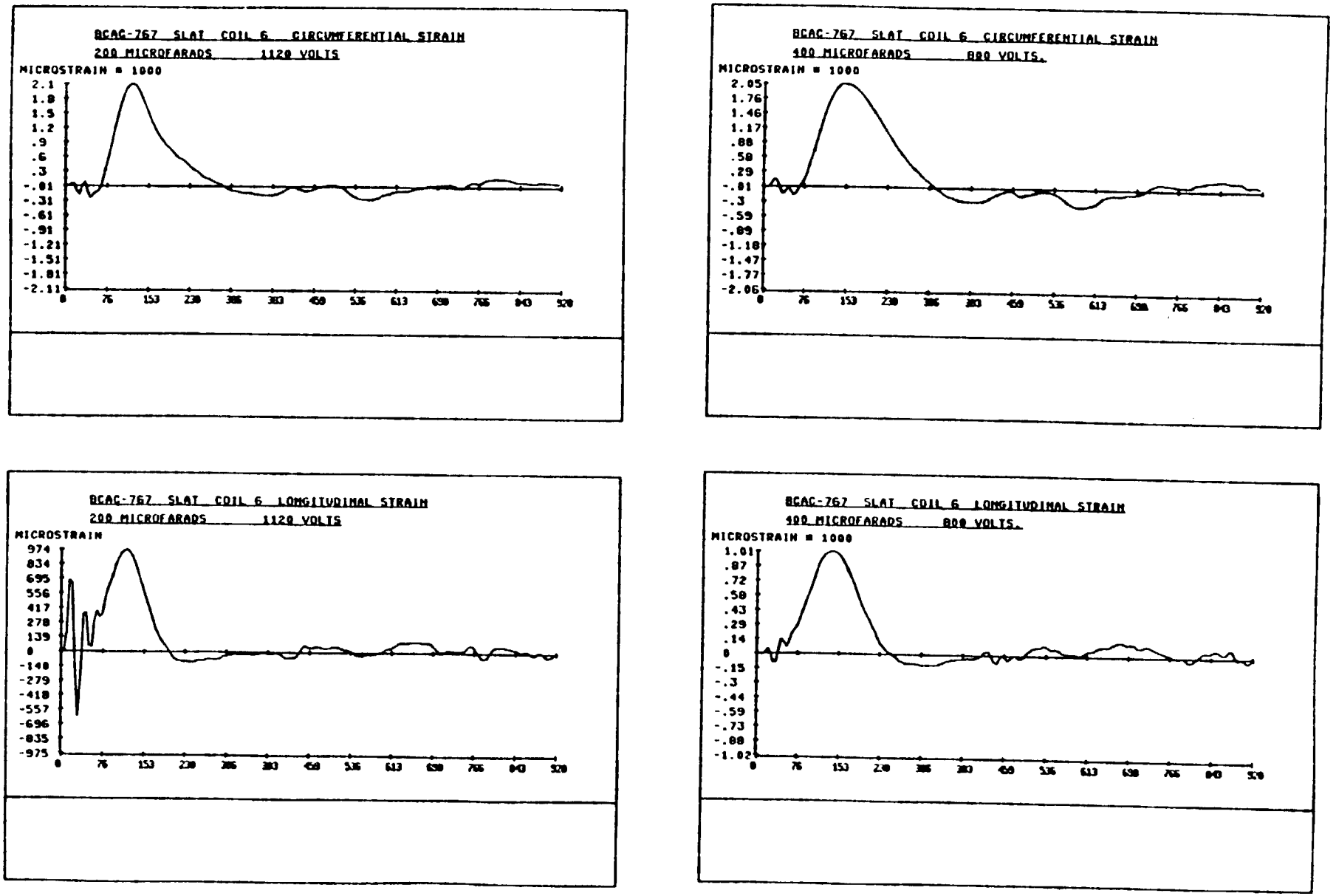

FIGURE 3-13. BCAC-767 L.E. SLAT. STRAINS AT COIL 6 (UPPER SURFACE).

IRT Test (8)	Chordwise Peak:	2,510 micro-strain
156 Joules	Spanwise Peak:	1,600 micro-strain
Upper Sfc.	Maximum Stress:	34,200 psi
Lower Sfc.	Chordwise Peak:	2,810 micro-strain
COIL LOCATION NUMBER (6):		
IRT Test (4)	Chordwise Peak:	2,050 micro-strain
128 Joules	Spanwise Peak:	1,010 micro-strain
Upper Sfc.	Maximum Stress:	26,900 psi
IRT Test (8)	Chordwise Peak:	2,100 micro-strain
125 Joules	Spanwise Peak:	974 micro-strain
Upper Sfc.	Maximum Stress:	27,300 psi

Coils 2 and 3 produce maximum stress values of 37,000 psi at the desired de-icing levels on the upper surface; this is extrapolated to 40,000 psi for the lower surface. While these values remain well below the yield strength for the material, the question of long term fatigue remains unanswered at this time. The skin mounted coil pair located at position 6, is clearly superior to the spar mounted configurations, with a maximum stress of 27,000 psi.

IV. SEMI-CYLINDER LEADING EDGE INVESTIGATIONS

A. Experimental Results

During April 1984, a semi-cylindrical leading edge type structure was designed and tested by Mr. Robert Friedberg. The semi-cylinder was selected as a representative candidate for de-icing studies, and subsequent analytical modeling. The semi-cylinder is 66 inches in length, an inside radius of 2.5 inches, and skin thickness of 0.040 inches. The material used in the fabrication was 2024-T3. The semi-cylinder is attached to a reasonably rigid spar fabricated from a fiberglass covered 40 pound density 3/4 inch thick foam core, it has no internal ribs or bulkheads except the closure ribs at each end. The semi-cylinder is attached to the spar and closure ribs with No. 10 sheet metal screws spaced two inches center to center. The semi-cylinder was equipped with two coil configurations, a single coil and a pair of series connected double coils for two different IRT tests. The first IRT test was performed on May 19, 1984 and employed a single coil located at the nose and mid-length of the semi-cylinder as shown in Fig. 3-16. The coil had a nominal radius of 1.25 inches with 50 turns of rectangular copper conducter and shaped to conform to the internal radius with provision for a 0.010 inch air gap.

Acceleration data was established for the single coil configuration and is displayed in Figs. 3-14 and 3-15 for the energy level of 36 Joules as noted. The accelerometer used in the investigation was an Endevco Model 22, which has a total weight with the attached cable of 0.4 grams and a physical size of 0.14 inches diameter, 0.095 inches in height and a response level of approximately 12,000 g's. Mass loading of the light weight aluminum leading structures is an important consideration

and this particular accelerometer has the largest g level per unit mass known to project personnel. Fig. 3-14 represents the spanwise variations of acceleration measured in three inch increments from mid-span. The data for S=+3" and S=-3" should of course be identical. The discrepancies shown are well within the variation of the shell boundary conditions and un-symmetric positioning of the coil. The spanwise response delays, indicated by the dashed line, is interesting and probably represents the longitudinal propagation of a circumferential bending wave. The velocity is on the order of 65,000 inches per second. The chordwise variations of acceleration, shown in Fig. 3-15, should again be equal for positions either side of the nose, e.g. C=+2" and C=-2". It is further noted that the 200 microfarad capacitance results produces peak accelerations whose magnitude of 10 kilo-g's is approximately twice those corresponding to the 400 microfarad results. This is attributed to the increased rise time for the EIDI pulse for smaller values of capacitance, and dramatizes the structural response sensitivity to changes in the EIDI electrical parameters.

Strain gages were installed on both the inner and outer surfaces of the semi-cylinder at mid-span. The position and numerical designation of each gage is noted in Fig. 3-16. Strain data was established for the single coil configuration for an energy level of 128 Joules; 400 micro-farads and 800 volts. Compensated gages were installed and the DC-bridge process was employed for the measurements. The data is presented in Figs. 3-17 through 3-20 for each of the four gage positions as analog records and includes the principal occurrence times for strain peaks. Some data is further presented as bending and membrane strains. Peak occurrence times for the chordwise and spanwise peaks do not coincide, hence it is difficult

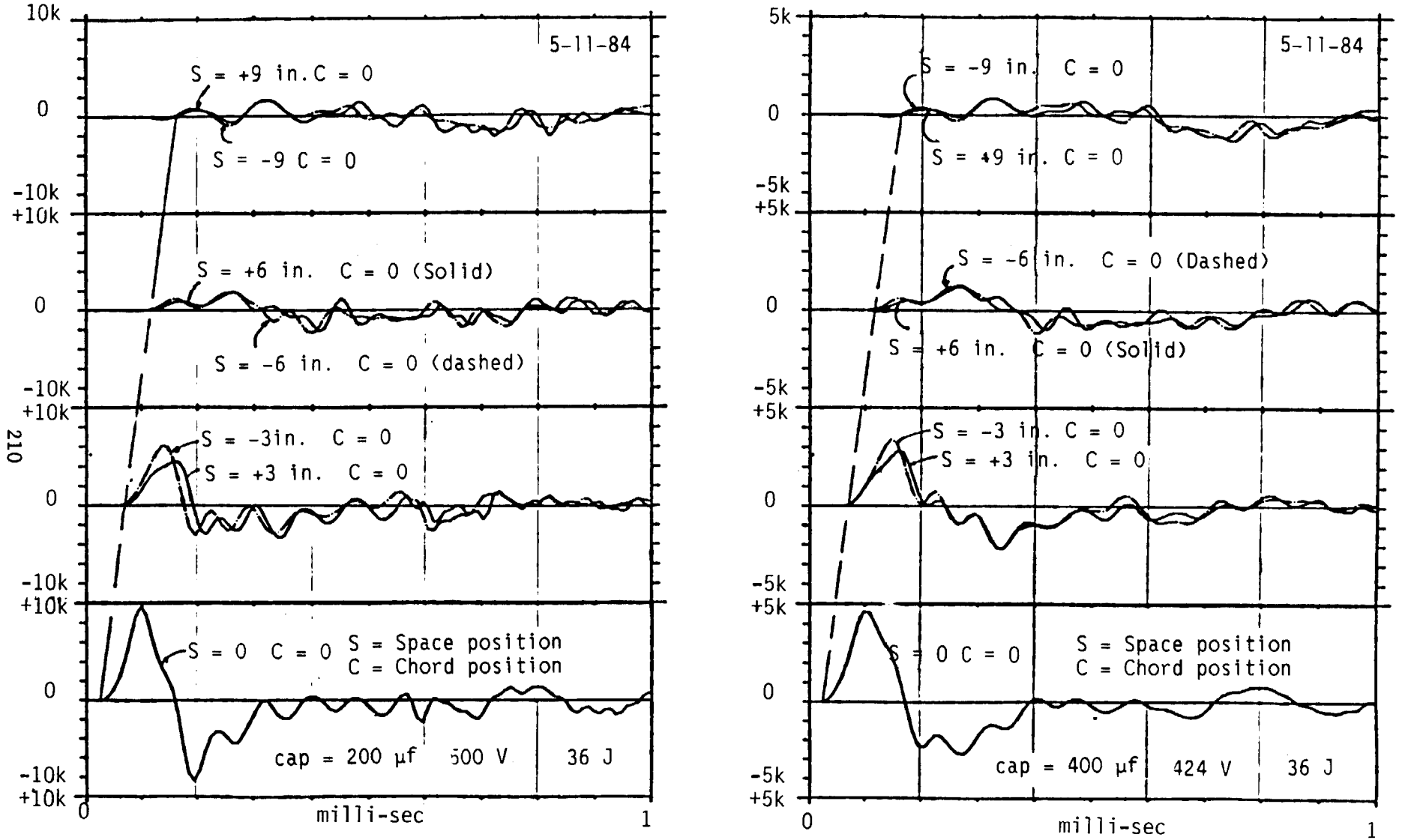

FIGURE 3-14. LONGITUDINAL (SPANWISE) ACCELERATION RESPONSE (g's).

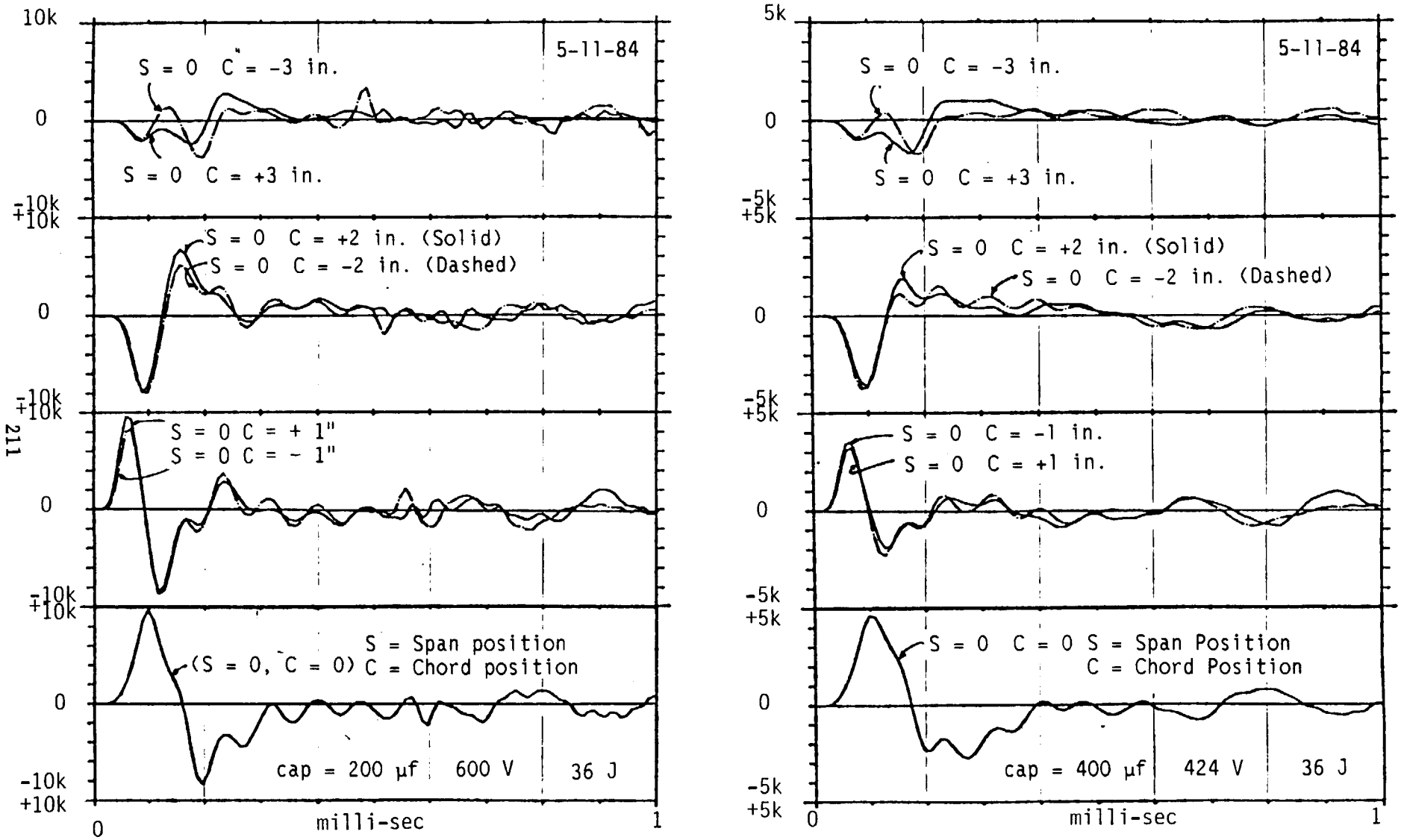

FIGURE 3-15. CIRCUMFERENTIAL (CHORDWISE) ACCELERATION RESPONSE (g's).

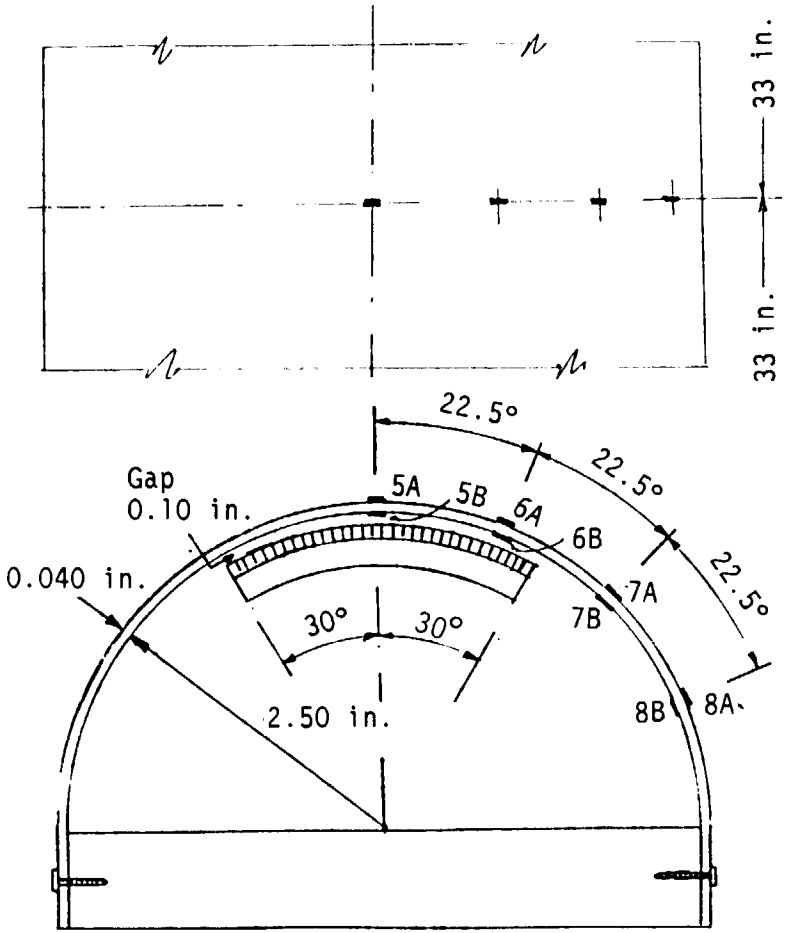

2.5" RADIUS SEMI-CYLINDER (SINGLE COIL).
CIRCUMFERENTIAL (CHORDWISE) STRAIN GAGE NUMBERS AND LOCATIONS

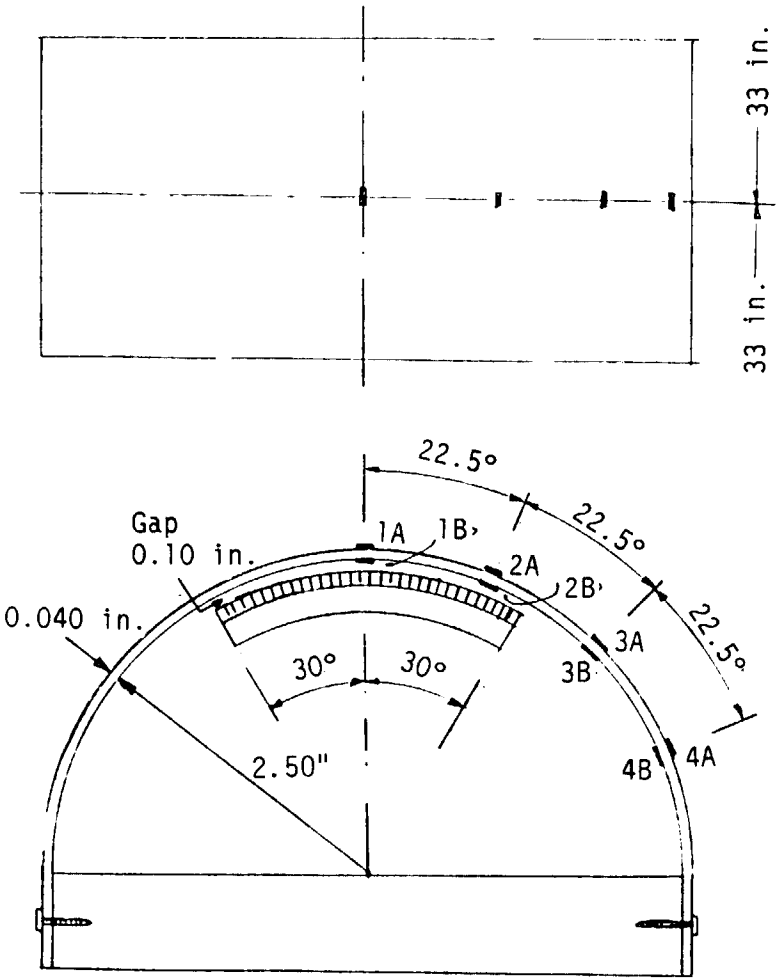

2.5" RADIUS SEMI-CYLINDER (SINGLE COIL).
LONGITUDINAL (SPANWISE) STRAIN GAGE NUMBERS AND LOCATIONS

FIGURE 3-16. STRAIN GAGE NUMBERS AND LOCATIONS.

2.5" RADIUS SEMI-CYLINDER (SINGLE COIL).
CIRCUMFERENTIAL (CHORDWISE) STRAIN: (C = 400 V = 800 JOULES).

2.5" RADIUS SEMI-CYLINDER (SINGLE COIL).
LONGITUDINAL (SPANWISE) STRAIN: (C = 400 V = 800 128 JOULES).

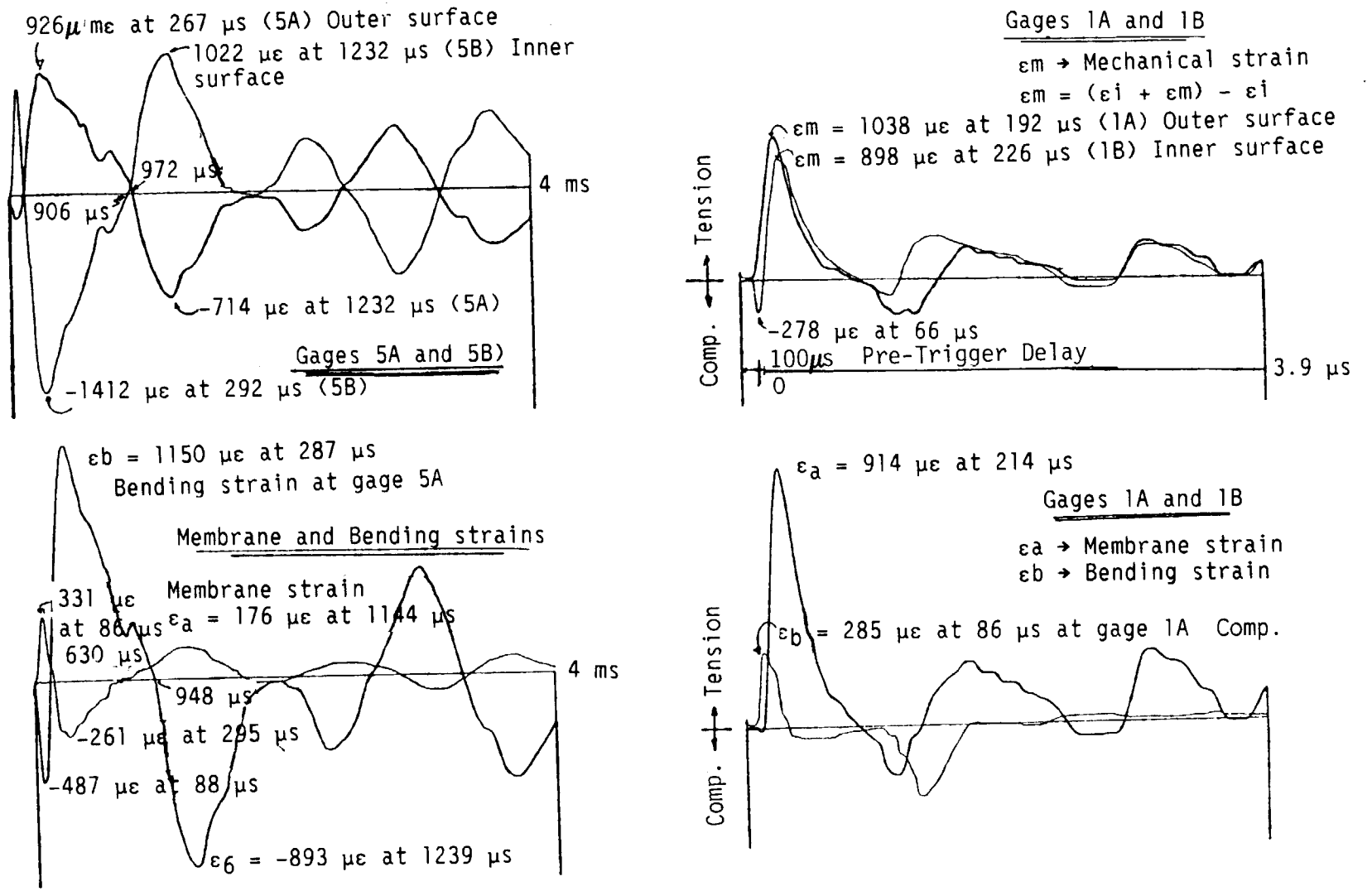

FIGURE 3-17. SEMI-CYLINDER STRAINS (GAGES 1 AND 5).

2.5" RADIUS SEMI-CYLINDER (SINGLE COIL).
CIRCUMFERNTIAL (CHORDWISE) STRAIN: (C = 400 V = 800 128 JOULES).

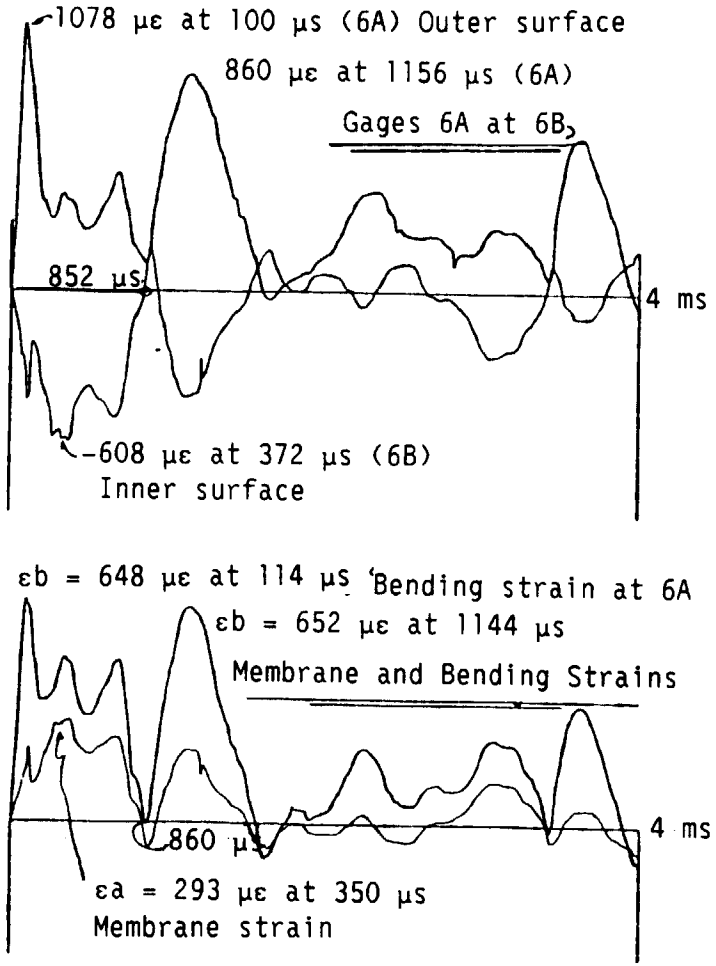

2.5" RADIUS SEMI-CYLINDER (SINGLE COIL).
LONGITUDINAL (SPANWISE) STRAIN: (C = 400 V = 800 128 JOULES).

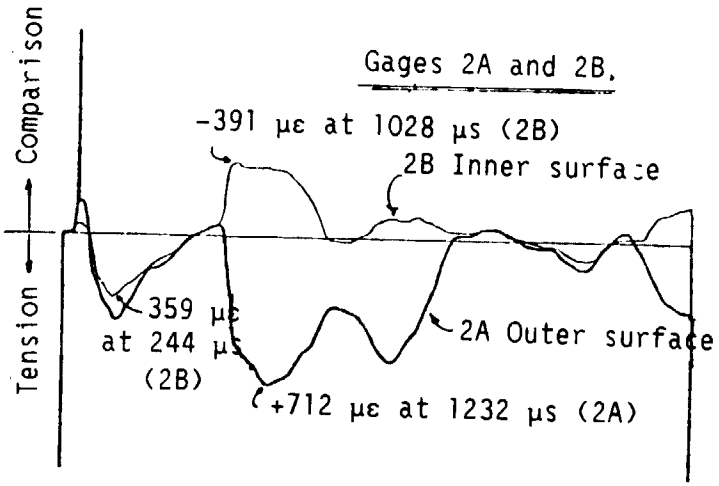

FIGURE 3-18. SEMI-CYLINDER STRAINS (GAGES 2 AND 6).

2.5" RADIUS SEMI-CYLINDER (SINGLE COIL).
CIRCUFERENTIAL (CHORDWISE) STRAIN: (C = 400 V = 800 128 JOULES).

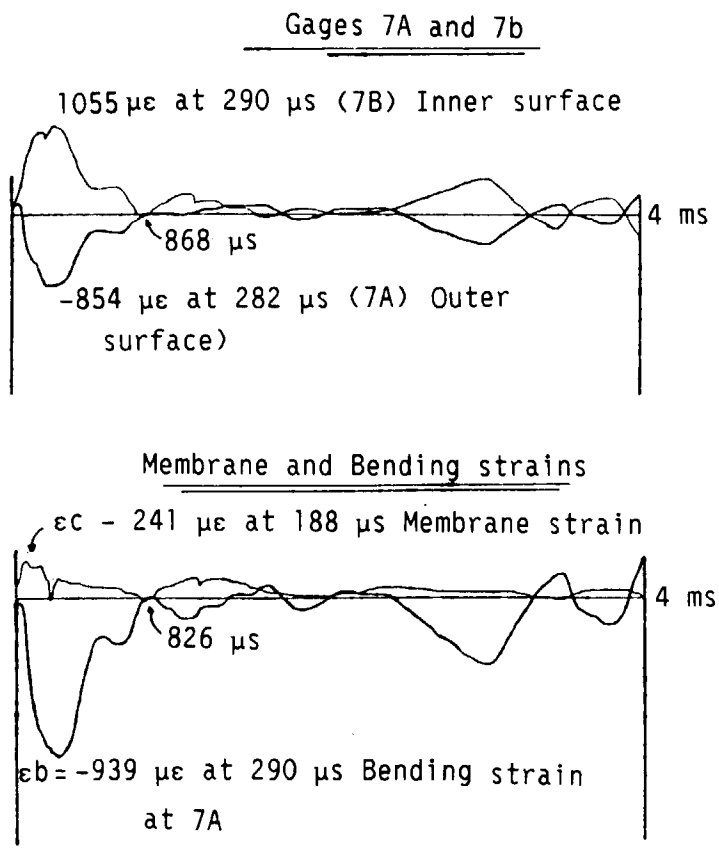

2.5" RADIUS SEMI-CYLINDER (SINGLE COIL).
LONGITUDINAL (SPANWISE) STRAIN" (C = 400 V = 800 128 JOULES).

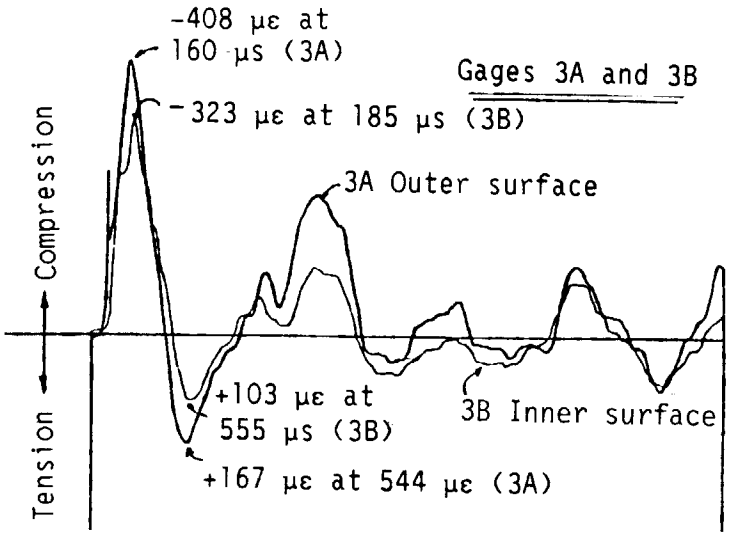

FIGURE 3-19. SEMI-CYLINDER STRAINS (GAGES 3 AND 7).

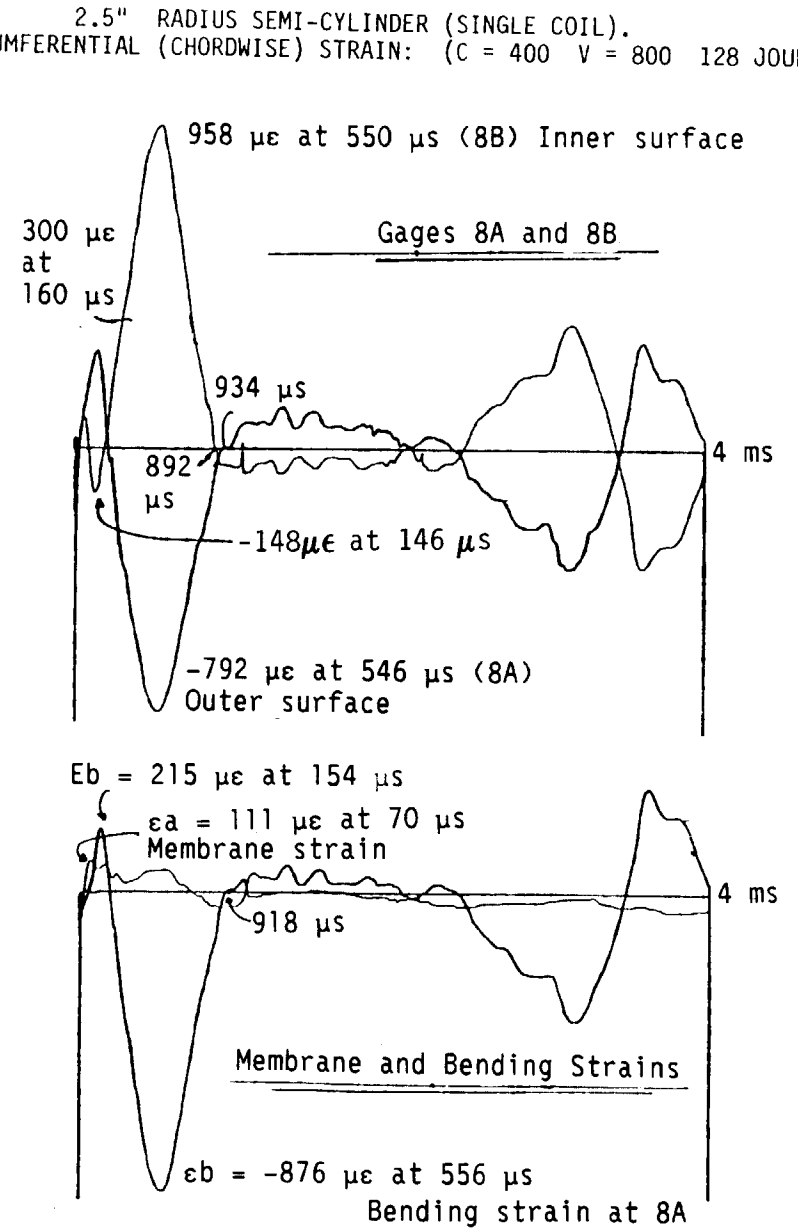

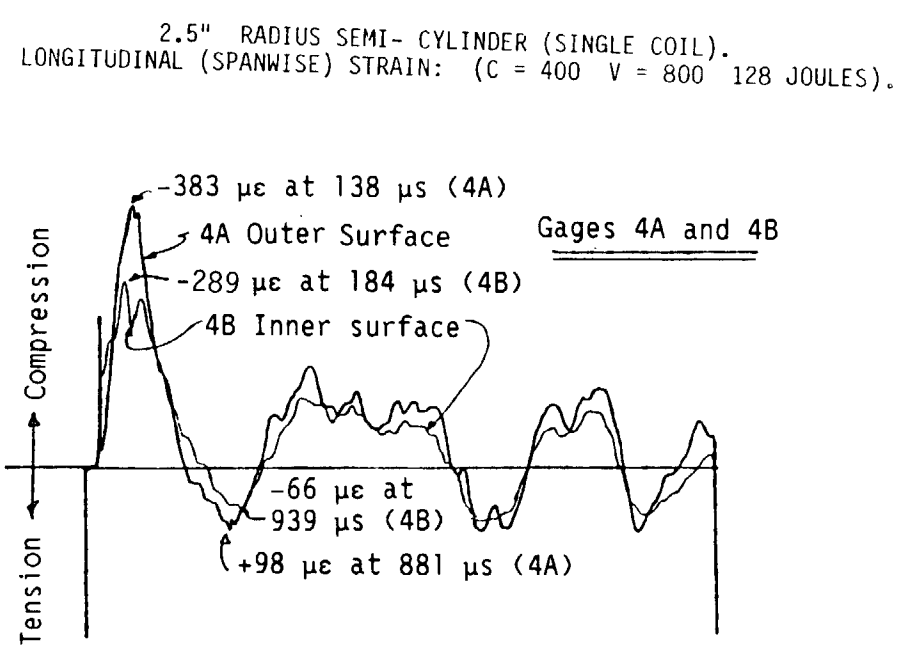

FIGURE 3-20. SEMI-CYLINDER STRAINS (GAGES 4 AND 8).

to establish the maximum stress values. The experimental strains indicate maximum values of about 1100 micro-strain, which corresponds to maximum stresses on the order of 14,000 psi for the 128 Joule test condition. The energy level used in the IRT test of May 19, 1984 was 162 joules; 400 microfarads and 900 volts. The corresponding stress level for this test condition is approximately 17,700 psi.

An additional test was conducted on gage position (1) to establish the spanwise membrane strain for three different capacitance values and equal energy levels. The data is displayed in Fig. 3-21 and clearly indicates the decreasing rise time of the strain response as the capacitance is decreased. The current delivered to the coil is also displayed with the membrane strain. Case (3) of this test, evaluated for a capacitance of 100 microfarads, serves as a measure of the maximum strain-rate response experienced for a EIDI pulse. The peak of 1300 micro-strain occurring at 141 microseconds represents an approximate strain-rate of 10 per second, which could reach 40 to 50 per second for increased values of voltage. Most authorities, Ref. 3-5, consider values below 100 per second as a intermediate strain-rate regime where quasistatic stress-strain properties are still applicable. Strain-rates in excess of 1000 per second are normally associated with elastic-plastic shock wave propagation and hence the EIDI pulse may be classified as a very mild shock environment.

The semi-cylinder was configured with a pair of EIDI coils and a second IRT test was conducted on August 17, 1984. The coils were connected in series, placed at mid-span, and oriented at equal angles of 45 degrees measured from the nose. The radius of each coil was 0.875 inches and shaped to conform to the cylindrical surface with

2.5" Radius Semi-Cylinder
Axial (Membrane) Strain at Gage Location 1.
A constant energy (1/2 CV^2 = 128J) for 3 values of capacitance.
Case (1) C = 400 μf V = 800 volts

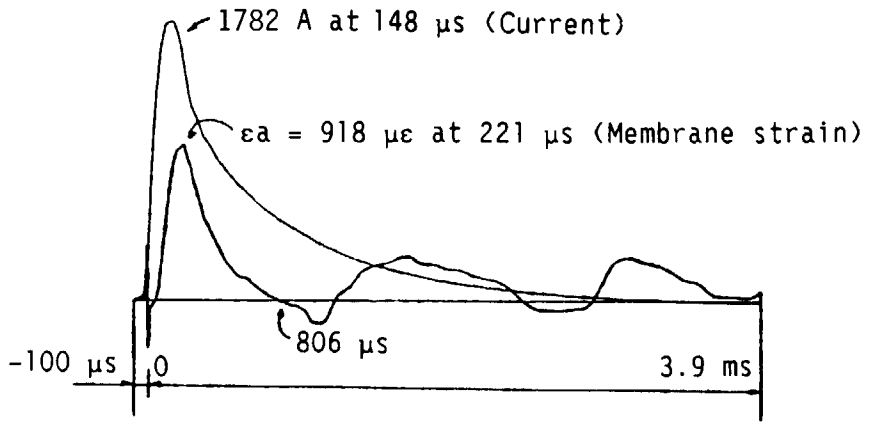

Case (2) C = 200 μf V = 1131 volts

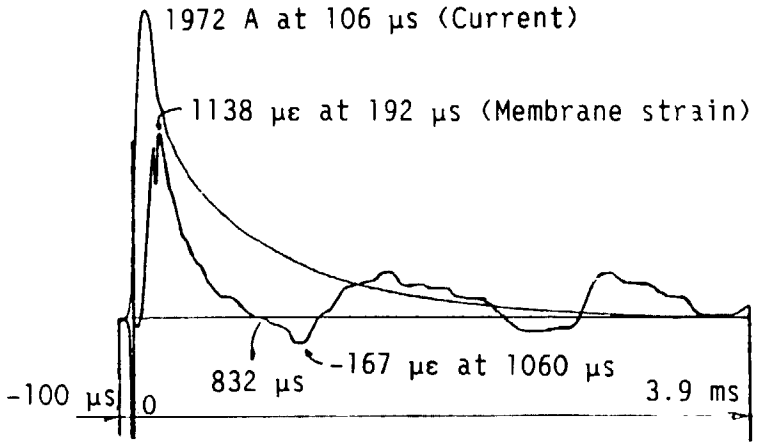

Case (3) C = 100 μf V = 1600 volts

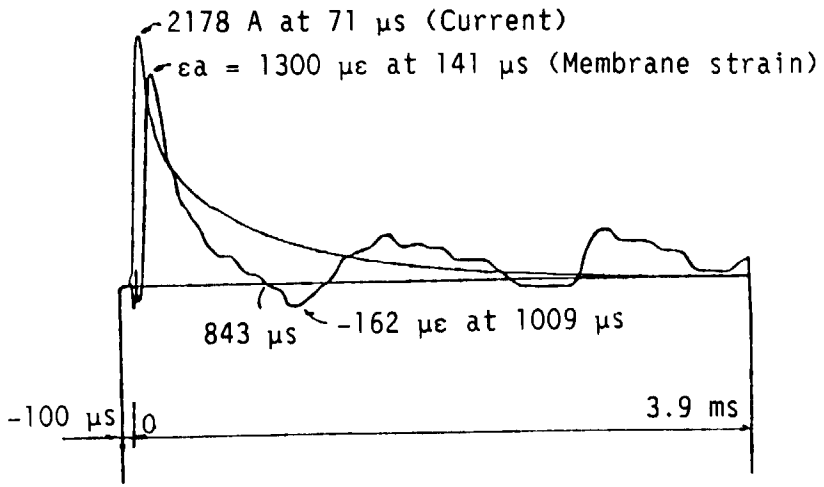

FIGURE 3-21. MEMBRANE STRAIN AT GAGE 1 FOR THREE VALUES OF CAPACITANCE.

an air gap. The established de-icing level was approximately 170 to 200 joules. The 400 microfarad and 1000 volt test condition was subjectively evaluated as optimum. The double coil configuration failed to perform as well as the single coil and this is attributed to the angular position of the coils from the nose. An angle of less than 45 degrees or the ability to independently pulse each coil would probably have been more efficient. A limited amount of strain data was acquired for the double coil configuration and this is presented in Fig. 3-22. During the August 17 IRT test, some data was acquired for the double coil configuration under icing conditions. The results confirmed earlier observations related to acceleration in that the peak values are reduced by approximately 20 to 30 per cent for the first pulse when ice is present on the airfoil. Circumferential bending strains for the double coil test exhibited reductions of approximately 15 to 25 per cent for the first coil pulse whereas the membrane strains remained basically unchanged.

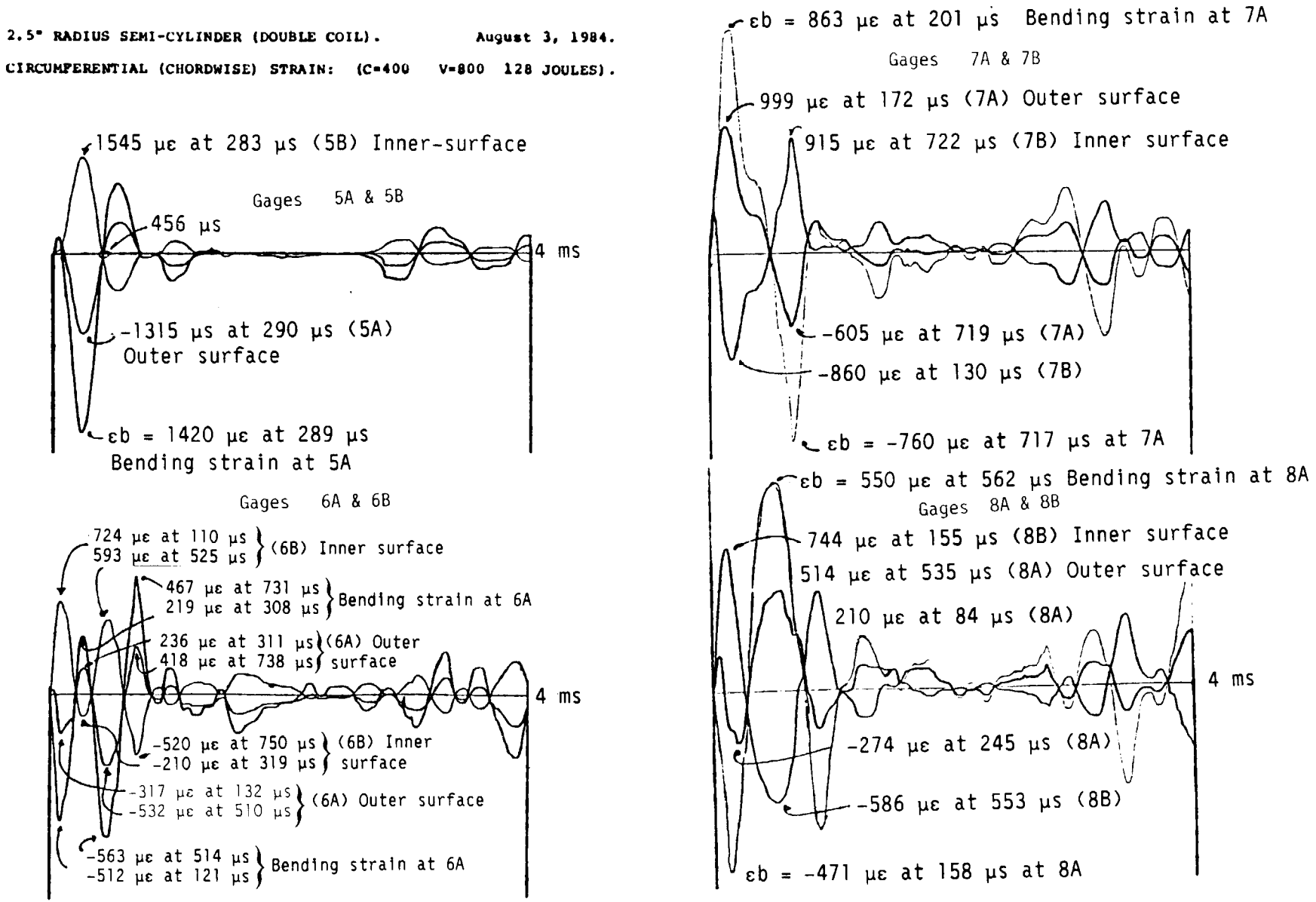

FIGURE 3-22. DOUBLE COIL CIRCUMFERENTIAL (CHORDWISE) STRAINS.

B. Analytical Studies (Idealized Boundary Condition).

The semi-cylindrical leading edge structure was chosen for analytical study because of its geometric simplicity and the vast literature which exists for open cylindrical shells. Leissa, Ref. 3-6, reports that there are no less than 18,496 distinct problems for this shell corresponding to the numerous combinations of boundary conditions that may be selected for the four edges. An overwhelming majority of investigations have been directed to but one of these sets of boundary values and that is when all edges of the shell are supported by shear diaphragms. The semi-cylinder is further classified as a deep open shell requiring a consideration of the transverse shearing force resultants and the inclusion of tangential inertia effects for dynamic studies.

The boundary conditions for an open cylindrical shell supported by shear diaphragms are exactly satisfied by choosing trigonometric displacement functions of the form:

$u = A \cos(\lambda s) \sin(N\theta)$ longitudinal displacement,
$v = B \sin(\lambda s) \cos(N\theta)$ transverse displacement,
$w = C \sin(\lambda s) \sin(N\theta)$ normal displacement;

where, $\lambda s = M\pi x/L$ R=shell radius L=shell length.

Theparameters $\lambda = M\pi/L$ and N are spatial wave frequencies with half wave lengths defined as follows:

(L/M) longitudinal direction,
$(R\pi/N)$ circumferential direction.

A computer code was written based on these ideal boundary conditions that employed both the Donnell-Mushtari and Love-Timoshenko equations of motion. The code was used in an attempt to duplicate some of the dynamic response effects observed in the experimental results. The values of 'M' and 'N' in the spatial wave frequency expressions are integers and

combinations of each will produce a corresponding discrete resonant frequency and vibratory mode shape. The first analytic study was related to finding the maximum values of these integers for a selected bandwidth or cutoff frequency. The results of this study are summarized in the table below for a semicylindrical shell with the following geometric shape and material properties.

L=66 inches R=2.52 inches H=0.040 inches (thickness).
E=10,500,000 psi U=0.30 Poison's ratio
0.10 pounds per cubic inch weight density.

Bandwidth Hertz	M(max)	N(max)	Love-Timoshenko Mode Count
3,000	20	7	95
4,000	27	8	148
6,000	40	9	265
8,000	54	11	434
10,000	67	12	623

The calculated dynamic response of the spanwise and chordwise acceleration levels with a single coil placed at mid-span was performed using the electrical parameters; 400 microfarads and 424 volts. The cutoff frequency was selected as 10,000 Hertz and the results are displayed in Fig. 3-23. The structural damping parameter used in this investigation is noted as a 1 per-cent damping factor at 1,000 Hertz; thus a frequency of 4,000 Hertz would have a corresponding damping factor of 4 percent. The calculated response has several matching characteristics with the experimental response shown in Fig. 3-14, in spite of the fact that the boundary conditions do not match for the two results. In addition, the temporal behavior of the 400 microfarad pulse was synthesized from the 600 microfarad experimental result reported by Schrag, Ref. 3-1. It is further observed that 155 of the potential 623 modes were active or participated in the dynamic response, the remaining 468 modes were inactive due to the

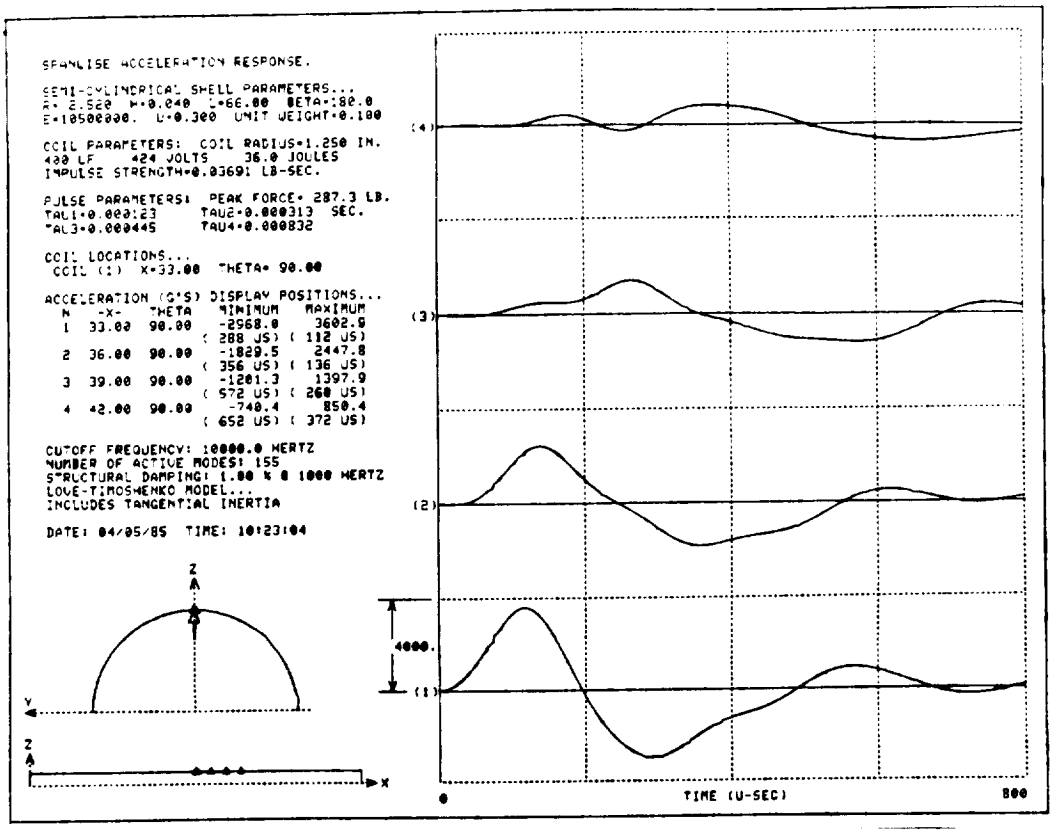

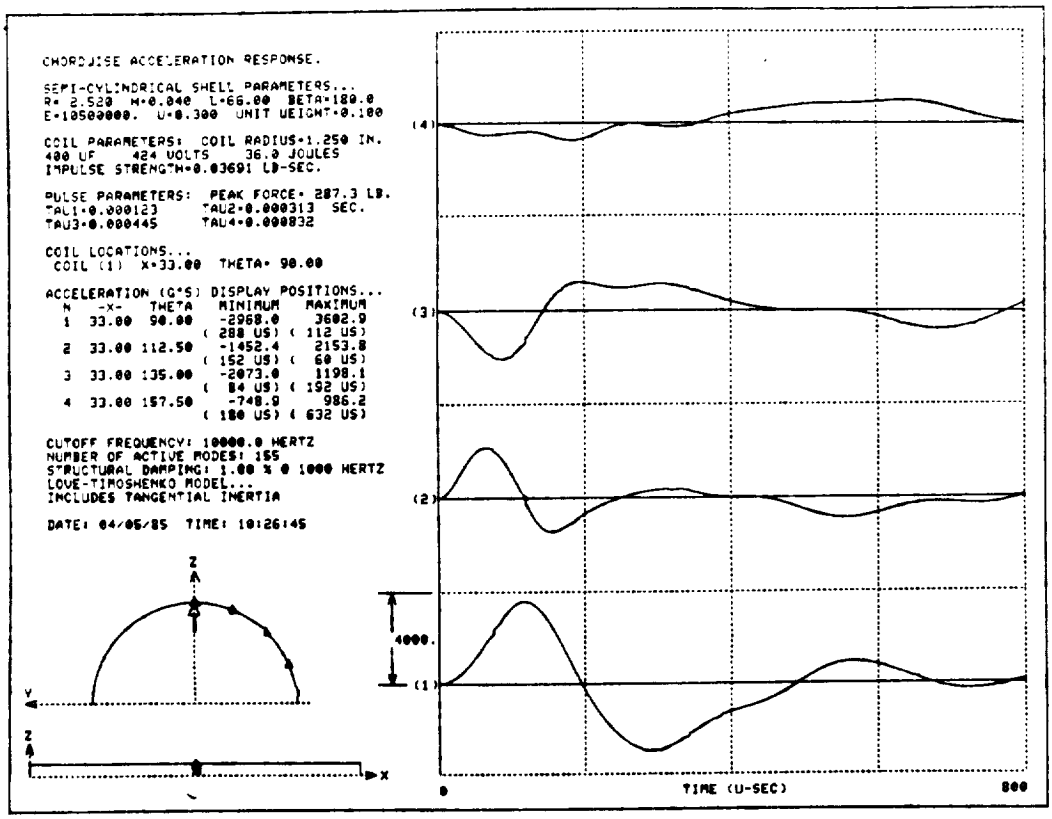

Figure 3-23 Spanwise and Chordwise Acceleration Response.

spatial symmetry of the pressure pulse. Moving the coil a slight distance in both the spanwise and chordwise directions from the symmetric nose and mid-length position will force a majority of the modes to participate, however the peak response values will change only slightly as shown in the upper portion of Fig. 3-24, even though 607 modes were active. The peak accelerations and corresponding occurrence times from Fig. 3-24 are noted below:

First Positive Peak: 3,619 g's at 112 microsec.
First Negative Peak: -2,960 g's at 288 microsec.

Fig. 3-25 is a display of the contribution of each of these 607 active modes to the two acceleration peaks noted above. The results are shown in an ascending frequency order and the two peak response accelerations have attained about 95 percent of their final value for a corresponding cutoff frequency of approximately 4,000 Hertz. This result is rather important for finite element shell studies, for it suggests that the approximate discrete model need only match the modal frequencies for the reduced bandwidth to produce a 92 percent confidence limit in peak response prediction. The lower portion of Fig. 3-24 represents the acceleration response corresponding to 4,000 Hertz cutoff frequency.

Two additional plots, Figs. 3-26 and 3-27 are included to present the analytical predicted mid-span circumferential strain response for the outer and inner surface and may be compared directly to the experimental results displayed in Figs. 3-17 through 3-20. The correlations agree in that longitudinal strains are dominated by membrane effects, whereas bending behavior is dominant in the circumferential strain response. Again, the results only indicate similarity to the experimental results and the peak response occurrence times cannot be accurately matched until the boundary conditions and forces pulse characteristics are properly represented.

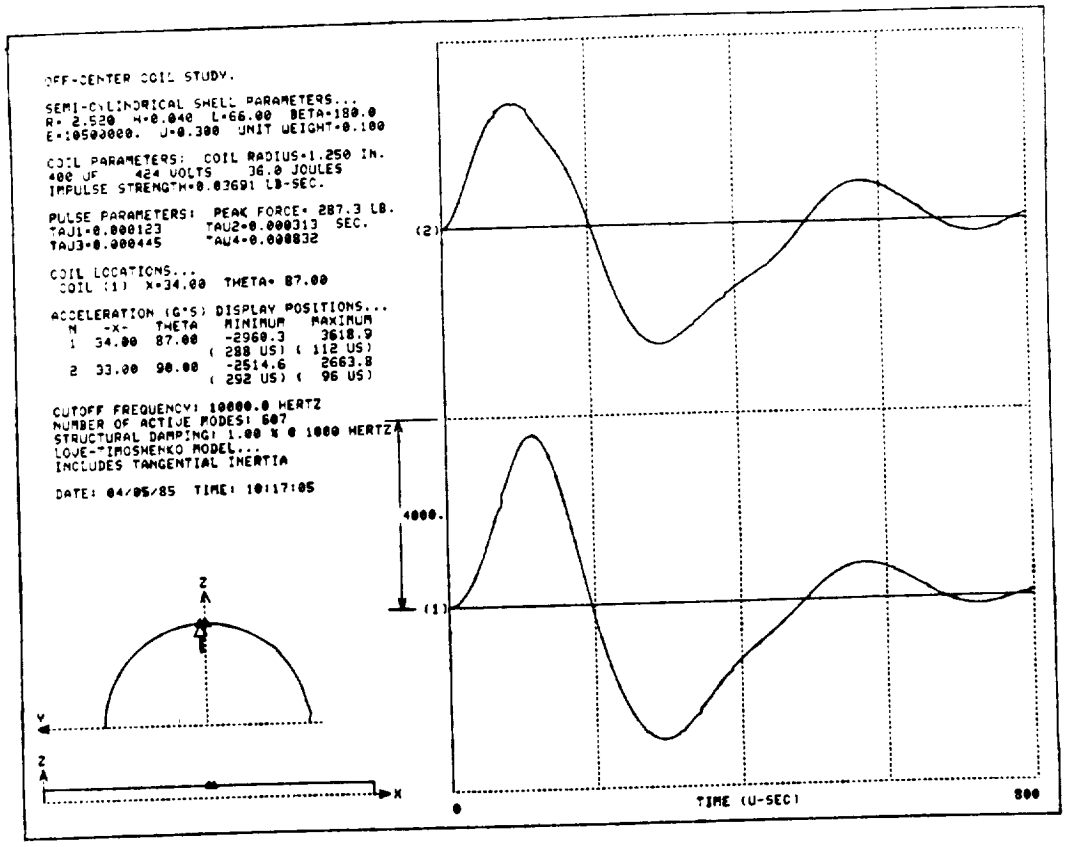

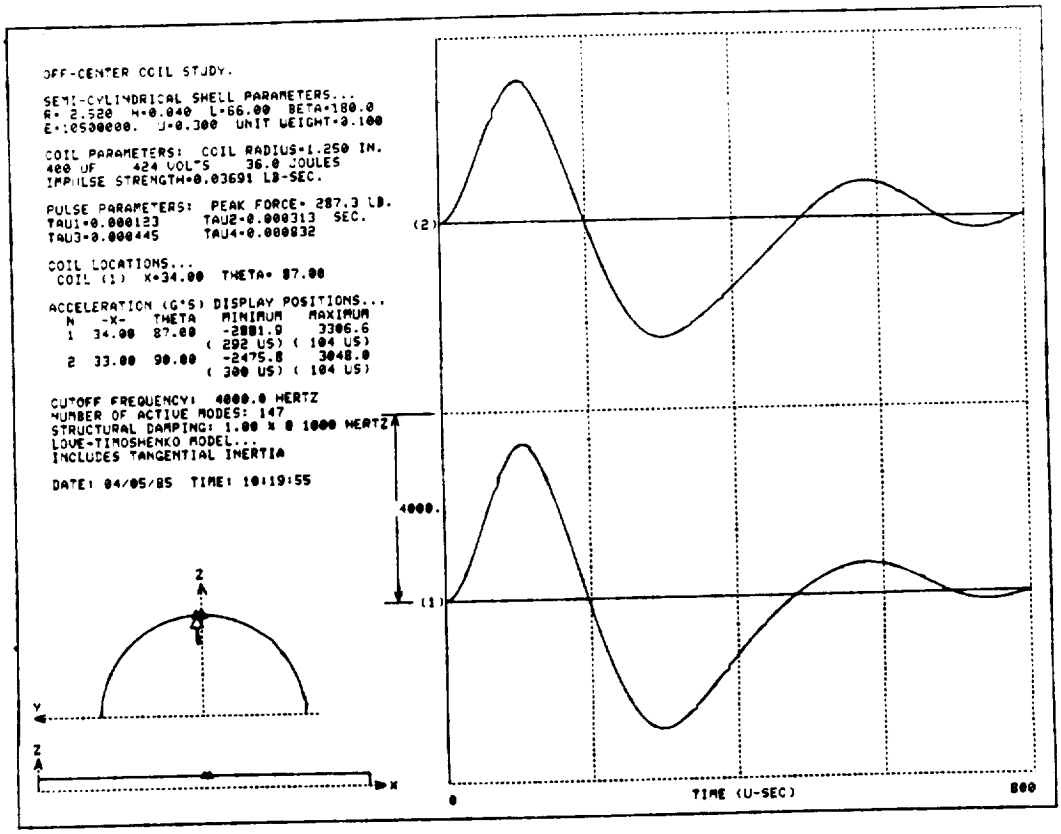

Figure 3-24 Peak Accelerations at Coil Location.

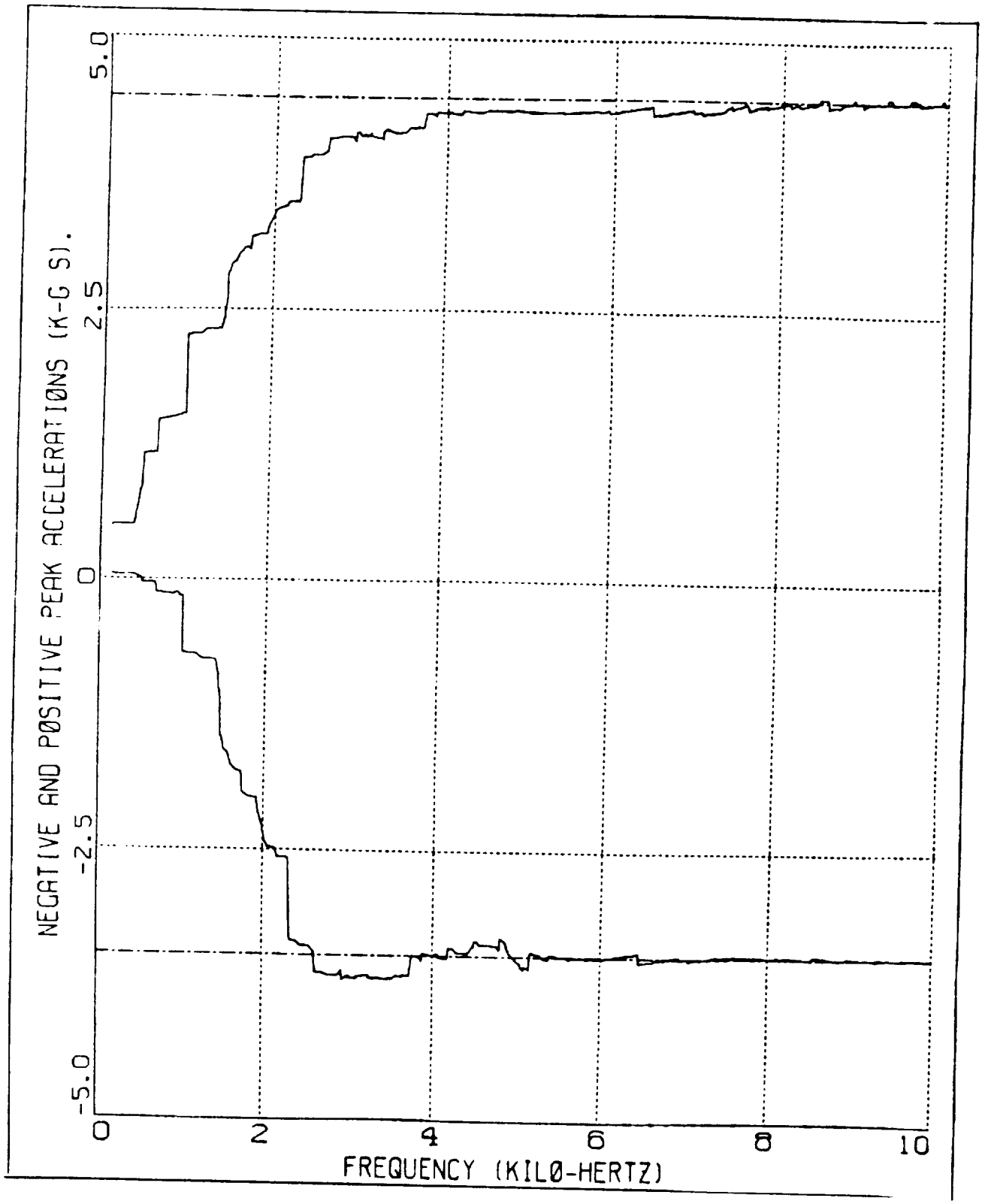

Figure 3-25 Modal Contribution to Peak Acceleration Response

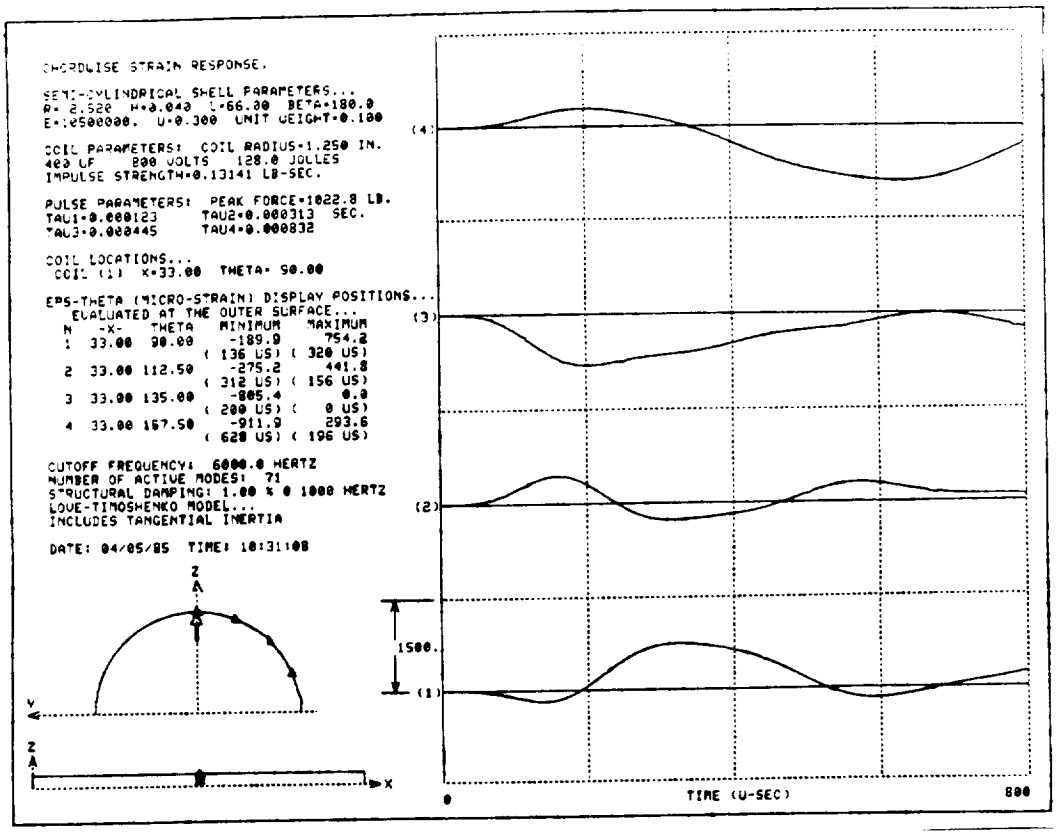

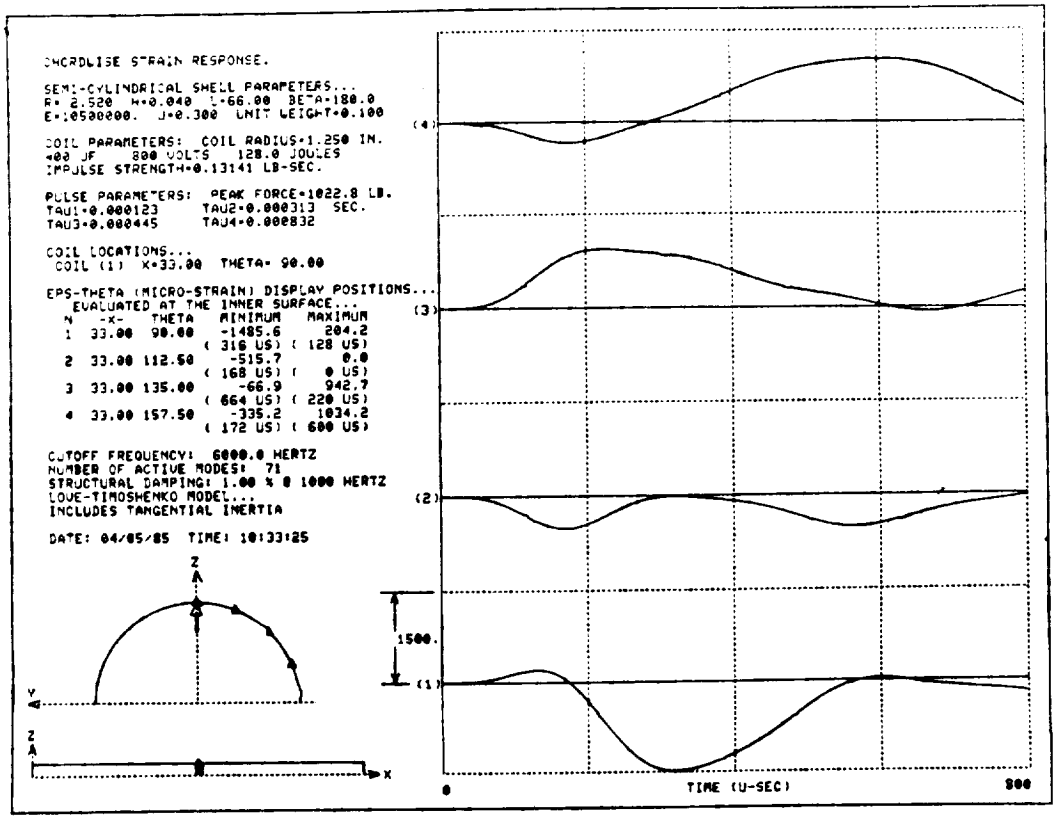

Figure 3-26 Circumferential Strain Response at Mid-Span.

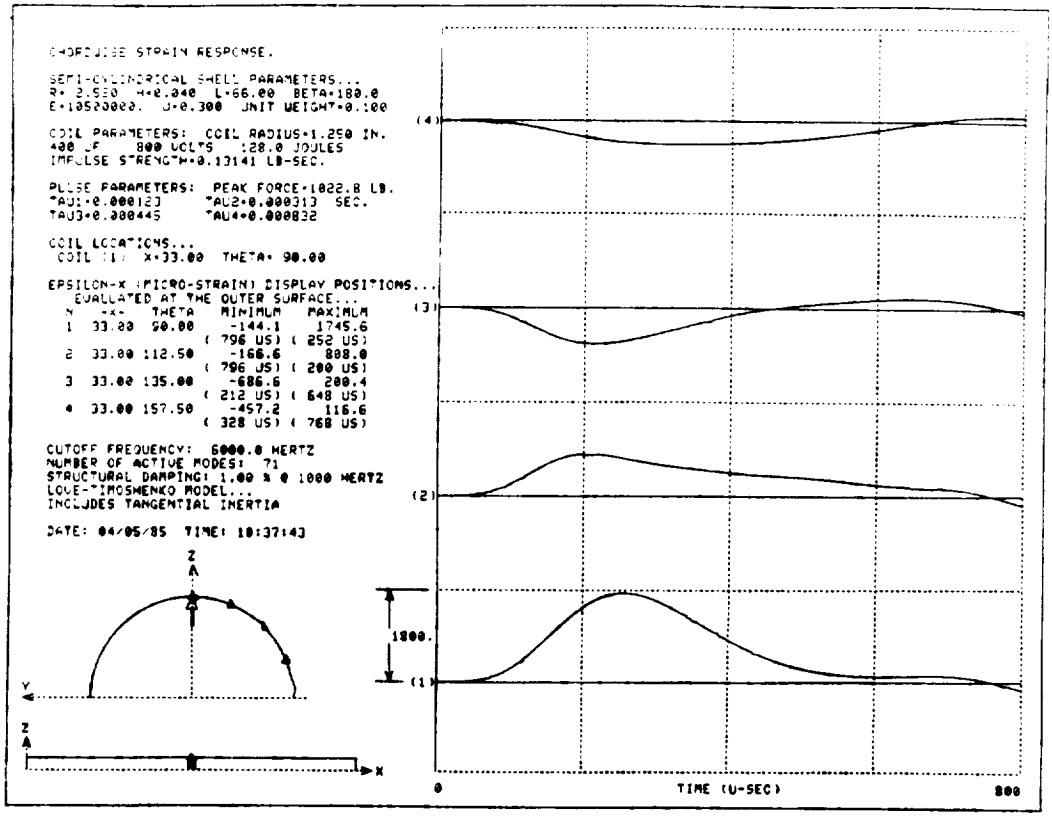

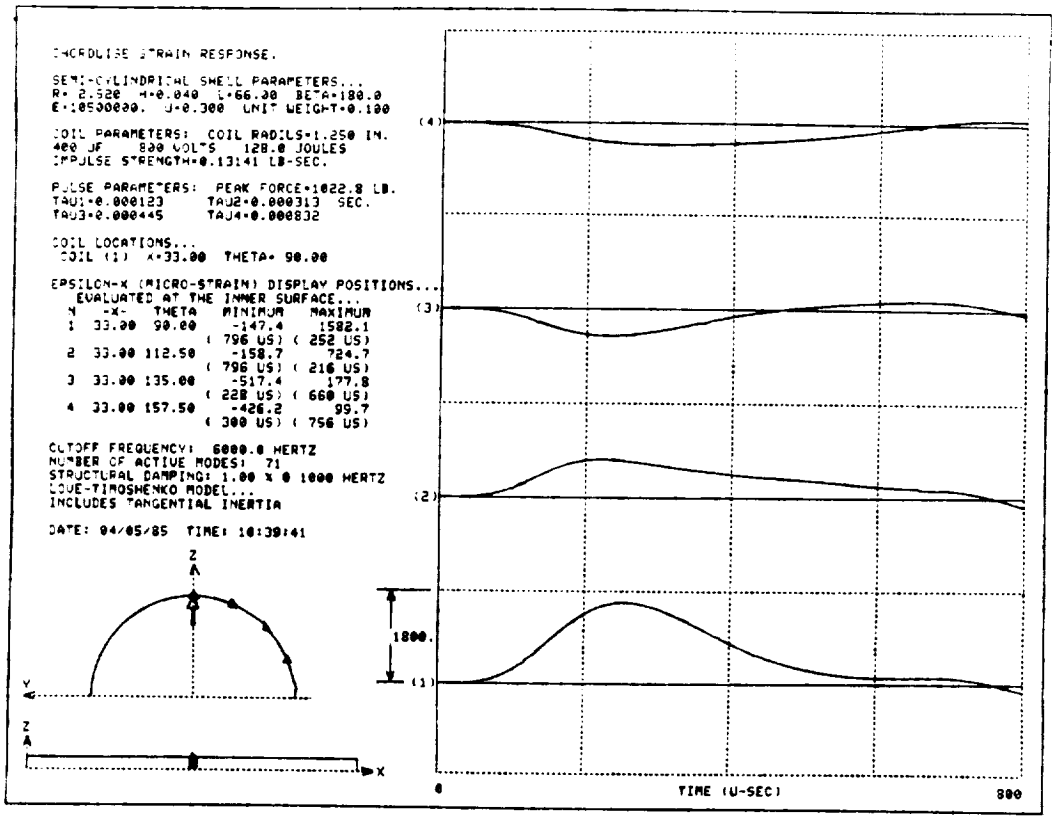

Figure 3-27 Longitudinal Strain Response at Mid-Span.

Two additional analytical studies related to the semi-cylindrical leading edge simulation has been completed by two M.S. graduate students in Aeronautical Engineering. Mr. Peter Gien Ref. 3-8 has documented the closed form solution characteristics and Mr. Bryan Wilson Ref. 3-9 was concerned with a matching finite element representation using the MSC/NASTRAN code. Their semi-cylinder is identical to the aforementioned study with the single exception of a selected 30 inch length. Their parallel investigations resulted in direct comparisons of the acceleration and strain dynamic response for the idealized shear diaphragm supported semi-cylinder.

The finite element model employs the popular 'QUAD4' element and the study contains a correlation of the element size to the half wave lengths described above. Letting 'a' and 'b' be the longitudinal and chordwise dimensions of the 'QUAD4' element, the following requirements must be satisfied.

$a \leq L/M$ and $b \leq R\pi/N$.

Thus, the required size of the 'QUAD4' elements is determined from the values of 'M' and 'N', which in turn are dependent on the bandwidth or cutoff frequency. These results are summarized below for a 30 inch long semi-cylinder.

Bandwidth Hertz	M(max)	N(max)	Love-Timoshenko Mode Count	a=L/M (inches)	b=R/N (inches)
2,000	6	5	21	5.00	1.58
3,000	9	7	42	3.33	1.13
4,000	12	8	65	2.50	0.99
5,000	15	9	92	2.00	0.88
6,000	18	9	119	1.67	0.88
7,000	21	10	154	1.43	0.79
8,000	24	11	193	1.25	0.72

Based on these data, Mr. Wilson selected square 'QUAD4' elements with a dimension of 0.75 inches. An eigensolution of this model exhibited a very strong mode correlation with the closed form results which may be summarized

as follows:

Bandwidth Hertz	Mode Count	Frequency Maximum Error	Frequency Average Error
2,000	22	2.9 % @ 1948 Hz.	1.43 %
3,000	42	5.9 % @ 2744 Hz.	2.14 %
4,000	65	11.6 % @ 3874 Hz.	3.44 %
5,000	92	21.3 % @ 4566 Hz.	4.80 %

In general, the finite element model together with its discrete boundary conditions appears to present a slightly stiffer shell as 56 of the 65 frequencies are larger than the corresponding closed form solution values. It is also interesting to note that the Love-Timeshenko equations of motion yield the best correlation of frequencies with the finite element model and they are clearly superior to the Donnell-Mushtari shell equations.

C. Analytical and Experimental Results

This section contains a summary of a comprehensive structural dynamic investigation of a semi-cylindrical simulated leading edge structure as shown in Fig. 3-28.

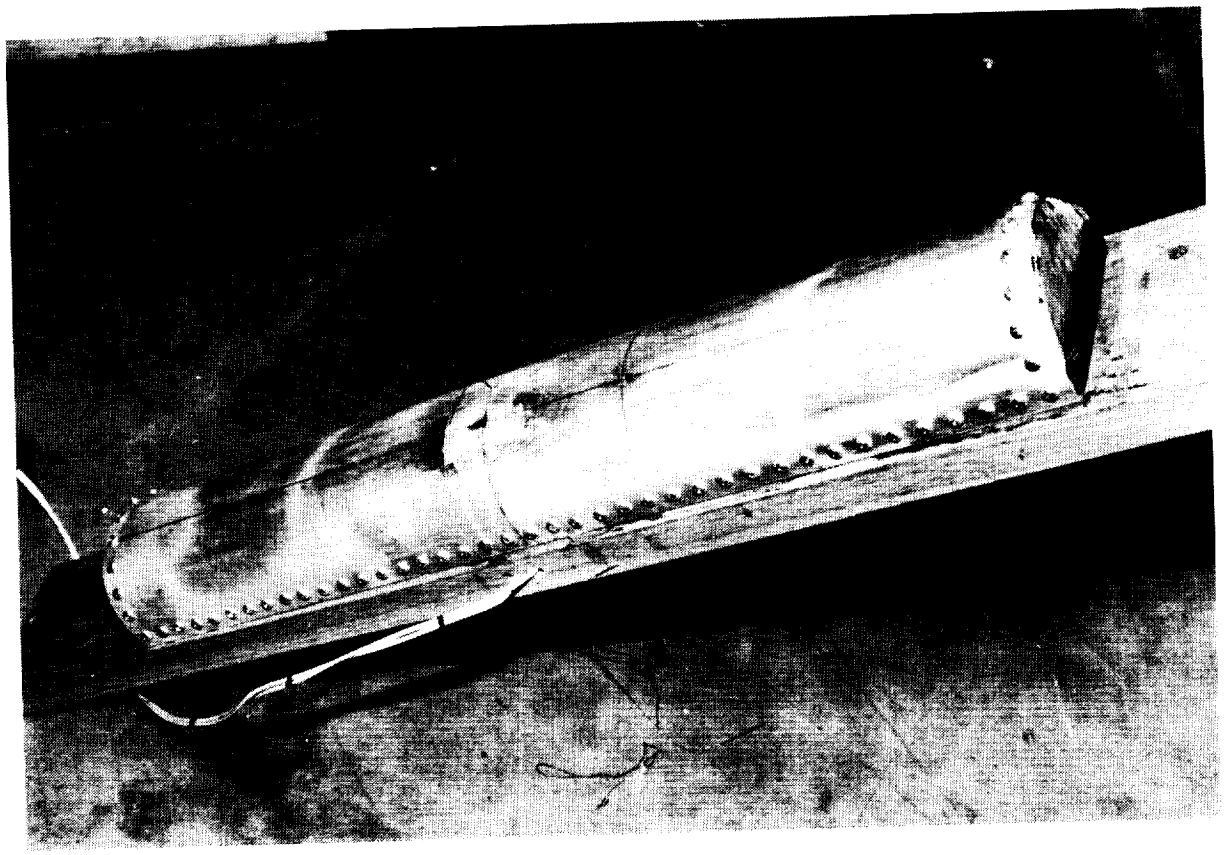

Fig. 3-28 30 Inch Semi-Cylinder Model

This investigation followed the idealized semi-cylinder model discussed in Section IV.B The results of the investigation were presented at the 24th Aerospace Sciences Meeting, January 1986, as AIAA Paper No. 86-0550. The discussion that follows is a summary of the published paper, Ref. 3-11.

Gien (Ref. 3-8) and Wilson (Ref. 3-9) have completed a detailed study on the development of a finite element model of an idealized semi-cylindrical leading edge structure subject to electro-impulsive de-icing forces. This two part study focused on the parallel development of the finite element model and a closed form solution using higher order shell theories, which gave a direct measure of the accuracy of the finite element model. The closed form solution utilized the Love-Timoshenko equations of motion including transverse shear force resultants and tangential inertia effects. In order to circumvent some of the analytical difficulties in the closed form solution, the boundary conditions were chosen as shear diaphragms on all edges, since out of the 18,496 possible boundary conditions, only shear diaphragms are amenable to a simple closed form solution. Both studies used the modal superposition technique to generate accelerations, velocities, displacements and strains as functions of time at various points on the shell. The closed form solution has the capability to predict the response of the shell to a high degree of accuracy due to the ease of varying the upper frequency band limitation in the modal superposition analysis.

The second study was an equivalent finite element solution, wherein element size was selected to satisfy an upper frequency requirement. The MSC/NASTRAN code was employed to extract the resonant frequencies and corresponding mode shapes. The finite element model consisted of 400 CQUAD4 elements; 40 divisions at 0.75 inches each in the longitudinal direction and 10 divisions at 18 degrees each in the circumferential direction. Additional details related to the element size selection process and correlation to frequency response, may be found in Section IV.B The resulting finite element grid structure is displayed in Fig. 3-29.

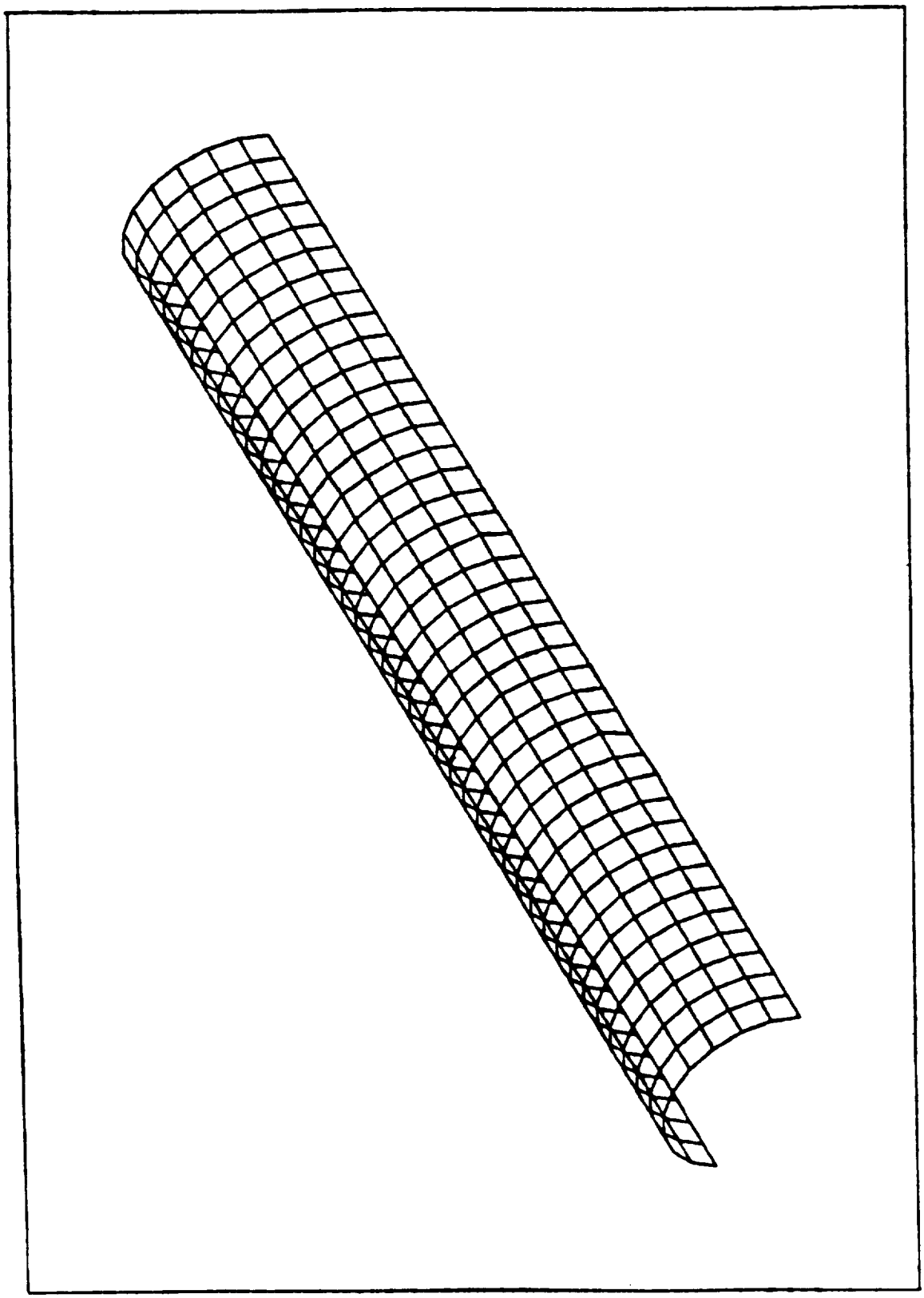

Fig. 3-29 Finite Element Grid

The selected geometric and physical parameters for this study are summarized below.

Internal radius	:	2.500 inches
Shell Thickness	:	0.040 inches
Shell Length	:	30.000 inches
Material	:	2024-T3 Alum.
Young's Modulus	:	10.5E6 p.s.i.
Poisson's Ratio	:	0.300
Weight Density	:	0.100 Lb/in^3

The electro-impulsive force characteristics used in this study are discussed in the EIDI force model below. The structural damping characteristics of the shell models were assumed to vary linearly with frequency with a reference value of one percent at 1000 Hertz.

A brief summary of the conclusions drawn from Ref. 3-8 and Ref. 3-9 are:

(1) The closed form solution and the finite element model gave comparable results for the same impulsive forces, however the peak magnitudes of typical responses in the finite element model were approximately 20% lower than those corresponding to the closed form solution. Fig. 3-30 shows the time variation of the peak positive and negative normal accelerations over the center of the coil. Superimposed on the time response, is a plot of the peak positive and negative accelerations as a function of the frequency of each contributory vibratory mode. These data represent the first 100 vibratory modes.

(2) The retention of vibratory modes below 6000 Hertz was mandatory for reasonable accuracy.

A primary focus of this study is to improve the results of Ref. 3-9 so that better agreement between the finite element and closed form solutions can be obtained, and then to extend the finite element analysis to

arbitrary boundary conditions to facilitate a comparison with experimental data.

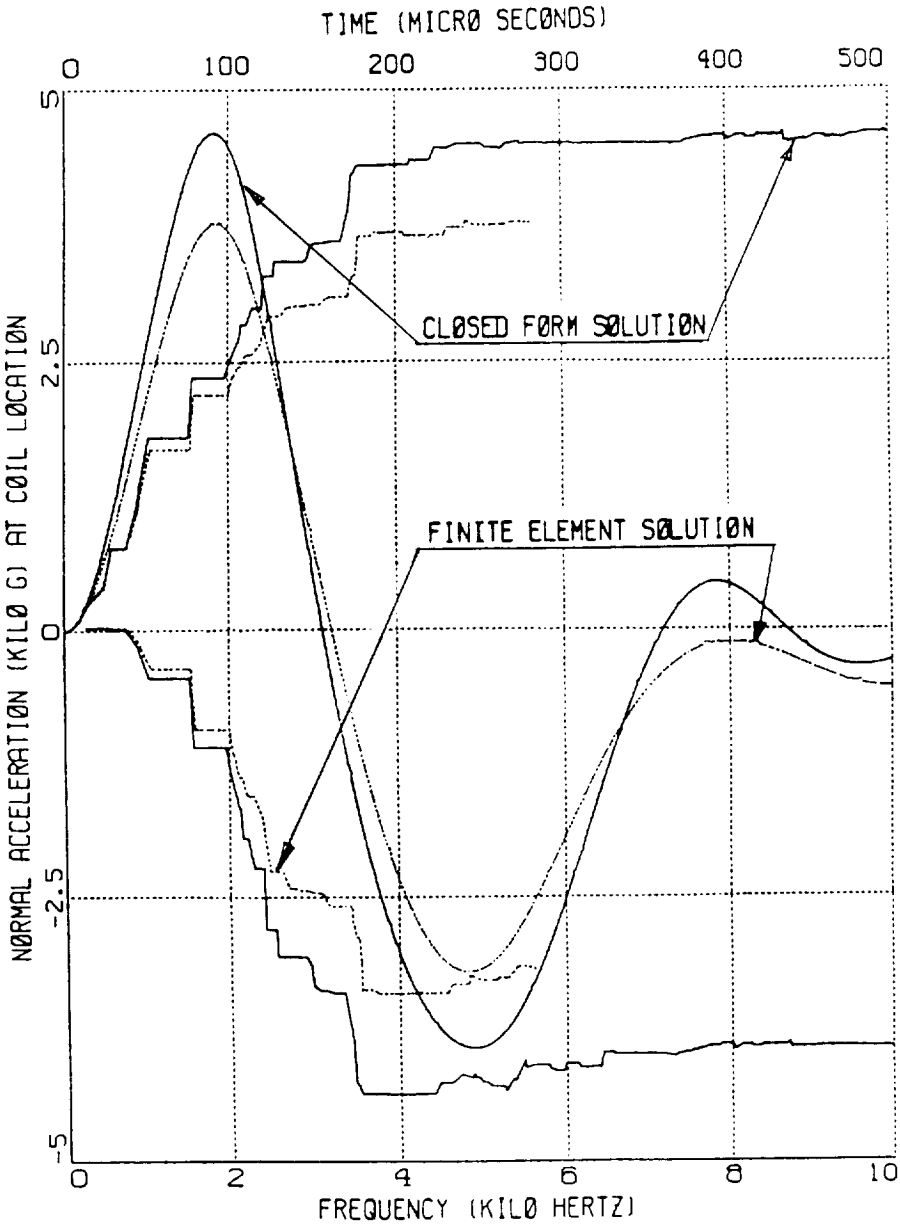

Fig. 3-30 Peak Response for Closed Form and Finite Element Solutions

While investigating the discrepancy between the finite element and closed form solutions, it was found that they converged to the same result as the coil diameter was reduced to nearly zero, which implied that the models were equivalent for point impulsive forces. This was expected since the actual EIDI force pulse is a spatially distributed time varying pressure that could not be adequately discretized in the finite element model, but was easily implemented in the continuous closed form solution. To overcome these difficulties, the refined finite element mesh shown in Fig. 3-31 was modeled into the shell in the region around the coil. The refined mesh consisted of 112 CQUAD4 shell elements arranged in concentric circles around the coil center, while sixteen triangular elements were used to close the central hole. The radial spacing of the elements was chosen to be consistent with an element aspect ratio of unity. The refined mesh replaced a region previously occupied by 16 CQUAD4 elements. Comparing the normal accelerations for this model to the closed form solution, yielded the results displayed in Fig. 3-32.

The refined mesh served to reduce the discrepancy between the closed form and finite element peak responses to 7% and 4% for the peak negative and positive accelerations respectively. The time response and frequency decomposition of the peak responses are shown in Fig. 3-32.

Additional benefits were gained since a much improved resolution of the response in the region around the coil was realized, which permitted a more accurate investigation of the strain distribution.

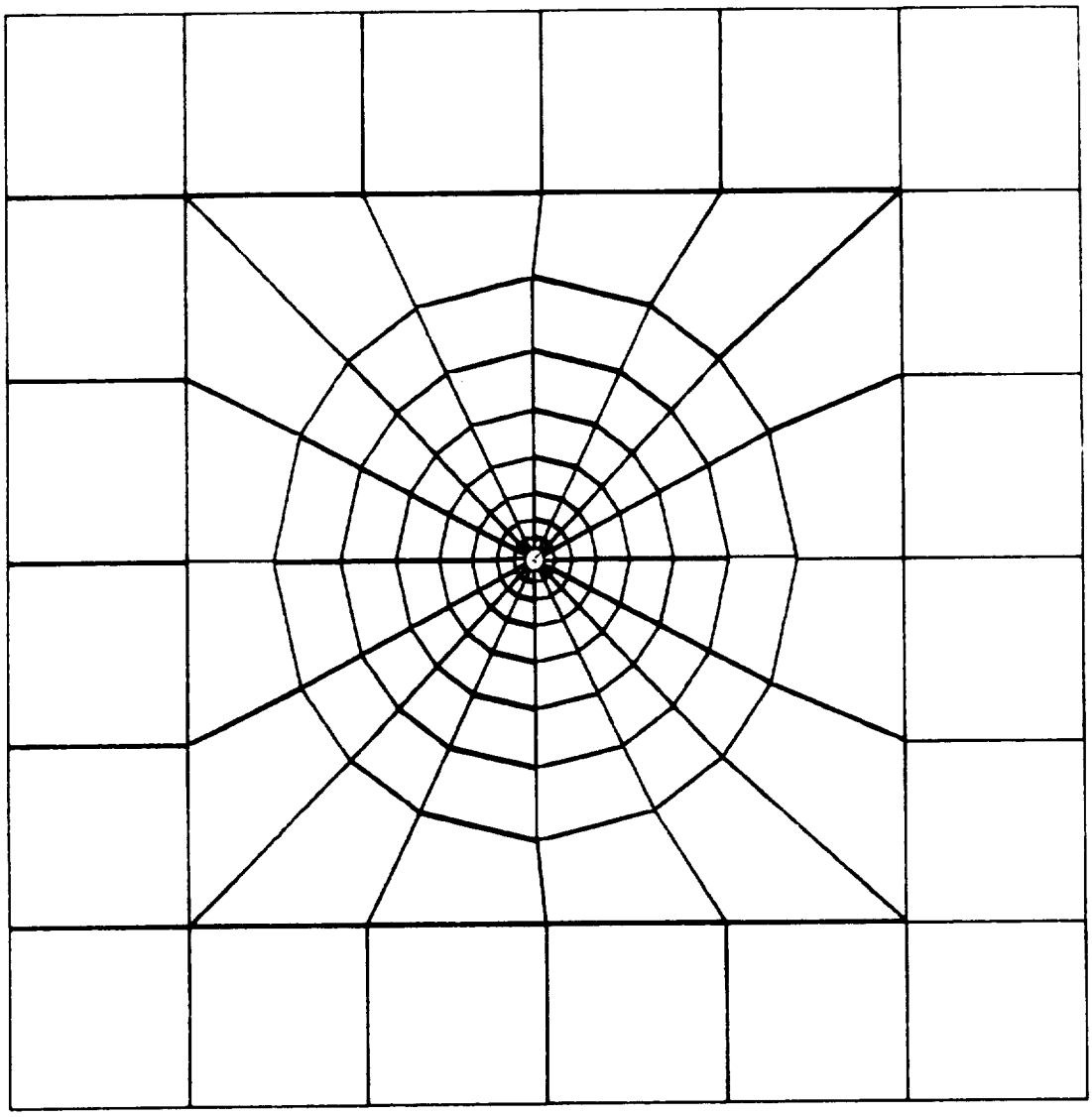

Fig. 3-31 Refined Mesh Around the Coil

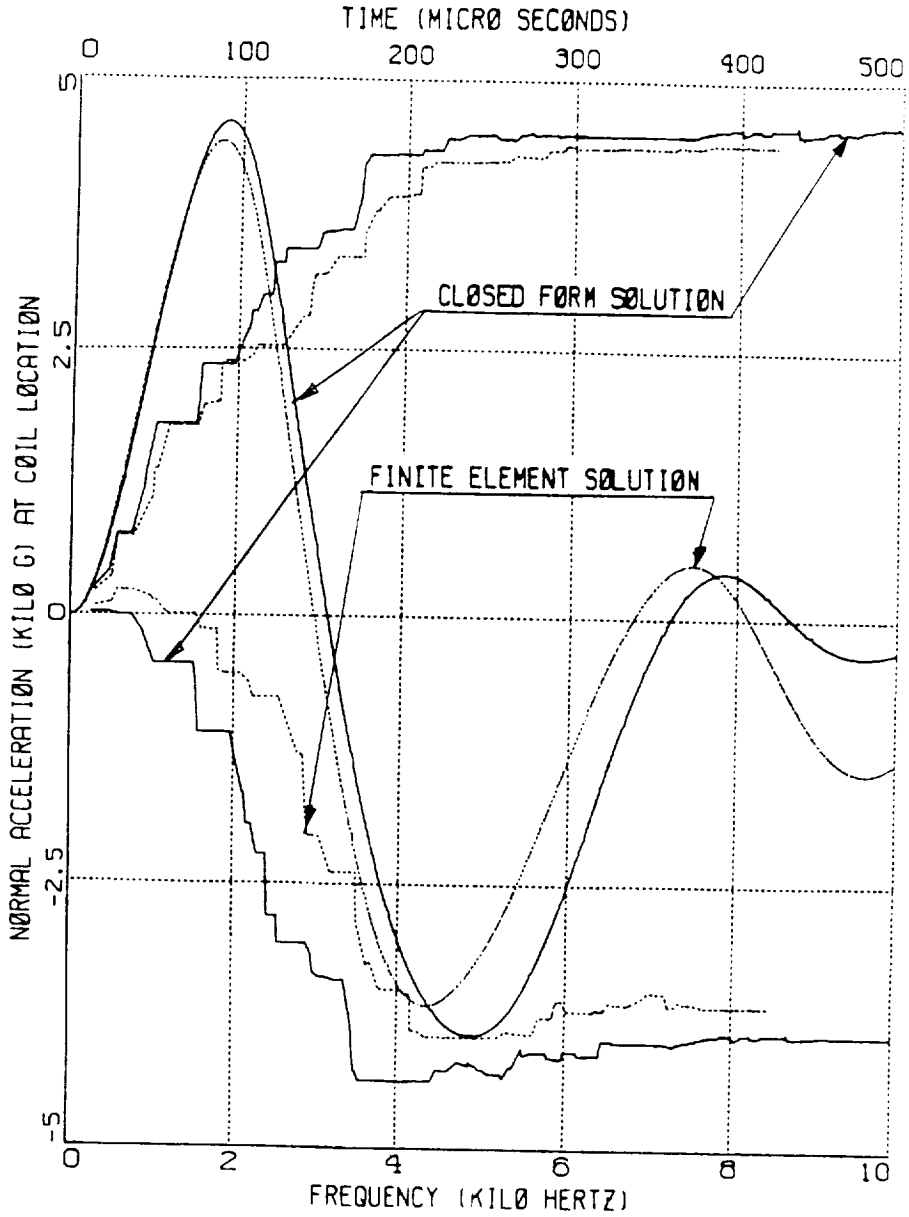

Fig. 3-32 Peak Response for Closed Form and Refined F.E.M. Solutions

The Semi-Cylindrical Shell Experiment

An experimental model of the semi-cylindrical shell was fabricated and fitted with a single pulsing coil as shown in Fig. 3-33. The experimental model was constructed so that the boundaries simulated pinned end conditions, furthermore, the attachment screws were placed directly over the constrained grid points in the corresponding finite element model.

The MSC/NASTRAN finite element model was modified to simulate pinned boundary conditions on all edges, and also employed the refined coil mesh.

Initial frequency studies revealed that the first four natural frequencies (620 to 1300 Hertz), were in agreement with the finite element solution with an error of less that 7%, indicating the equivalence of the model and test article.

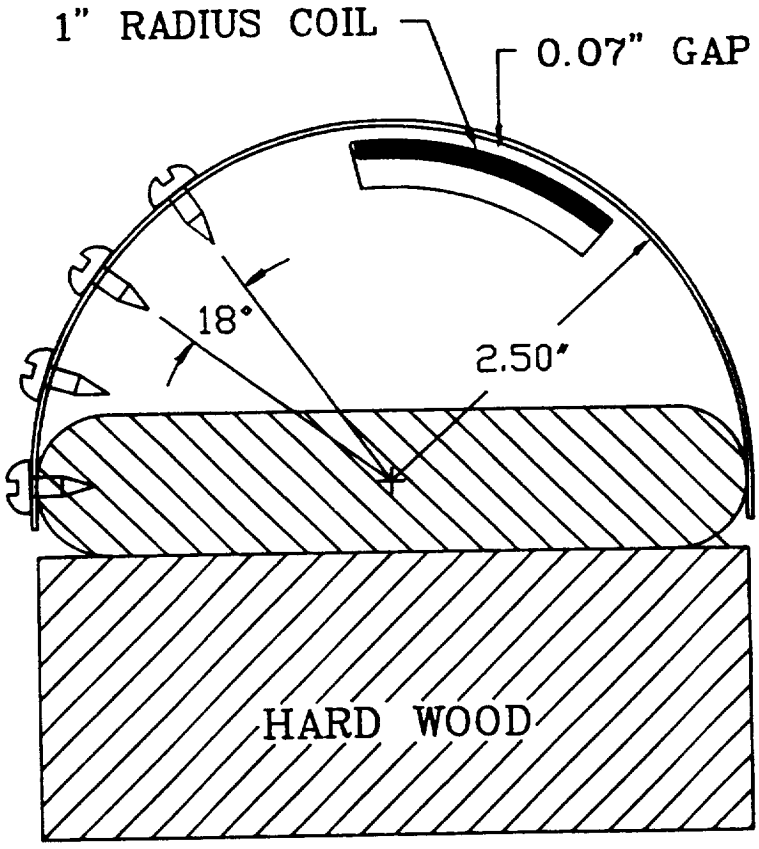

Fig. 3-33 Semi-Cylinder Experiment

The EIDI Force Model

Before any comparisons can be made with experimental data, it is absolutely essential to determine the particular EIDI force pulse characteristics used in the experiment, and then to model these characteristics in the computer code. The spatial and temporal behavior of the normal pressure imparted to the leading edge skin is dependent on a large number of parameters, including circuit voltage and capacitance, skin thickness and electrical conductivity, coil dimensions and the air gap between the coil and skin. The inductance of the lead wires to the coil also has a considerable influence on the force pulse and associated dynamic response as shown in Chapter 2.

Schrag (Ref. 3-1) has reported the form and character of the pressure pulse of a single set of coil and circuit parameters. The results were experimentally established by means of a magnetic field measuring plate. Bernhart (Ref. 3-2) synthesized these data into the product of a prescribed radial pressure distribution with a temporal relation consistent with the measured normal force pulse. This model has been used in virtually all EIDI transient simulations conducted to date. The spatial pressure pulse model is shown in (Fig. 3-34), however, the temporal behavior is widely different for different coil installations and electrical parameters.

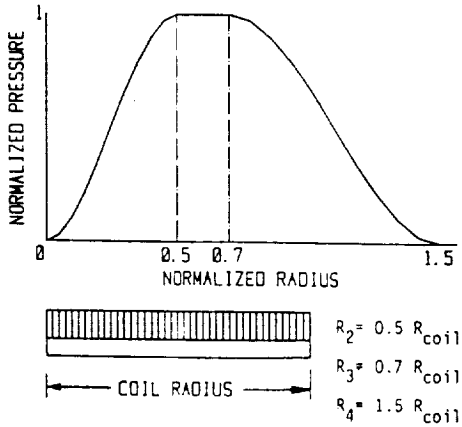

Fig. 3-34 Normalized Spatial Pressure Distribution

The temporal behavior of the force model used in this paper was obtained experimentally using the polycarbonate rod experiment (Ref. 3-1). Since this information would eventually be incorporated into the computational model of the experimental semi-cylinder, close attention was paid to reproducing a planar version of the coil installed in the semi-cylinder. Thus the only difference between the coils was the slight curvature introduced into the semi-cylinder coil which was necessary to ensure an even air gap between the coil and shell.

The two coils were fabricating using copper ribbon wire with the following cross section:

Bare copper size: 0.017 X 0.135 inches.
With Polyimide enamel insulation:
0.020 X 0.140 inches.

The 40 turn coils have a nominal radius of 1 inch, however the measured radius of the flat coil is 0.97 inches. A 5 inch diameter aluminum target (2024-T3 0.040 thick) was bonded to the polycarbonate rod and a gap of 0.07 inches was provided between the coil face and target.

The pulsing system was manufactured by Simmonds Precision in October 1982 and has been extensively used in IRT tests and laboratory studies. The voltage used in these experiments and analytical studies was 400 volts and a nominal capacitance of 600 microfarads. The two coils yielded the following current statistics:

1460 Amp. @ 149 microsec. (semi-cylinder)
1410 Amp. @ 142 microsec. (Lexan Rod)

The experiment is shown in Fig. 3-35. A polycarbonate rod (Lexan) was suspended from two parallel wires, with a target and accelerometer on opposing ends of the rod. Data was sampled every microsecond using a Nicolet 3091 digital oscilloscope connected to a micro-computer for storage

and further processing.

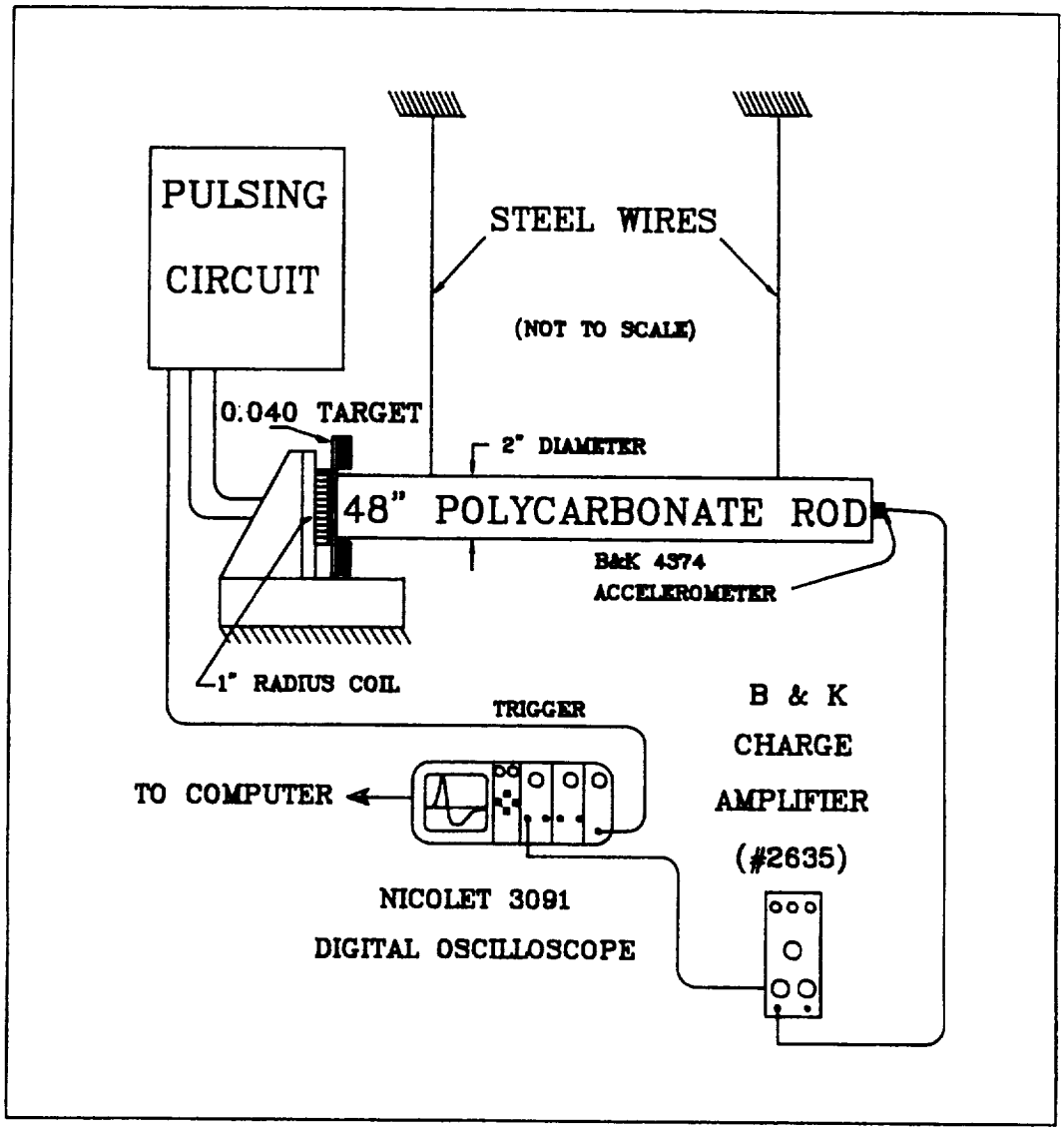

Fig. 3-35 Rod Experiment

Elementary wave mechanics predicts that the velocity measured at the free end of the rod is proportional to the impulsive force delivered at the target. The assumption inherent in this prediction is that the rod is subject to plane wave mechanics, which is not entirely true since the rod material introduces dispersion and attenuation of the signal (Ref. 3-7). Furthermore, the pressure applied by the coil to the target has a spatial variation and is not uniform.

The attenuation of the signal as it travels along the rod may easily be accounted for by measuring the exponential decay of successive reflections of the wave. The dispersion effects are a very complex problem, however Bernhart (Ref. 3-2) has identified the important parameters of the force pulse. These are the magnitude and occurrence time of the positive peak as well as the slope and occurrence time of the first zero crossing.

The time parameters discussed above may be established from the rod experiment by determining the time between successive peaks of reflected waves. This gives an accurate measure of the time required for the wave to travel over two rod lengths. Once the propagation time for the rod is established, the start time of the pulse may be determined and the time to peaks and zero crossing may be measured relative to this point. After the time and peak parameters have been measured, the force is modeled using two cubic polynomials for the positive segments and an exponential curve for the last negative segment. The final force model is shown in Fig. 3-36.

The parameters used in the force model are summarized below.

Peak Force	225 lbs @ 112 us.
Zero crossing slope	1.15E6 lb/sec @ 268 us.
Impulse strength	0.02 lb. sec.

The rod experiment and variations thereof, allow some simple parametric studies to be performed. Firstly, impulse strengths may be evaluated by

either integrating the force signal, or by observing the rigid body motion of the rod which acts as a ballistic pendulum.

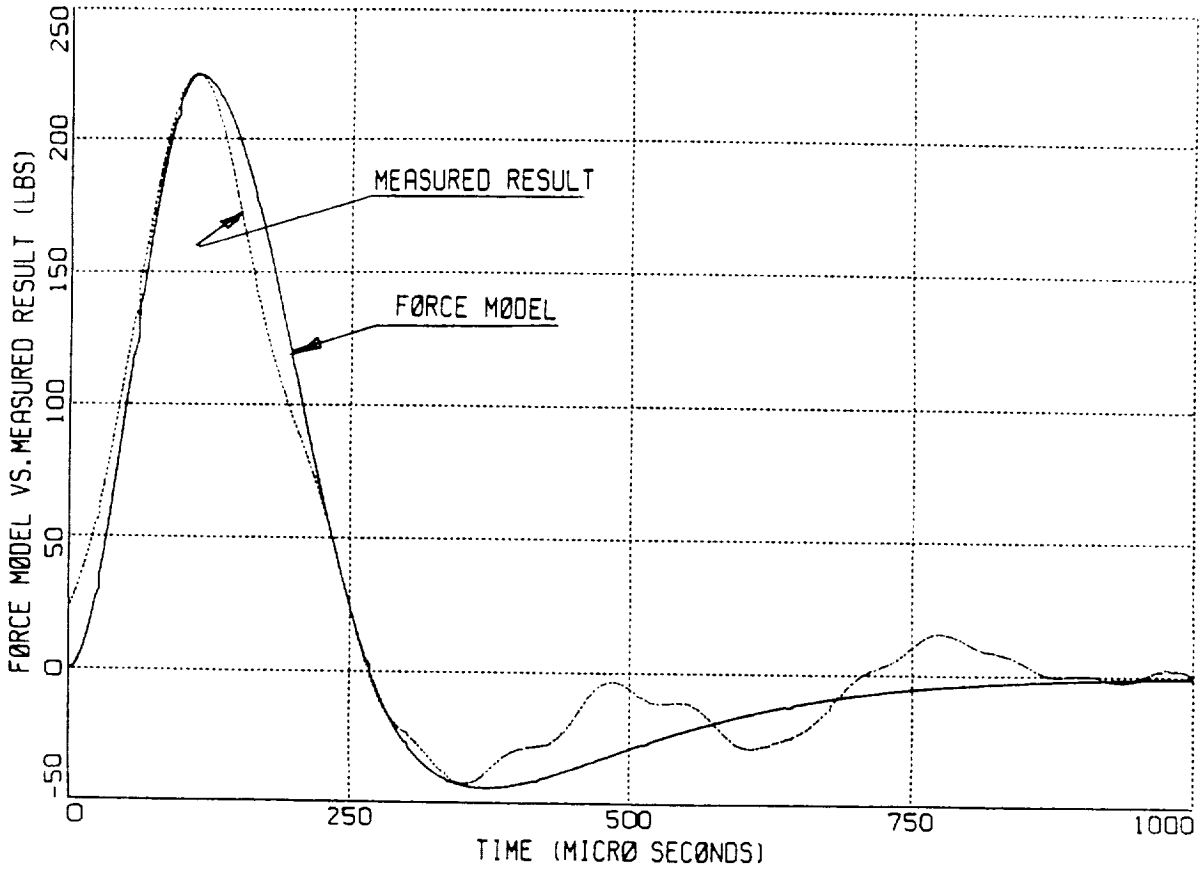

Fig. 3-36 Temporal Force Model

Comparison of Analytical and Experimental Results

The normal acceleration response was measured at two positions on the shell; directly over the coil location and at a second position 4.5 inches from the mid-span and 18 degrees from the shell center line. A Bruel & Kjaer model 4374 accelerometer was employed for the measurements. This accelerometer has a weight of less than one gram, including the attachment cable; a maximum shock rating of 25 kilo-g and an exceptionally low magnetic sensitivity. Fig. 3-37 and 3-38 display the predicted and measured normal accelerations for these two positions.

The correlation between the predicted and normal acceleration response at the coil location is quite favorable. The positive peak has a magnitude error of 6% and the negative peak, a 28% error. The difference in occurrence time for the two peaks is about 5 microseconds.

The response at the second position, 4.5 inches from the coil, indicates a discrepancy of 60 microseconds in the peak occurrence time and a 53% error in the positive peak magnitude.

Two (M&M EA-13-045AL-350) strain gages were bonded to the exterior surface directly over the coil. One gage was oriented in the circumferential direction and the other in the longitudinal direction. The gages had a single magnetic compensation loop as described in Ref. 1, page 77. The induced magnetic noise was on the order of 5% of the total signal strength and of a short duration; less than 50 microseconds. These results are shown in Fig. 3-39 and 3-40.

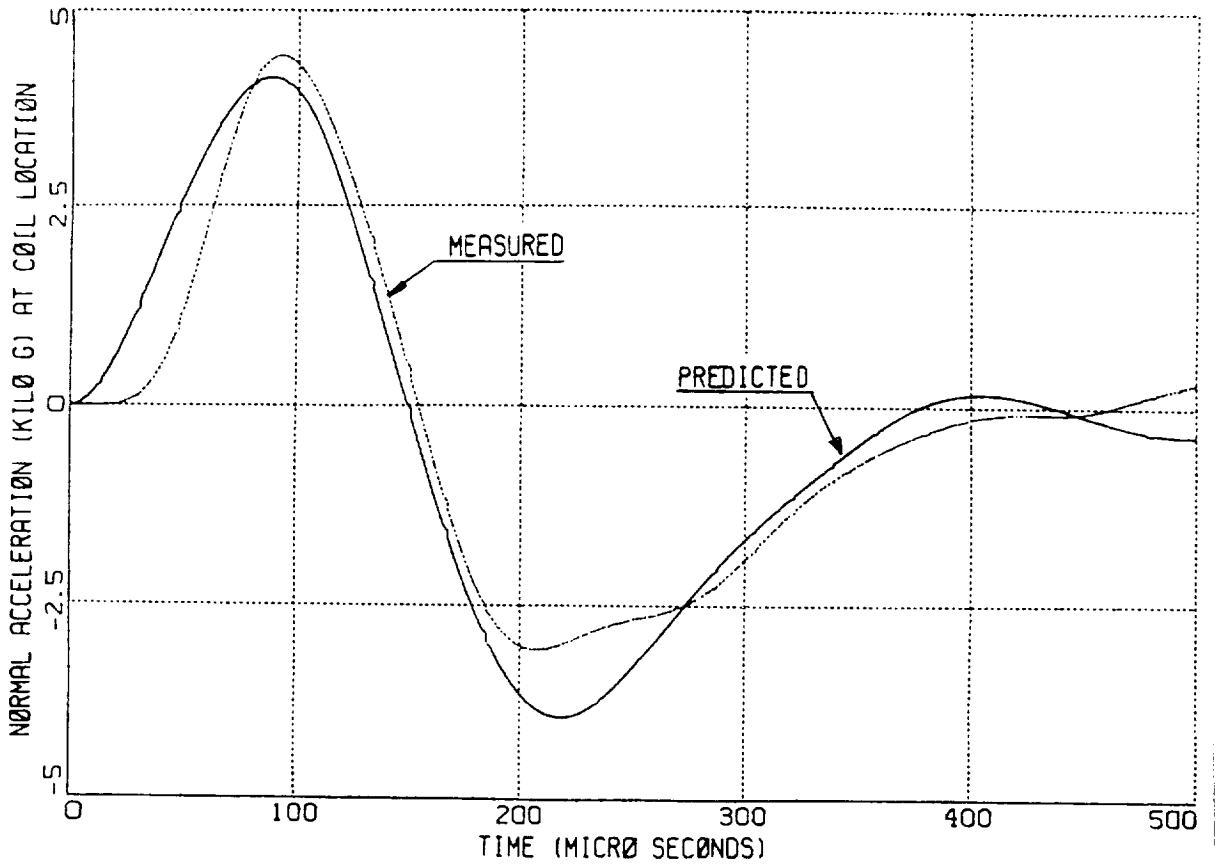

Fig. 3-37 Acceleration Response at Coil Location

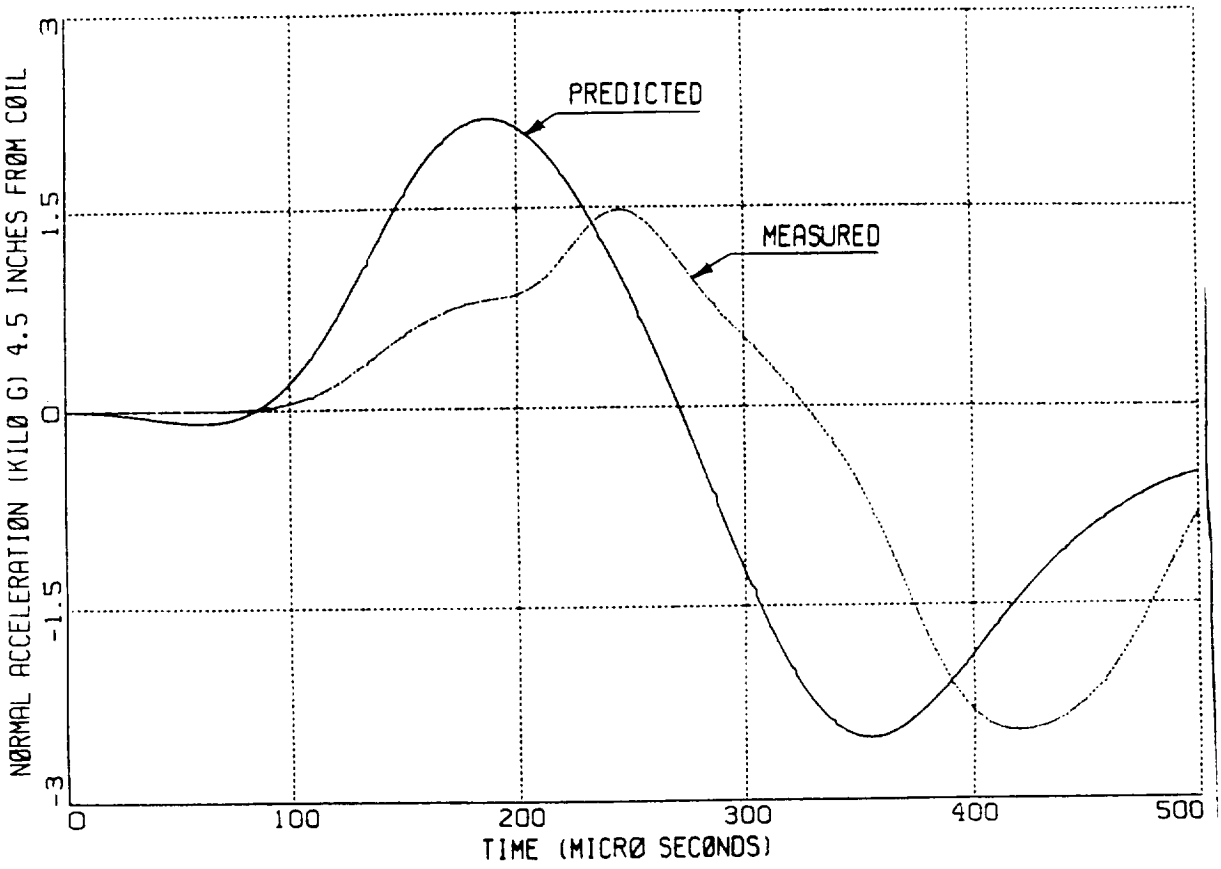

Fig. 3-38 Acceleration Response at X = 4.5 Inch and Theta = 18 Deg.

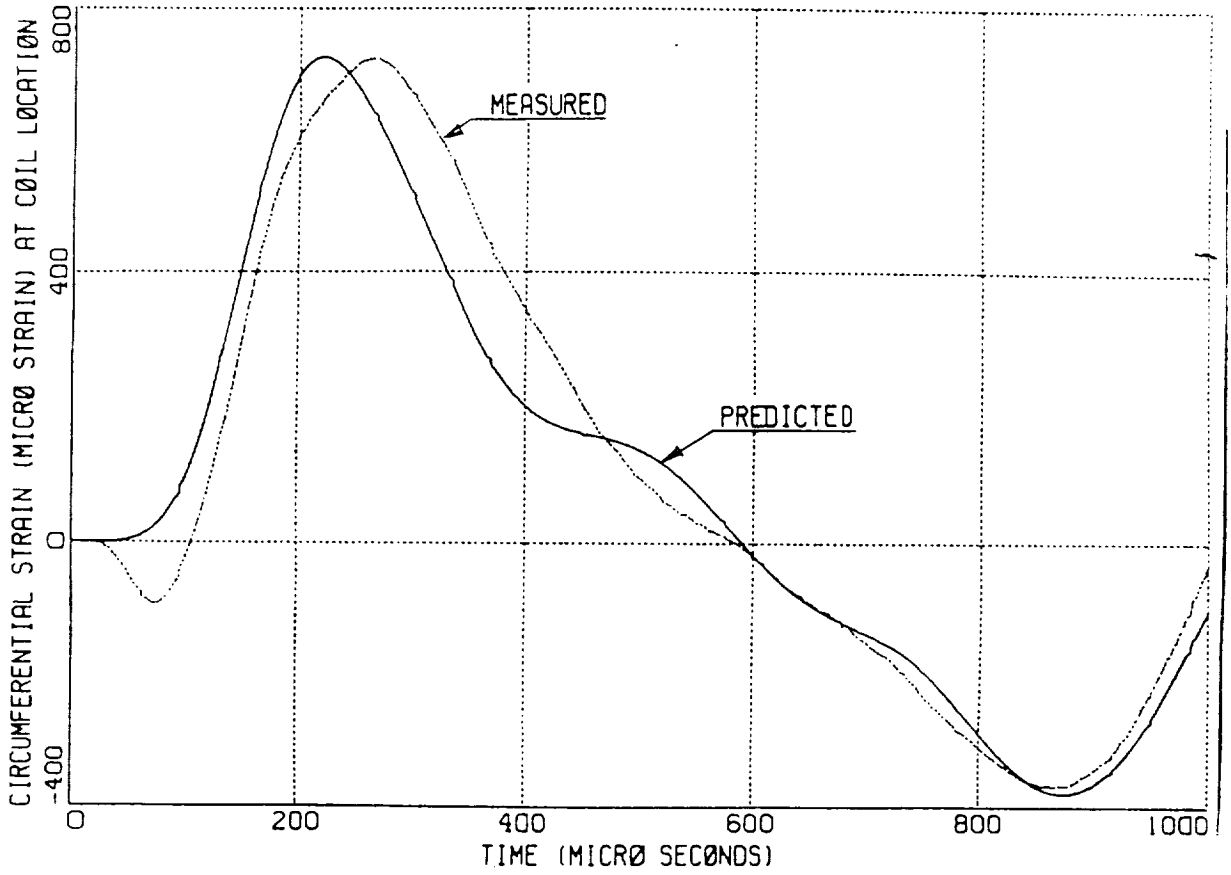

Fig. 3-39 Circumferential Strain at the Coil Location

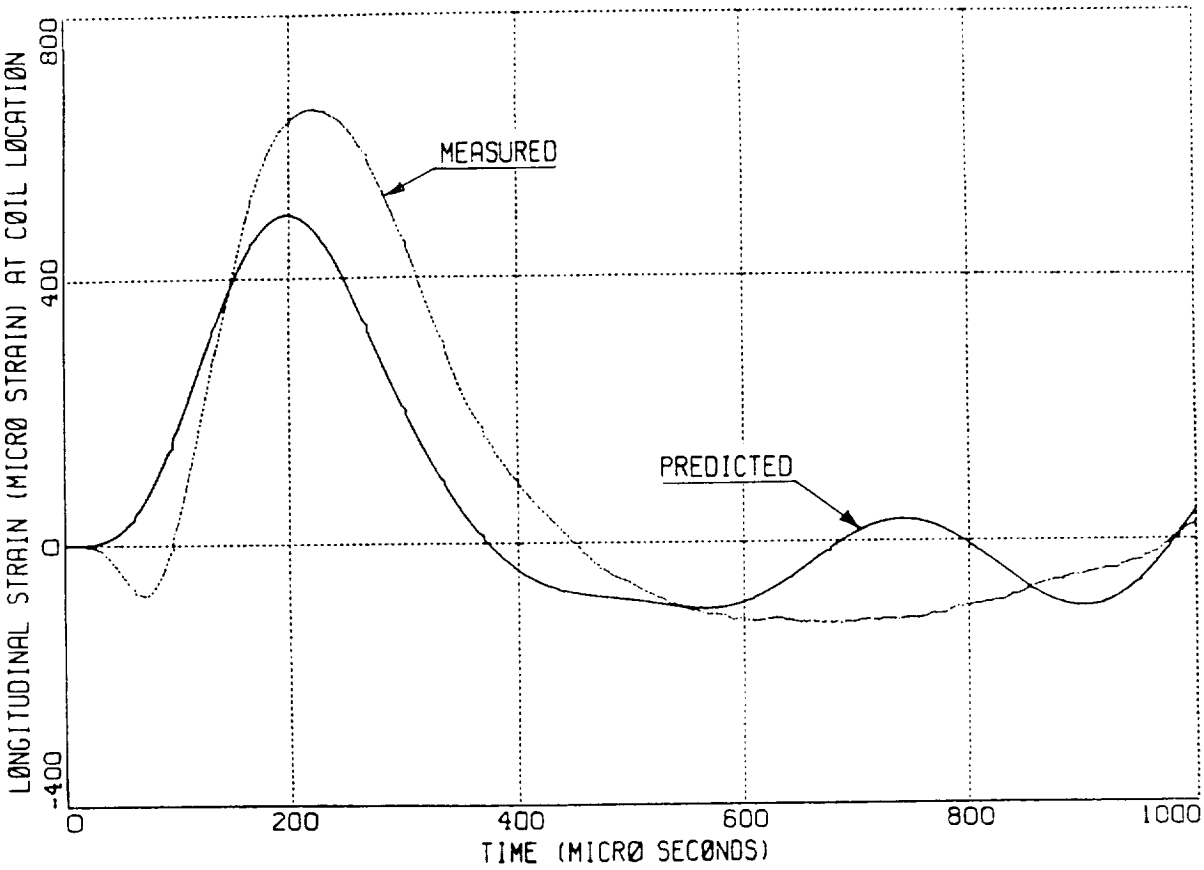

Fig. 3-40 Longitudinal strain at the coil location

The circumferential (chordwise) strain has a remarkable correlation in peak magnitudes, however the positive peak occurrence time is approximately 50 microseconds in error. The positive peak for the longitudinal (spanwise) strain is 32% in error with an occurrence time shift of 25 microseconds.

Observations

A primary objective of this study was to establish the desired dynamic responses in the near coil field for time durations on the order of the force pulse. This objective has been partially met for the acceleration and circumferential strain at the coil location.

A second objective relates to dynamic response sensitivities to various geometric and electrical parameters. The response at different voltages, for a fixed capacitance, has been experimentally verified to follow a voltage ratio square relationship. The influence of capacitance serves to change the time parameters, as well as amplitudes and is not discussed herein. It must be pointed out that the coil in the semi-cylinder model does not have a uniform gap; varying from 0.060 to 0.090 inches, with an average value of 0.07 inches used in this investigation. The impulse strengths were experimentally established for several coil target gaps. These data are summarized below.

TABLE 1. Gap Sensitivity

GAP	IMPULSE STRENGTH (lb. sec.)
0.01	0.028
0.05	0.022
0.07	0.020
0.10	0.017
0.15	0.013

The variation in the region of interest is nearly linear from which acceleration sensitivity parameters may be calculated and are -20700 g/inch and 19600 g/inch for the positive and negative peaks respectively. The calculated normal acceleration response parameters at the coil center with a 0.07 inch gap are:

Positive peak 4140 g at 88 microseconds.
Negative peak -3920 g at 218 microseconds.

Thus a gap of 0.090 inches would reduce the peak values to 3680 and -3460 g respectively.

A second possible source of error in the calculated results is the coil radius which was previously reported to be about 0.97 inches. Rather than the 1 inch nominal value for a 40 turn coil. The calculated sensitivity factors for this geometric parameter are:

Positive peak: -8320 g/inch
Negative peak: 6240 g/inch

Thus the expected peak acceleration response values for a 0.97 inch coil would be:

Positive peak: 4140-8320(-0.03) = 4390 g
Negative peak: -3920+6240(-0.03) = 4110 g

Sensitivity co-efficients for the synthesized pressure pulse (Fig. 3-34) may also be calculated and are summarized below; unit are g/inch.

TABLE 2. Pressure Distribution Sensitivity

Parameter	Positive Peak g/inch	Negative Peak g/inch
R2	-970	680
R3	-2130	1430
R4	-4170	3050

Finally a sensitivity parameter for the peak force occurrence time (112 microseconds in Fig. 3-36) may be established and is

Positive peak : -24 g/microsecond
Negative peak : -20 g/microsecond

A review of the sensitivity data dramatizes the need for rather exacting experimental procedures to ensure conformance with a dynamic simulation.

The shell boundary conditions in the finite element solutions encompassed both the shear diaphragm case and pinned boundaries. A third solution with clamped boundaries was also obtained and the results of the three solutions are summarized below for the acceleration response at the coil center.

TABLE 3. Boundary Condition Sensitivity

Boundary Condition	Positive peak g	us	Negative peak g	us
Shear Dia.	4430	92	-3640	244
Pinned	4140	88	-3920	218
Clamped	4100	88	-4070	222
Experiment	4405	93	-3070	207

Thus the near coil field acceleration response is not severely altered by the shell boundary conditions.

V. OBSERVATIONS AND CONCLUSIONS

The successful EIDI computer code discussed in Chapter II and Ref. 3-13 will be widely used in future structural dynamic investigations. The code has been tested on a non-stationary target simulation representative of the motion of the leading edge skin during the EIDI pulse. This study has clearly shown that the pressure pulse may be separated into a radial pressure distribution multiplied by the corresponding temporal behavior.

$$p(r,t) = p(r)\, f(t)$$

This simplification appears to be sound when the electrical frequency is selected to be at least twice as large as the mechanical frequency associated with the target motion. While this concept has been shown to be valid for a single discrete mechanical frequency, it needs to be examined for the broader case of a multi-mode expansion, typical of the motion of a pulsed aircraft leading edge skin. The EIDI code may also be used to evaluate a system of radial forces that are tangent to the leading edge surface. The influence of these radial forces also requires examination.

The two published EIDI structural dynamic investigations, Ref. 3-2 and 3-11, both used an empirical form of the normal pressure pulse shape. The EIDI code has been used to predict the form of this pressure distribution for a wide class of coil and target combinations. The predicted vs. empirical forms are shown in Fig. 3-41. (At the end of this section).

The code has also been used to predict the form of the normal force on a stationary target corresponding to the parameters in the semi-cylinder dynamic response investigation of Ref. 3-11. Certain assumptions for two of

the parameters had to be introduced in the code to establish the force trace, and these are discussed below. The comparison to experimental data is discussed in Ref. 3-13 and shown in Fig. 3-42. (At the end of section)

It would be very desirable at this point to utilize the EIDI results discussed above in the semi-cylinder dynamic response investigation presented in Section IV.C and Ref. 3-11. The EIDI code has revealed extreme sensitivities to two circuit parameters, the lumped circuit resistance and inductance associated with the cable attachments to the coils. Unfortunately, these two parameters were not recorded during the experimental phase of the semi-cylinder investigation and it would only serve to introduce more uncertainties to assume some specific values for a comparative solution. It was mentioned earlier that Mr. Peter Gien is proposing a detailed investigation of the total EIDI process. The problems outlined above, together with other anomalies associated with EIDI structural dynamics will be addressed by Mr. Gien.

One final observation has emerged from the structural dynamic studies and tests of the EIDI de-icing program. The aspect ratio of internal rib spacing to the chord dimension is normally on the order of 4 or more. This ratio will yield spanwise or longitudinal strains over the pulsed coil that are predominantly membrane strains, whereas the chordwise or circumferential strains are associated with bending effects and are highly influenced by the coil placement in the airfoil leading edge, e.g. to excite a particular chordwise mode. The EIDI pulse will produce a donut shaped bulge in the airfoil which propagates longitudinally and is impeded some by the internal ribs. This can be partially alleviated by permitting the skin to rotate as freely as possible over the rib attachment. During several IRT tests of the 66 inch long semi-cylinder, a single coil was pulsed several times. Each

pulse served to remove a larger portion of accumulated ice which suggests that the propagating bulge is instrumental in the ice removal process associated with EIDI. It also appears that the spatial gradient of the propagating bulge is an important parameter, and serves to "peel" the ice away from the airfoil with each succeeding pulse.

A primary objective of the EIDI project was do demonstrate the feasibility of de-icing leading edge surfaces using electro-magnetic pulsing techniques. This has been suitably demonstrated, however the fundamental question of the ice removal mechanism has yet to be adequately answered, although the peeling observation noted above may be a partial clue. Thus, once this phenomenon has been solved, and some of the aforementioned structural dynamic problems have been addressed, the structural analyst can begin to include ice in the dynamic model. This will permit comparative studies of the shedding mechanisms in the analytical model to the observations in IRT tests.

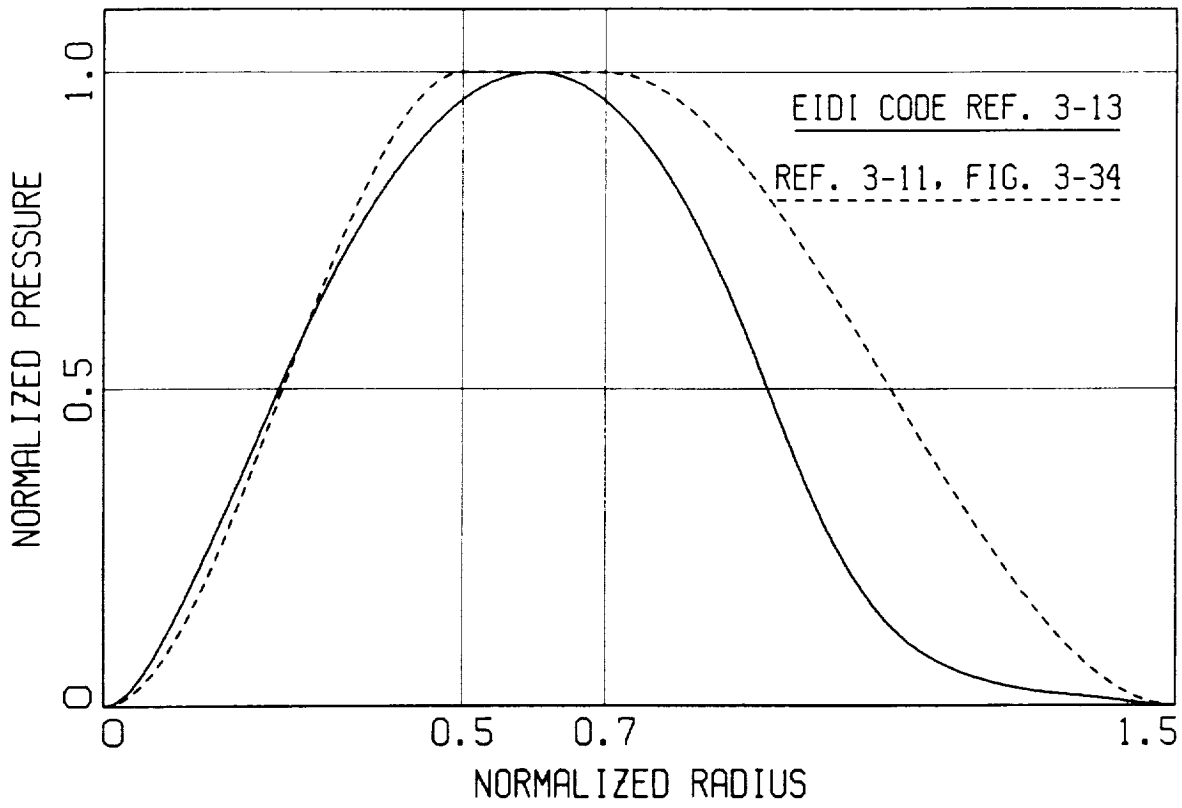

Figure 3-41 Normal Pressure Comparison

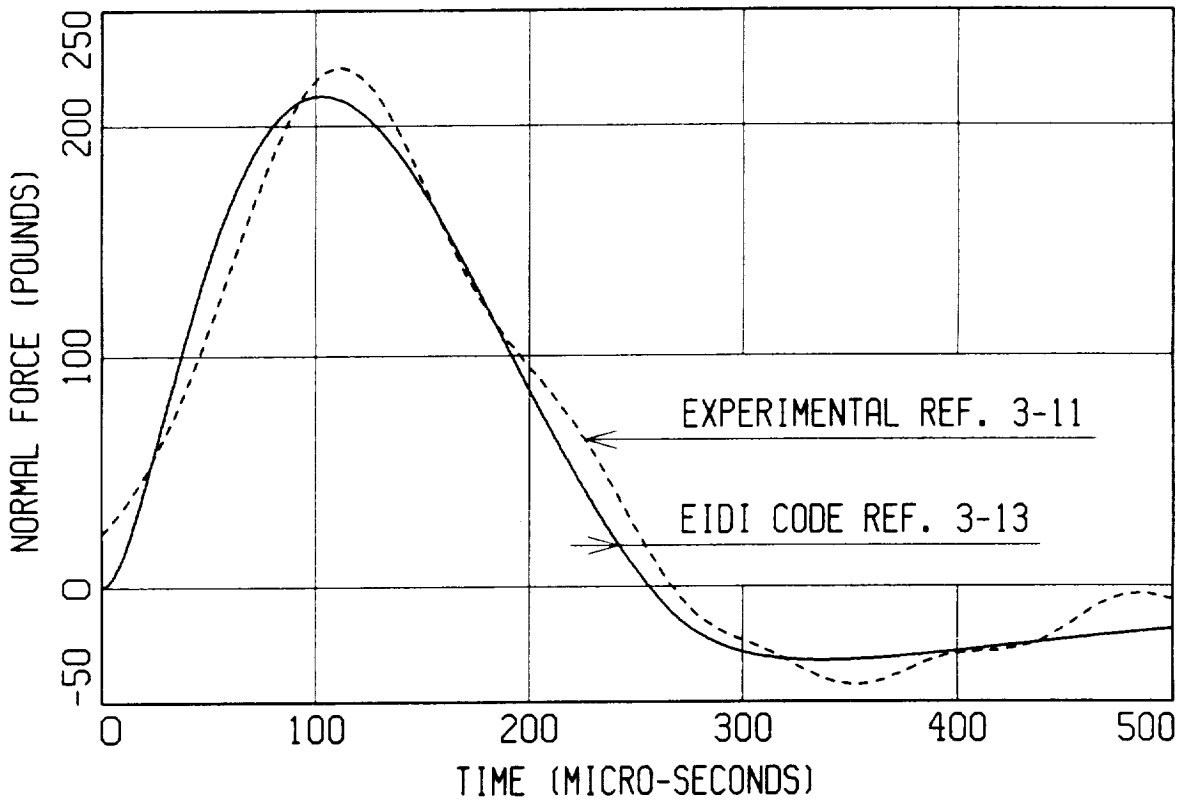

Figure 3-42 Normal Force Comparison
Experimental Vs. EIDI Code

VI. REFERENCES

3-1. Schrag, R.L. and Zumwalt, G.W., "Electro-Impulse De-Icing: Concept and Electrodynamic Studies", AIAA 22nd Aerospace Sciences Meeting, Reno, NV, Jan. 9-12, 1984, Paper No. 84-0021.

3-2. Bernhart, W.D. and Zumwalt, G.W., "Electro-Impulse De-Icing: Structural Dynamic Studies, Icing Tunnel Tests and Applications," AIAA 22nd Aerospace Sciences Meeting, Reno, NV, Jan. 9-12, 1984, Paper No. 84-0022.

3-3. Bowley, R.M., et. al. "Production of Short Mechanical Impulses by Means of Eddy Currents", IEEE Proc., V. 130, Pt. B, No. 6, p.415-423, Nov. 1983.

3-4. Measurements Group, Inc., Rayleigh, NC, "Strain Gages Operate in 50,000 Gauss Magnetic Fields for Fusion Research", Epsilonics, Vol. II, Issue 3, Dec. 1982.

3-5. Zukas, J.A., et. al., "Impact Dynamics", John Wiley & Son, New York, 1982.

3-6. Leissa, A.W., "Vibration of Shells", NASA SP-288, 1973.

3-7. Kolsky, H.,"The Propagation of Stress Pulses in Viscoelastic Solids", Phil. Mag., 8, 1956, pp. 693-710.

3-8. Gien, P.H., "Free Vibration and Transient Analysis of a Semi-Cylinder Subject to Electro-Impulse De-Icing Forces," M.S. Thesis, The Wichita State University, May 1985.

3-9. Wilson, B.K., "A Finite Element Solution to the Dynamic Response of a Semi-Cylindrical Shell Subjected to Electro-Impulse De-Icing Forces," M.S. Thesis, The Wichita State University, May 1985.

3-10. Zumwalt, G.W., Schrag, R.L., Bernhart, W.D., and Friedberg, R.L., "Analysis and Tests for Design of an Electro-Impulse De-Icing System," NASA Contractor Report 1749919 May 1985.

3-11. Bernhart, W.D., Gien, P.H.,"A Structural Dynamics Investigation Related to EIDI Applications," AIAA 24th Aerospace Sciences Meeting, Reno, NV, Jan. 6-9, 1986, Paper No. 86-0550

3-12. Henderson, R.A., "Theoretical Analysis of the Electrical Aspects of the Basic Electro-Impulse Problem in Aircraft De-Icing Applications," Ph.D. Thesis, The Wichita State University.

3-13. Bernhart, W.D., Schrag, R.L., "Electro-Impulse De-Icing Electrodynamic Solution by Discrete Elements," AIAA 26th Aerospace Sciences Meeting, Reno, NV, Jan. 11-14, 1988, Paper No. 88-0018.

(3-10) Zumwalt, G.W., Schrag, R.L., Bernhart, W.D., and Friedberg, R.L., "Analysis and Tests for Design of an Electro-Impulse De-Icing System," NASA Contractor Report 1749919 May 1985.

(3-11) Bernhart, W.D., Gien, P.H.,"A Structural Dynamics Investigation Related to EIDI Applications," AIAA 24th Aerospace Sciences Meeting, Reno, NV, Jan. 6-9, 1986, Paper No. 86-0550

(3-12) Henderson, R.A., "Theoretical Analysis of the Electrical Aspects of the Basic Electro-Impulse Problem in Aircraft De-Icing Applications," Ph.D. Thesis, The Wichita State University.

(3-13) Bernhart, W.D., Schrag, R.L., "Electro-Impulse De-Icing Electrodynamic Solution by Discrete Elements," AIAA 26th Aerospace Sciences Meeting, Reno, NV, Jan. 11-14, 1988, Paper No. 88-0018.

CHAPTER 4. FABRICATION TECHNIQUES

Wichita State University supports EIDI research by fabricating coil and coil mounts, by fabricating models for laboratory, icing tunnel, and flight tests, and by installing instrumentation on these models.

Of these, WSU's first and most important function is the production and mounting of high quality electro-magnetic coils in various test models.

I. Coil Wire Rolling

Coil wire starts with the purchase of annealed magnet strip wire insulated with a polyimide/polyester alloy. Virgin insulated wire, as received, measures approximately .033 x .180 inches. This is the smallest standard cross-section wire available from our sources.* Rectangular wire is used because it provides the largest copper cross-section for a given coil cross-section.

However, the .033 inch thickness is too large for coil making. A wire rolling operation reduces the wire to a thickness of .021 to .026 inches for coil winding. Rolling is done in one pass to minimize work hardening of the wire and damage to the wire insulation. The virgin wire is squeezed between a milling machine arbor and a ball bearing outer race as shown in photo 4-1. Note that current practice has eliminated both the steel feed pipe and the take-up reel. Both the pipe and the take-up reel tended to scrape off the wire insulation. In addition, the take-up reel work hardens the copper wire.

Photo 4.2 shows wire thickness being checked during wire rolling. Typical finished dimensions are .024 x .195 inches (average). The word average is used because the wire comes from the mill with non-uniform dimensions, a condition which is worsened by our secondary rolling operation.

II. Coil Making

Photo 4-3 shows the first step in coil winding, which is attaching an electrical connector to the wire. In this case, that connector is a gold plated brass pin. In addition to serving as a connector, the pin also serves to anchor the wire in the coil winding tool.

* A custom-wire supplier has been found who may greatly simplify the process described here.

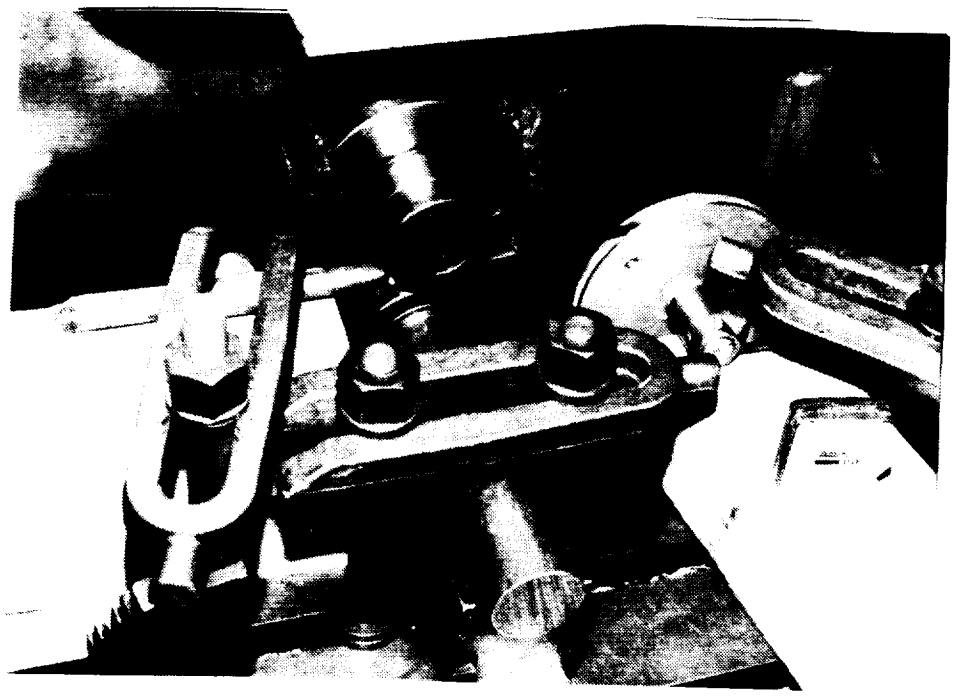

Photo 4-1

Photo 4-2

Many automated schemes of winding were tried, but hand winding has proven to produce better quality coils in about the same amount of time. Coils are either wound flat or curved depending on the coil installation.

Photo 4-5 shows the second electrical connector being soldered into place. Here again, the pin serves a secondary function which is holding the coil together during manufacture. In this case, the coil was wound flat.

The next step is adding a layer of 9.8 oz fiberglass, as shown in photos 4-6 and 4-7. The fiberglass serves three functions: 1) it provides insulation; 2) it gives the coil mechanical strength and integrity; and 3) it provides impact and scuff protection for the coil.

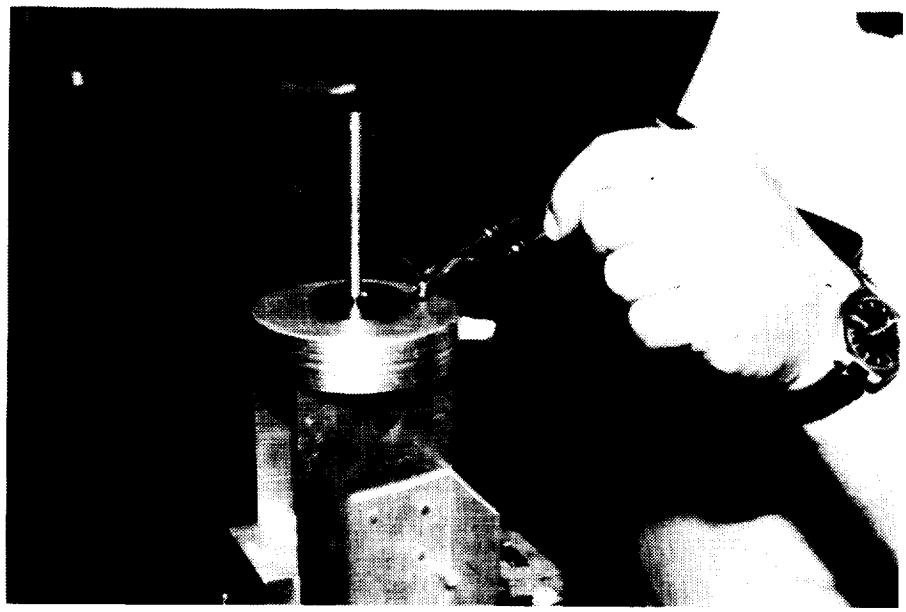

Photo 4-5

Photo 4-3

Photo 4-4 shows the actual winding operation. Winding is done by hand.

Photo 4-4

Photo 4-6

Photo 4-7

Photo 4-8 shows a heat lamp being used to speed epoxy/fiberglass cure time. Care must be taken at this time, because too much heat will degrade the insulating properties of the epoxy by making it porous from too much "out-gassing."

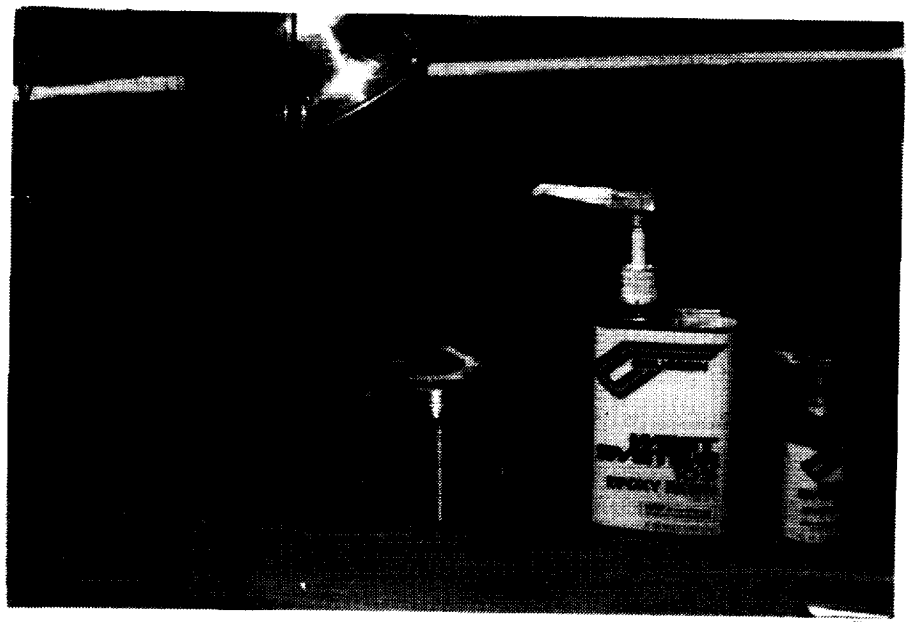

Photo 4-8

As mentioned earlier, coils must often be curved to match the contours of a leading edge. Photo 4-9 shows form blocks, which are one of three ways currently used to produce curvature. These particular form blocks are made of 40 lb/ft^3 polyurethane foam. Photo 4-9 shows the form blocks and the newly finished coil. Photo 4-10 shows the form blocks pressing a coil into shape.

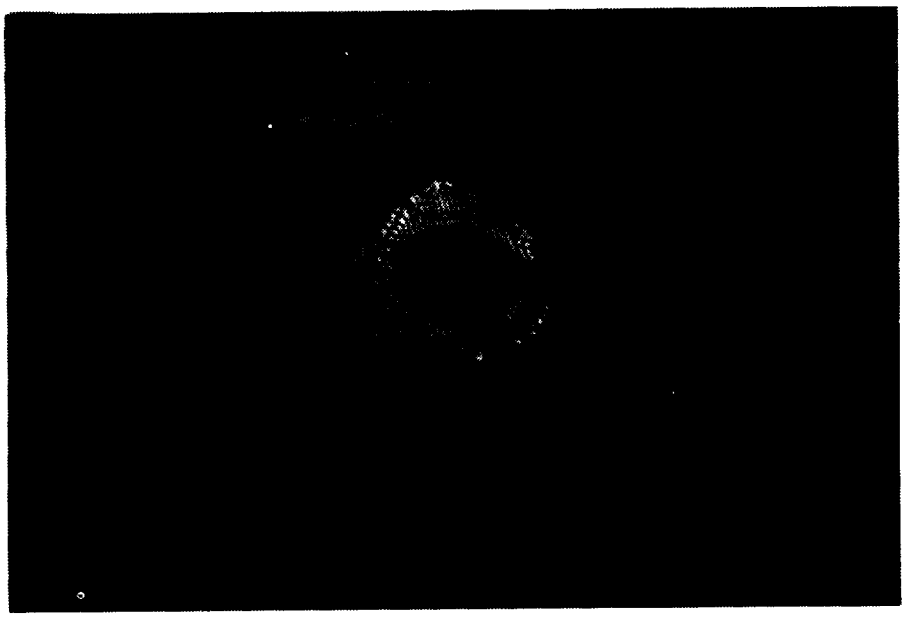

Photo 4-9

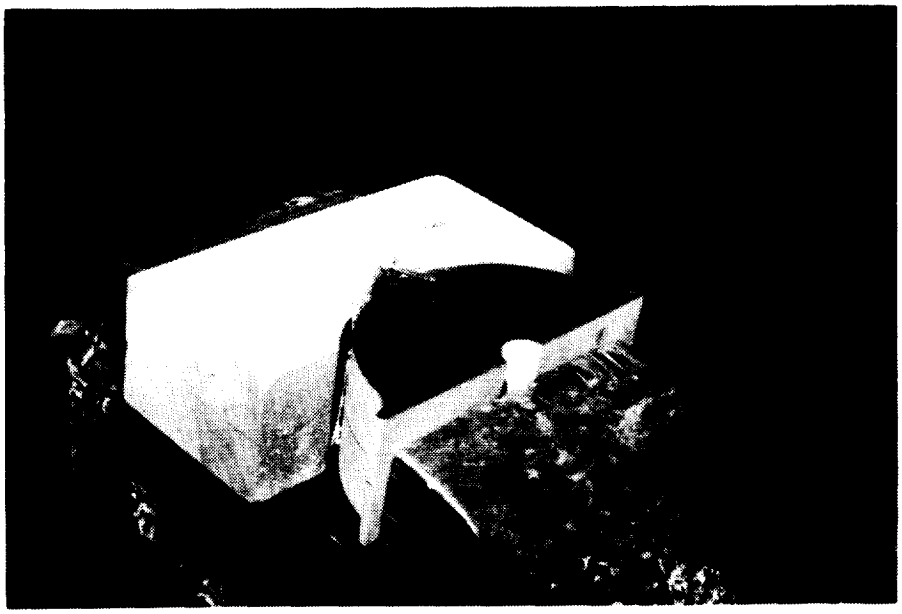

Photo 4-10

The second method is to wind the coil in a curved shape, a job which is more easily said than done.

The third method is to actually machine the coil to shape. Photo 4-11 shows this operation on a rotary die mill. This operation is only performed for high precision laboratory coils because it is a time consuming and difficult job. The very soft copper in the coils is nearly impossible to machine. Many different methods have been tried but nothing seems to work very well. After machining, the coils must be etched in concentrated nitric acid to remove electrical shorts induced by this machining.

After acid etching, manufacture is completed by repeating the steps shown in Photos 4-6 through 4-8.

III. Coil Mounts

Fabricating coil mounts is the next step. Photos 4-12 through 4-15 illustrate the basic method used for making almost all coil mounts. While details may vary from coil mount to coil mount, the basic design philosophy is constant.

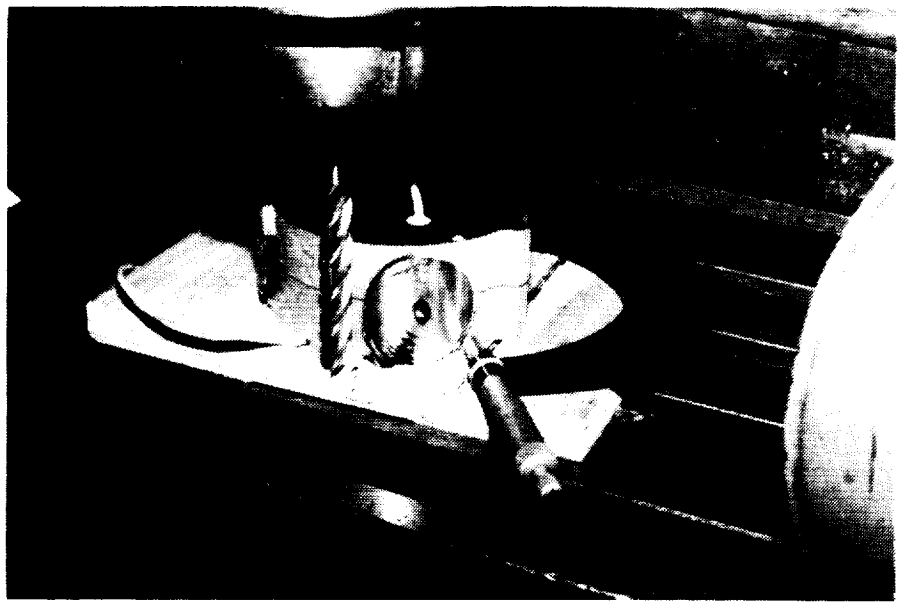

Photo 4-11

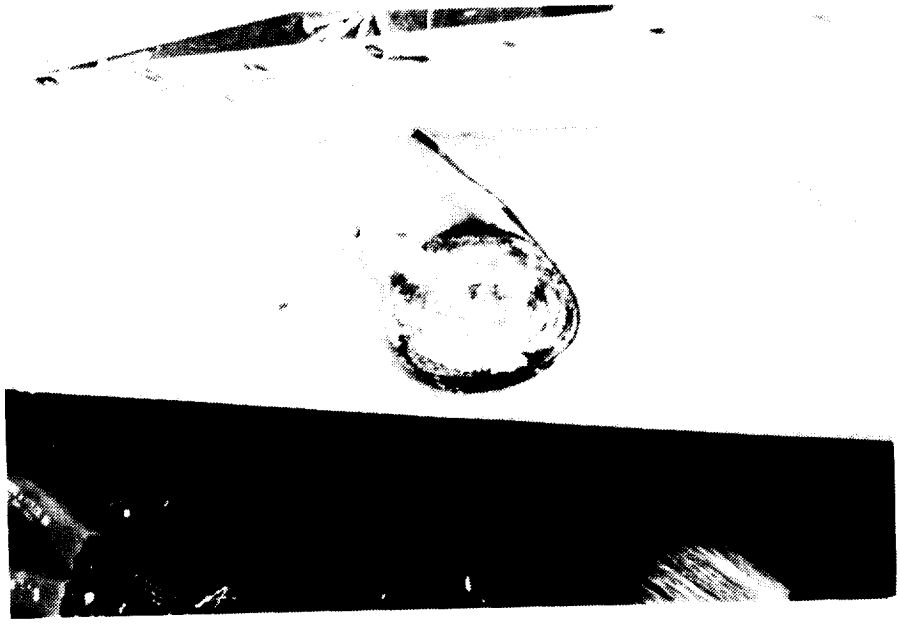

Photo 4-12

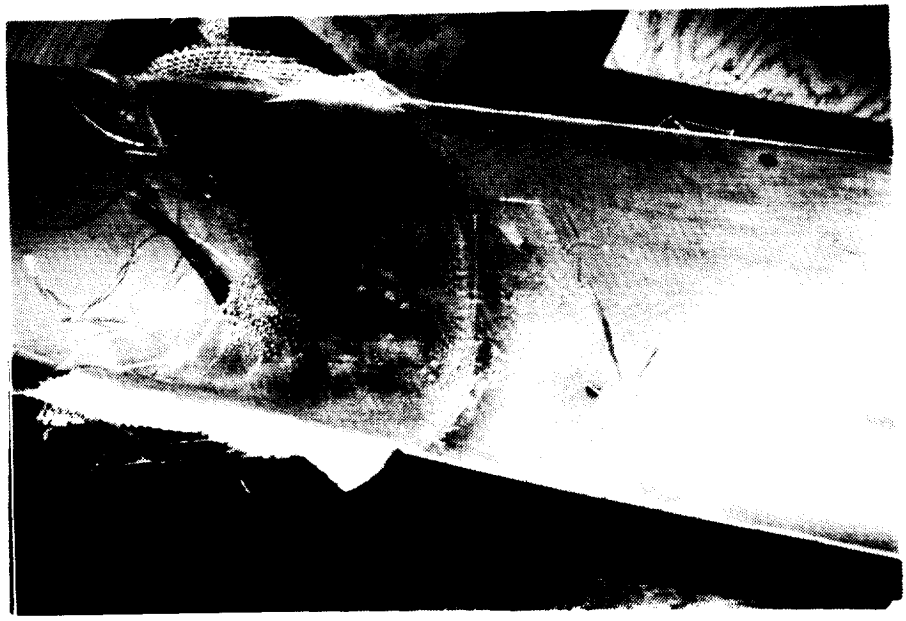

Photo 4-13

Photo 4-14

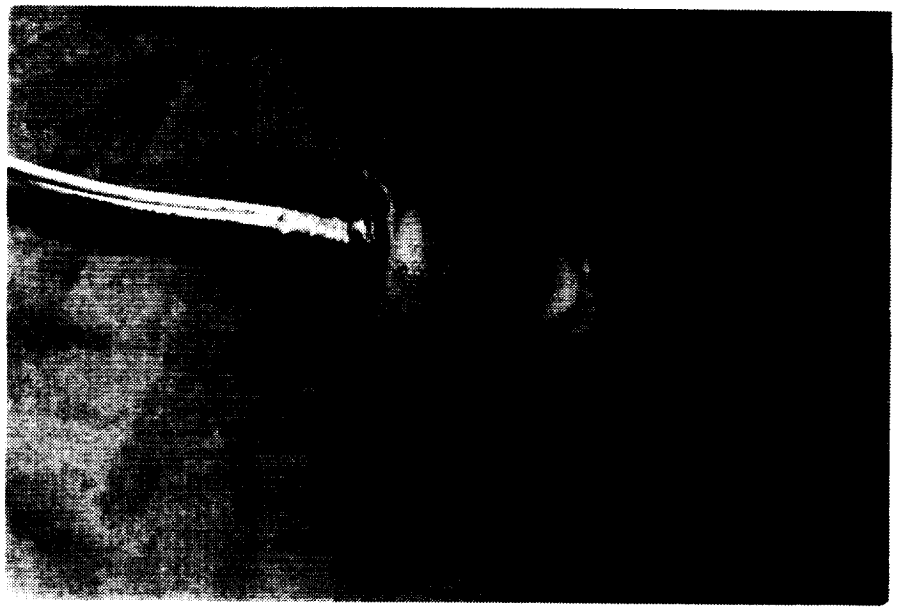

Photo 4-15

Coil mounts are made with epoxy/fiberglass and polyurethane rigid foam . Composites are used because they do not conduct electricity and because composite structures can be made both rigid and light. The first question is, "Why use fiberglass and not Kevlar or graphite?" Graphite is not used because it conducts electricity and Kevlar is not used because it's resistance to abrasion is much inferior to fiberglass.

Fiberglass seems to have the best mix of desired properties. These desired properties are high abrasion and impact resistance, structural stiffness, and good electrical insulating properties.

The second question is, "Why use polyurethane rigid foam as a composite sandwich material?" Polyurethane foam is used because it is compatible with epoxy/fiberglass construction and because polyurethane foam can be formulated to have good bearing strength and good impact resistance.

At this point, comments on the quality of available materials are appropriate. Regardless of manufacturer's guaranteed specifications, components must be chosen carefully. Not all epoxies work equally well, nor are all urethane foams equal. Specifications seem to mean very little. For epoxy, we use Gougeon "Brothers" West System. It's specifications are unimpressive when compared to competitive products, but it's performance is outstanding. Our two part pour-in-place urethane foam comes from General Plastics Inc. who also supplies our pre-cast rigid urethane blocks.

Now we will return to actual construction techniques. Photo 4-12 shows the first stages of mount construction. This photo shows the interior surface of a LearJet Model 55-Century III leading edge. The interior surface is treated with an epoxy release agent and then a two ply fiberglass spacer is laid up using the leading edge as a mold. This spacer is about .03 inches thick and appears as the long rectangular part in Photo 4-12. Spacers can be made of sheet wax or just about anything else. The spacer's sole purpose is to provide a .05 inch stand off distance between the interior surface of the leading edge and the opposing coil face and an .03 inch air gap between the coil mount and the interior surface of the leading edge. The spacer is discarded upon final installation.

The spacer is then trimmed to the desired size and treated with an epoxy release agent. A single ply of 9.8 oz fiberglass is laid up on the spacer and the leading edge. This ply is the outer layer of the coil mount and is the square part shown in Photo 4-12. The coil or coil pair is then

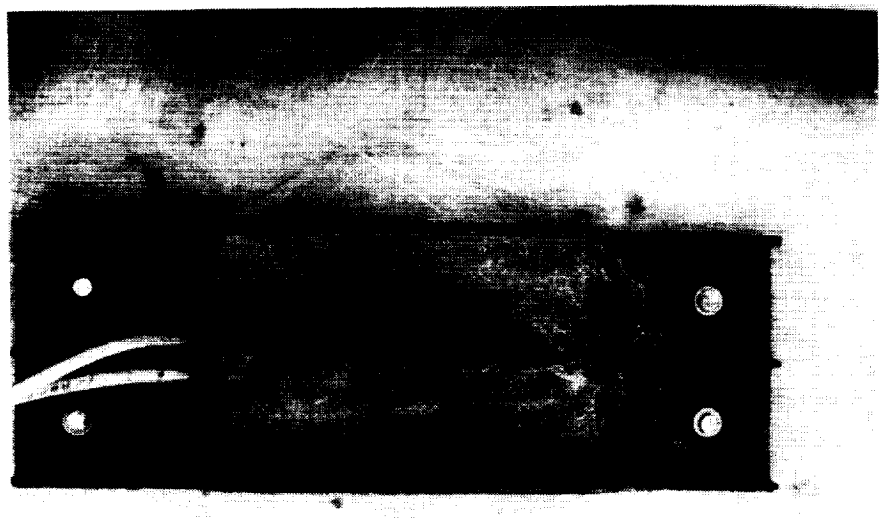

Fig. 4-15A Bandaid

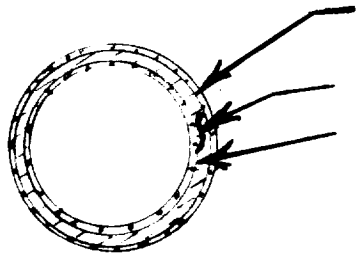

Fig. 15B Low Inductance Cable Coaxial Design

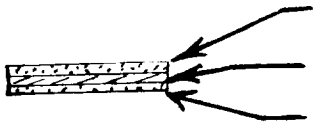

Fig. 15C Low Inductance Cable Flat Design

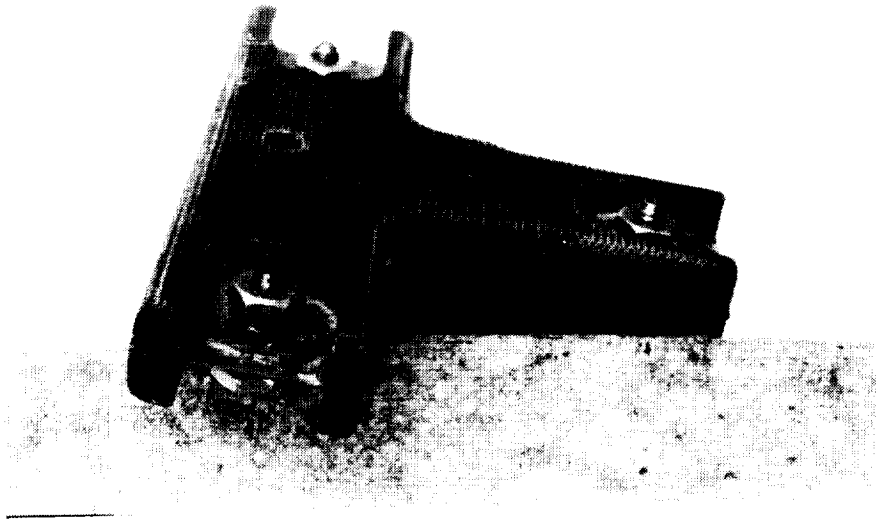

Fig. 15D Low Inductance Connector

bonded to this outer layer. This layer provides abrasion protection, impact protection and electrical insulation for the coil, and is most important. Two more plies of fiberglass are added behind the outer layer completely capturing and encapsulating the coil. Total ply count now stands at 3 layers.

For lighter gauge leading edges of .03 inch or less only 2 layers of 9.8 oz fiberglass are required. The Learjet leading edge requires three plies because it is 0.63 inch thick and is extremely stiff. We now have a three ply arch with the exact shape of the leading edge less the thickness of the standoff spacer.

A three ply back plate arch is now added for extra strength. Photo 4-13 shows the spacer and the 3-ply back plate arch. The encapsulated coil appears as a dark shadow behind the semi-transparent back plate. Note that for lighter gauge aluminum leading edges 2 plies have the necessary strength. The six ply double arch is allowed to cure until it is almost hard. At this time the double arch is separated from the mold which is the leading edge and spacer. Next, the double arch is sawed to the desired size. Photo 4-14 shows the mount after removal and trimming to size.

Wire leads are then soldered to the coil, and the space between the two arches is filled with 2 part foam-in-place rigid urethane foam, Photo 4-15. In this case, 12 lb/ft^3 foam was used, however foam as light as 2 lb/ft^3 will work for light guage leading edges. Photo 4-15A shows a skin mounted coil assembly known as a bandaid. Bandaid coil mounts have proven to be the lightest in weight, and they exhibit the highest electro-mechanical efficiency of any mount.

IV. Electrical Leads

Care must be taken or the leads to the coil will fatigue with repeated coil firings. Photo 4-15 shows the best method found to date of connecting up coils; note the fiberglass strain relief which protects the two lead wires.

Placing screw terminals on coil mounts can lead to broken mounts or broken power cable terminals. The illustrated design arrangement eliminates exposed terminals and wires and provides double and triple insulation for all electrical components. To limit power losses and excess system weight high current cables should be kept as short as possible, even if storage capacitors must be remotely mounted. Short efficient cable (low inductance cables) are doubly important when designing systems that de-ice thick surfaces, say .060 inch or more thick. Figure 15B and Figure 15C show two very low inductance cable configurations. This is especially important when designing systems with waveform rise times of 100 microseconds or less. Equally important are low inductance connectors. Figure 15D shows a prototype of a very low inductance connector which would be essential to proper design of short rise time systems.

To this point actual cable resistance has closely approximated published D. C. resistance values as long as multi-stranded conductors are used.

V. Measuring System Performance

Installed system performance can be accurately measured using a high voltage probe and a digital oscilliscope. Accurate values of resistance and inductance can be deduced.

VI. Outline of Method

1. Assume capacitance effects to be small.

2. Use the follcwing equation.

$$V_t = L \frac{di}{dt} + i R$$

V_t = voltage drop across the component(s) of interest at any given time.

L = inductance of component(s)

$\frac{di}{dt}$ = time rate of charge of current

i = current through a given component(s)

R = resistance of a given component(s)

3. Find "R" first

At the time of peak current

$\frac{di}{dt}$ becomes 0

So $$V_t = L \frac{di}{dt} + i R$$

and $$R = \frac{V_t}{i}$$

4. To find "L"

Choose a time (usually 4 to 10 microseconds into a discharge) when $\frac{di}{dt}$ is nearly a maximum value and the second derivative $\frac{d^2 i}{dt^2}$ is small and plug into the equation

$$V_t = L \frac{di}{dt} + i R$$

so L becomes

$$L = \frac{V - i R}{\frac{di}{dt}}$$

When $\frac{di}{dt}$ is very large,

i is small and any error in measuring i or in calculating R generally represents a very small error in calculating L.

VII. Weight Estimates

Single coils have an outside diameter of about 2.5 inches and 40 turns. The wire measure about .025 x .195 inches, and completed coils weight about 5 ounces.

Typical coil pairs are composed of two 30 turns coils having an outside diameter of 1.8 inches, and weighing 5.5 to 6.0 ounces.

Reducing coil thickness will reduce weight. A coil pair made from .025 x .100 inch wire should weigh 2 to 10 ounces depending on size and strength requirements. The mount in Photo 4-15 weighs about 3 ounces after subtracting the weight of the coil and lead wires.

An absolute minumum design weight using aluminum coils would appear to be in the 3 to 4 ounce range.* A more practical design weight would be 5.0 to 7 ounces, a figure which has already been achieved.

VIII. Coil Attachment

Coil mounts are attached to models in two ways. The first way is screw attachment to the front wing spar or to a false spar positioned ahead of the front wing spar.

The second method is direct bonding to the leading edge interior surface. The mount pictured in Photo 4-15 is a direct bonding type mount. The bonding surfaces are the flat, slightly extended strips adjacent to the table in the photograph. Bonding to the interior surface of the leading edge skin is a difficult task because the bond lines are subject to both peel and impact. To this point, only three adhesives have proven cabable of performing this job, Loctite 324, Hexcel Uralite 3140, a Gougon Epoxy with natural fiber reinforcement. Hexcel 3140, a urethane potting resin, has proven to be the best of the lot. Aluminum 1100 series electro-magnectic doublers are currently bonded to thin skins using Hexcel 3140.

*Bandaid mounts have already met this weight estimate using copper coils.

IX. Icing Tunnel Models

Model preparation is another major task performed at WSU. WSU uses sheet metal and composite fabrication techniques which are common to all aircraft experimental shops. Unlike some wind tunnel test models, most EIDI models are actual parts or pieces taken from real aircraft. Photo 4-16 shows a LearJet Model 55 wing being prepared for Icing Tunnel tests. The wing has been sawed off to proper length and threaded steel angles have been added to accept a wind tunnel mounting plate. The LearJet wing has quite thick skin (.125 in) and so the angle brackets are attached to the skin. More commonly, angle are attached to wing spars. Photo 4-17 shows the model mounting plate. The plate bolts to the steel angles in the reinforced LearJet wind and in turn the plate/wing assembly bolts to the wind tunnel turntable. The plate measures 1/2 inch thick and is made of 6061 T-6 aluminum.

X. Test Model Instrumentation

The third major WSU shop function is instrumenting test models. This primarily involves the installing of strain gages, but with a sinister twist. EIDI pulsers do terrible things to strain gages. Firstly, EIDI coils physically knock strain gages off the surface of the leading edges. Secondly, The coils electrically energize the gages, turning every strain gage into a miniature high voltage transformer.

Photos 4-18 through 4-20 show partial solutions to both problems.

The first problem, physical de-bonding, is eased by installing a thin sacrificial layer of fiberglass above the strain gage.

The second problem, electrical interference, is limited by special wiring techniques developed by Dr. Robert Schrag.

Strain gage installation starts with metal preparation. Metal preparation steps are:

1. De-grease the metal
2. Sand the metal with 60 to 100 grit sand paper
3. De-grease the metal
4. Mark the desired strain gage location with 6H drafting pencil
5. De-grease the metal
6. Acid etch the metal
7. Neutralize the metal with ammonium hydroxide solution
8. De-grease the metal twice
9. Bond strain gages to metal surfaces using M-Bond 200 or Perma-Bond 200 and adhesives. Step 9 is shown in the center of Photo 4-18.
10. Solder a small gauge insulated wire to one of the solder tabs (shown in bottom of Photo 4-18).
11. Solder a second small gauge insulated wire to the second solder tab and double back the wire across the middle of the strain gage, Photo 4-19. This doubling back causes the gage to self-cancel much of the induced error signal.
12. The two leads are now twisted together to again reduce induced signals; see Photo 4-19.
13. Finally a 4 mil layer of fiberglass cut on a 45° line is bonded over the gage to greatly slow gage debonding, Photo 4-20. The fiberglass is oriented to cause little or no strengthening to the metal while at the same time retaining the gage.

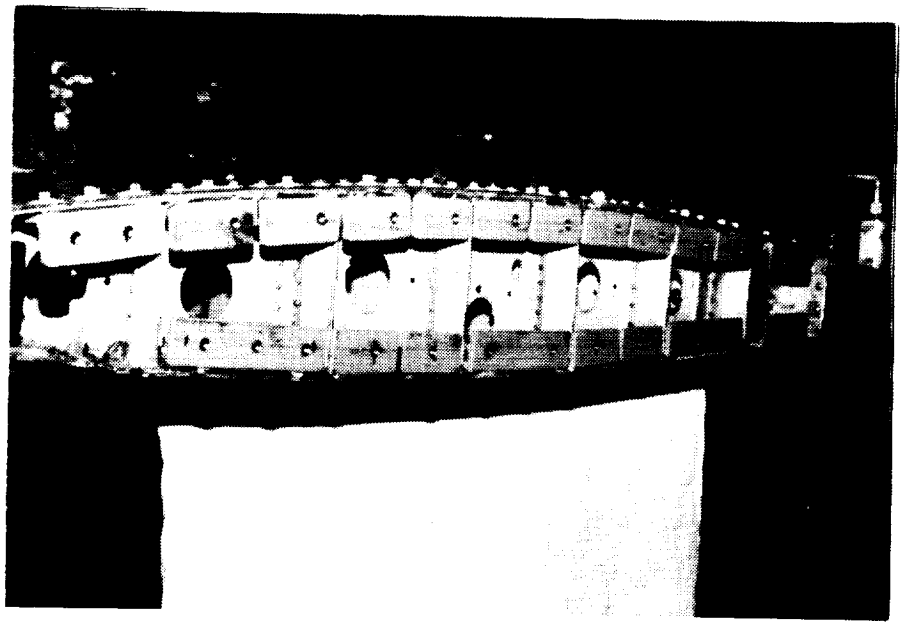

Photo 4-16

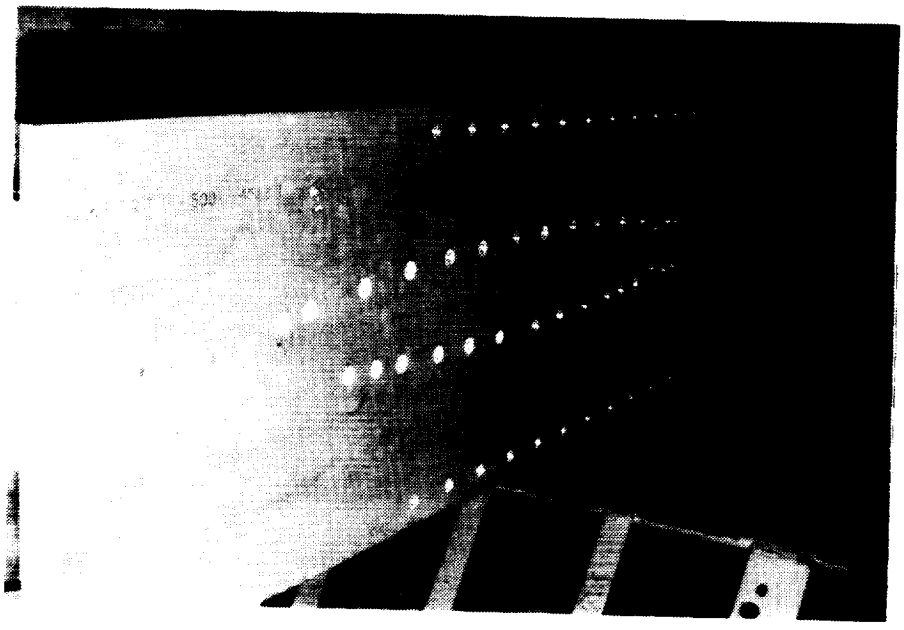

Photo 4-17

Photo 4-18

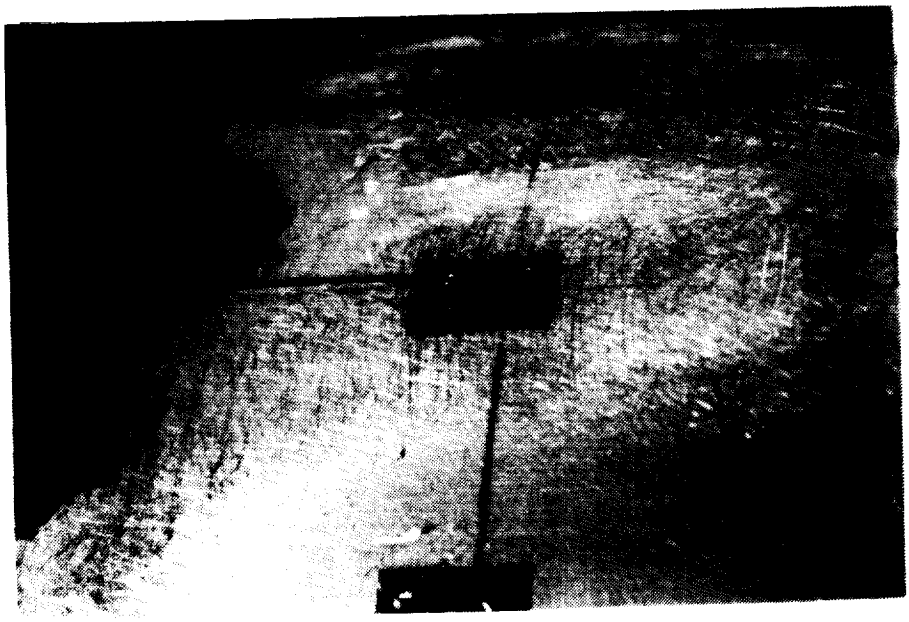

Photo 4-19

Photo 4-20

Strain gages being used have a resistance of 350 ohms, are temperature compensated and have a foil grid which measures 1/8 x 1/8 inch.

Chapter 5. ICING TUNNEL TESTS

An essential part of developing the EIDI system was testing in the NASA Icing Research Tunnel (IRT) at the Lewis Research Center in Cleveland, Ohio. This is a unique facility. The test section of 2 by 3 meters permits full-scale testing of many aircraft components such as wing sections, engine inlets and tail sections. Air speeds over 250 MPH and temperatures below 20°F can be obtained. The spray system provides a range of subcooled water droplets with median volume diameters from 10 to 20 microns and a fair range of liquid water content values.

The first test in Oct.-Nov. 1982 was a feasibility demonstration. This resulted in the decision to proceed with a full development project for the EIDI system. The ten test periods in the IRT are briefly summarized below.

I. Oct. 25 - Nov. 5, 1982 Tests

A. Two Models Tested.

1. Beech Bonanza wing; aluminum leading edge, skin thickness 0.032 inches; tapered; very small distance from spar to high-light, giving a stiff leading edge.
2. Cessna 206 wing; aluminum leading edge, skin thickness 0.025 inches; no taper or twist; over 10 inches from spar to high-light gave a soft, flexible leading edge. Ribs were spaced from 9 to 15 inches apart.

B. Test Descriptions:

1. Beech Bonanza Wing

   * Coils in 3 positions, 14 inches apart, racetrack shaped coils, two side coils in series at each position.

   * 31 runs

   * Tunnel conditions:

110 MPH	25°F	1.2g/m^3	15 microns
110	25	2.4	20
160	25	0.83	14
160	25	1.7	20
230	25	10.6	12
230	25	1.2	20
110	5	1.2	15
160	5	0.83	14
160	5	1.7	20
230	5	0.6	12
110	20	2.4	20

2. Cessna 206 Wing

   * Coils in 3 positions between ribs, supported from beam-between-ribs. Coils were round; side pairs of coils were series wired. After 21st run, the center coil was replaced by a "racetrack" shaped coil at the nose.

   * 36 runs

   * Tunnel conditions:

110 MPH	25°F	1.2g/m^3	15 microns
110	25	2.4	20
160	25	0.83	14
160	25	1.7	20
160	5	0.83	14
160	5	1.7	20
110	5	1.2	15
110	5	2.4	20
110	-15	1.2	15
160	-15	0.83	14
160	-15	1.7	20
110	29	1.2	15
110	29	2.4	20
160	29	0.83	14
160	29	1.7	20
160	15	1.7	20

In addition to the above variables, angle of attack and capacitance were also varied.

C. Major Results and Conclusions

1. The EIDI system can de-ice two General Aviation wings, one stiff and one flexible in leading edge properties, over a wide range of atmospheric and icing conditions.
2. The energy required for a de-icing cycle was about 800 joules per foot of span.
3. High speed movies gave insight into the de-icingphenomenon.

D. Participants

These tests were performed under W.S.U. direction with participation at the IRT by persons from Beech and Cessna Aircraft Companies and Simmonds-Precision. Beech and Cessna provided wing sections for the test models, while Simmonds designed and fabricated the power-and-sequencing box. This Simmonds-Precision power box was used in the first eight IRT tests to date with some modifications. It can supply up to 1800 volts at capacitances from 100 to 750 micro-farads.

II. April 18-22, 1983 Tests

A. Two Models Tested:

1. Cessna 206 wing with 0.025 aluminum leading edge skin.
2. Cessna 206 wing with 0.040 aluminum leading edge skin. Both were on an unswept, untapered, untwisted wing.

B. Test Descriptions (See diagrams on the next two pages).

1. Cessna 206 wings; 0.025 inch aluminum skin.
   * Coils in 5 bays between ribs; 5 different coil-mount combinations.
   * 31 runs
   * Tunnel conditions were kept constant: 160 MPH, 15^{o}F, 1.7 g/m^{3}, 20 microns, 2^{o} angle of attack, 600 uFd.

* Primarily a comparison between different coil or mount designs.

* Variations on a few runs were:
  (a) reduce capacitance to 400 uFd.
  (b) "full-cycle" voltage by removing the diode clamp.
  (c) insertion of false spars to stiffen skins in 3 bays.
  (d) reduced voltage to find number of impulses vs voltage required to de-ice.

2. Cessna 206 wing; 0.040 inch aluminum skin.

   * Coils in 5 bays between ribs; 5 different coil-mount designs.

   * 28 runs

   * One bay had skin replaced by a graphite composite leading edge with a copper doubler.

   * Primarily a comparison between different coil/mount designs, two of which were different from those used for the previous, thin-skin, leading edge.

   * Variations on a few runs were:
     (a) reduce capacitance to 200 uFd.
     (b) "full-cycle" voltage cycle.
     (c) insertion of false spars.
     (d) application of de-icing fluid, ICEX, on the composite leading edge.
     (e) gap between coil and skin filled with plastic material to see structural damping due to "no gap" condition.
     (f) one run at air temperature 29°F.

ELECTRO-IMPULSE DE-ICER PLACEMENT IN WING FOR ICING TUNNEL TESTS, APRIL 18-22, 1983

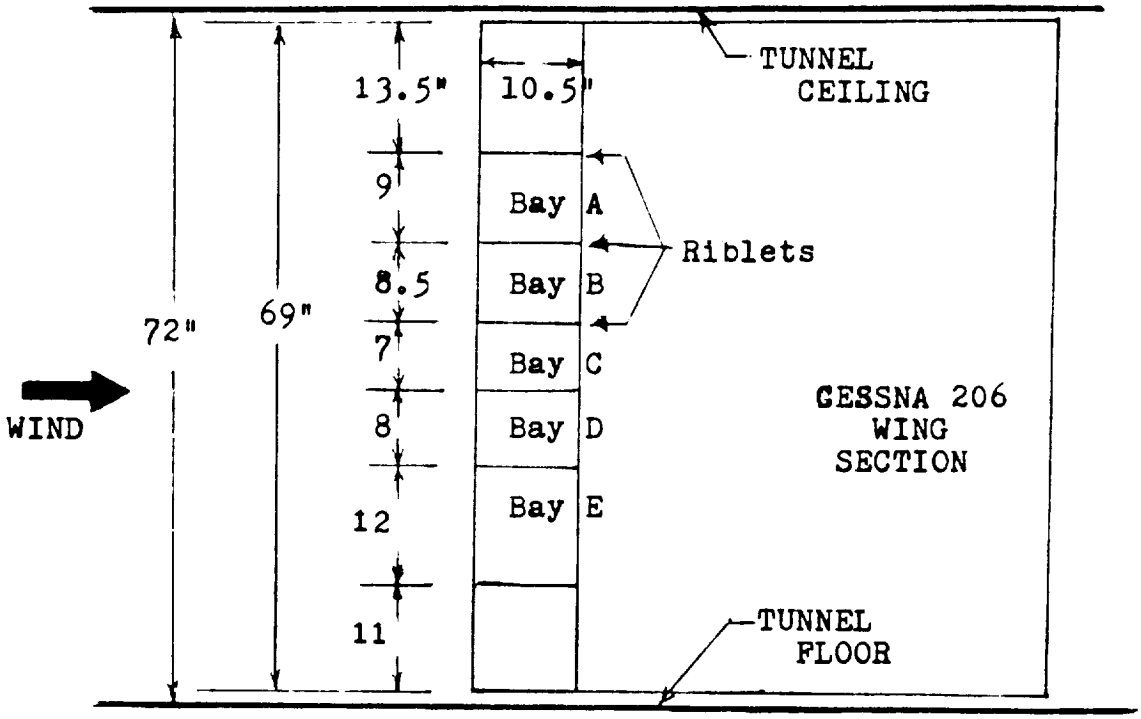

Thin-Skin Leading Edge (0.025 in.)

Bay A. Two Side Coils, With Doublers (Spar)* (Zero Gap)*
Bay B. Two Side Coils (Spar) (Zero Gap)
Bay C. One Nose Coil, With Doubler

Bay D. One Nose Coil (Zero Gap)
Bay E. Push-Pull Design (Spar) (Zero Gap)

Thick-Skin Leading Edge (0.040 in.)

Bay A. Two Side Coils, With Doublers (Spar)
Bay B. Two Side Coils (Spar)
Bay C. Two Side Coils Off-set Spanwise

Bay D. One Nose Coil

Bay E. Composite Leading Edge Inserted One Nose Coil of Inverse Design

*Indicates changes which can be made without removing the wing from the tunnel. A false spar will be inserted or a semi-soft plastic will be placed between the coil and skin to simulate the effect on skin movement of placing the coil directly against the skin.

COIL DESIGNS TESTED APRIL 18-22, 1983

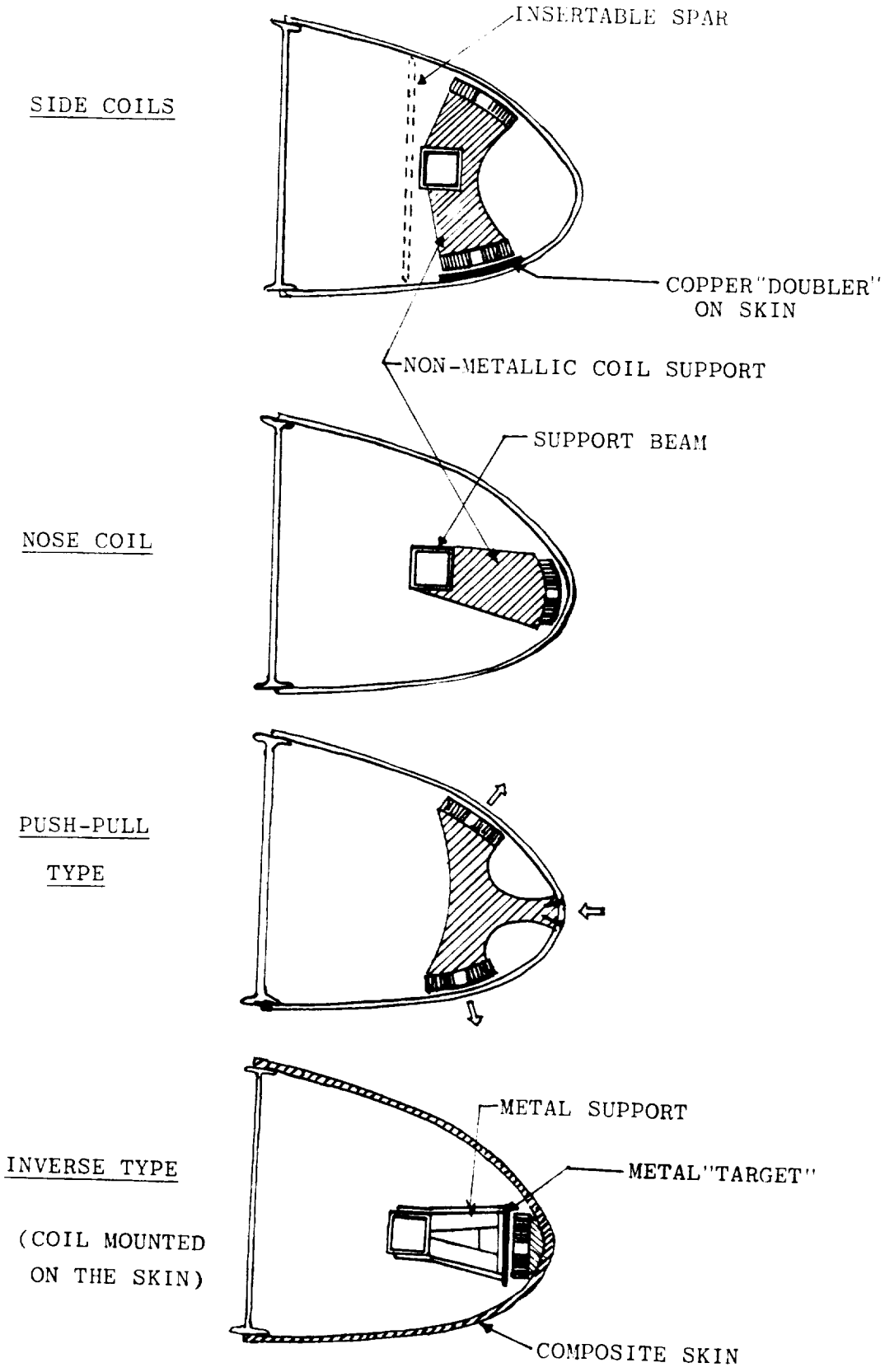

C-4

C. Major Results and Conclusions

1. Using 0.050 inch aluminum doubler with the 0.025 inch skin decreases the required energy by 50% both for nose and side coils. For the 0.040 inch thick skin with side coils, the doubler energy reduction was (surprisingly) over 50%.
2. With doublers, de-icing energy was under 600 Joules per foot of span.
3. One bay had two side coils off-set spanwise from each other, at about the 1/3 span positions,in an attempt to twist the leading edge. This was inferior to aligned coils.
4. Anti-icing attempts were disappointing. Almost the same energy is required to expel 1/8 inch and 2 inches of ice thicknesses.
5. The "full cycle" voltage slightly reduced energy-to-de-ice, but the reduction was judged to be too small to justify the shortened capacitor life which would result from reverse charging.
6. A single nose coil was at least as good for de-icing as a pair of side coils.

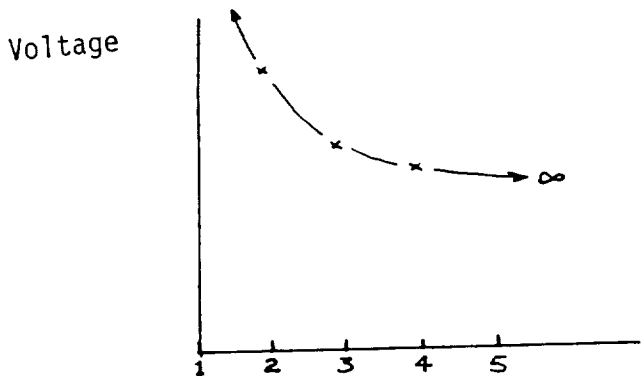

D. Participants

In addition to W.S.U. personnel, Alan Mueller of Cessna Aircraft Company, conducted the test. Cessna provided the leading edges; the wing model from the 1982 test was used again.

III. August 15-18, 1983 Tests

A. One Model Tested:

A 50 inch span "glove" or "cuff" placed on a six-foot section of DHC-6 Twin Otter wing. The glove was identical in shape and material to the base wing, but extended three inches forward of the leading edge. Skin thickness was 0.025 inches with leading edge radius of 2.5 inches. These tests were preliminary to flight tests using the same glove on the NASA Icing Research Aircraft (a Twin Otter).

B. Test Descriptions:

* four nose coils, one each in four 12.5 inch bays; out separated by ribs. Coils were skin-mounted by rivets about 3 inches behind the stagnation line.

* 35 icing runs.

* Tunnel conditions:

100 MPH	28°F	1.4g/m^3	= 10°	15 microns MVD
100	28	2.2	10	18
124	28	1.1	7	14
124	28	2.0	7	19
170	28	0.85	5	13
170	28	1.65	5	20
170	15	0.85	5	13
170	15	1.65	5	20
124	15	2.0	5	19
100	15	2.2	10	18
124	15	2.0	7	19
100	15	2.2	14	18
170	15	1.65	5	20
170	15	0.85	5	13
124	15	1.1	7	14
124	15	0.85	vary 4-9	12

124	15	1.1	7	14
124	30	2.0	7	19

* Capacitance was fixed at 400 uFd. Doublers of 0.050 inch thick No. 1145 aluminum were riveted opposite the coils.

* Coils were impulsed both singly, simultaneously by wiring adjacent-bay coils in series, and by series wiring of every other bay. Series connecting was done for 2, 3 and all 4 bays.

C. Results and Major Conclusions.

1. When impulsed separately, energy required for de-icing was about 600 Joules per foot of span (3 impulses of 200 Joules each). This was reduced for series-connected coils as follows:

Coil Connections	Voltage Required	Energy (Joules/Ft.)
Single Bay	1000	600
Two Bays in Series	1100	363
Two Alternate Bays	1200	280 (center bay not completely clean)
Three Bays in Series	1200	280
Four Bays in Series	1400	292

2. Some runs were made with continuous icing for up to 21 minutes with impulses 3 or 6 minutes apart. De-icing improved after the first impulse sequence in all cases.

3. When angle of attack was varied during the run, ice width was greater in the chord-wise direction, but ice expulsion was not affected.

D. Participants

W.S.U. was joined by Robert Goehner of Simmonds-Precision for these tests.

LEADING EDGE GLOVE
DHC-6 TWIN OTTER

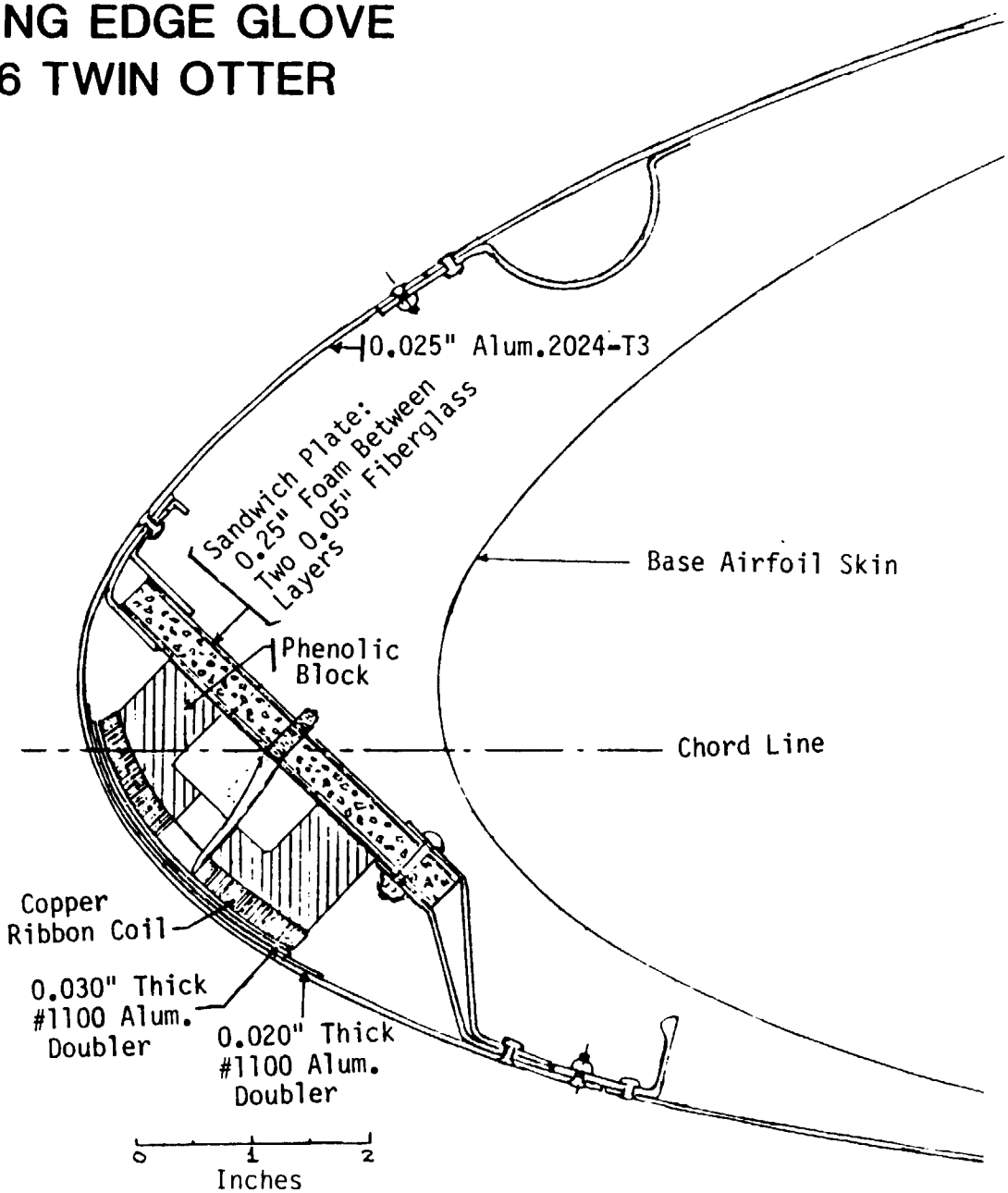

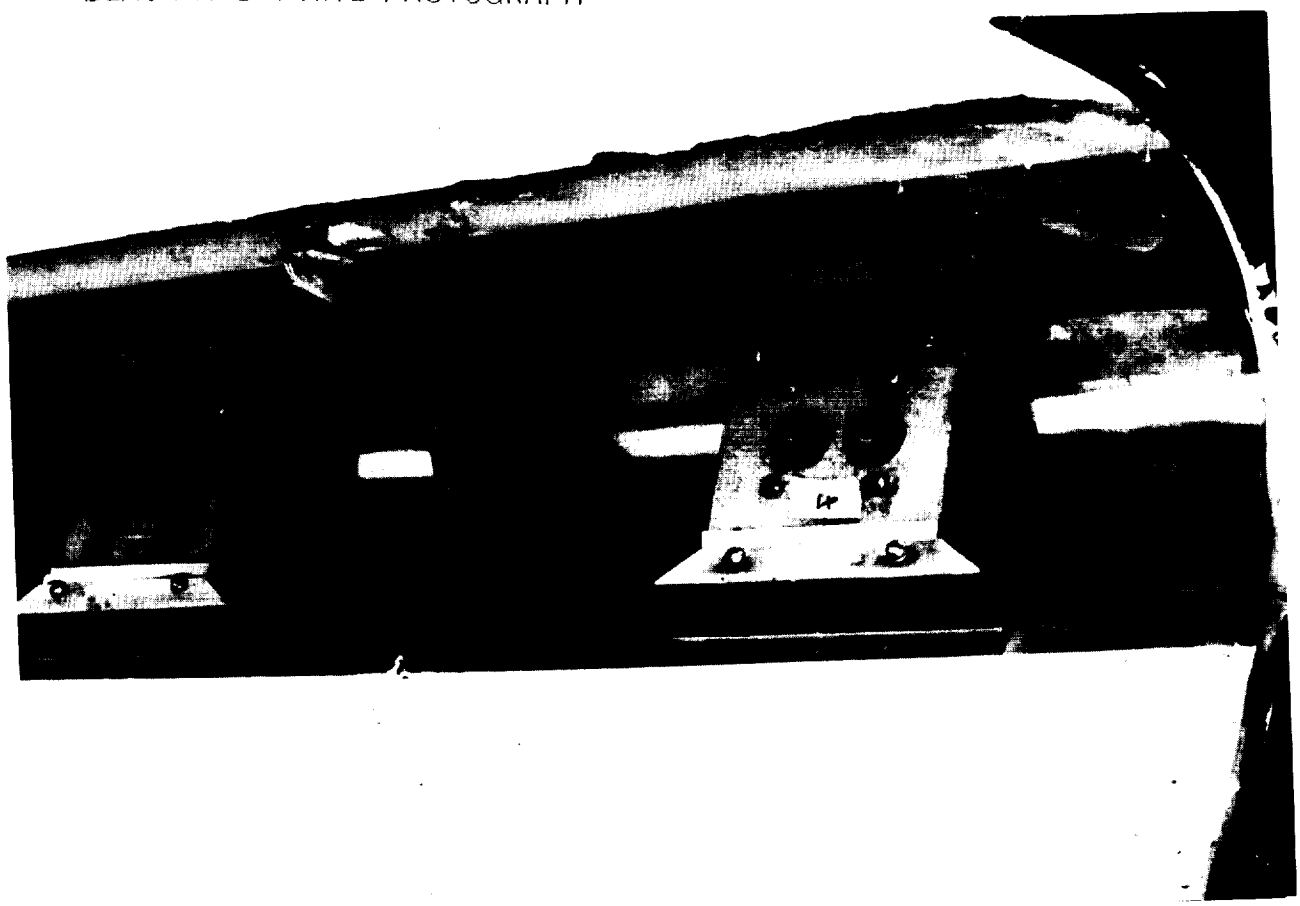

Coil Mounts Attached to the Skin
of the Wing Glove for the DHC-6
Twin Otter

IV. November 7-9, 1983 Tests

A. Two Models Tested:

1. The 50 inch Twin Otter glove (same as previous test).
2. A 38 inch span section from a LearFan wing made of Kevlar epoxy composite. Coils were placed at the quarter and three-quarter positions, giving 19 inch spacing between coils. The leading edge had no ribs. A new type of coil mount was tested for use with composite wings. The coil was separated from the leading edge by a fiberglass-wrapped foam piece mounted on a thin aluminum plate. The plate was opposite the coil and provided the force to the foam wedge which transferred the impulse to the leading edge nose. Half of the composite surface was painted.

B. Test Descriptions

1. Twin Otter glove.

   * Coils in the 4 bays were series-connected in two pairs of alternating bays (1-and-3; 2-and-4) for the first glove test series. Capacitance was kept at 400 micro-Farads.

   * Only one coil was impulse for a second series while the electrical pulse time was varied by changing capacitance and adding external "dummy" coils in series. The purpose was to determine the optimum capacitance value.

   * 8 runs for first series; 11 runs for second series.

   * Tunnel Conditions:

100 MPH	28°F	1.4g/m^3	15 microns MVD
124	28	1.1	14
170	28	0.85	13

2. LearFan Composite Wing.

   * The two coils were impulsed separately and simultaneously.

   * 10 runs

   * Test Conditions:

160 MPH	25°F	0.83g/m^3	14 microns MVD

* Capacitance of 200, 400 and 600 microFarads.

C. Major Results and Conclusions.

1. For the Twin Otter (DHC-6) glove, the use of odd-and-even coil pairs reduced the needed impulses from 3 to 2 for good de-icing. The energy was thus reduced to about 200 Joules/ft.
2. For the second series of glove tests, the effect of capacitance was clear. The minimum energy for de-icing was obtained for 400 microFarads for this wing.
3. The Kevlar composite LearFan leading edge de-iced, but not well. Side coil impulses are probably needed since the leading edge radius was small and the rest of the adjacent walls were relatively flat. About 500 joules/ft. was required to de-ice.
4. Painted and unpainted Kevlar surfaces de-iced alike.

D. Participants

Mr. James Chase of LearFan took part in the test along with W.S.U. personnel.

NOTE: At this point the energy required to de-ice a general aviation wing had been reduced dramatically, as shown in the table and plot on the following two pages.

SUMMARY OF RESULTS OF

ICING RESEARCH TUNNEL TESTS
OF

ELECTRO-IMPULSE DE-ICING

DATE	WING	METHOD	n = NO. IMPULSES PER POSITION	E = ENERGY (Joules/Ft)	ENERGY TO DE-ICE = nE
Oct.1982	Beech Bonanza	Two Side Coils; Single Bay Hits.	2	383	766
Nov.1982	Cessna 206	Two Side Coils; Single Bay Hits.	2	440	880
Apr.1983	Cessna 206	Two Side Coils; Single Bay Hits.	2	450	900
	"	One Nose Coil; Single Bay Hits.	2	414	828
	"	Two Side Coils With Skin Doublers; Single Bay Hits.	2	289	578
	"	One Nose Coil With Skin Doubler; Single Bay Hits.	2	272	544
Aug.1983	DHC-6 Twin Otter	One Nose Coil With Skin Doubler;			
		Single Bay Hits.	3	200	600
		Two-Bay Hits.	3	121	363
		Two-Bay With Bay Skipped Between	3	98	294
		Three-Bay Hits	3	96	288
		Four-Bay Hits	3	98	294
Nov.1983	DHC-6 Twin Otter	One Nose Coil With Skin Doubler; Two-Bay Hits, With "Odds-then-Evens" Sequence. (Bays 1 & 3 hit twice simultaneously, Then Bays 2 & 4 hit twice simultaneously.	2	90	180

Note: For this method, four impulses clean four bays.

These are plotted on the following page, with the "Total Energy Per Position Required To De-Ice" plotted against time when the tests were performed.

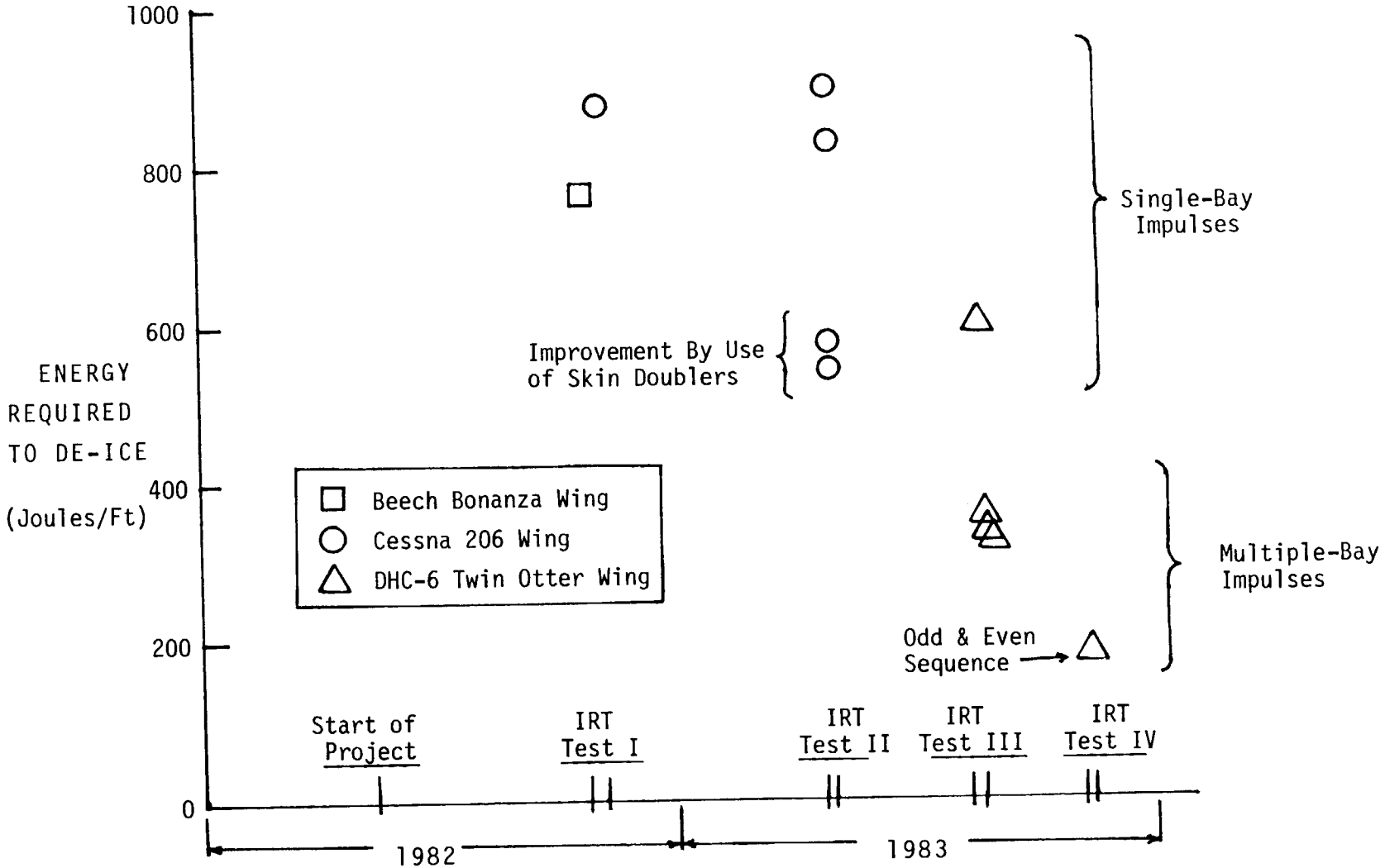
1000
800
600
400
200
0
ENERGY
REQUIRED
TO DE-ICE
(Joules/Ft)
Improvement By Use
of Skin Doublers
Single-Bay
Impulses
Multiple-Bay
Impulses
Odd & Even
Sequence
Beech Bonanza Wing
Cessna 206 Wing
DHC-6 Twin Otter Wing
Start of
Project
IRT
Test I
IRT
Test II
IRT
Test III
IRT
Test IV
1982
1983

V. May 14-23, 1984 Tests

A. Four Models Tested:

1. Learjet wing with the standard (but modified) leading edge; skin thickness 0.063 inches; sweepback 17°.
2. Learjet wing with a composite material replacement leading edge which was 50% thicker and 100% stiffer, but had the same shape as the metal one.
3. A semi-cylinder of 5.0 inch diameter mounted with no sweepback; skin thickness 0.040 inches.
4. A Cessna 206 horizontal tail section; skin thickness 0.025 inches. This was tested to support the planned full-aircraft prototype program. Of the four models in this test, only this one had ribs in the leading edge.

B. Test Descriptions:

1. Learjet; metal leading edge.

   * Coils in 6 positions; 4 coil-mount combinations.
   * 15 runs with doublers added and 9 runs with doublers removed.
   * Capacitances of 200, 400 or 600.
   * Tunnel conditions:

144 MPH	28°F	1.0g/m^3	14 micron MVD
144	15	1.0	14
225	15	1.4	20
225	-10	0.6	12
225	-10	0.6	12

2. Learjet; composite leading edge.

   * Coils in 6 positions; 5 types of coil/mountings.
   * 12 runs
   * Tunnel Conditions:

144 MPH	15°F	1.0g/m^3	14 microns MVD
144	15	1.4	20
144	-10	0.6	12

3. Semi-cylinder (See Chapter 3, Section IV-A for structural tests)

   * One nose coil at mid-span, spar mounted.

   * 13 runs

   * Tunnel conditions:

100 MPH	24°F	1.4g/m^3	15 microns MVD
100	24	2.2	18
100	10	2.2	18
160	15	1.7	20

4. Cessna horizontal stabilizer

   * Coils in 4 positions; one without doublers.

   * 11 runs with the production-type rubber abrasion shield; tunnel conditions for this were:

100 MPH	28°F	1.4g/m^3	15 microns MVD
124	28	1.1	14
160	28	0.83	14
160	15	0.83	14

   * 14 runs with the rubber abrasion shield removed; tunnel conditions for this were:

100 MPH	28°F	1.4g/m^3	15 microns MVD
100	15	1.4	15
100	15	2.2	18
124	28	1.1	14
124	15	1.1	14
124	15	2.0	19
160	28	0.83	14
160	15	0.83	14

C. Major Results and Conclusions.

1. Learjet leading edge needs re-designed coil/mount system due to its peculiar, drooped nose shape and unsymmetrical support.
2. Doublers are slightly helpful for 0.050" thick skins.
3. The composite material posed no special problem. It was only slightly more difficult to de-ice than its metal counterpart.
4. Painting the composite skin made no difference in de-icing.
5. The one coil in the semi-cylinder expelled ice from over five feet of length. Good high-speed movies were obtained for this.

6. The Cessna tail section was easily de-iced despite small size and skin thickness.

D. Participants

1. Gates-Learjet supplied the wing model and participated in the IRT test.
2. Cessna supplied an empennage for making the tail model and participated in the test.
3. Simmonds-Precision sent a participant for the IRT test.

ORIGINAL PAGE
BLACK AND WHITE PHOTOGRAPH

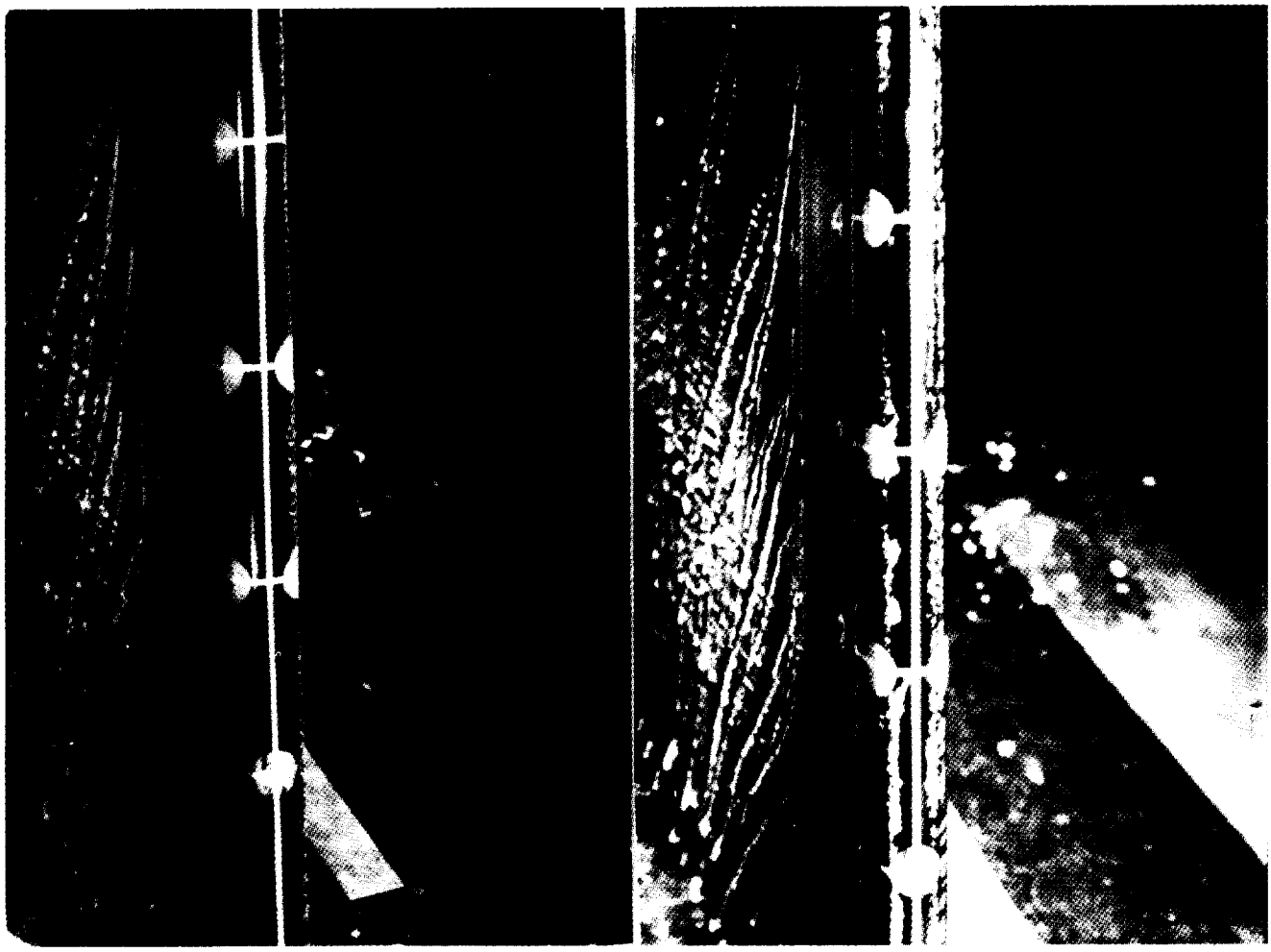

20 micron droplet size	12 micron droplet size
1.4 g/m3 LWC	0.6 g/m3 LWC
5 minutes spray	10 minutes spray
700 volts/coils station	800 volts/coil station

Test Conditions For Both:
225 Miles/Hour Airspeed
15oF Air Temperature
4o Angle of Attack
400 MicroFarads

LEARJET ALUMINUM LEADING EDGE AFTER DE-ICING: ILLUSTRATION OF GREATER DIFFICULTY DE-BONDING SMALL-DROPLET ICE

VI. August 13-17, 1984

A. Three Models Tested:

1. A slat from the wing of a Boeing 767; sweepback 34°; skin thickness, 0.062 inches. This portion of the slat was from a wing station about 65% of span from the fuselage.
2. The Learjet wing with its standard metal leading edge was returned for a second IRT test.
3. The 5 inch diameter semi-cylinder was returned with a pair of spar-mounted side-coils placed 45° to the nose. This pair was at mid-span.

B. Test Descriptions:

1. Boeing 767 (See Chapter 3, Section III, for structural tests)

   * Coils in 6 positions; 3 coil/mount types.
   * 21 runs.
   * Tunnel conditions

170 MPH	28°F	0.85g/m^3	13 micron MVD
170	28	1.65	20
240	27	0.85	20
240	15	0.6	14
240	15	1.1	20
240	-10	0.54	10
240	-10	1.1	20

2. Learjet

   * Coils in 4 positions; 4 coil/mount types.
   * 22 runs
   * Tunnel conditions:

144 MPH	28°F	1.0g/m^3	14 microns MVD
144	15	1.0	14
225	15	1.0	15
225	15	1.4	20

3. Semi-cylinder (See Chapter 3, Section IV-A for structural tests)

   * Two side-coils were spar-mounted in one mid-span position.

* 14 runs

* Recordings were made for signals from strain gages and, sub-miniature accelerometers mounted near the coils.

* Tunnel conditions:

100 MPH	24°F	2.2g/m^3	18 microns MVD
100	24	1.4	15
100	10	2.2	18
160	15	1.7	20

C. Major Results and Conclusions.

1. The Learjet wing still defied de-icing without unacceptable residual ice particles.
2. The Boeing 767 slat de-iced quite well using spar-mounted side-pair coils.
3. Best de-icing was achieved using low (200 uFd) capacitance giving very short electrical pulse times for the 767 slat; this gave higher skin stresses than desired. An optimized coil design and re-test is needed.
4. For the semi-cylinder, a nose coil is clearly superior to a pair of side coils. Good high-speed movies were obtained for the cylinder.
5. A skin-mounted coil-pair gave the best performance and lower stresses.

D. Participants

W.S.U. was joined by three men from McDonnell-Douglas, one each from Boeing and Gates Learjet and two observers from the Lockheed-Georgia Co. Boeing supplied the B-767 slat.

VII. Sept. 17-21, 1984

A. Two Models Tested:

1. The Learjet wing was returned for a third set of tests. Three new coil/mount types were installed, including the skin-mounted "band-aid" mounting.

2. A Falcon Fanjet engine inlet (supplied by Rohr Industries) was equipped with EIDI coils.

B. Test Descriptions:

1. Learjet

   * 6 types of coil-and-mount configurations were tried in 6 positions.

   * 10 runs

   * Tunnel conditions:

144 MPH	28oF	1.0g/m3	14 micron MVD
144	15	1.0	14
225	15	0.6	12
225	15	1.4	20

2. Falcon Fanjet Engine Inlet (Reference 5-3)

   * coils were placed in 8 equally-spaced positions; 6 coil/mount types, including one with "band-aid" mounts.

   * 29 runs

   * Four capacitance from 200 to 750 uFd were used.

   * Tunnel conditions:

110 MPH	27oF	1.2g/m3	= 0o	15 micron MVD
110	27	1.2	10	15
110	15	1.2	0	15
110	15	1.2	10	15
110	15	2.4	0	20
170	15	0.85	0	13 (with 66% blockage)
170	15	1.65	0	20
170	26	0.85	0	13
225	15	0.6	0	12
225	27	0.6	0	12

C. Major Results and Conclusions

1. A new transverse skin-mount ("band aid" mount) proved to be the most effective de-icer for both the Learjet wing and the engine inlet. It has the added advantage of very light weight. The only question concerning its usefulness is in its resistance to de-bonding during long-time use.
2. The Learjet wing was finally de-iced well by either of two coils, both using a single coil well off-set from the nose.
3. Two icing conditions continue to be the most difficult to de-ice. Both of these lack structural integrity to produce a peel failure. The second is cold, small droplet rime ice ice. The photographs on the following page demonstrate the second case.
4. The engine inlet's curvature-induced stiffness was no problem for electro-impulse de-icing.
5. For the 36 inch diameter engine nacelle inlet, six coil positions are easily adequate, giving 300 joules per foot of circumference.
6. Ice fragments were caught in a net and photographed for the engine inlet tests. These seem to be small enough to be safely ingested by a turbofan engine. A general rule was formulated: Effective diameter of an ice piece will not exceed three times its thickness.
7. A rear blockage plate was used on eight runs to force the ice formation inside the lip. No difficulty was found in expelling ice due to blockage or due to 10o yaw.

D. Participants

W.S.U. personnel were assisted by one industry participant from Simmonds-Precision, Cessna, Boeing, and Gates Learjet. Three participants were present from Rohr Industries.

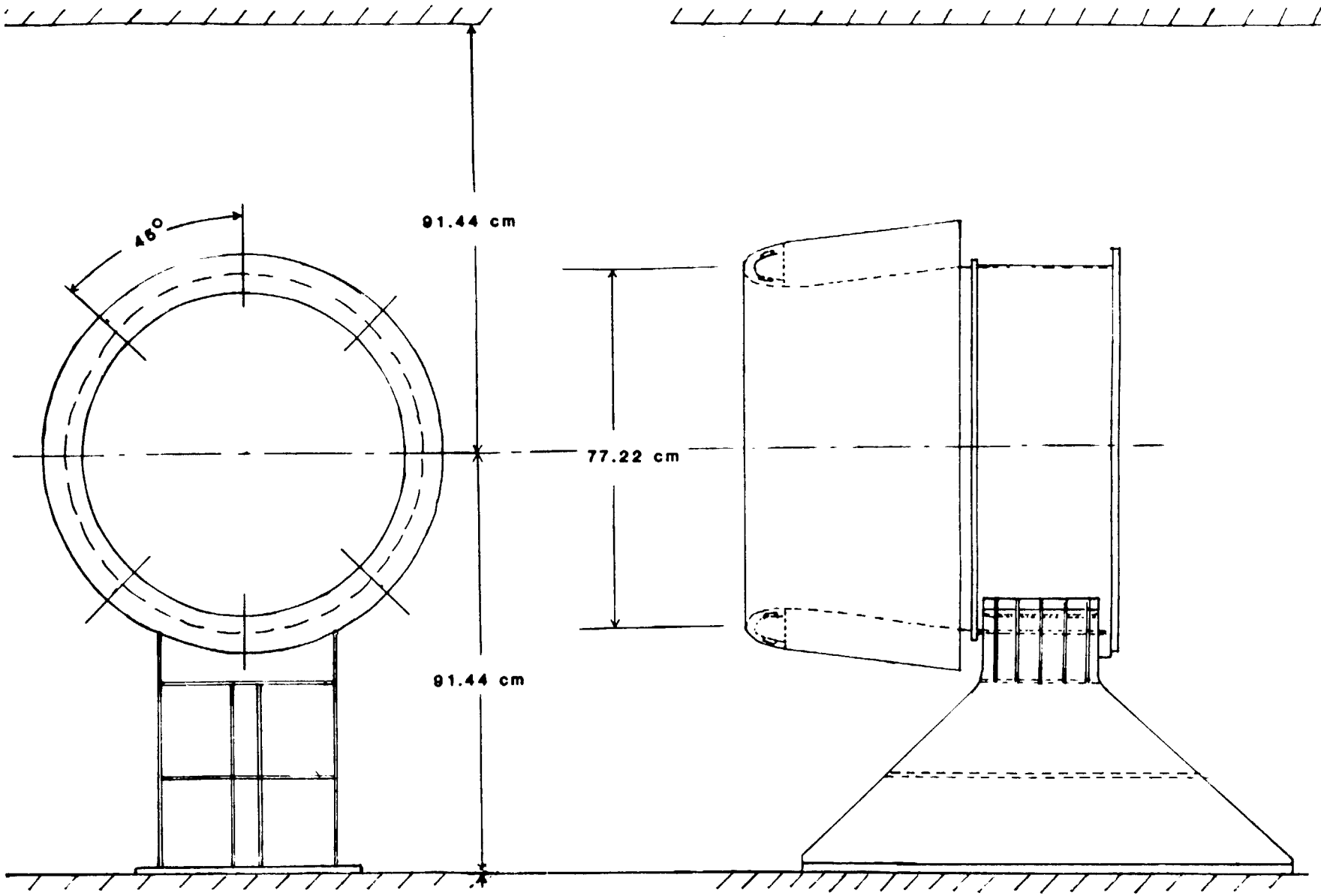

FALCON FANJET 20 ENGINE INLET TEST MODEL

FALCON FANJET ENGINE INLET DURING DE-ICING CYCLE

COBRA HELICOPTER BLADE ICED

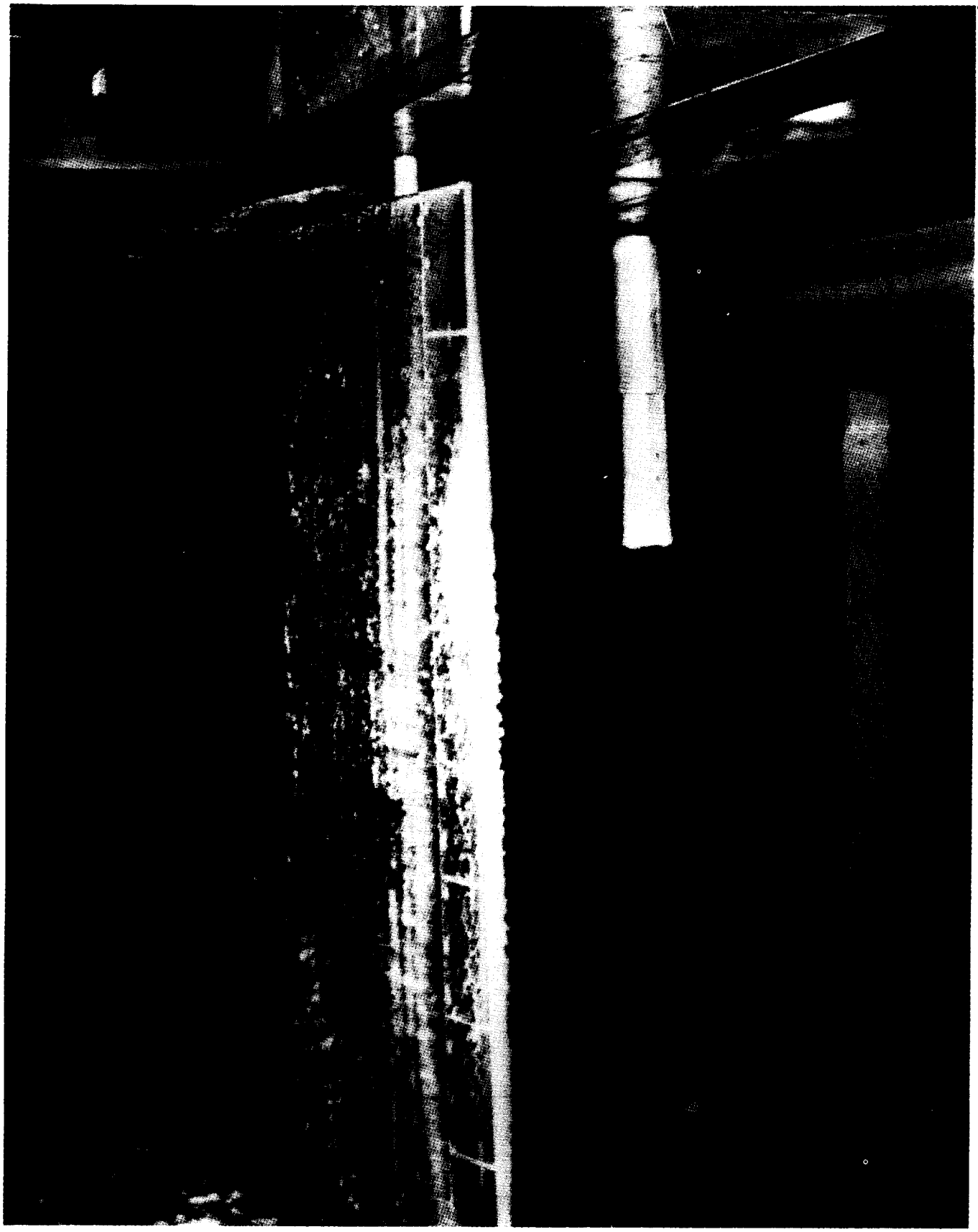

COBRA HELICOPTER BLADE AFTER DE-ICING

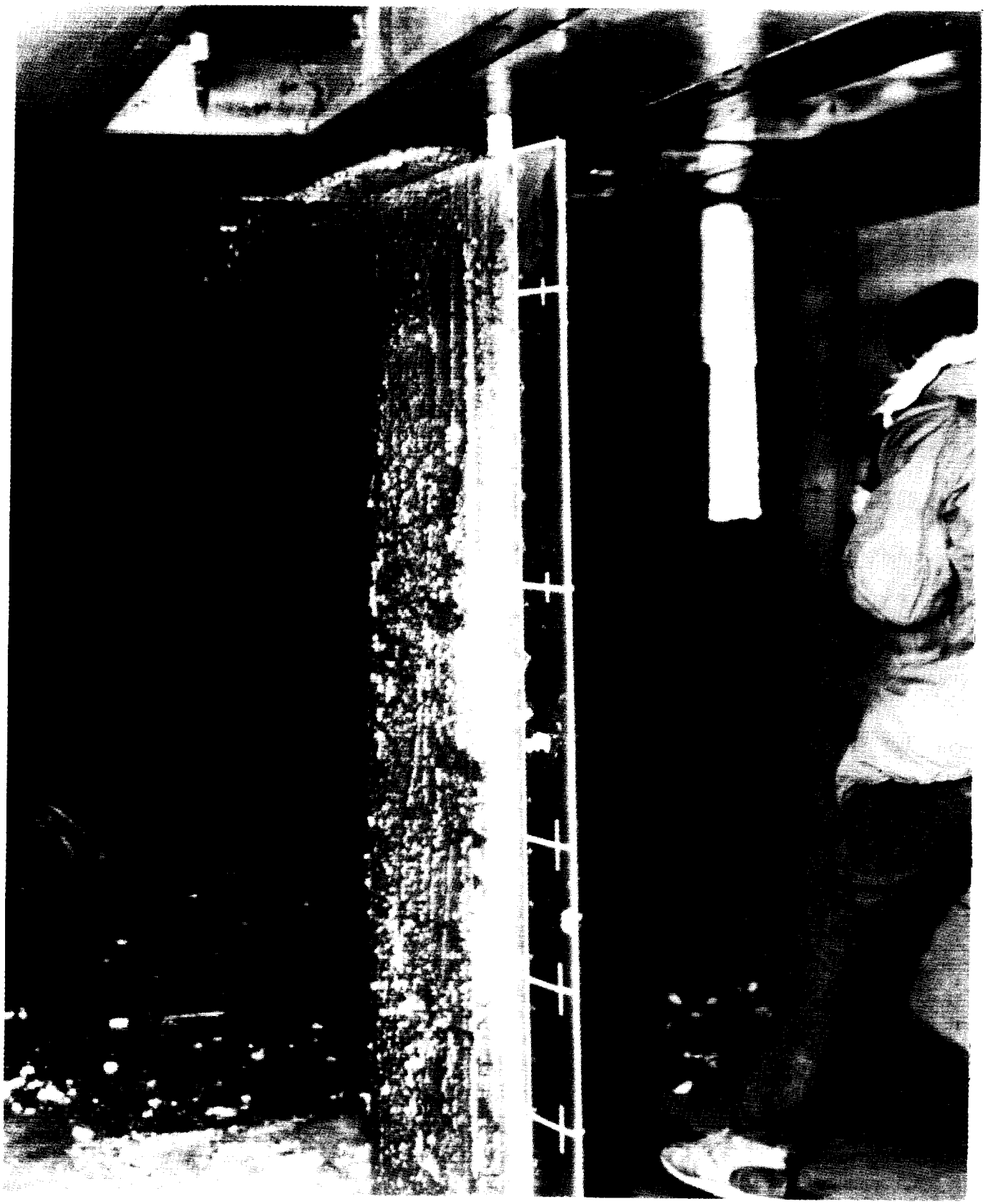

VIII. Nov. 26 - Dec. 4 1984 Tests

A. Six Models Tested

1. Cessna 206 horizontal stabilizer modified for retrofitting EIDI coils. A cuff extending the leading edge 3 inches was attached by rivets at the front spar.
2. Cessna 206 wing strut modified for retrofitting EIDI coils. A sheet metal (aluminum) airfoil shape was wrapped around the original elliptical-shaped strut .
3. Cessna 206 wing strut modified for new production to be more compatible with EIDI installation. Aluminum sheet airfoil was supported by an interior, load bearing, I-beam.
4. Cessna 206 wing section, outboard , skin thickness of 0.025 inches.
5. Cessna 206 wing section, inboard, modified for optimum EIDI rib spacing (18 inches) with 0.040 inch skin thickness.
6. Helicopter blade, mid-span section from AH-1 Cobra; this is an all-composite blade with 31 inch chord and slight twist.

B. Test Descriptions

1. C-206 Horizontal Stabilizer; 0.032 inch aluminum skin.

   * Two coil positions between 22 and 19 inch rib spacings; One position had side-pair coils mounted on an arch supported from the skin 3 inches behind the nose. The second had a composite beam version of the transverse skin-mount (band-aid) single coil on the pressure side of the leading edge. Doublers were used with all coils.

   * 48 runs

   * Tunnel conditions:

110 MPH	27oF	2.4g/m3	= 4o	20 micron drop diameter
110	27	1.2	4	15
160	27	1.7	0	20
160	27	0.83	0	14
110	10	2.4	-4	20
110	10	1.2	-4	15

160	10	0.83	0	14
160	10	1.70	0	20
160	-10	0.83	0	14

All of these were run with both metalized and electrolytic capacitors except the last two, which were done only with electrolytic. (At previous wind tunnel tests, the more expensive metallized type were used.)

* To represent two or three coils in series, each coil was connected to one or two identical coils, outside the tunnel, which had "dummy" aluminum skins.

2. and 3. C-206 Wing Struts (Both types).

* Two coil positions 24 inches apart; one position had side-pair coils supported on a skin-mounted arch; the second was a single "band-aid" mounted coil, one one side only immediately behind the nose.

* 42 runs

* Tunnel conditions

110 MPH	27oF	2.4g/m3	20 micron MVD
110	27	1.2	15
160	27	1.7	20
160	27	0.83	14
110	10	2.4	20
110	10	1.2	15
160	10	1.7	20
160	10	0.83	14
160	-10	0.83	14

* Electrolytic capacitors were used (500 microFarads).

4. C-206 Wing, 0.025" skin thickness.

* A current-production leading edge was used which had 3 bays of differing span. In a 13 inch bay, a nose coil was mounted on an aluminum beam mounted to the ribs; In a 15 inch bay, a nose coil was mounted on a stiff, 6 inch long, composite bar attached (spanwise) to the skin at its ends; In a 17 inch bay, a band-aid type coil mount was placed on both upper and lower surfaces behind the nose; (these were wired separately). Doublers were used with all coils.

* 19 runs

* Tunnel Conditions

110 MPH	27oF	2.4g/m3	20 micron MVD
110	27	1.2	15

160	27	1.7	20
160	27	0.83	14

* Electrolytic capacitors; 375 microFarads.

5. C-206 Wing; 0.040" skin thickness.

   * Three 18 inch bays each had identical nose coils, but were mounted differently. One was skin-mounted on a composite arch, one was a band-aid type, and one was supported by a composite rib mounted to the ribs. Doublers were used with all coils.

   * 32 runs

   * Electrolytic capacitors; 375 and 500 microFarads. Two runs were made with metalized capacitors for comparison.

   * Tunnel conditions were the same as listed above for the horizontal stabilizer.

6. Helicopter blade

   * The outer 32 inches had an aluminum leading edge of 0.032 inch thick aluminum; the composite underneath was cut back to the first spar and two band-aid type coil mounts were placed 16 inches apart on the lower (pressure) surface. The inner 38 inches of the blade had an aluminum leading edge stretched against the solid composite leading edge, but bonded to it only aft of the nose region. Small "racetrack" shaped coils were recessed into the composite material and aluminum doublers bonded to the skin opposite them. Coil dimensions were 0.75 x 1.3 inches, and 0.125 inches thick. These were recessed into positions 8 inches part at three lower surface positions and 12 inches apart at two upper surface positions.

   * 15 runs

   * Tunnel conditions

230 MPH	$27^{o}F$	$1.2g/m^3$	= 10^{o}	20 micro MVD
230	27	0.6	10	12
230	27	0.6	0	12
230	10	1.2	5	20
230	10	0.6	5	12
230	-10	1.2	5	20
230	-10	0.6	5	12

   * Metalized Capacitors, 400 microFarads.

C. Major Results and Conclusions

1. For the horizontal stabilizer, rib spacings of 22 inches

are acceptable. Coils can be connected for three side-pairs in series and impulsed three times to de-ice with the 375 micro-Farads electrolytic capacitors. This gives a total energy of 246 Joules per foot of span. The band-aid type, similarly connected, would require 215 J/ft.

2. The wing struts de-iced well with three impulses using about 200 J/ft. The band-aid mounts were somewhat superior to side-pair types.

3. For the wing leading edges, the beam-between-ribs and simple band-aid coil mounts de-iced well. The attempts to devise a rigid band-aid mount were not successful. Energy required was about 400 J/ft. with three impulses.

4. For the helicopter blade, the outer section was used as a comparison with similar sized wing tested previously. This de-iced easily, but is not typical of a helicopter leading edge structure. The inner blade section was believed to be a viable helicopter EIDI design. Best de-icing was achieved using the three lower surface mini-coils in series with 1300 volts and three impulses. This gave 400 Joules per foot of span as energy requirement. Ice shedding was good for all cases. A continuous icing run was made with de-icing every 2 minutes for 10 minutes; Results were very good. Attempts to use only two coils 16 inches apart were unsuccessful. Upper surface coils used alone or in series with lower coils were inferior to lower coils impulsed alone. The photographs on the next two pages show the blade before and after de-icing.

are are acceptable. Coils can be connected for three side-pairs in series and impulsed three times to de-ice with the 375 micro-Farads electrolytic capacitors. This gives a total energy of 246 Joules per foot of span. The band-aid type, similarly connected, would require 215 J/ft.

2. The wing struts de-iced well with three impulses using about 200 J/ft. The band-aid mounts were somewhat superior to side-pair types.

3. For the wing leading edges, the beam-between-ribs and simple band-aid coil mounts de-iced well. The attempts to devise a rigid band-aid mount were not successful. Energy required was about 400 J/ft. with three impulses.

4. For the helicopter blade, the outer section was used as a comparison with similar sized wing tested previously. This de-iced easily, but is not typical of a helicopter leading edge structure. The inner blade section was believed to be a viable helicopter EIDI design. Best de-icing was achieved using the three lower surface mini-coils in series with 1300 volts and three impulses. This gave 400 Joules per foot of span as energy requirement. Ice shedding was good for all cases. A continuous icing run was made with de-icing every 2 minutes for 10 minutes; Results were very good. Attempts to use only two coils 16 inches apart were unsuccessful. Upper surface coils used alone or in series with lower coils were inferior to lower coils impulsed alone. The photographs on the next two pages show the blade before and after de-icing.

D. Participants

W.S.U. test conductors were joined by industrial participant representatives from Cessna, Simmonds-Precision, and Kamen Aerospace Co.

IX. June 12-19, 1985 Tests

A. Three Models Tested:

1 & 2. Two Falcon Fanjet engine inlets similar to that tested in Sept., 1984, as described in Section 5 VII.

3. A six-foot span, 5.0 inch diameter semi-cylinder. This model was also used in the May, 1984 tests, (Sections 5 V) and the August, 1984 tests (Section 5 VI). As before, this was made of 0.040 inch thick aluminum, had no sweepback and was solidly mounted to a spar and a tapering, symmetrical afterbody.

B. Test Descriptions:

1. Falcon Fanjet Engine Inlet No. 1. (Reference 5-3)

*Coils were place in six equally-spaced positions, about 16 inches apart. All coils were side-pair type, bulkhead supported, 0.125 in thick, 1.8 inch diameter, 28 turns. Unalloyed aluminum doublers, 0.050 inches thick, 1.90 in. diameter were bonded opposite each coil with a 0.070 inch gap.

*13 runs at zero angle of attack.

*Tunnel conditions

110 MPH	27o	1.2g/m3	15 microns MVD
110	15	1.2	15
110	15	2.4	20
170	27	0.85	13
170	15	0.85	13

2. Falcon Fanjet Engine Inlet No. 2

*Coils were placed at four equally-spaced positions. These were single "band-aid" coils, mounted on the inner side four inches thick, 2.2 inch diameter, 40 turns with an 0.070 inch gap. Two positions had doublers and two did not.

*7 Runs at zero angle of attack.

*Tunnel conditions were the same as for inlet No. 1.

3. Semi-cylinder

*Three contoured nose coils were place at three span-wise positions. They were spar-mounted. The coils had diameters of 1.53, 1.85 and 1.25 inches and all had 40 turns. Eight strain gages measured strain levels along the span. This was mainly a structural dynamics test. Also, the effect of coil diameter for coils of equal D.C. resistance was studied.

*25 Runs at zero angle of attack.

*Tunnel conditions were constant at 200 MPH 15oF 1.0g/m3, 15 micron MVD.

*Capacitance was changed from 600 to 400 to 200 microFarads.

C. Major Results and Conclusions

1. Six coil positions were adequate to de-ice the engine inlet, with two successive pulses. Since coils were connected in pairs, six impulses requiring 20 seconds of time and nearly 2,000 joules of energy constituted a de-icing cycle. The energy per foot for one cycle was about 240 joules. One test was run with continuous heavy icing (2.4g/m3). An EIDI cycle was performed each 3 minutes for 15 minutes. The inlet lip had ice build-up never exceeding 0.2 inches. Then for 6 minutes the EIDI system cycled completely every 20 seconds. Anti-icing was not achieved; some small, grainy residual ice was present on some part of the inlet at all times. But ice particles expelled were quite small. For a one-minute de-icing cycle, about 40 watts would be required.

2. The second engine inlet lip did not de-ice as well as the first. The 90o intervals, giving over two feet between coils, was too great for consistent cleaning. Ice was often left at the four intermediate positions, but mainly on the surface outside the

high light. Doublers gave only slight advantage.

3. For the semi-cylinder, a nose coil is clearly superior to a pair of side coils. The lower capacitances, 200 and 400 uFd, de-iced equally well with equal energies, but 600 uFd (with its longer impulse time) was less effective. Results from strain gage measurements were sued as test cases for computer modeling of the structural dynamics.

D. Participants

W.S.U. test conductors were joined by Rohr Industries personnel led by Donald Nelepovitz

X. Sept. 10-16, 1985 Tests

Tests in the NASA Icing Research Tunnel performed during this period were funded by Grant NAG 3-607 from NASA-Lewis to Wichita State University. The purpose was to determine the feasibility of using EIDI for the corner turning vanes for an icing wind tunnel. This was part of the design study of converting the Altitude Wind Tunnel (AWT) at the Lewis Research Center to a transonic, altitude simulating, icing tunnel. For the proposed higher speeds, cleanliness of the turning vane surfaces was important. Disposing of the collected moisture in the form of ice was preferable to melting or boiling it from the vane, since the moisture would simply freeze on components farther downstream. The proposed corner vanes were much larger than any models previously tested under this program. Since a full 90 degree turn was involved, the entire concave side of the vanes were expected to collect ice. This was a chordwise length of about four feet, while vane lengths would be a great as 27 feet. Also, the surface material was different. The vanes were to be made of stainless steel 0.062 inches thick.

It was therefore much stiffer than any other materials de-iced before by EIDI. Due to low electrical conductivity of stainless steel, rectangular copper doublers, 0.062 inches thick, were bonded to the skin opposite all coils.

The model vane was made full size in the chordwise direction and seven feet in length. It was designed to be placed downstream of the test section in the NASA/Lewis Icing Research Tunnel, just upstream of the first corner vanes of the IRT where the tunnel cross-section was about 13 feet square. The test vane was accompanied by two "dummy" vanes on either side to give realistic airflow past the test vane. Only the center vane was fitted with de-icing coils. The 7 foot vanes were supported in the center of the 13 x 13 foot area to avoid wall interference and to be in the uniform flow region.

The arc shaped airfoil had two main spars and a strengthened trailing edge.

Visual data were taken by a remote television camera as well as by hand held still and motion picture cameras. A wide variety of temperatures, liquid water contents and nominal droplet sizes were used. Reference 5.4 contains the data records for twenty test runs, each including several combinations of the 19 installed coils. The coils differed in number of turns (35-51) diameters (3 to 4 inches) and placement in their bays. Ice thicknesses varied from 0.25 to 3.5 inches at the leading edge. Ice texture varied widely as a function of airspeed and icing conditions.

In every case, ice could be expelled with only light grainy residual pieces remaining on the inner surface. The feasibility was determined to be demonstrated.

XI. References

5-1. Zumwalt, G.W. and Mueller, A.A., "Flight and Wind Tunnel Tests of an Electro-Impulse De-Icing System," AIAA/NASA General Aviation Technology Conference, Hampton, VA, July 10-12, 1984. AIAA Paper No. 84-2234.

5-2. Zumwalt, G.W., "Icing Tunnel Tests of Electro-Impulse De-Icing of an Engine Inlet and High-Speed Wings," AIAA 23rd Aerospace Sciences Meeting, Reno, Nevada, January 14-17, 1985. AIAA Paper No. 85-0466.

5-3. Zumwalt, G.W., "Electro-Magnetic Impulse De-Icing Applied to a Nacelle Nose Lip," AIAA/SAE/ASME 21st Joint Propulsion Conference, Monterey, CA, July 8-10, 1985. AIAA Paper 85-1118.

5-4. Zumwalt, G.W. and Ross, Richard, "De-Icing of the Altitude Wind Tunnel Turning Vanes by Electro-Magnetic Impulse" Wichita State Univ., Aeronautical Report AR 86-3, Final Report for NASA Grant 3-607, March 1986.

6. FLIGHT TESTS

Two flight test series were completed and reported in Refs. 6-1 and 6-2. Other related flight experiences will also be described here.

I. NASA Icing Research Aircraft

During January 1984, the EIDI system was tested in twenty-one flights from NASA Lewis Research Center over the Lake Erie area in the well-instrumented NASA/Lewis Icing Research Aircraft, a DeHavilland DHC-6 Twin Otter. Robert Friedberg of W.S.U. operated the EIDI Equipment on the flight. NASA pilots were Rich Ranaudo and Robert McKnight. The purposes were:

1. To make direct comparisons between the EIDI performance in the icing tunnel and in natural icing conditions.
2. To explore possible electro-magnetic interference (EMI) problems.
3. To obtain flight operation experience safely in natural icing with an aircraft and crew having extensive prior experience flying in icing conditions.

Twenty-one flight were made from NASA/Lewis in Cleveland, Ohio, over the Lake Erie area in January, 1984.

A. Equipment Used

A power supply-and-sequencing box was designed and built by Simmonds-Precision. While considerably lighter than that used in the IRT tests, this was still a research tool rather than a production model. It provided capacitance of 400 uFd and voltage from 800 to 1200, with automatic sequencing of either 2 or 3 impulses per station as fast as the capacitors recharged, an interval of 3 to 4 seconds.

Since the aircraft was already fitted with deicing boots, a cuff section was constructed for the tests which would not interfere with boot operation. The cuff (or "glove") was a 50 inch long section constructed from a cannibalized DHC-6 wing, and its leading edge extended 3 inches forward of the wing's leading edge. Thin fences were placed at each end to minimize end effects on the flow. Like the main wing, the cuff section was unswept with ribs at 12.5 inch spanwise spacing, and had a leading edge made of 2024 T-3 aluminum, 0.025 inches thick, with radius of approximately 2.5 inches. The cuff was placed at about two-thirds semi-span position from the fuselage on the right wing as shown in Figure 6-1. The cuff assembly was fabricated and coils installed by WSU, and tested first in the Icing Research Tunnel, as described in 5. IV.

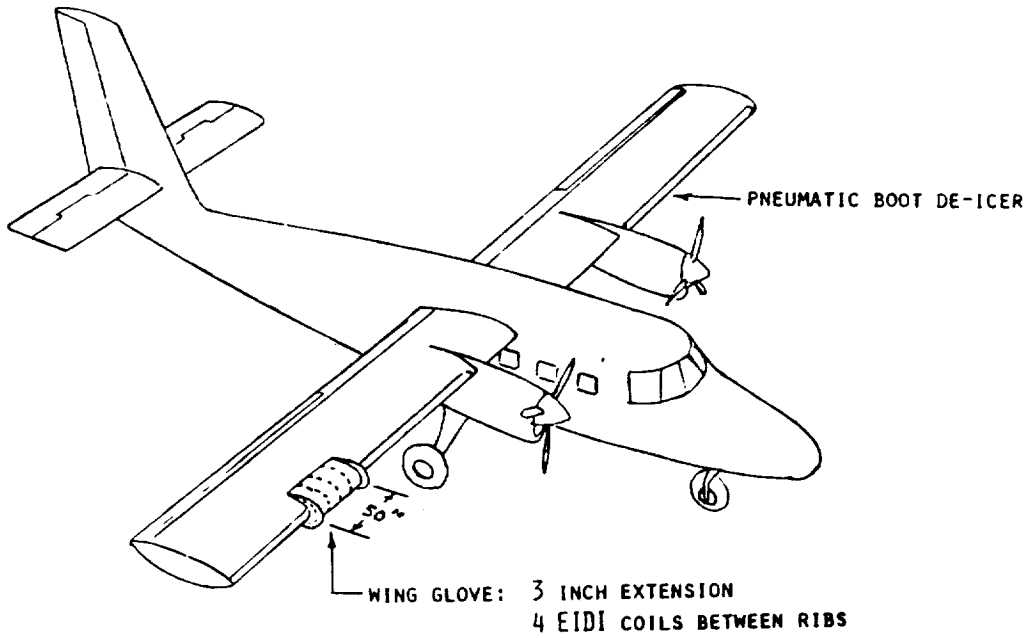

Fig. 6-1 DHC-6 Twin Otter Aircraft
for E.I.D.I.

A single, contoured coil was placed at the center of each bay, mounted on a composite plate which was riveted to the skin about 4 inches aft of the leading edge. The coils had 40 turns of copper ribbon wire, 0.024 x 0.190 inches, giving a 2.5 inch coil diameter. An aluminum doubler, 0.050 thick, was bonded to the inside of the skin opposite the coil, with a gap of 0.050 inches between doubler and coil. The coils were connected in alternating pairs and were impulsed two times each (bays 1-and-3 twice, then 2-and-4 twice) with 1000 volts at 400 uFd. This gave an energy of 96 joules per impulse per foot of span per impulse.

Cameras are installed in right side of the forward fuselage, including a steroscopic system to permit determination of ice shapes.

B. Test Procedures

Due to the effect of Lake Erie on the atmosphere above it, a wide variety of icing conditions are available during the winter months. The pilots sought a range of temperatures and ice types. Rime ice was encountered on 3 flights, clear glaze ice on 8 flights, and mixed on the remaining 10.

Indicated airspeeds were 85 to 140 knots at altitudes 3000 to 6000 feet. Ice thickness ranged from 0.1 to nearly 1.0 inches. Air temperatures were -8 to -3°C (17.5 to 27°F). Generally, ice was collected at almost constant speed, but on four tests the speed was varied (three decreasing and one increasing), with resulting angle of attack change, to obtain a wider ice collection on the wing.

After the desired ice was accreted, the altitude was increased to reach a cloud-free atmosphere for obtaining good photographs.

C. Results

Figure 6-2 shows a sequence during de-icing, with pictures taken at about 4 second intervals. For this test, conditions were: TAS 139 knots, altitude 3075 ft, outside air temperature -5°C, LWC 0.38 g/m^3, ice thickness about 0.7 inches.

Ice removal was very good, being (by pilots' testimony) always better than the adjacent boots. Two de-icing attempts were judged to be fair-to-poor. If a very thin layer of ice (about 0.1 inch) was pulsed, then only half of the ice was shed. A second sequence of impulses removed half of the residual. Changing speed during ice accretion had no noticeable effect. When ice was accumulated beyond about 2% chord on top or bottom, some residual ice tended to be left after de-icing. This suggests that for leading edges of this 2.5 inch radius or greater, two coils (upper and lower) may be needed rather than the single nose coil.

No EMI problems could be found, even though all flight and data acquisition instruments were turned on and monitored. The sound made by the electrical discharge could not be heard inside the cabin in flight.

D. Conclusions

The system worked well and de-iced the aircraft well and reliably. The natural icing was easier to remove than that encountered in the icing tunnel.

II. Cessna TV 206 Flights (1984)

In February-March 1984, Cessna Aircraft company made fifteen flight over the Wichita, Kansas area in a Cessna 206 partially protected by an EIDI system. Alan A. Mueller of Cessna's Pawnee Division was Project Engineer and operated the EIDI system during these flights. The 206 pilot was Doug

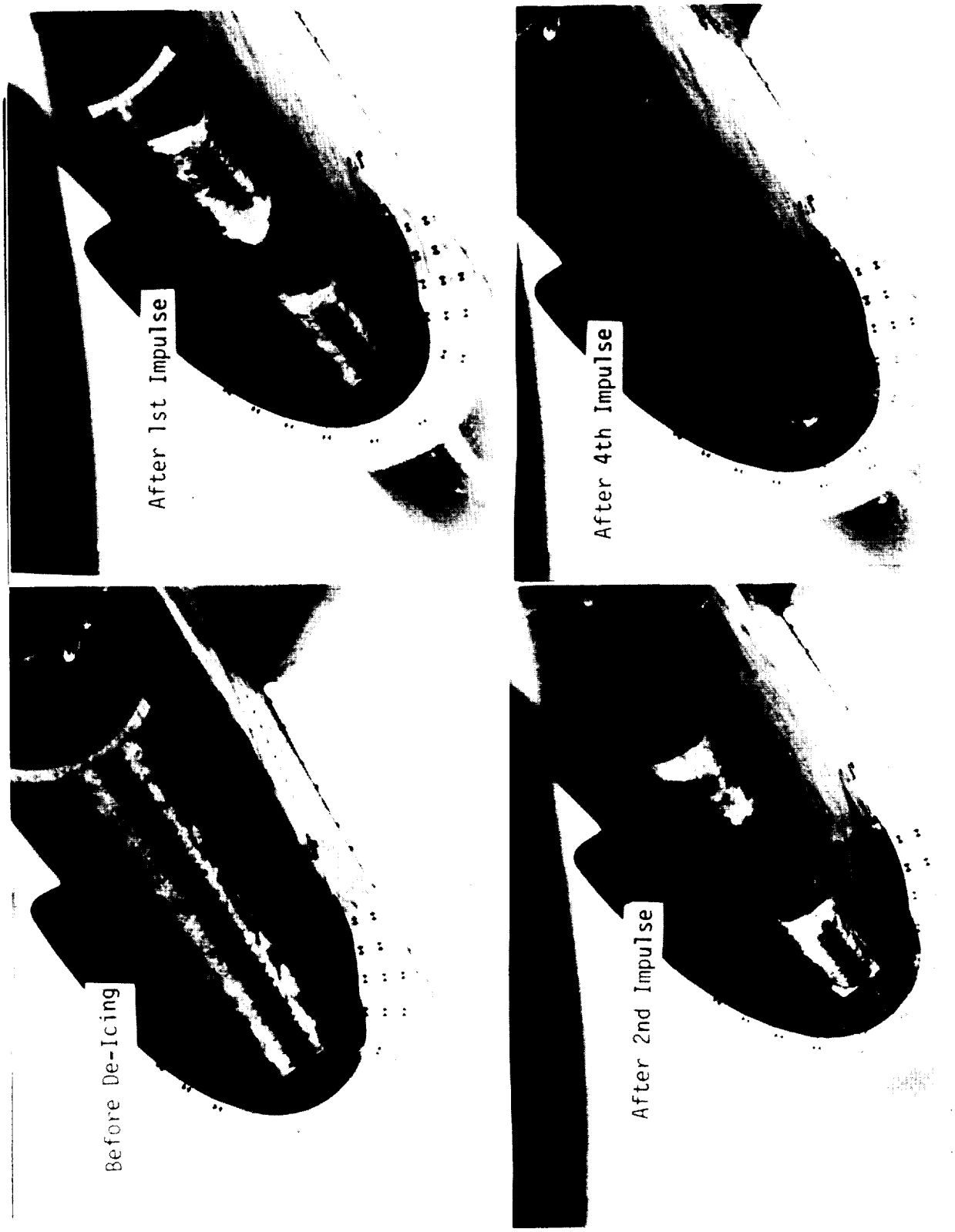

Fig. 6-2 Removal of Natural Ice Shown in Four Impulses.

Bassett and tanker pilot was Tom Wallis. Prior to this time, the C-206 wing had two test series in the NASA Icing Research Tunnel with EIDI coils installed. A grant from the State of Kansas Advance Technology Commission enabled W.S.U. to give more specific support than would otherwise have been possible. The purposes were:

1. To expand experience with the EIDI system/206 wing combination to include flight in tanker icing spray and natural icing conditions in addition to the previous wind tunnel experience.
2. To bring experience in-house for both the operational and design aspects of the system.
3. To increase the visibility and credibility of the program within the company.

Fifteen flights were made over the Wichita, Kansas, area during February-March, 1984.

A. Equipment Used

The test vehicle was the engineering prototype Turbo-206, a single engine, propeller-driven, high wing, six-place aircraft. Wichita State University personnel fabricated and installed seven, 2.25 inch diameter electro-impulse coils in a production leading edge assembly supplied by Cessna. The EIDI coils were supported by composite beams suspended between ribs. Doublers and gaps were similar to those in the Twin Otter. The modified leading edge was then installed on the TU-206 in the Cessna experimental shop. The portion of the right wing that was to be de-iced was painted black to make the ice more visible and the rib locations were highlighted with a yellow stripe to mark the bays; Fig. 6-3. Coil locations were marked, and the bays identified, with three inch numbers. Seven bays were equipped, having rib spacings varying from 7 to 18 inches, for a total

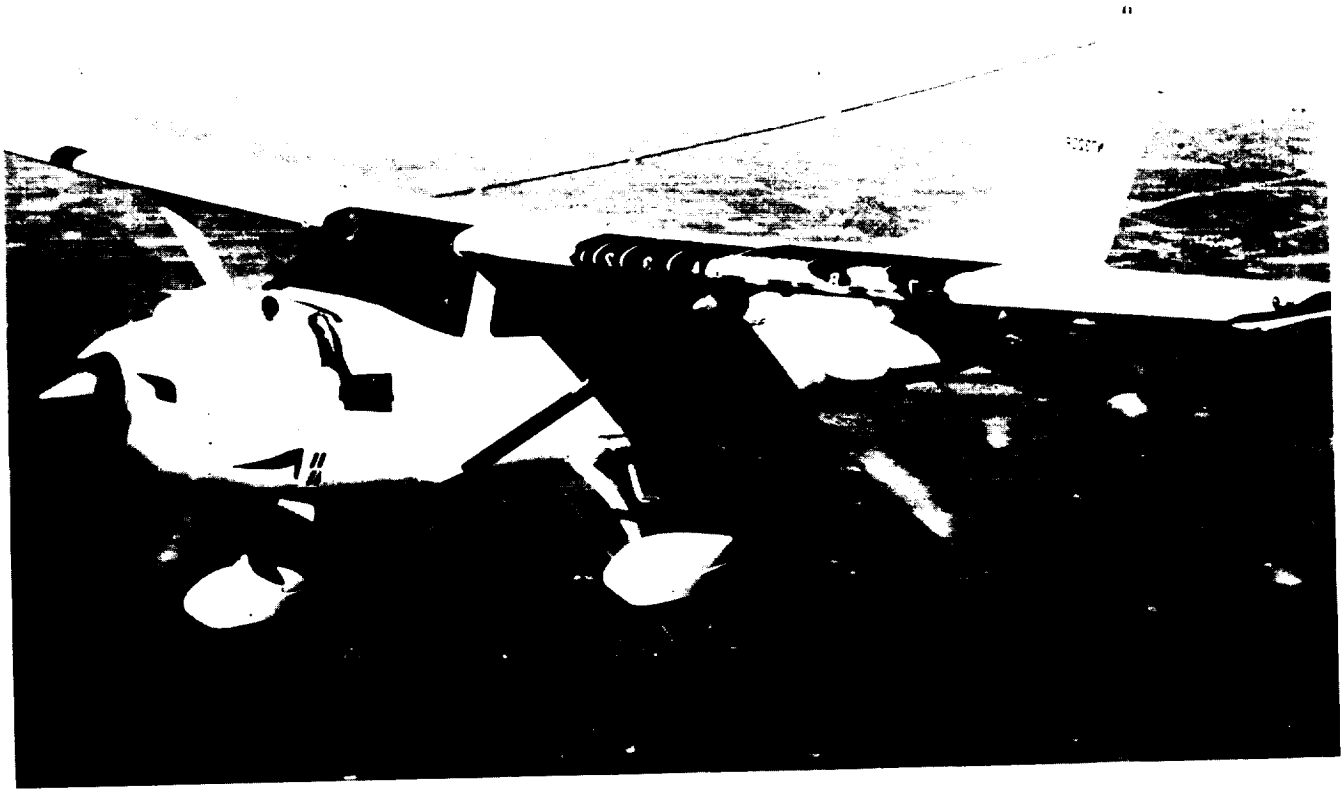

Fig. 6-3 Cessna TU 206 Test Aircraft

Fig. 6-4 Cessna 206 with Icing Tanker

span of 8 feet. Metal tabs with 1/2 inch wide stripes were mounted on the wing leading edge as an aid in gauging the ice thickness. In addition to the wing installation, a pair of coils were installed in the wing strut. Two, 1.5 inch diameter coils, wired in series, were embedded in foam inside the strut. (Note that the number 8 on the strut is not over the coils but is about 8 inches above the coils).

The coils were connected in alternating pairs (1-3, 2-4, 5-7, and 6-8) and were pulsed two or three times each. The EIDI control box and power supply were the same as those used in the DHC-6 tests, above.

The tanker used was a Cessna 404 equipped with two 100 plus gallon water tanks, a pump system, and spray bars mounted on top of the vertical tail. About forty minutes of spray time was available on each flight, with a spray plume about 4 feet wide. The 206 is shown in formation with the tanker during ice accretion in Figure 6-4.

Documentation was provided by camera(s) mounted in the blister on top of the 206 cowl and cameras in the tanker and/or a separate photo chase plane.

B. Test Procedures

After locating an altitude where the desired temperatures were available, the tanker pilot would turn on the spray pump. Once started the pump could not be stopped without freezing the spray system. Unable to see the test vehicle, the tanker pilot was required to hold altitude, heading and airspeed so that the pilot of the 206 test vehicle could maneuver behind him and position the spray over the portion of the airframe to be iced.

As the ice accumulated the airspeed decreased due to drag, and the pitch attitude increased. A typical flight would start at 115 to 120 KIAS and would decrease to about 95 KIAS by the time 1/2 inch of ice had built up. This required close coordination between the two aircraft on airspeed control.

For most of the test program, a photographer rode in the tanker which required the 206 to move out of the water spray and reform on the left wing of the tanker. Starting with flight 12, a separate photo chase plane was use which allowed the 206 to remain in the water spray during the de-ice cycle. This was found to have a significant effect on the operation of the system as discussed below.

The primary form of data acquisition was photographic. On the early flight a video camera was mounted in the cowl camera housing, and a 35mm still camera was carried in the tanker. The video camera allowed the flight test engineer to monitor the image while it was being recorded. Since no processing was required, it provided instant review of the flight on the ground after the test. On later flights, the video camera was replaced with a 500 frames per second movie camera and a 35mm still frame camera with a motor drive. The video camera was used from the tanker as a back-up in case the other cameras should fail to operate. On the last flights the video camera in the tanker was replaced by a 16mm movie camera running at normal speed and a 35mm still camera in a photo chase plane. Each media added its own unique contribution to the understanding of the de-icing mechanism on the electro-impulse system.

C. Tanker Ice

Twelve flight were made with tanker icing. The photo sequence shown in Figure 6-5 was taken on flight 5. This sequence illustrates the clearing pattern adopted for the bulk of the tests. Three pulses were sent to alternating pairs of bays wired in series. Bay 6 was wired in series with the coil pair in the strut. The two stage clearing action of fracture and expel are clearly shown. In this test, two pulses were adequate to clear the bays. However, on other tests three pulses were required. In all cases, each impulse had energy of less than 140 joules per bay.

Test conditions were varied on subsequent flights to cover a range of temperatures and ice thicknesses. The system was successful in clearing ice ranging in thickness from 1/10th of an inch to in excess of one inch. The temperature was varied from 5° to 30°F. The most difficult ice to clear was the extremely thin, warm ice. In this case, some residue was left on the rib locations with approximately 90% of the area between the ribs clean.

On the flights using a separate photo chase plane the system was activated while the airplane remained in the water spray. This caused a significant degradation in system effectiveness. Up to three cycles of the system were required to clear ice that had cleared easily in one cycle on previous tests. There were three significant variables different on these tests. The presence of liquid water on the surface of the ice caused the fractures in the ice to fill with water. This water apparently damped the action of subsequent pulses and allowed the ice to refreeze between cycles. It was also estimated that the 206 was flown closer to the tanker than on previous flights and that the water in the tanker was warmer than on earlier flights. This tended to create a greater amount of runback with clear ice extending 12 to 14 inches along the lower surface of the wing. Examination

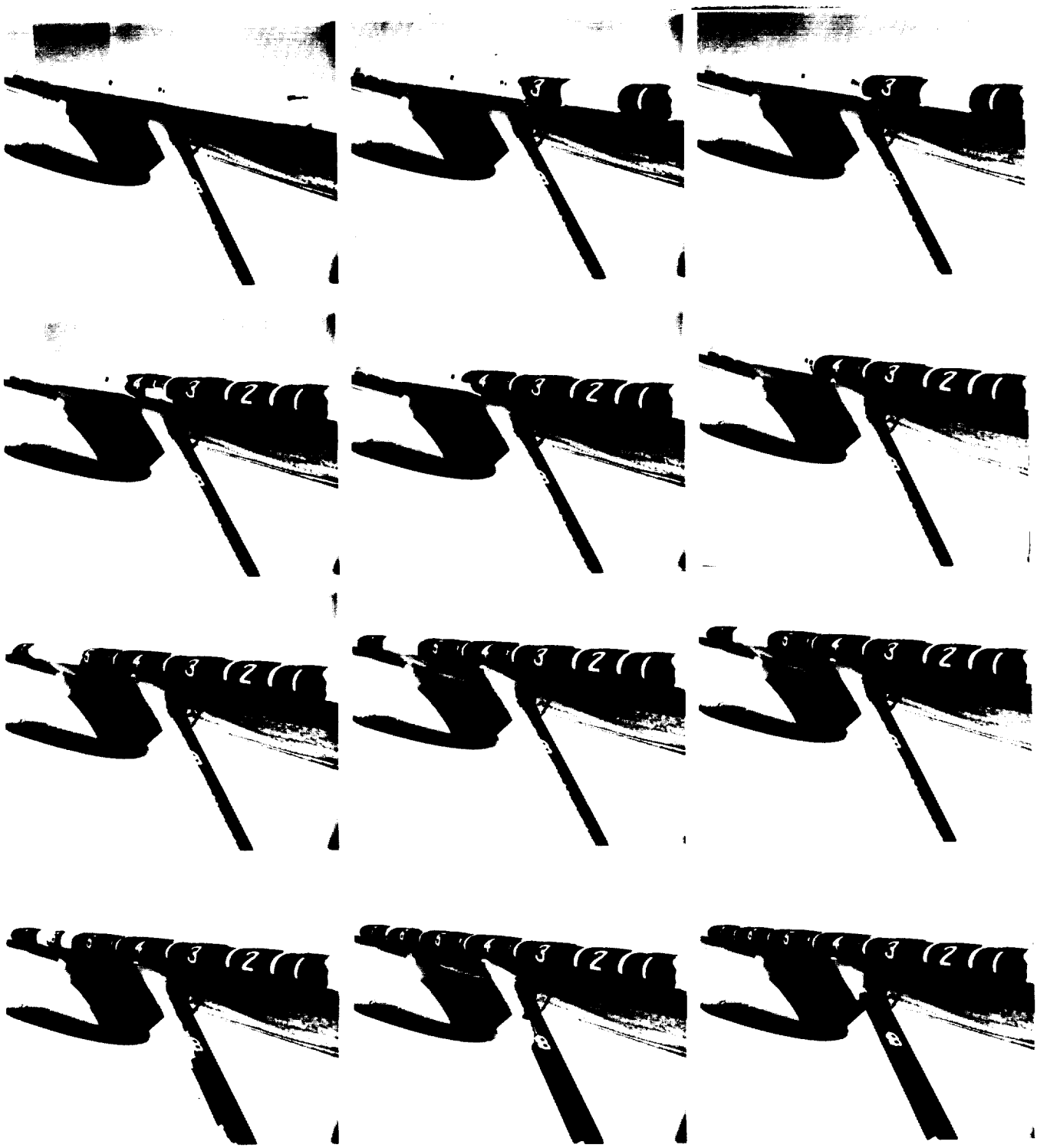

Fig. 6-5 De-icing Sequence of Cessna 206 Wing with Tanker Spray Ice

of the high speed movies revealed that ice was being fractured and pushed free of the wing, only to be pushed back into its original location by the air pressure and held by the ice ridge behind it.

D. Natural Ice

Natural ice flights were limited due to safety consideration. Other than the de-icing provided by the EIDI system and propeller de-ice, there were no other de-ice provisions on the airplane. We were therefore limited to icing conditions with warm air below and clear skies above. The two natural icing encounters were in thin stratus layers with a low liquid water content (not measured). One quarter inch of ice took approximately 20 to 25 minutes to accumulate and was a soft agglomerate of ice particles. This resulted in a considerable residue after the first clearing cycle. This residue provided seed points from which the next accretion grew and seemed to promote a more rapid and solid ice growth resulting in more complete clearing of the second ice build-up. Figure 6-6 shows the clearing cycle in light natural icing.

E. EMI/RFI

There was no evidence of any electro-magnetic or radio frequency interference problems on any of the flights. The equipment installed on all flights included two digital display NAV/COMs, ADF, RNAV, Autopilot, and Weather radar. In addition there was a LORAN-C installed for part of the flights with no detrimental effect on its operation.

F. Noise

The noise level when operated on the ground is quite startling but in the air is noticeable but not disconcerting. It may even be comforting to

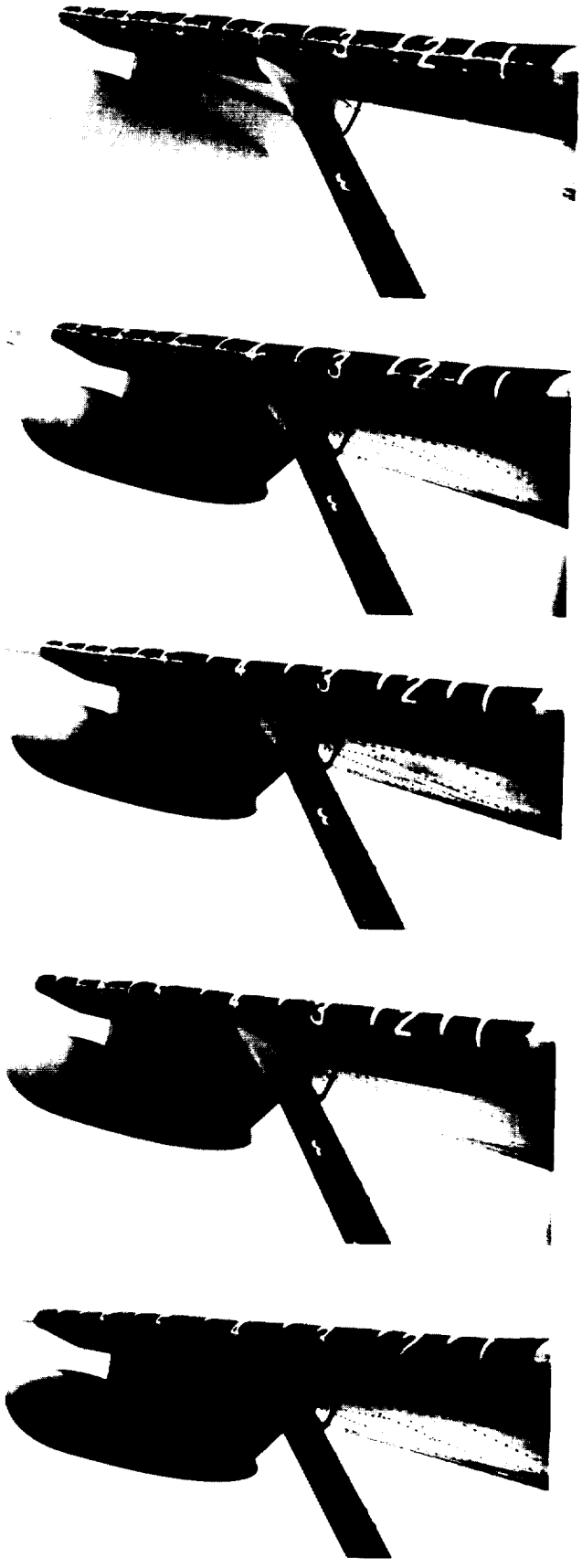

Fig. 6-6 Natural Ice De-icing Sequence

know that the system is working without requiring constant monitoring. A production aircraft would be quieter with a full interior installed in the cabin and some soundproofing in the wing root.

G. Conclusions

It is important that the coil mounts be stiff. The original mounts were too soft and absorbed some of the de-icing energy.

System components must be properly matched. Coils wound a little small had the compounding effect of reducing efficiency and limiting the voltage of the system due to approaching the current capacity of the SCR's.

Ice thickness ranging from 1/10th inch to over one inch can be shed successfully. As in the tunnel, warm soft ice is the most difficult to clear.

The presence of liquid water on the surface of the ice can effect the system operation. There are probably two mechanisms at work here: (1) The water coming out of the tanker was quite warm and did not cool to near freezing before impinging on the aircraft. This kept the ice temperature near the freezing point. (2) Liquid water on the surface quickly fills the cracks after the first pulse, damping subsequent pulses, and then refreezes. The quantity and temperature of this water probably does not represent natural ice. It does, however, point out the need to look at the effect of flight in natural ice near the freezing point.

In general, tanker ice is more difficult to shed than natural ice. Since the system was able to shed the tanker ice on all tests, natural ice should provide no significant surprises. Reference 6-2 gives further details of this test.

III. Other Flight Experience

Two other aircraft were equipped with EIDI and flown by members of the Consortium with some involvement of Wichita State university personnel.

A. Cessna 206

After the tests reported in Section II of this chapter, the Cessna model 206 airplane was fitted with a complete EIDI system. This included coils in both wing, both wing struts, and all three tail surface leading edges. Anticipating both new production installations and retrofit, several design changes were made from the wing and strut installation tested above. In addition, empennage installations were designed. Changes were made in wing rib spacings (to 18 inches) and skin thickness to be more congenial to the EIDI components, and to the strut and tail to facilitate EIDI installation under both field and factory conditions. All these changes were tested in the IRT on Nov.-Dec. 1984. These are the changes that Cessna would perform for retro-fitting EIDI to this aircraft.

The plane was flown for a limited number of natural icing natural test flights and on at least one cross country flight which had icing encounters. On a flight from Wichita to Cleveland, OHio, on June 12, 1985, the 206 was flying along the rear of a storm front and the airplane collected ice at two different times. The plane was well and easily de-iced both times.

Due to the severe recession in general aviation aircraft sales in the 1984-88 period, the Cessna 206 was taken out of production along with almost all other piston engine Cessna products. Therefore the planned development of EIDI for Cessna products has been delayed.

B. Boeing 575

In February 1987, flight test of a Boeing 757 test aircraft were conducted with EIDI coils installed in two of the five leading edge slats of the left wing. (Reference 6-3) These were the most inboard slat and the second slat from the tip. One central power supply was used; several departures were made from the EIDI design tested in this program. In an attempt to use only one coil per span station, higher energy level per coil were used. Capacitor voltage used was up to 3,000 and current peaks were about 3,000 amps. The single coil was placed on the pressure side of the stagnation line. Since energy varies as the square of the voltage, well over four times as much energy per impulse coil was used as on any other reported in this report.

Numerous natural icing encounters were made and the system performed well. Difficulty expelling ice was encountered only for the most inboard section of the inner slat, where the slat was very large. The noise of the discharges were audible only to a person sitting immediately adjacent to the inboard leading edge. No electro-magnetic interference was detected, even though the EIDI power lines shared the leading edge with the engine control lines for part of the span. Fatigue tests were also conducted, which will be described in Chapter 7.

IV. References

6-1. Zumwalt, G.W. and Mueller, A.A., "Flight and Wind Tunnel Tests of an Electro-Impulse De-Icing System", AIAA/NASA General Aviation Technology Conference, July 10-12, 1984, Hampton, VA. AIAA Paper No. 84-2234.

6-2. Mueller, A.A., Ellis, D.R., and Bassett, D.C., "Flight Evaluation of an Electro-Impulse De-Icing System on a Light General Aviation Airplane." AIAA/AHS Aircraft Designs, Systems and Operations Meeting, San Diego, CA., October 1984. AIAA Paper No. 84-2495.

Chapter 7. FATIGUE AND ELECTRO-MAGNETIC INTERFERENCE TESTS

I. Fatigue Testing

A question which always arises when EIDI is described is the effect of repeated impulsive loads on the structure and skin of the aircraft surface being ice protected. Little work has been reported on fatigue of materials subjected to impulsive blows. Therefore, a set of fatigue tests have been performed on aircraft wing leading edges. It may seem that such testing would have been done much earlier in the development program. In all candor, it must be admitted that the reason for delaying these tests was very practical. For much of the program only one general purpose power-and sequencing box was available for laboratory and icing tunnel testing. It was feared that a fatigue test would reveal that the weak link was the power/sequencing system itself. A failure would bring all of the EIDI testing to a halt. With the acquisition of another six-channel power supply, fatigue testing was begun. It was found that the fears for the life expectancy of the Simmonds-Precision power box were unfounded. Well over 100,000 impulses have been added to those of the previous four years of testing, and no deterioration is to be seen.

A. Metal Leading Edges

Two metal leading edge sections from Cessna 206 Wings were made for the test at Cessna Aircraft Company in Wichita, using standard manufacturing methods. Both were six-foot long spans with ribs at 18 inch spacings. A single nose coil was placed in the center of each resulting 18 inch bay. One model had then skin of 0.025 inch thickness, and the other had 0.040 inch thickness. Both were 2024 - T3 aluminum. Using the coil mounting methods used in the flight test C-206 aircraft, the coils were mounted on a

beam of fiberglass supported between ribs. The beams had a U-shaped cross section, with the coil formed around the bottom of the U as shown in Figure 7-1. The coils were then fitted into the nose of the leading edge with a 0.10 inch gap between coil and skin The beams were attached to the ribs by stretch-formed aluminum brackets. One of these can be seen in Figure 7-2 .

The coils were connected in alternate pairs; i.e. bays 1 and 3 were connected in series, and 2 and 4 were also series connected. The capacitors were charged to 1,000 volts and 400 micro-Farads. This gives 67 Joules per foot of span.

Accelerated testing was done with impulses at ten second intervals. The required impulse strength for ice removal for this aircraft wing had been established in three icing tunnel test and two flight tests for this same structure and EIDI system. A twenty year use of the system in normal flight was estimated to be 15,000 hits. Before beginning the tests, the models were inspected and current traces were recorded, since changes in the coil-to-skin gap is readily detectable from current-time plots. The current trace was monitored at least once per hour, and the model was visually inspected at these intervals.

After 7,500 impulses, the model was removed from the cold box for a more thorough inspection. No damage could be detected except for some more fretting around rivets at the end ribs where the leading edge skin had been cut off. At about 11,500 hits the sound of one bay changed for both models. The model was then removed and inspected and a crack was found in one of the sheet metal brackets attaching rib to coil beam (Fig. 7-3). Testing was resumed and continued to 15,000 impulses. A final inspection indicated that beam bracket cracks had occurred on three of the four beams for the

thicker skin model. Clearly, the brackets needed re-designing. No surface deformation, delamination, skin cracking or rib de-bonding was detected. Current traces for the bays with ribs intact at the end were compared with those made at the start of the test and were essentially identical.

B. Composite Leading Edge

A composite leading edge was similarly tested for fatigue. A leading edge from a Learfan aircraft was made of Kevlar for bird impact capability. It had a small radius nose and nearly straight upper and lower surfaces just behind the nose. This called for a coil-pair at each span station, one on upper and one on lower surfaces. The length was 38 inches with no ribs. Two spanwise coil stations were used, giving 19 inches to be cleaned by each coil station. The two coil stations were connected in series and supplied with 1200 volts and 550 microfarads stored energy, giving 125 joules per foot. Doublers were bonded to the skin opposite the coils. An ultrasonic scan was made of the model before the test to insure that there were no voids or delaminations. After 20,000 impulses no damage was visible. An ultrasonic scan showed no detectable change from the original. Again the energy levels used were those previously determined from icing tunnel tests.

C. Band-aid Coil Mount

A coil mounting method which is superior in most ways to any other is the skin-supported design termed "band-aid". A semi-rigid rectangular fiberglass plate has a coil at its center and is bonded to the skin at its ends, resembling an oversized adhesive bandage. The advantages are: (1) light weight, about 5 ounces; and (2) effective de-icing since all of the energy is put into the skin. The only drawback is that the impulse force

puts the adhesive bond in tensile "peel" which is perhaps the worst stress condition. Riveting the mount to the leading edge is an obvious alternative, but many structural designers dislike punching holes in their leading edges. Therefore, fatigue tests of a band-aid coil were performed.

This mount had been used previously in several icing tunnel tests, and although it de-iced with less that 70% as much energy as any other design, difficulty was experienced in maintaining a good bond to the skin. A similar difficulty had occurred for doublers which were bonded to the skin. The impulses had the same effect as repeated blows with a ball peen hammer; the edges tended to curl and initiate de-bonding. A bonding agent was needed which would not become brittle, but would retain a rubbery consistency with adequate strength. Number 3840 urethane by Hexcell had been found to be good for the doublers and was used in these fatigue tests for the band-aid.

The tests were performed in the same manner as described above for the metal leading edges. 20,000 impulsive blows were delivered, with an inspection after each 5,000. No change occurred in the current trace and no de-bonding was discernible by ultrasonic scanning. Electrical parameters were 650 volts and 550 microfarads.

D. Boeing Tests

Boeing Commercial Airplane Company conducted a series of ground and flight tests to evaluate the EIDI system for the 7J7 aircraft. The flight tests were performed in early 1987 in a Boeing 757 airplane. Coils were placed in two leading edge slats on the left wing; no. 2 (second inboard from the tip) and no. 5 (inboard slat). Fatigue tests were run in the

laboratory before the flight tests. A lifetime maximum impulse total of 60,000 hits was predicted and, to allow for the possible effects of combined stresses, a multiple of this number was deemed to be required. With 0.062 inch thick 7075 aluminum skin, and a doubler bonded opposite the coil over 200,000 impulses were endured without damage. A Boeing proprietary bonding agent was used on these doublers.

II. Electromagnetic Interference Tests

In addition to the electromagnetic interference (EMI) tests reported in Chapter 6 in connection with flight tests, laboratory tests have been performed.

Near the beginning of the project, Simmonds-Precision Engine Systems Division conducted EMI laboratory in 1983 using Military Specifications. Coils were placed in a simulated aluminum leading edge in a electrical shielded room. For EIDI coils contained in an aluminum enclosure the emissions were well within the Mil. Specs. When one end of the wing was open, however, sizable interference signals were emitted.

In January, 1988, EMI tests were conducted by W.S.U. personnel at the Boeing Military Airplane Company EMI test facility. A Cessna airplane leading edge with 0.025 inch thick 2024 aluminum was fitted with two coils. Emission were far below both FAA and Mil. Spec. requirements as long as all wires external to the wing were well shielded.

When a composite (Kevlar) leading edge was similarly tested, emissions were far above the acceptable level unless all wires were well shielded. The wires were the major source of emissions rather than the coil. Much of the coil emissions were shielded by grounding the aluminum doubler. The

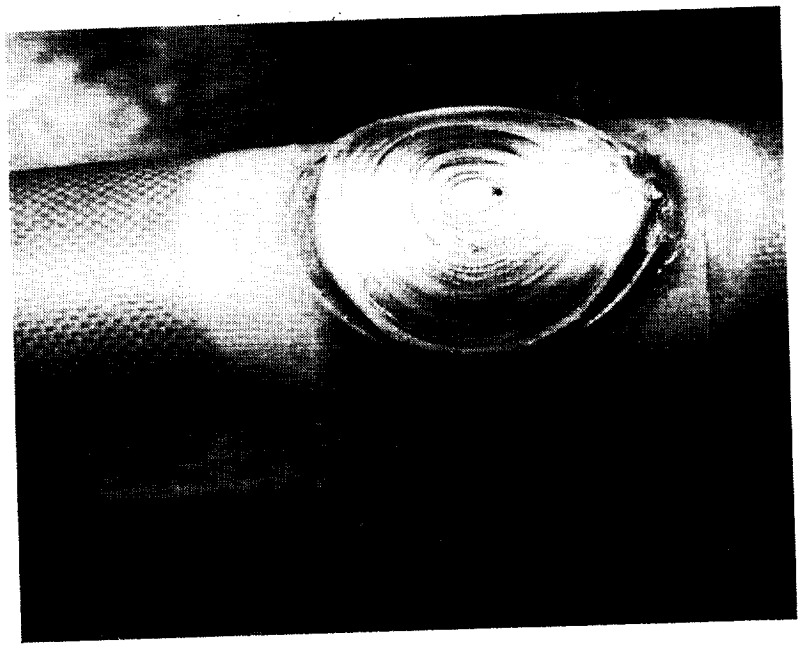

Figure 7-1 Coil on U-shaped Beam

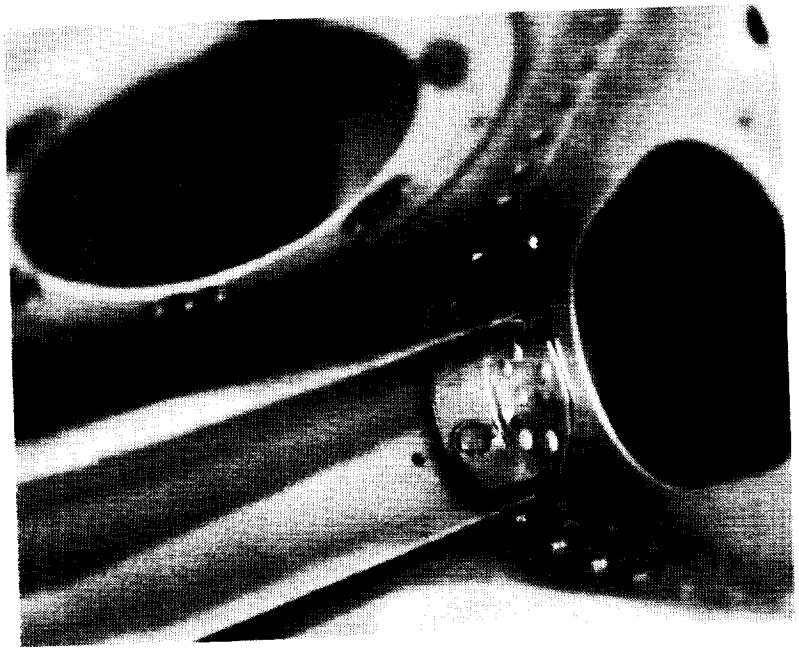

Figure 7-2 Beam-to-Rib Bracket

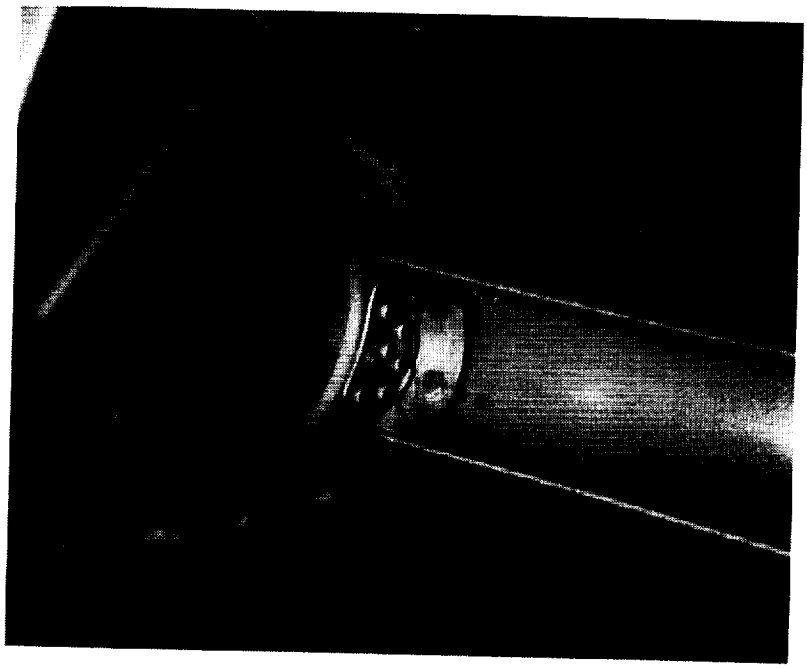

Figure 7-3 Broken Bracket

CHAPTER 8

APPENDIX A

W.S.U. Participants on EIDI Project

Glen W. Zumwalt, Ph.D., Distinguished Professor of Aeronatical Engineering, Project Director, May 1982 to October 1987.

Robert L. Schrag, Ph.D., Professor of Electrical Engineering, Leader of Electro-Dynamic Research, May 1982 to October 1987.

Walter D. Bernhart, Ph.D., Professor of Aeronautical Engineering, Leader of Structural Dynamic Research, May 1982 to October 1987.

Thangavel Paramasivam, Ph.D., Ass't. Professor of Aeronautical Engineering, Research on Composite Materials Dynamics, May 1982 to March 1983.

Robert Friedberg, M.S.A.E., Research Associate in Aeronautical Engineering, Leader of Manufacturing Methods, May 1982 to October 1987.

Robert E. Henderson, M.S.E.E., Ass't Professor of Electrical Engineering, January 1984 to December 1986.

Curtis Luginbill, Chief Technician, Dec. 1982 to Dec. 1983.

Fred Cook, Chief Technician, Jan. 1984 to Apr. 1984

Vernon L. Hagnauer, Chief Technician, May 1984 to October 1987

B. Keith Wilson, B.S.A.E., Research Assistant, Jan. 1984 to March 1985

Peter Gien, M.S.A.E., Research Assistant, May 1984 to October 1987

Elias Bounajm, M.S.A.E., Research Assistant, Sept. 84 to May 1985.

Dan Christmore, M.S.A.E., Doctoral Fellow, Aug. 1984 to December 1985.

Michael Schmitt, Student Assistant, Feb. 1984 to May 1986.

John Schwartz, Student Assistant, Feb. 1984 to October 1987.

Mondhes Yahiaou, Student Assistant, Feb. 1985 to May 1985.

INDUSTRIAL PARTICIPANTS

APPENDIX B

Beech Aircraft Company, 9707 E. Central, Wichita KS 67201
Harold Riesen 316/681-7944

Bell Helicopter Textron, P.O. Box 492, Ft. Worth, TX 76101
Herbert J. Coffman 817/280-4003

Boeing Commerical Aircraft Co., P.O. Box 3707, Seattle, WA 98124
Douglas Cozby, M.S. 47-03 206/237-6021

Boeing Vertol Co., P.O. Box 16858, Ridley Park, PA 19142
Andrew A. Peterson 215/591-2675

Cessna Aircraft Company, P.O. Box 7704, Wichita, KS 67277
David Ellis 316/946-6602

Electro-Delta, Inc., P.O. Box 8, White Oak, TX 75693
George Massey 214/759-3942

Gates Learjet Corp., P.O. Box 7707, Wichita, KS 67277
Allyn Heinrich 316/946-2881

Douglas Aircraft Div. of McDonnell-Douglas Co., 3855 Lakewood Blvd.,
Long Beach, CA 90846
David Blyther M.C. 212-12 714/229-7191
Lou Baretto, M.C. 212-12 714/224-7189

Rohr Industries, Inc., P.O. Box 878, Chula Vista, CA 92010
Herman A. Rosenthal, M.Z. 19T, 619/691-3420
Don Nelepovitz, M.Z. 19T, 619/691-2038

Simmonds-Precision Co., Engine Systems Div., P.O. Box 310, Norwich NY 13815
Albert Kodet 607/335-5358

Sikorsky Aircraft Co., North Main St., Stratford, CT 06601
Robert Flemming 203/386-5789

NASA
National Aeronautics and Space Administration

Report Documentation Page

1. Report No.	2. Government Accession No.	3. Recipient's Catalog No.
NASA CR-4175		

4. Title and Subtitle	5. Report Date
Electro-Impulse De-Icing Testing Analysis and Design	September 1988
	6. Performing Organization Code

7. Author(s)	8. Performing Organization Report No.
G.W. Zumwalt, R.L. Schrag, W.D. Bernhart, and R.A. Friedberg	None (E-4279)
	10. Work Unit No. 505-68-11

9. Performing Organization Name and Address	11. Contract or Grant No.
Wichita State University Department of Aeronautical Engineering Wichita, Kansas 67208-1595	NAG3-284
	13. Type of Report and Period Covered Contractor Report Final

12. Sponsoring Agency Name and Address	14. Sponsoring Agency Code
National Aeronautics and Space Administration Lewis Research Center Cleveland, Ohio 44135-3191	

15. Supplementary Notes

Project Manager, John J. Reinmann, Propulsion Systems Division, NASA Lewis Research Center.

16. Abstract

Electro-Impulse De-Icing (EIDI) is a method of ice removal by sharp blows delivered by a transient electromagnetic field. Ribbon wire coils are rigidly supported just inside the aircraft skin. A high voltage capacitor is discharged through the coil, producing a repulsive force between the coil and a conductive skin. The advantages are very low energy, reliable de-icing and minimal maintenance. This report gives the results of a five year EIDI research and development program at Wichita State University, sponsored by the NASA Lewis Research Center and involving ten participating aerospace industrial companies. Detailed results are given for studies of the electrodynamic phenomena by laboratory tests and by analytical and computational studies. Structural dynamic tests and computations are described. Also reported are results of ten sets of tests at NASA's Icing Research Tunnel and flight tests by NASA and Cessna Aircraft Company. Fabrication of system components are described and illustrated. Fatigue and electromagnetic interference tests are reported. This report provides the necessary information for the design of an EIDI system for aircraft.

17. Key Words (Suggested by Author(s))

Electro-impulse de-icing
Ice protection system

Date for general release September 1989

Subject Category 05

19. Security Classif. (of this report)	20. Security Classif. (of this page)	21. No of pages	22. Price*
Unclassified	Unclassified	352	A16